DISSERTATION

INVESTIGATING THE ORIGINS OF SLOW MAGNETIC RELAXATION OF $S = ½$ NI(III) CYCLAMS

Submitted by

Thomas L. Morrison

Department of Chemistry

In partial fulfilment of the requirements

For the Degree of Doctor of Philosophy

Colorado State University

Fort Collins, Colorado

Summer 2023

Doctoral Committee:

Advisor: Matthew P. Shores

Joe Zadrozny

Alan Kennan

Martin Gelfand

ABSTRACT

INVESTIGATING THE ORIGINS OF SLOW MAGNETIC RELAXATION OF $S = ½$ NI(III) CYCLAMS

This dissertation describes the syntheses and characterizations of several Ni(III) and Ni(II) complexes in an attempt to better understand the origin of slow magnetic relaxation, or spin reversal, in $S = ½$ systems by utilizing Ni(III) cyclam (1,4,8,11-tetraazacyclotetradecane) as a toy model system. The content is organized as follows:

Chapter 1 provides the historical context and theory surrounding the class of materials called single molecule magnets (SMMs). Therein I describe the prototypical SMM and its primary figures of merit and characteristics, such as S and D, followed by the observation of how $S = ½$ systems, which have previously been shown to act as SMMs, do not fit within the context currently provided by the literature. The choice of using the Ni(III) cyclam system is then elaborated upon, along with its quirks and foibles.

In Chapter 2 I describe the synthesis and magnetic characterization of three Ni(III) cyclams. The first two contain halides in the axial positions, which are 100% abundant in isotopes containing nuclear spin, and the third complex has perchlorate bound in the axial position, where oxygen is nearly nuclear spin free. Neither halide systems showed slow magnetic relaxation, but it was not clear whether it was due to the superhyperfine coupling between the nuclear and

electronic spins or due to the antiferromagnetic interactions present at low temperatures. The perchlorate containing complex did show slow magnetic relaxation, consistent with the literature and our predictions.

Chapter three describes the crystallographic tuning tools and corresponding magnetic properties of novel $S = ½$ Ni(III) cyclam complex salts: strong antiferromagnetic coupling in sulfate-bridged chain $\{[Ni(cyclam)(\mu^2\text{-}SO_4)]ClO_4 \cdot H_2O\}_n$ and field-, temperature-, and size-dependent slow magnetic relaxation in molecular $[Ni(cyclam)(HSO_4)_2]HSO_4$. I have reported two methods of manipulating the dynamic magnetic response of these coordination molecules: particle size selection and deuteration. I find that particle size dependency, which I attribute to the phonon bottleneck effect, for the magnetic dynamics in the parent protiated compound is removed in deuterated isotopologue, revealing only the faster molecular relaxation mode(s).

Chapter 4 describes the synthesis and characterization of four novel Ni(III) cyclams utilizing neutral ligands in the axial positions as opposed to the anionic ones considered previously, namely $[Ni(cyclam)(acetonitrile)_2]X_3$ (X = OTf, ClO_4, BF_4) and $[Ni(cyclam)(butyronitrile)_2]OTf_3$. Through these complexes we probe the role of ligand charge, identity, and subtle differences in the hydrogen-bonding network on the slow magnetic relaxation of the Ni(III) ion.

Chapter 5 describes the solution phase studies of $[Ni(cyclam)(MeCN)_2]OTf_3$ and $[Ni(cyclam)(butyronitrile)_2]OTf_3$ in glassy and non-glassy solvents, as well as their suitability for studying other novel species *in situ* that may not be able to be synthesized and measured traditionally. We find that there are significant differences in the magnetic relaxation of the Ni(III) cyclams between glassy and non-glassy solutions and discuss the possibilities these findings present.

In Chapter 6 I summarize the key findings from Chapters 2-5 and propose new avenues of research for further investigating this phenomenon.

Finally, in Chapter 7 I describe a different ligand involving intra-ligand π-π interactions and explore the feasibility of using such interactions for intelligently controlling and tuning the first coordination sphere geometry and electronic structure. By introducing new substituents, changes to the aromaticity, and oxidation of the ligand we are able to exhibit rational control over the crystallographic and electronic structure of the metal center.

ACKNOWLEDGEMENTS

I consider myself extremely lucky to have found myself in the position I have, surrounded by friends, family, and mentors who have guided and supported me throughout my studies. First and foremost, I would like to thank my wife Erin. Without her constant love and support, in good times and bad, I would not have been able to reach as far as I have and probably would have withered into nothing. I would also like to thank my parents, Jerry and Dianne Morrison, for being such a large and supportive part of my life. It wasn't until I moved away that I truly realized what wonderful parents I have, and the upbringing they've given me has given me the foundation I need so that I can stand and grow on my own, even though their support has never stopped. Next, I would like to thank my siblings, Chad, Amy, and Ray. I know recently I haven't been the most attentive brother, but even so you all have been there for me when I needed you most and I look forward to doing the same.

To my mother-, father-, and brother-in-law, thank you all for welcoming me into your family. I truly feel as if I have two families, and have felt that way for long before Erin and I were married. The love and support you've given me over these years has been every bit as important to me as the love and support I get from my parents, so thank you.

To my best friends, Jeremy and Joshua Jones, thank you for the good times, jokes, and the silent acceptance when I rage about the instruments being down. The levity you bring to my life keeps me grounded and focused.

To my lab mates: Rob Higgins, thank you for teaching me how to research effectively, even if I wasn't able to demonstrate it while you were watching. Romeo Portillo, thank you for teaching me how to do everything else in the lab, from using the glovebox to making base baths to how to (not) set clamps on fire. Justin Joyce, thank you for all the advice you've given me. Every bit of it has proven true, and has ignited my drive for learning as much as I can. I honestly think you are one of the smartest people I've met, even if you gave me my coffee addiction. Brooke Livesay, thank you for teaching me what kind of person and chemist I want to be. Claire Shugart, Brody Lennon, and Sam DalCais, although our time spent together has been short I have enjoyed our time together and the interesting conversations we've had. I hope you all find happiness.

To my mentors in the ARC, Brian Newell and Indrani Bhowmick, thank you for teaching me the skills I needed to know to pursue my research and for your help in realizing it.

Lastly, thank you Matt Shores for accepting me into your group. I know you were taking a chance when you accepted me and I can only hope that you found it as rewarding as I have.

DEDICATION

For my wife and best friend, Erin O. Bower

TABLE OF CONTENTS

LIST OF TABLES

LIST OF FIGURES

Chapter 1: Magnetic Relaxation in Single Molecule Magnets and the Draw of S = ½ `Systems

1.1 Motivation for Studying Single-Molecule Magnets

Single-molecule magnets (SMMs) are molecules that show a barrier toward spin reversal without the ferromagnetic interactions of traditional magnetic materials. SMMs are a promising area of research for their potential use as quantum bits (qubits) in emerging quantum computers, high-density data storage, and as gates for spin-polarized currents.[1–7] Although lanthanide SMMs currently operate at higher temperatures, SMMs derived from first-row transition metal ions are of interest due to their potential cost efficiency and increased sensitivity to local environments; and they present an opportunity to investigate the unique magnetic relaxation of $S = ½$ systems.[5] A small number of 3d coordination complexes containing V(IV),[8–10] Mn(IV),[11] low spin Co(II),[12–14] Ni(I, III),[7,15] and Cu(II)[16,17] ions have demonstrated slow magnetic relaxation in the $S = ½$ state, and present an opportunity to study the smallest unit of molecular superparamagnetic materials.

SMMs with $S > ½$ have an inherent barrier to transitions between the ground states, which can be overcome through quantum tunneling or energy absorption from vibrations to pass over the barrier. In contrast, the physical mechanisms behind the barrier and slow magnetic relaxation pathways in SMMs with $S = ½$ ground states are less straightforward and may result from intermolecular interactions influenced by spin-phonon dynamics.

This first chapter aims to introduce and familiarize the reader with the fundamentals of single molecule magnets (SMMs), commonly encountered experimental techniques, and an analysis of the possible relaxation pathways for these systems. I then introduce the peculiarities of the model systems that will be discussed in the later chapters.

1.2 Interactions with Neighboring Magnetic Units

Broadly speaking, the interactions between magnetic units can be categorized as paramagnetic, ferromagnetic, or antiferromagnetic. Other interactions exist but are far less commonly observed and are beyond the scope of this chapter. Paramagnetic interactions are those whose magnetic moments are noninteracting with each other, resulting in a random orientation of magnetic moments within the material, which averages to a net zero magnetic moment in the absence of an applied magnetic field, but can be influenced by applying a magnetic field. Ferromagnetic interactions are between magnetic moments that interact and affect each other in such a way that the magnetic moments align parallel to one another, resulting in an observable net magnetic moment even without applying an external magnetic field. These ferromagnetic interactions can occur through space (dipole-dipole) or through bonds and are responsible for what many people consider to be magnetic materials. Lastly, the antiferromagnetic interactions align the magnetic moments with one another such that they are antiparallel to their neighbors, resulting in an (approximately) net zero magnetic moment for the material, with or without an external magnetic field. Of course, applying a sufficiently strong external field can interrupt these interactions, allowing for even antiferromagnets to align their spins with the field.

The primary way to distinguish the type and strength of magnetic interactions a material has is by applying a static (DC) magnetic field and measuring the temperature dependence of the magnetic susceptibility, χ_M, or as I prefer, the susceptibility-temperature product, $\chi_M T$. Plotting the susceptibility as $\chi_M T$ allows for a quick inspection of the spin state and magnetic interactions of the material, as according to the Curie law, the $\chi_M T$ for systems where S is a good quantum is,[18]

$$\chi_M T = \frac{Ng^2\beta^2 S(S+1)}{3k} \approx \frac{g^2 S(S+1)}{8\ \mathrm{cm^{-3}K^{-1}mol}} \qquad \text{(Equation 1.1)}$$

where N is Avogadro's number, g is the gyromagnetic ratio, β is the Bohr magneton, and k is the Boltzmann constant. Since the spin is quantized, this allows us to quickly see the spin state of most systems by comparing the $\chi_M T$ value at saturation to the values in Table 1.1.

Table 1.1 Values of $\chi_M T$ as a function of the spin S.

S	$\chi_M T$ (g = 2, cm^3 K mol^{-1})
1/2	0.375
1	1.000
3/2	1.876
2	3.001
5/2	4.377

As the material is cooled, there are fewer thermal fluctuations that can disrupt any magnetic ordering, so the low-temperature $\chi_M T$ can give insight into such magnetic orderings, as shown in Figure 1.1. In the paramagnetic case, the $\chi_M T$ will stay relatively constant at all temperatures but may have a downward trend at low temperatures due to zero field splitting, which is the energy difference between magnetic states at zero applied field. In the ferromagnetic case, the $\chi_M T$ will increase significantly as the temperature decreases, the increase proportional to the strength of the ferromagnetic interaction. In the antiferromagnetic case, the $\chi_M T$ decreases as the temperature decreases, and if the interaction is strong enough, then the magnetic susceptibility will go to zero as the magnetic moments fully compensate for one another.

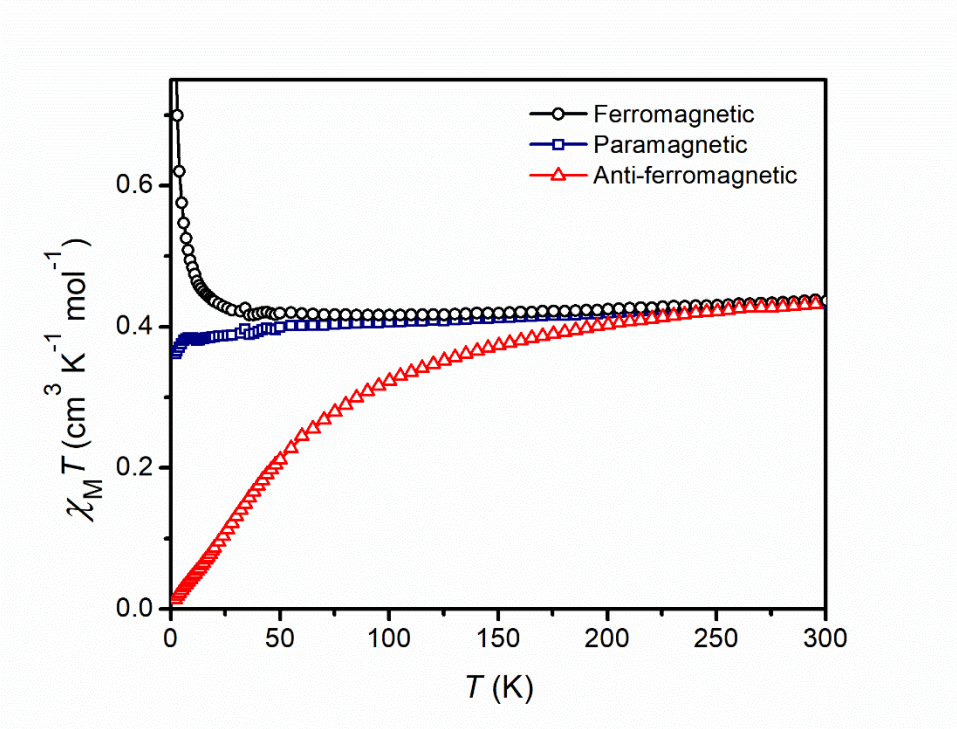

Figure 1.1 Representative magnetic susceptibility-temperature plot of an S = ½ system with paramagnetic (blue squares), ferromagnetic (black circles), and anti-ferromagnetic (red triangles) interactions. Data presented are for [Ni(cyclam)$(HSO_4)_2$]HSO_4, a fictitious S = ½ system, and [Ni(cyclam)(SO_4)]ClO_4, respectively.

1.3 Milestones within the SMM Community and the State of the Field

Superparamagnetism is the hallmark of SMMs and is the ability of a paramagnet to possess a barrier towards spin reversal, similar to those of ferromagnets.[12,19,20] Unlike ferromagnets, however, the barrier towards spin reversal does not come from the coupling to nearby magnetic moments but is intrinsic to the magnetic unit itself. The origin of this barrier has been investigated for several decades, and the field has done an admirable job of identifying the phenomena that affect the barrier height; however, our understanding of the origin has evolved and continues to grow.

The first single molecule magnets reported are widely considered to be $[Mn_{12}O_{12}(OAc)_{16}(H_2O)_4]\cdot 2HOAc\cdot 4H_2O$ and $[Mn_{12}O_{12}(O_2CPh)_{16}(H_2O)_4]$ when Novak *et al.* and Sessoli *et al.* reported on their magnetic properties in 1993.[21,22] Both complexes exhibited a barrier towards spin reversal in the alternating current (AC) magnetic measurements, the first systems to show such behavior without magnetic intermolecular interactions. This milestone study precipitated the field of single molecule magnets, and soon after its publication many other groups began to investigate this novel phenomenon.

Next, we will consider the theory as to why these Mn_{12} systems possess this superparamagnetism. The systems had $S = 10$ and $S = 9$, respectively, with significant and negative zero-field splitting (ZFS). The ZFS is responsible for splitting the energies of the magnetic states according to the Hamiltonian $H = DS_z^2 + E(S_X^2 - S_y^2)$, where S_x, S_y, and S_z are the spin along the x, y, and z directions, D is the axial ZFS term, and E is the rhombic ZFS term. The negative D parameter for the Mn_{12} complexes results in the $m_s = \pm 10$ (± 9) states being the ground state with $m_s = 0$ being the highest energy magnetic state.[23] These magnetic states can then be represented by a double well diagram, as shown in Figure 1.2. This double well diagram allows us to easily visualize where the barrier towards spin reversal may originate from as the transition between the ground states is forbidden, and so for reversal to occur directly we must go through the various microstates and through the $m_s = 0$ state.[24,25] The barrier height, or separation between the ground state and the maximal magnetic excited state, is then given by $U_{eff} = |D|S_z^2$ (or $U_{eff} = |D|(S_z^2 - ¼)$ for half-integer spin systems), and is approximately 60 cm^{-1} for both complexes.[26]

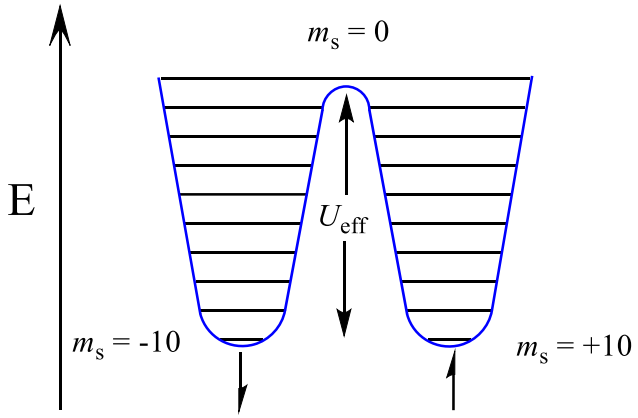

Figure 1.2 Double well diagram of the magnetic levels of the $S = 10$ Mn_{12} core.

These findings precipitated a new field of research, and for the next two decades research in the SMM community was consumed with increasing the U_{eff}, and it appears trivial to see that this can be easily done by increasing the D parameter and the S. Given that the scaling is quadratic with the S and the multi-nuclear nature of the original complexes it should be of little surprise that the early years were spent investigating the magnetic relaxation of metal clusters. Mn clusters were of particular interest, and not only due to precedence. High spin Mn(III) is $S = 2$ and is subjected to Jahn-Teller distortions when in an octahedral crystal field, leading to axial anisotropy, where the material has different (magnetic) properties along one axis than the other two axes, and significant ZFS.[26] However, while both of those properties are beneficial researchers showed that simply increasing the nuclearity of the clusters was not a viable path towards increasing the barrier height. For example, one Mn_{19} cluster had an impressive $S = 83/2$ but with a negligibly small D, producing a $U_{eff} = 4$ cm^{-1}. Indeed, many of the larger clusters showed similar symptoms, the symmetric cores of the clusters reduced the ZFS more than the larger S could compensate for. Thus, the field began to focus more on the anisotropy of the complexes to enhance the ZFS.

In general, there are two strategies towards designing complexes with very large magnetic anisotropy. Firstly, low-coordinate, mononuclear transition metals produce very anisotropic systems with very large values for *D*, and such systems normally possess extremely weak ligand fields, favoring spin-orbit coupling, but are difficult to synthesize and usually very reactive. Secondly, lanthanide coordination ions have extremely high anisotropy and significant spin-orbit coupling. In the case of the former there have been many examples, such as [K(2.2.2-cryptand)][Fe(C(SiMe$_3$)$_2$] reported by Zadrozny *et al.*,[27] and [(NHC)CoNDmp] reported by Gao *et al.* (Dmp = 2,6-dimesitylphenyl).[28] Both complexes show significant SOC and their calculated U_{eff} are much higher over the original Mn_{12} clusters at 226.4 cm^{-1} and 413 cm^{-1}, respectively. The first example of a mononuclear lanthanide SMM was reported in 2003 by Ishikawa when he reported on a Tb(III)(phthalocyanine)$_2$ sandwich type complex.[29] The strong spin-orbit coupling of this Tb complex (and of most lanthanides) results in the spin not being the unique source of angular momentum, and as a result the magnetic states are split into m_J levels instead of m_s. While not exactly the same, the interpretation is still similar and Ishikawa's Tb complex displayed a U_{eff} = 230 cm^{-1}.

It is from these principles that the molecule [Dy(Cp^{ttt})$_2$]$^+$ was designed, 14 years after the initial lanthanide-based SMM, and currently holds the record for the highest operating temperature.[30,31] This molecule possesses a spin S = 7/2, although the strong spin-orbit coupling makes J = 15/2 a more accurate description. It also possesses a strong and negative zero field splitting, resulting in the m_J = ± 15/2 states being the ground state. The U_{eff} = for [Dy(Cp^{ttt})$_2$]$^+$ is calculated to be 1,223 cm^{-1}, however experimental evidence shows that the true barrier height is lower than that of what is calculated. Despite this, the effective blocking temperature is still above 77 K, a milestone as liquid nitrogen is sufficiently cold to allow for observable slow magnetic

relaxation. The discrepancy between the calculated and experimentally determined U_{eff} is often waived away as being due to 'under the barrier' relaxation pathways. This is an apt, albeit vague, description and we will discuss these relaxation pathways and complications in greater detail *vide infra*.

1.4 Superparamagnetic Relaxation Pathways

The magnetic relaxation of SMMs and superparamagnets can occur through multiple processes, almost all of which involve phonons, or lattice vibrations, interacting with the magnetic states. These different processes scale differently with temperature and identifying which process is dominant can give us insight into the moieties involved in magnetic relaxation. The most commonly encountered relaxation pathways are the quantum tunneling of magnetization, direct, Orbach, and Raman pathways, and are shown in Figure 1.3.

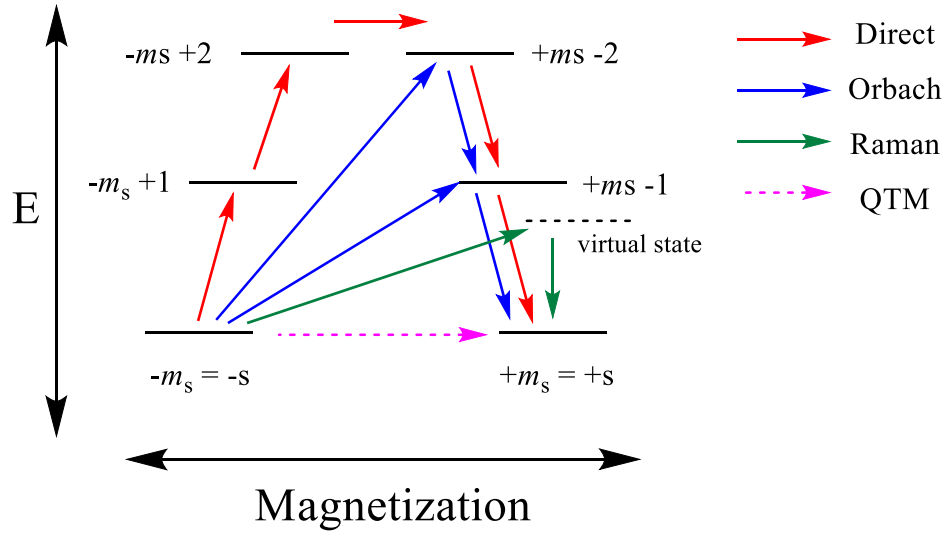

Figure 1.3 Schematic of the possible relaxation pathways for magnetic relaxation from the $-m_S$ state to the $+m_S$ state. Direct relaxation shown in red, Orbach relaxation shown in blue, Raman relaxation shown in green, and quantum tunneling of magnetization is shown in magenta.

Quantum tunneling of magnetization (QTM): The first relaxation pathway we will discuss requires no external stimuli, such as phonons, and happens spontaneously: the quantum tunneling of magnetization. This relaxation mechanism occurs when the energies of the $\pm m_S$ (or $\pm m_J$) are approximately equal and is often the dominant pathway at low temperatures. The QTM pathway is aptly named and is simply the quantum tunneling through the U_{eff} barrier from one ground state to the other. The related thermally-assisted quantum tunneling of magnetization (TA-QTM) is similar, but tunnels through degenerate excited states. While QTM happens spontaneously, research has shown that there are several design strategies that one can utilize in order to minimize its contribution. Firstly, weak intermolecular interactions should be reduced as much as possible as they can produce transverse magnetic fields that ultimately favor QTM. This is usually done by choosing large, bulky ligands to produce well separated magnetic units. Another option is to magnetically dilute the system with a diamagnetic analogue, provided such an ion also crystallizes in the same crystal structure. Secondly, reducing the role of hyperfine interactions between the electrons and nuclei (or super-hyperfine, if the electronic and nuclear spins originate from different atoms) is another strategy towards diminishing QTM. Practically speaking, however, this is done by using isotopically pure metals, which can be prohibitively expensive. The last, and perhaps simplest method is to apply an external magnetic field to split the degeneracy of the magnetic states. This quenches the QTM, but also means that the material requires an applied magnetic field in order for magnetic blocking to occur, which to some researchers signals that the material was never a SMM to begin with.

Direct relaxation: The relaxation between the two time-reversal conjugates ($m_s = \pm ½$) of $S = ½$ states is forbidden and is known as 'Van Vleck cancellation' as the transition matrix element must be zero between those two conjugates.[32] But the Zeeman interaction can lift that degeneracy

between the time-reversal conjugates of Kramer ions with an applied static (DC) magnetic field. The Zeeman interaction creates a small, finite energy difference between the spin 'up' and 'down' states and allows direct relaxation where the spin can absorb or release the low-energy acoustic phonon. The relaxation rate of the magnetization in direct relaxation is $\tau^{-1} = AH^nT$, where τ is the relaxation time, A is the coefficient containing the spin-phonon coupling matrix elements, H is the applied magnetic field, and T is temperature. For a Kramer ion (S = ½ in this case) n = 4, but if the hyperfine coupled state between electronic and nuclear spins are involved n = 2.[33] Note that direct relaxation is inversely proportional to temperature and magnetic field, thus at high applied magnetic field and/or temperature, this does not contribute significantly towards the overall slow relaxation of magnetization.

Raman relaxation: Raman relaxation is a two-phonon process involving all of the phonons within the system. In this process, the spin from a higher energy level absorbs a phonon to transit to a virtual state. Simultaneously it releases another phonon to the lower energy spin state, where the difference between the two phonon frequencies equals the energy of the spin level separation. Suppose the frequencies of the phonons participating in the Raman process are lower than the Debye frequency of the lattice, the temperature of a material's highest normal mode of vibration. In that case, the magnetic relaxation of Kramer ion follows a power law dependence of temperature, $\tau^{-1} = CT^9$, where C is the coefficient for the matrix elements. The experimental data of the Raman relaxation process of S = ½ electron in the molecular system does not always follow the $\tau^{-1} = CT^9$ relationship, but rather the power law varies as $\tau^{-1} = CT^n$ with $2 < n < 9$.[24,34,35] One of the hypotheses for the varied n values is that in a molecular system, due to many low-energy deformation modes, the optical phonon can also participate in spin-lattice relaxation, and the strict Debye model is not followed. Theoretical derivations show that depending on the eigenstates of

the optical and acoustic phonon in the latices that can interact with the spin, the T^n term can vary as n = 2-9 at low temperature.[24,34]

Orbach relaxation: Orbach relaxation is also a two-phonon process similar to the Raman process. Instead of a virtual intermediate state, the relaxation occurs via the definite low-lying magnetic excited states below the Debye temperature. The magnetic relaxation follows an exponential temperature dependence as $\tau^{-1} = \tau_0^{-1} exp(-U_{eff}/kBT)$, where the τ_0^{-1} is the pre-exponential constant and U_{eff} is the energy separation between the ground and exited state of the spins. Thus, the Orbach relaxation is not applicable for an S = ½ ground state with no possible excited state below Debye energy. In the case of significant orbital contributions not quenched by the ligand field of the molecule, the ground electronic S = ½ state can mix with the orbital terms to create spin-orbital ground and excited states (m_J states) inside the boundary of the Debye model. In this scenario, the Orbach relaxation process can still be applicable with only one unpaired electron.

Phonon-bottleneck relaxation: Unlike the previous relaxation pathways discussed, the origin of the phonon bottleneck relaxation is not molecular, but it can participate in the relaxation of a sample. The phonons related to the direct relaxation can couple with the other phonons in the lattices anharmonically and thus build up an excited phonon population (phonon bottleneck) in the lattice that slowly dissipates their energy to their surroundings. If the annihilation of these bottlenecked photons is slower than their creation (from spin-lattice relaxation), it can cause a thermal excitation of the spin states that will prevent further spin-lattice relaxation. Such phonon-bottleneck relaxation is usually observed in magnetically dense systems, and seldom in molecular systems. For an S = ½ system affected by the phonon bottleneck, the relaxation of the magnetic

moments usually follows the relation $\tau^{-1} = BT^2$ (B is constant, depending on the temperature, field, and concentration dependence of phonon lifetimes, τ_{ph}).[36]

1.5 Detecting Slow Magnetic Relaxation

AC susceptometry is a theoretically simple technique that can give us details about the susceptibility, *dM/dH*. A sample is inserted into a small primary coil with a small alternating current, producing an alternating magnetic field that is usually less than 10 Oe. This is shown in Figure 1.4. The applied magnetic field is then given by Eqn. 1.2,

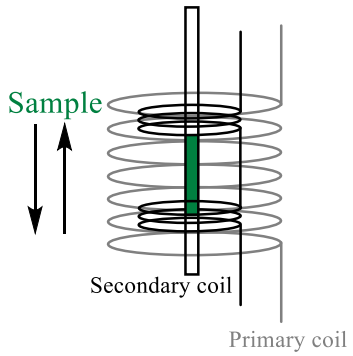

Figure 1.4 Schematic of the coils commonly found in AC susceptometers.

$$H = H_0 + h\cos\omega t \qquad \text{(Equation. 1.2)}$$

where ω is the angular frequency of the AC current in the primary coil, H_0 is the static applied magnetic field, and *h* is the oscillating magnetic field strength. A secondary coil, wound inside the primary one such that the induced voltage from the primary coil is zero, then detects the magnetic moment of the sample as it oscillates as an effect of the AC field. The advantage of this technique is that it allows us to easily investigate the frequency dependence of the susceptibility by varying ω. The static applied field, H_0, is applied through an additional coil outside the primary coil.

The population of a state, most relevantly the *m* component of an *s* multiplet, is given by

$$p_m = \frac{\exp\left(-\frac{E_m}{k_B T}\right)}{\sum_m \exp\left(-\frac{E_m}{k_B T}\right)} \qquad \text{(Equation. 1.3)}$$

The magnetization of a sample then depends on p_m as

$$\langle M \rangle = \sum_m p_m M_m \qquad \text{(Equation. 1.4)}$$

Thus, for a S = ½ system of N spins, the equilibrium population of the two states (m_s = ± ½) oscillates with time as

$$\frac{p_1}{p_2} = \exp\left[-\frac{g\mu_B(H_0 + h\cos\omega t)}{k_B T}\right] \qquad \text{(Equation. 1.5)}$$

If we define τ as the time it takes for the system to return to equilibrium then we can identify two limits. When the frequency is much lower than the recovery time such that $\omega\tau << 1$, the measured susceptibility is the isothermal one, $\chi = \chi_T$. On the other hand, when the frequency is much greater than the recovery time, $\omega\tau >> 1$, then the system has no time to exchange with the external world and we measure the adiabatic susceptibility, $\chi = \chi_S$. As for the intermediate region, Casimir and Du Pré proposed the interpolation formula in 1938,[37]

$$\chi(\omega) = \chi_S + \frac{\chi_S - \chi_T}{1 + i\omega\tau} \qquad \text{(Equation. 1.6)}$$

This then yields the real and imaginary components of the susceptibility,

$$\chi' = \frac{\chi_T - \chi_S}{1 + \omega^2\tau^2} + \chi_S \qquad \text{(Equation. 1.7)}$$

$$\chi'' = \frac{(\chi_T - \chi_S)\omega\tau}{1 + \omega^2\tau^2} \qquad \text{(Equation. 1.8)}$$

Thus, the complete complex susceptibility can be defined as,

$$M(t) = M_0 + Re\left[(\chi' - i\chi'')he^{i\omega\tau}\right] = M_0 + (\chi'\cos\omega\tau + \chi''\sin\omega\tau)h \qquad \text{(Equation. 1.9)}$$

Typically, when we measure the AC susceptibility we sweep frequency, as shown in Figure 1.5, and look at the χ' value at the extremes of the frequency and the peak position in the χ'' plot. We then fit the data to Eqn. 1.8 and Eqn. 1.9, or a modified formula that accounts for a distribution of relaxation times when necessary, to extract τ. These extracted relaxation times can then be fit to the various relaxation mechanisms presented in section 1.4.

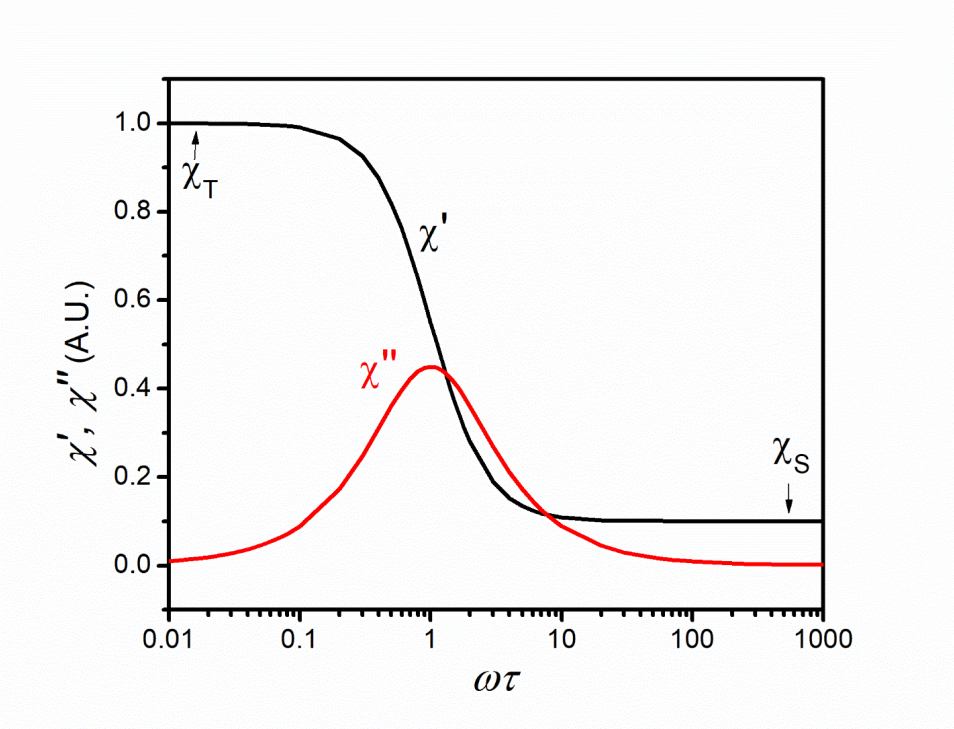

Figure 1.5 Calculated frequency dependence of the real (χ') and imaginary (χ'') magnetic susceptibility.

1.6 Introduction to S = ½ Ni(III) Cyclam

Consider an S = 3/2 system, but where the zero field splitting parameters are large and positive, as shown in Figure 1.6. In such a situation one would expect the magnetic relaxation to be very rapid and barrierless, however there have been many examples of such materials showing slow magnetic relaxation.[38,39] Furthermore, consider a S = ½ system, which contains no zero field

splitting at all. Such a system completely lacks the higher magnetic states that might make for a barrier, but like the systems with positive ZFS there are many such complexes that still show slow magnetic relaxation.[7,8,10,11,40] As such, the barrier towards magnetic relaxation cannot be composed solely of magnetic states and relaxation mechanisms. Instead, recent efforts in the field have investigated the spin-phonon coupling in SMMs, finding that only certain phonons, or lattice vibrations, couple strongly to the electronic spin. It is these phonons that are responsible for magnetic relaxation in SMMs, and possibly produce the barrier in these exceptional systems.[24,25,41–44]

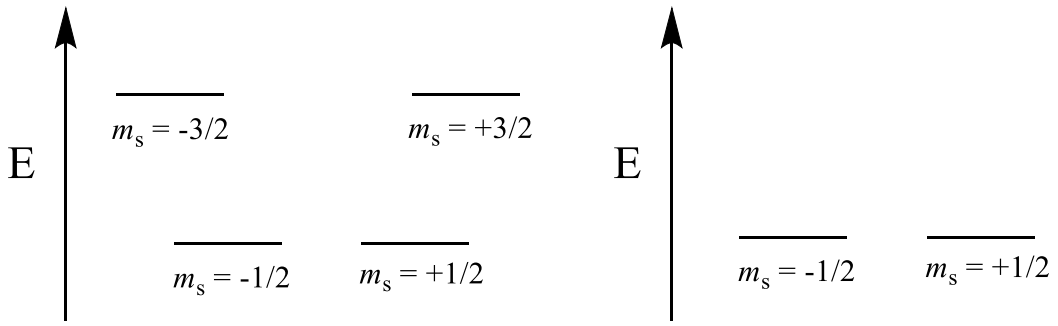

Figure 1.6 Left: Magnetic energy diagram of an $S = 3/2$ system with positive ZFS. Right: Magnetic energy diagram of an $S = 1/2$ system.

Chapters two through six focus on a family of Ni(III) complexes utilizing the ligand 1,4,8,11-tetraazacyclotetradecane, better known as cyclam, and are $S = ½$. Cyclam is one of the few ligands known to stabilize the Ni(III) oxidation state, which is isoelectronic with low-spin Co(II), and high-spin Co(II) has dominated the first-row transition metal-based single molecule magnets. Often times the Ni(III) state will be reduced by the ligands, resulting in a Ni(II) center with a ligand-stabilized radical.[45–47] The distinction between Ni(III) and a Ni(II)-stabilized radical can be made by electron paramagnetic resonance (EPR) as the latter exhibits an isotropic *g*-value

close to that of a free electron (2.0032), whereas the former can range from 2.0-2.2 and is usually anisotropic.[48,49]

In 1974 Mocella and Barefield reported on the redox chemistry of these Ni(III) cyclam complexes, as well as related macrocyclic amine ligands, and found that they were highly sensitive to base.[50] They discovered that the proton loss from one of the amines initiated an oxidative dehydrogenation, reducing the metal center and forming an imine. While the solid complexes were stable effectively indefinitely, the crystallization of them from aqueous solutions proved challenging. Naturally, the discovery of this reduction mechanism resulted in several methods of preventing, or at least mitigating this problem. The first, and simplest method was to keep the pH acidic in order to prevent the amines from becoming deprotonated and initiating the reduction of the metal center. There have been several studies on different acids and ions that help preserve the Ni(III) oxidation state in solution, which are briefly summarized in Table 1.2.[51,52] The second is to methylate the amines to form tetramethylcyclam (TMC), however this has the unfortunate side effect of blocking one of the axial sites, usually resulting in a pentacoordinate, square pyramidal complex. Another ligand that has been shown to help stabilize the Ni(III) oxidation state is hexamethylcyclam (HMC), which has methyls on the propylene bridges according to Scheme 1.1, and significantly helps prevent the oxidative dehydrogenation that occurs in the parent cyclam.

Table 1.2 Half-life of select aqueous Ni(III)CyclamX_2 at varying pH.

Equitorial Ligand	Axial ligand (X)	pH	Half-life	reference
Cyclam	OH_2	2.0	120 hours	[52]
		9.0	1.5 sec	[52]
HMC	OH_2	2.0	~1.2 min	[51]
HMC	Cl^-	2.0	75 min	[51]
Cyclam	SO_4^{2-}	2.0	5 days	[49]
		6.0	64 hours	[52]
HMC	SO_4^{2-}	2.0	> 1 year	[51]
Cyclam	F^-	6.0	17 hours	[52]

Scheme 1.1. Left: cyclam; center: tetramethylcyclam; right: hexamethylcyclam

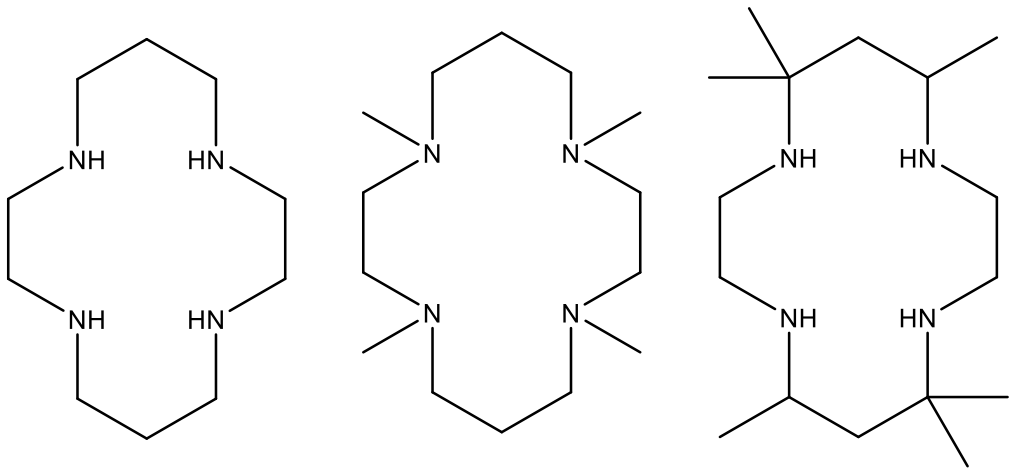

The first report of a Ni(III) complex showing slow magnetic relaxation was published in 2018 by the Shores group.[7] That study showed that the complexes $[Ni(cyclam)(NO_3)_2]X$ ($X = NO_3$, ClO_4) showed field-induced slow magnetic relaxation, whereas the complex $[Ni(cyclam)(NCS)_2]ClO_4$ did not. Computations of the complexes suggested that the nuclear spin in the axial positions, namely the N in isothiocyanate, coupled to the electronic spin on the Ni center. The inference was that this superhyperfine coupling sped up the magnetic relaxation to the point that it was not detectable. Since oxygen is very nearly nuclear spin-free, the NO_3 ligated systems do not show such a phenomena and are able to undergo slow magnetic relaxation as a result.

In sum, the ligand cyclam allows us the opportunity to study the magnetic relaxation of rare $S = ½$ Ni(III) ions, however the pH sensitivity of the system requires careful consideration of ligands and solvent conditions in order to successfully crystallize pure Ni(III) samples.

1.7 Outline of Chapters

Chapter 2 will discuss the magnetic properties of a series of $S = ½$ Ni(III) cyclam salts and the role of nuclear spin on the presence of superparamagnetism. Chapter 3 will utilize the design principles learned from Chapter 2 and discuss the isotopic tuning of Ni(III) cyclam salts, the role of intermolecular interactions, and their role in determining the magnetic relaxation pathways. Chapter 4 will study how the charge of the ligand affects the magnetic relaxation and will refine the design principles learned in Chapter 2. Chapter 5 will discuss the magnetic properties of these systems in solution and the effect of utilizing glassy/non-glassy solvents. Chapter 6 summarizes the broad conclusions and presents interesting future directions for uncovering more fundamental design principles in $S = ½$ SMMs. Finally, Chapter 7 introduces a different ligand featuring intra-ligand π-π interactions and explores the feasibility of having fine control over the first coordination sphere geometry and electronic structure through molecular tuning of the π-stacking.

1.8 References

(1) Martínez-Pérez, M. J.; Cardona-Serra, S.; Schlegel, C.; Moro, F.; Alonso, P. J.; Prima-García, H.; Clemente-Juan, J. M.; Evangelisti, M.; Gaita-Ariño, A.; Sesé, J.; Van Slageren, J.; Coronado, E.; Luis, F. Gd-Based Single-Ion Magnets with Tunable Magnetic Anisotropy: Molecular Design of Spin Qubits. *Phys. Rev. Lett.* **2012**, *108* (24), 1–5. https://doi.org/10.1103/PhysRevLett.108.247213.

(2) Brunet, G.; Safin, D. A.; Jover, J.; Ruiz, E.; Murugesu, M. Single-Molecule Magnetism Arising from Cobalt(II) Nodes of a Crystalline Sponge. *J. Mater. Chem. C* **2017**, *5* (4),

835–841. https://doi.org/10.1039/c6tc04703c.

(3) Mannini, M.; Pineider, F.; Sainctavit, P.; Danieli, C.; Otero, E.; Sciancalepore, C.; Talarico, A. M.; Arrio, M. A.; Cornia, A.; Gatteschi, D.; Sessoli, R. Magnetic Memory of a Single-Molecule Quantum Magnet Wired to a Gold Surface. *Nat. Mater.* **2009**, *8* (3), 194–197. https://doi.org/10.1038/nmat2374.

(4) Aromí, G.; Aguilà, D.; Gamez, P.; Luis, F.; Roubeau, O. Design of Magnetic Coordination Complexes for Quantum Computing. *Chemical Society Reviews*. **2012**, 537–546. https://doi.org/10.1039/c1cs15115k.

(5) Frost, J. M.; Harriman, K. L. M.; Murugesu, M. The Rise of 3-d Single-Ion Magnets in Molecular Magnetism: Towards Materials from Molecules? *Chem. Sci.* **2016**, *7* (4), 2470–2491. https://doi.org/10.1039/c5sc03224e.

(6) Craig, G. A.; Murrie, M. 3D Single-Ion Magnets. *Chem. Soc. Rev.* **2015**, *44* (8), 2135–2147. https://doi.org/10.1039/c4cs00439f.

(7) Bhowmick, I.; Roehl, A. J.; Neilson, J. R.; Rappé, A. K.; Shores, M. P. Slow Magnetic Relaxation in Octahedral Low-Spin Ni(III) Complexes. *Chem. Sci.* **2018**, *9* (31), 6564–6571. https://doi.org/10.1039/c7sc04482h.

(8) Stinghen, D.; Atzori, M.; Fernandes, C. M.; Ribeiro, R. R.; De Sá, E. L.; Back, D. F.; Giese, S. O. K.; Hughes, D. L.; Nunes, G. G.; Morra, E.; Chiesa, M.; Sessoli, R.; Soares, J. F. A Rare Example of Four-Coordinate Nonoxido Vanadium(IV) Alkoxide in the Solid State: Structure, Spectroscopy, and Magnetization Dynamics. *Inorg. Chem.* **2018**, *57* (18), 11393–11403. https://doi.org/10.1021/acs.inorgchem.8b01117.

(9) Tesi, L.; Lucaccini, E.; Cimatti, I.; Perfetti, M.; Mannini, M.; Atzori, M.; Morra, E.; Chiesa, M.; Caneschi, A.; Sorace, L.; Sessoli, R. Quantum Coherence in a Processable Vanadyl Complex: New Tools for the Search of Molecular Spin Qubits. *Chem. Sci.* **2016**, *7* (3), 2074–2083. https://doi.org/10.1039/c5sc04295j.

(10) Albino, A.; Benci, S.; Tesi, L.; Atzori, M.; Torre, R.; Sanvito, S.; Sessoli, R.; Lunghi, A. First-Principles Investigation of Spin-Phonon Coupling in Vanadium-Based Molecular Spin Quantum Bits. *Inorg. Chem.* **2019**, *58* (15), 10260–10268. https://doi.org/10.1021/acs.inorgchem.9b01407.

(11) Ding, M.; Cutsail, G. E.; Aravena, D.; Amoza, M.; Rouzières, M.; Dechambenoit, P.; Losovyj, Y.; Pink, M.; Ruiz, E.; Clérac, R.; Smith, J. M. A Low Spin Manganese(IV) Nitride Single Molecule Magnet. *Chem. Sci.* **2016**, *7* (9), 6132–6140. https://doi.org/10.1039/c6sc01469k.

(12) Cui, H. H.; Sun, T. M.; Wang, M.; Chen, L.; Tang, Y. F. Bulky Anion Supported a Five-Coordinate Spin-Crossover Cobalt(II) Complex with Slow Magnetic Relaxation. *J. Solid State Chem.* **2020**, *289* (June), 121535. https://doi.org/10.1016/j.jssc.2020.121535.

(13) Chen, L.; Song, J.; Zhao, W.; Yi, G.; Zhou, Z.; Yuan, A.; Song, Y.; Wang, Z.; Ouyang, Z. W. A Mononuclear Five-Coordinate Co(Ii) Single Molecule Magnet with a Spin Crossover between the S = 1/2 and 3/2 States. *Dalt. Trans.* **2018**, *47* (46), 16596–16602. https://doi.org/10.1039/C8DT03783C.

(14) Bhowmick, I.; Shaffer, D. W.; Shaffer, D. W.; Yang, J. Y.; Shores, M. P. Single Molecule

Magnet Behaviour in a Square Planar: S = 1/2 Co(II) Complex and Spin-State Assignment of Multiple Relaxation Modes. *Chem. Commun.* **2020**, *56* (49), 6711–6714. https://doi.org/10.1039/d0cc01854f.

(15) Lin, W.; Bodenstein, T.; Mereacre, V.; Fink, K.; Eichhöfer, A. Field-Induced Slow Magnetic Relaxation in the Ni(I) Complexes $[NiCl(PPh_3)_2]\cdot C4H8O$ and $[Ni(N(SiMe_3)_2)(PPh_3)_2]$. *Inorg. Chem.* **2016**, *55* (5), 2091–2100. https://doi.org/10.1021/acs.inorgchem.5b02497.

(16) Boča, R.; Rajnák, C.; Titiš, J.; Valigura, D. Field Supported Slow Magnetic Relaxation in a Mononuclear Cu(II) Complex. *Inorg. Chem.* **2017**, *56* (3), 1478–1482. https://doi.org/10.1021/acs.inorgchem.6b02535.

(17) Cui, H. H.; Lv, W.; Tong, W.; Chen, X. T.; Xue, Z. L. Slow Magnetic Relaxation in a Mononuclear Five-Coordinate Cu(II) Complex. *Eur. J. Inorg. Chem.* **2019**, *2019* (43), 4653–4659. https://doi.org/10.1002/ejic.201900942.

(18) Kahn, O. Molecular Magnetism (Kahn, Olivier). *J. Chem. Educ.* **2009**, *72* (1), A19. https://doi.org/10.1021/ed072pa19.2.

(19) Ma, Y. J.; Hu, J. X.; Han, S. De; Pan, J.; Li, J. H.; Wang, G. M. Manipulating On/Off Single-Molecule Magnet Behavior in a Dy(III)-Based Photochromic Complex. *J. Am. Chem. Soc.* **2020**, *142* (5), 2682–2689. https://doi.org/10.1021/jacs.9b13461.

(20) Benelli, C.; Gatteschi, D. SMM Past and Present. In *Introduction to Molecular Magnetism: From Transition Metals to Lanthanides*; John Wiley & Sons, 2015; pp 195–215. https://doi.org/10.1002/9783527690541.ch12.

(21) Novak, M. A.; Sessoli, R.; Gatteschi, D.; Caneschi, A. Magnetic Bistability in a Metal-Ion Cluster. *Nature* **1993**, *365* (365), 141–143.

(22) Sessoli, R.; Tsai, H.; Schake, A. R.; Wang, S.; Vincent, J. B.; Foiling, K.; Gatteschi, D.; Christou, G.; Hendrickson, D. N. High-Spin Molecules: $[Mn_{12}O_{12}(O_2CR)_{16}(H_2O)_4]$. *J. Am. Chem. Soc.* **1993**, *115*, 1804–1816.

(23) Linert, W.; Verdaguer, M.; Marvaud, V.; Herrera, J. M.; Barilero, T.; Tuyeras, F.; Garde, R.; Scuiller, A.; Decroix, C.; Cantuel, M.; Desplanches, C. *Molecular Magnets Recent Highlights*; **2002**. https://doi.org/10.1007/978-3-7091-6018-3_6.

(24) Gu, L.; Wu, R. Origins of Slow Magnetic Relaxation in Single-Molecule Magnets. *Phys. Rev. Lett.* **2020**, *125* (11), 117203. https://doi.org/10.1103/PHYSREVLETT.125.117203.

(25) Moseley, D. H.; Stavretis, S. E.; Zhu, Z.; Guo, M.; Brown, C. M.; Ozerov, M.; Cheng, Y.; Daemen, L. L.; Richardson, R.; Knight, G.; Thirunavukkuarasu, K.; Ramirez-Cuesta, A. J.; Tang, J.; Xue, Z. L. Inter-Kramers Transitions and Spin-Phonon Couplings in a Lanthanide-Based Single-Molecule Magnet. *Inorg. Chem.* **2020**, *59* (7), 5218–5230. https://doi.org/10.1021/acs.inorgchem.0c00523.

(26) Zabala-Lekuona, A.; Seco, J. M.; Colacio, E. Single-Molecule Magnets: From Mn_{12}-Ac to Dysprosium Metallocenes, a Travel in Time. *Coord. Chem. Rev.* **2021**, *441*, 213984. https://doi.org/10.1016/j.ccr.2021.213984.

(27) Zadrozny, J. M.; Xiao, D. J.; Atanasov, M.; Long, G. J.; Grandjean, F.; Neese, F.; Long, J. R. Magnetic Blocking in a Linear Iron(I) Complex. *Nat. Chem.* **2013**, *5* (7), 577–581.

https://doi.org/10.1038/nchem.1630.

(28) Yao, X. N.; Du, J. Z.; Zhang, Y. Q.; Leng, X. B.; Yang, M. W.; Jiang, S. Da; Wang, Z. X.; Ouyang, Z. W.; Deng, L.; Wang, B. W.; Gao, S. Two-Coordinate Co(II) Imido Complexes as Outstanding Single-Molecule Magnets. *J. Am. Chem. Soc.* **2017**, *139* (1), 373–380. https://doi.org/10.1021/jacs.6b11043.

(29) Ishikawa, N.; Sugita, M.; Ishikawa, T.; Koshihara, S. Y.; Kaizu, Y. Lanthanide Double-Decker Complexes Functioning as Magnets at the Single-Molecular Level. *J. Am. Chem. Soc.* **2003**, *125* (29), 8694–8695. https://doi.org/10.1021/ja029629n.

(30) Goodwin, C. A. P.; Ortu, F.; Reta, D.; Chilton, N. F.; Mills, D. P. Molecular Magnetic Hysteresis at 60 Kelvin in Dysprosocenium. *Nature* **2017**, *548* (7668), 439–442. https://doi.org/10.1038/nature23447.

(31) Guo, F. S.; Day, B. M.; Chen, Y. C.; Tong, M. L.; Mansikkamäki, A.; Layfield, R. A. Magnetic Hysteresis up to 80 Kelvin in a Dysprosium Metallocene Single-Molecule Magnet. *Science (80-.).* **2018**, *362* (6421), 1400–1403. https://doi.org/10.1126/science.aav0652.

(32) Orbach, R. On the Theory of Spin-Lattice Relaxation in Paramagnetic Salts. *Proc. Phys. Soc* **1961**, *77*, 821. https://doi.org/10.3367/ufnr.0172.200201e.0085.

(33) Bartolomé, E.; Arauzo, A.; Luzón, J.; Melnic, S.; Shova, S.; Prodius, D.; Nlebedim, I. C.; Bartolomé, F.; Bartolomé, J. High Relaxation Barrier in Neodymium Furoate-Based Field-Induced SMMs. *Dalt. Trans.* **2019**, *48* (41), 15386–15396. https://doi.org/10.1039/c9dt02047k.

(34) Gu, L.; Wu, R. Origin of the Anomalously Low Raman Exponents in Single Molecule Magnets. *Phys. Rev. B* **2021**, *103* (1), 14401. https://doi.org/10.1103/PhysRevB.103.014401.

(35) Shriyastava, K. N. Theory of Spin-Lattice Relaxation. *Phys. Status Solidi B* **1983**, *117* (2), 437. https://doi.org/https://doi.org/10.1002/pssb.2221170202.

(36) Stoneham, A. M. The Phonon Bottleneck in Paramagnetic Crystals. *Proc. Phys. Soc.* **1965**, *86* (6), 1163–1177. https://doi.org/10.1088/0370-1328/86/6/302.

(37) Casimir, H. B. G.; du Pré, F. K. Note on the Thermodynamic Interpretation of Paramagnetic Relaxation Phenomena. *Physica* **1938**, *5* (6), 507–511. https://doi.org/10.1016/S0031-8914(38)80164-6.

(38) Peng, M.; Wu, X. F.; Wang, L. X.; Chen, S. H.; Xiang, J.; Jin, X. X.; Yiu, S. M.; Wang, B. W.; Gao, S.; Lau, T. C. Slow Magnetic Relaxation in High-Coordinate Co(II) and Fe(II) Compounds Bearing Neutral Tetradentate Ligands. *Dalt. Trans.* **2021**, *50* (42), 15327–15335. https://doi.org/10.1039/d1dt02575a.

(39) Lou, H.; Yin, L.; Zhang, B.; Ouyang, Z. W.; Li, B.; Wang, Z. Series of Single-Ion and 1D Chain Complexes Based on Quinolinic Derivative: Synthesis, Crystal Structures, HF-EPR, and Magnetic Properties. *Inorg. Chem.* **2018**, *57* (13), 7757–7762. https://doi.org/10.1021/acs.inorgchem.8b00812.

(40) Tesi, L.; Lunghi, A.; Atzori, M.; Lucaccini, E.; Sorace, L.; Totti, F.; Sessoli, R. Giant Spin-Phonon Bottleneck Effects in Evaporable Vanadyl-Based Molecules with Long Spin

Coherence. *Dalt. Trans.* **2016**, *45* (42), 16635–16643. https://doi.org/10.1039/c6dt02559e.

(41) Gómez-Coca, S.; Urtizberea, A.; Cremades, E.; Alonso, P. J.; Camón, A.; Ruiz, E.; Luis, F. Origin of Slow Magnetic Relaxation in Kramers Ions with Non-Uniaxial Anisotropy. *Nat. Commun.* **2014**, *5*, 1–8. https://doi.org/10.1038/ncomms5300.

(42) Escalera-Moreno, L.; Baldoví, J. J.; Gaita-Ariño, A.; Coronado, E. Spin States, Vibrations and Spin Relaxation in Molecular Nanomagnets and Spin Qubits: A Critical Perspective. *Chem. Sci.* **2018**, *9* (13), 3265–3275. https://doi.org/10.1039/c7sc05464e.

(43) Stavretis, S. E.; Moseley, D. H.; Fei, F.; Cui, H. H.; Cheng, Y.; Podlesnyak, A. A.; Wang, X.; Daemen, L. L.; Hoffmann, C. M.; Ozerov, M.; Lu, Z.; Thirunavukkuarasu, K.; Smirnov, D.; Chang, T.; Chen, Y. S.; Ramirez-Cuesta, A. J.; Chen, X. T.; Xue, Z. L. Spectroscopic Studies of the Magnetic Excitation and Spin-Phonon Couplings in a Single-Molecule Magnet. *Chem. - A Eur. J.* **2019**, *25* (69), 15846–15857. https://doi.org/10.1002/chem.201903635.

(44) Garanin, D. A. Towards a Microscopic Understanding of the Phonon Bottleneck. *Phys. Rev. B - Condens. Matter Mater. Phys.* **2007**, *75* (9), 1–13. https://doi.org/10.1103/PhysRevB.75.094409.

(45) Zilbermann, I.; Maimon, E.; Cohen, H.; Meyerstein, D. Redox Chemistry of Nickel Complexes in Aqueous Solutions. *Chem. Rev.* **2005**, *105* (6), 2609–2625. https://doi.org/10.1021/cr030717f.

(46) Lati, J.; Meyerstein, D.; Lati, J.; Meyerstein, D. Trivalent Nickel. I. A Pulse Radiolytic Study of the Formation and Decomposition of the Ammoniacal Complex in Aqueous Solution. *Inorg. Chem.* **1972**, *11* (10), 2393–2397. https://doi.org/10.1021/ic50116a021.

(47) Lati, J.; Meyerstein, D.; Lati, J.; Meyerstein, D. Trivalent Nickel. II. A Pulse Radiolytic Study of the Formation and Decomposition of the Ethylenediamine and Glycine Complexes in Aqueous Solution. *Inorg. Chem.* **1972**, *11* (10), 2397–2401. https://doi.org/10.1021/ic50116a021.

(48) Haines, R. I.; Mcauley, A. Kinetics of the Reaction of the (1, 4, 8, 11-Tetraazacyclotetradecane)Diaquonickel(III) Cation with Halide and Thiocyanate Ions in Aqueous Perchlorate Media. *Inorg. Chem.* **1980**, *19* (3), 719–723. https://doi.org/10.1021/ic50205a027.

(49) Zeigerson, E.; Ginzburg, G.; Becker, J. Y.; Kirschenbaum, L. J.; Cohen, H.; Meyerstein, D. Difference in the Stabilities of the Diastereoisomers of the Tervalent Nickel Complex with 5,7,7,12,14,14-Hexamethyl-1,4,8,11 -Tetraazacyclotetradecane in Sulfate- and Perchlorate-Containing Aqueous Solutions. An Electrochemical and Pulse Radiolysis Study. *Inorg. Chem.* **1981**, *20* (11), 3988–3992. https://doi.org/10.1021/ic50225a078.

(50) Barefield, E. K.; Mocella, M. T. Mechanism of Base Promoted Reduction of Nickel(III) Complexes of Macrocyclic Amines. Coordinated Ligand Radical Intermediate. *J. Am. Chem. Soc.* **1975**, *97* (15), 4238–4246. https://doi.org/10.1021/ja00848a015.

(51) Zeigerson, E.; Bar, I.; Bernstein, J.; Kirschenbaum, L. J.; Meyerstein, D. Stabilization of the Tervalent Nickel Complex with Meso-5,7,7,12,14,14-Hexamethyl-1,4,8,11-Tetraazacyclotetradecane by Axial Coordination of Anions in Aqueous Solution. *Inorg. Chem.* **1982**, *21* (1), 73–80. https://doi.org/10.1021/ic00131a014.

(52) Shamir, D.; Zilbermann, I.; Maimon, E.; Shames, A. I.; Cohen, H.; Meyerstein, D. Anions as Stabilizing Ligands for Ni(III)(Cyclam) in Aqueous Solutions. *Inorganica Chim. Acta* **2010**, *363* (12), 2819–2823. https://doi.org/10.1016/j.ica.2010.03.057.

Chapter 2: Probing the Role of Nuclear Spin in Ni(III) Cyclam Magnetic Relaxation

2.1 Introduction

Understanding the synthetic moieties responsible for magnetic relaxation have fascinated magnetochemists long before the first SMM was reported, and the need to understand the physical processes responsible for magnetic relaxation is more important now than ever before. Progress on developing SMM with higher operating temperatures and slower relaxation, typically defined by the barrier height between magnetic ground states, has diminished greatly since the initial report of low-coordinate $DyCp^*_2$ type complexes, and as a result the field has begun to look towards new avenues of slowing magnetic relaxation beyond increasing the spin and zero field splitting.[1] Recently, the focus has shifted towards investigating the spin-phonon couplings responsible for magnetic relaxation within SMM systems.[2–6] Understanding these phonons are key towards understanding how the magnetic units interact and communicate with each other and their surroundings. While $DyCp^*_2$ type complexes feature record-breaking magnetic relaxation, the many magnetic states, high reactivity, and air sensitivity make it a cumbersome system to study the fundamentals of magnetic relaxation. Ni(III), on the other hand, is a simple $S = ½$ without spin-orbit coupling and almost completely deficient of nuclear spin, where ^{61}Ni is the only isotope containing nuclear spin but is only 1.1% naturally abundant. This makes for a good toy-model system for investigating the magnetic relaxation mechanisms that might normally be buried in the more complex systems.

In 2018 Shores and coworkers reported on the slow magnetic relaxation of a series of Ni(III) cyclam complexes.[7] In short, that study showed that $[Ni(cyclam)(NO_3)_2]X$ (X = NO_3^- or

ClO_4^-) exhibited slow magnetic relaxation, the first example of a Ni(III) SMM, whereas the similar $[Ni(cyclam)(NCS)_2]ClO_4$ did not. Calculations of the complexes revealed that nuclear spin in the axial positions interacted with the electronic spin of the Ni center. Nitrogen has two naturally occurring isotopes, ^{14}N and ^{15}N, both of which possess nuclear spin. Oxygen, on the other hand, has three naturally occurring isotopes, ^{16}O, ^{17}O, and ^{18}O. Of the three, only ^{17}O has nuclear spin with $I_O = 5/2$, but is < 1 % naturally abundant. As a result, the O-donor ligands are far less likely to show the super-hyperfine interactions between the electronic and nuclear spin that speed up magnetic relaxation compared to N-donor ligands. Despite these two complexes, I was unconvinced in the role of nuclear spin in the magnetic relaxation due to the small energies involved and sought other examples of Ni(III)cyclam complexes showing magnetic relaxation. We note that very recently a study was published on the magnetic relaxation of $[Co_{0.9}Ni_{0.1}(cyclam)Cl_2]ClO_4$ and showed that the material did exhibit slow magnetic relaxation.[8] Herein, we report the synthesis and characterization of three additional complexes in order to study their magnetic relaxation. The first two, $[Ni(cyclam)Cl_2]Cl$ (**1**) and $[Ni(cyclam)Br_2]Br$ (**2**), feature halogens that are 100% in isotopes with nuclear spin and whose EPR spectra show explicit super-hyperfine coupling, and the third was $[Ni(cyclam)(ClO_4)_2]ClO_4$ (**3**), which possesses the same first coordination sphere as the nitrate studies previously studied.

2.2 Division of Labor

The original syntheses of **2** and **3**, the collection of their crystal structures, and the collection of magnetic susceptibility data of the original sample of **3** were performed by Dr. Indrani Bhowmick and Andy Roehl. The follow-up syntheses of **1**, **2**, and **3** and the collection of their magnetic susceptibility data, EPR, and powder x-ray diffraction were performed by Tom Morrison.

Brody Lennon assisted with finding the final synthetic route towards **3**. Maddie Roach and the Reynolds lab assisted with the collection of mass spectrometry data. We thank the ARC staff for their assistance with the collection of crystallographic and magnetic data.

2.3 Experimental

2.3.1 Preparation of Compounds. Unless noted otherwise, all manipulations were performed in air and with Millipore deionized water. The compound $[Ni(cyclam)](ClO_4)_2$ was prepared as described elsewhere.[9] All other reagents were purchased commercially and were used without further purification.

$[Ni(cyclam)Cl_2]Cl$ (**1**): Two methods were used to synthesize **1**, Scheme 2.1. Method A follows a literature procedure, but did not produce x-ray quality single crystals.[10] Method B uses a modified procedure and was able to afford x-ray quality single crystals.[7] Powder x-ray diffraction patterns of the material obtained from Method A do not match that of the crystal structure obtained from Method B, however washing the powders with different solvents (water, methanol, acetonitrile) changed the powder diffraction patterns of the samples, showing that different solvatomorphs of **1** exist. As a result, all the data presented herein of **1** is of the polycrystalline samples obtained from Method B unless otherwise specified.

Method A: A literature procedure was used without modification.[10] $NiCl_2 \cdot 6H_2O$ (150.3 mg, 1.02 mmol) and cyclam (204.1 mg, 1.02 mmol) were dissolved in a 1:20 HCl:MeOH (20 mL) solution and H_2O_2 (30% w/w, 60 uL, 0.52 mmol) was then added. The solution was stirred for 1 hour, whereupon an orange precipitate formed and the sparingly soluble **1** was isolated by filtration, washed with cold MeOH, and then dried in the vacuum oven overnight (16 hours, 82% yield). ESI^+-MS (H_2O): *m/z* 292.18 ($[Ni(H_3cyclam)Cl]^+$). *Anal. Calcd.* for $C_{10}H_{24}N_4NiCl_3$: C, 32.87; H, 6.62; N, 15.33; Found: C, 32.67; H, 6.70; N, 14.98.

Method B: A solution of $Na_2S_2O_8$ (35.5 mg, 0.15 mmol) in 1 mL water was added to a solution of [Ni(cyclam)Cl_2] (82 mg, 0.25 mmol) in 2 mL of water in a scintillation vial with and stirred for one hour. The resulting solution turned green and was filtered. Conc. HCl (4 drops) was then added to the filtrate, changing the solution from green to yellow-green. The solution was then allowed to rest for 2 hours, whereupon copious amounts of large crystals formed (58% yield). The crystals grown this way were polycrystalline, likely due to their rapid growth, and so x-ray quality single crystals were grown by the vapor diffusion of HCl into the green oxidized solution.

Scheme 2.1 Synthetic routes towards [Ni(cyclam)Cl_2]Cl (**1**).

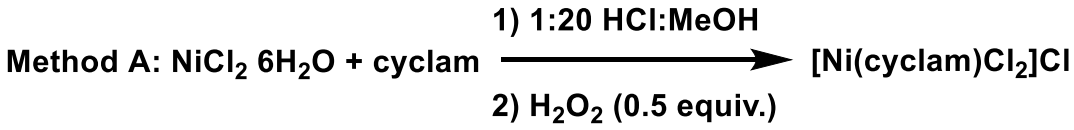

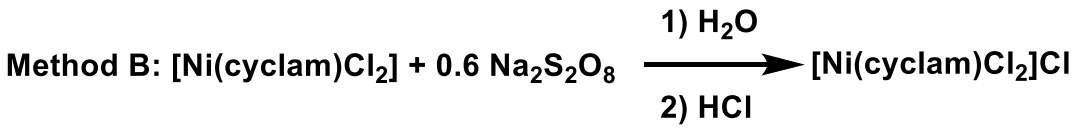

[Ni(cyclam)Br_2]Br (**2**): A solution of $Na_2S_2O_8$ (23 mg, 0.1 mmol) in 1 mL water was added to a solution of [Ni(cyclam)Br_2] (42 mg, 0.1 mmol) in a scintillation vial with 2 mL of water and stirred for one hour. The resulting solution turned green and an excess of KBr was added. The color changed to brown, and a red-brown precipitate formed. The precipitate was isolated via gravity filtration, washed with cold water, and dried in a vacuum oven at 60° C for two hours. (37% yield). X-ray quality single crystals were grown by the slow evaporation of a concentrated solution of **2**. *Anal. Calcd.* for $C_{10}H_{24}N_4NiBr_3$: C, 24.1; H, 4.8; N, 11.2; Found: C, 24.2; H, 4.6; N, 11.3.

[Ni(cyclam)(ClO_4)$_2$]ClO_4 (**3**): Multiple synthetic routes towards this complex have been attempted. While the original synthesis provided single-crystal x-ray diffraction quality crystals,

further attempts at the synthesis proved unsuccessful and resulted in amorphous oils instead of solid material. Due to the lack of an elemental analysis to assess purity, the uncommonly high amount of temperature independent paramagnetism in the $\chi_M T$ plot, and the inability to repeat the synthesis, an alternate synthetic route was developed and the magnetic data were recollected. We note that the recollection was consistent with the original data collection.

Initial synthesis: [Ni(cyclam)]$(ClO_4)_2$ (40 mg, 0.1 mmol) was added to a 20 mL scintillation vial containing 2 mL of water and stirred for 1 hour. Next $Na_2S_2O_8$ (11 mg, 0.1 mmol) was added, turning the solution green and producing a green precipitate (discussed in Ch. 3). Excess perchloric acid (70% w/w) was then added, turning the solution red-brown, and stirred for another two hours. The solution was allowed to rest for two days under standard pressure before crystallizing red-orange x-ray quality crystals, (72% yield). *Anal Calc.* for $C_{19}H_{24}Cl_3N_4O_{12}Ni$: C, 21.55; H, 4.34; N, 10.05. Found: C 21.62; H, 4.58; N, 10.18.

Follow-up synthesis: [Ni(cyclam)]$(ClO_4)_2$ (121 mg, 0.217 mmol) was added in ~15 mg batches to a 20 mL scintillation vial containing 1 mL perchloric acid (70% w/w). After the first addition of metal complex, H_2O_2 (15 µL, 30% w/w) was added to the solution and stirred for 2 minutes. After the mixture stopped effervescing the subsequent batches of metal complex were added, with 2-5 minutes between additions. The purple saturated solution was then stirred for 1 hour and then centrifuged to separate the precipitate. After decanting the supernatant, the purple precipitate was dissolved in 5 mL THF. Et_2O (15 mL) was then added to the THF solution to precipitate out the products, centrifuged again, and then the dissolution and precipitation process was repeated twice more. After the third precipitation from THF the product was dissolved in 2 mL DMSO, filtered to remove the sparingly soluble Ni(II) starting material, and then precipitated with the addition of EtOAc to yield the product as a purple powder (*Extreme caution advised! DMSO and $HClO_4$ are*

explosively incompatible). ESI$^+$-MS (MeCN): *m/z* 356.02 ([Ni(cyclam-H)(ClO_4)]$^+$), *m/z* 456.00 ([Ni(cyclam)(ClO_4)$_2$]$^+$). *Anal. Calcd.* for $C_{10}Cl_3H_{24}N_4NiO_{12}$: C, 21.55; H, 4.34; N, 10.05. Found, C, 21.86; H, 4.56; N, 9.79.

2.3.2 X-ray structure determinations. Crystals suitable for single-crystal x-ray analysis were coated with Paratone-N oil and supported on a Cryoloop before being mounted on a Bruker Kappa Apex II CCD diffractometer under a stream of N_2 gas. Data collections were performed at low temperature using a Siemens KFF Mo_2K-90 sealed tube (Mo Kα, λ = 0.71073 Å) x-ray source and a curved graphite monochromator, targeting complete coverage and 4-fold redundancy. Crystallographic data and metric parameters are presented in Table 2.2. Determination of unit cell parameters through refinement, data collection, reduction, and correction for Lorentz and polarization effects was performed using the SAINT software package.[11] Data were sorted, scaled, averaged, and corrected for semiempirical absorption effects with SADABS.[12] The structures were solved with the ShelXT structure solution program and refined with the ShelXL-2018/3 refinement package.[13] Thermal parameters for all non-hydrogen atoms were refined anisotropically for **2** and **3**, while **1** was refined isotropically. Hydrogen atoms were added at calculated positions and were refined using a riding model.

2.3.3 Magnetic measurements. Magnetic susceptibility data were collected using a Quantum Design MPMS3 SQUID magnetometer for **1**, **2**, and the recollection of **3**, and a Quantum Design MPMS XL magnetometer for the original collection of **3**. The ground polycrystalline samples were loaded into polyethylene bags and sealed, then the bags were inserted into drinking straws and inserted into the instrument. Ferromagnetic impurities were checked through a variable field analysis (0 to 10 kOe) of the magnetization at 100 K: overall linearity in the collected data for all three compounds indicated the lack of significant ferromagnetic impurities. Static (DC) magnetic

susceptibility data for the samples were collected at temperatures ranging from 2 K to 300 K at a 1 kOe measuring field. Alternating current (AC) magnetic susceptibility measurements were performed from 0.1 Hz to 1400 Hz and from 1.8 K to 17 K with an alternating field of 4 Oe. Data were corrected for the magnetization of the sample holder by subtracting the susceptibility of an empty container, and for the diamagnetic contributions of the sample by using Pascal's constants.[14]

Temperature-dependent DC magnetic susceptibility data were modeled with the program PHI[15] to single-ion species with temperature independent paramagnetism, weakly interacting with the spin bath. The AC magnetic susceptibility data for **3** were fit to several multicomponent relaxation models. Using equation 2.1, the variables A, B, b_1, and b_2 were allowed to refine freely.

$$\tau^{-1} = AH^4T + \frac{b_1}{1+b_2H^2} + BT^2 \qquad \text{(Eq. 2.1)}$$

Here, the first term represents the direct pathways, the second the quantum tunnelling of magnetization (QTM), and the third the phonon bottleneck effect (PBE).

2.3.4 Other physical characterizations. LC-MS analyses were carried out on an Agilent 6224 high resolution time-of-flight mass spectrometer coupled to an Agilent 1260 high performance quaternary liquid chromatograph. The sample was introduced via direct injection, and therefore no column separation was used. The mobile phase was composed of Millipore water or acetonitrile, and the flow rate was 0.350 mL/min with a 3-minute runtime. Spectra were acquired in positive ionization mode. Infrared spectra were obtained using a Bruker Tensor II FT-IR spectrometer. Electron paramagnetic resonance spectra were obtained using a Bruker ESR-300 spectrometer equipped with an X-band microwave source and an ultra-high sensitivity resonator. Data were collected with a 5 G modulation amplitude and 100 kHz frequency, and were simulated using Easy Spin.[16] Powder x-ray diffraction data were collected at room temperature using a Scintag X-2 powder x-ray diffractometer equipped with Cu Kα radiation, Peltier detector and stationary sample

stage, collecting diffraction angles between 5° and 30° 2θ. Elemental analyses were performed by Midwest Microlabs, Indianapolis, IN.

2.4 Results and Discussion

2.4.1 Synthesis and Characterization of Ni(III)cyclam Complexes. The synthesis of **1** was carried out using a literature procedure without issue, producing orange powders. However, we were unable to produce single-crystal x-ray quality crystals during the reaction or through recrystallization attempts afterwards. The synthesis of **2**, however, produced crystals in good yield and so the synthesis was adapted for **1**, from which x-ray quality single crystals were able to be obtained. While the two halide materials are molecularly similar, the crystal structure of them is not, as evident by the powder x-ray diffraction patterns shown in Figure 2.1 and Figure 2.2. Furthermore, washing **1** with different solvents resulted in similar looking orange powders, but with different powder x-ray diffraction patterns, suggesting a variety of solvatomorphs. While the powder x-ray diffraction pattern of the material produced by Method B is different from that of Method A, both materials can be converted to the same structure by vacuum drying the crystals (Figure 2.3), although such a procedure cracks the crystals significantly.

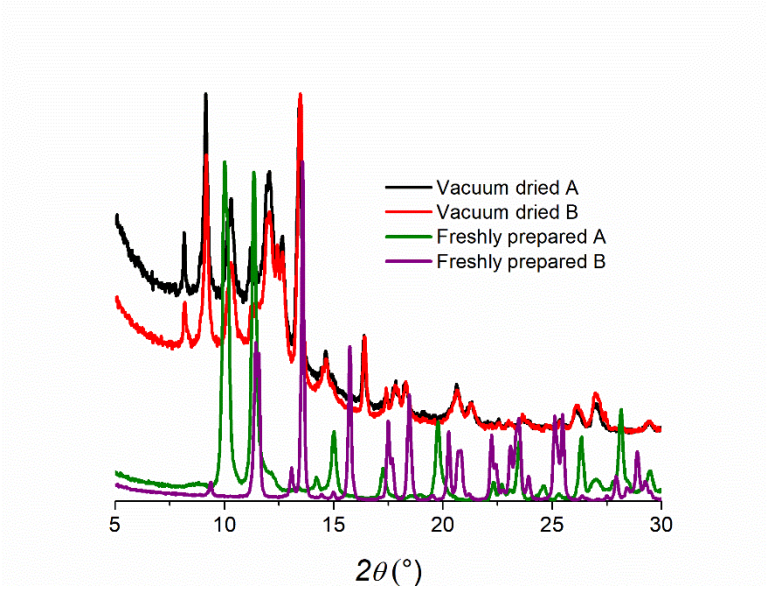

Figure 2.1 Powder x-ray diffraction patterns of **1** freshly synthesized from Method A and Method B compared to the pattern of the vacuum dried materials.

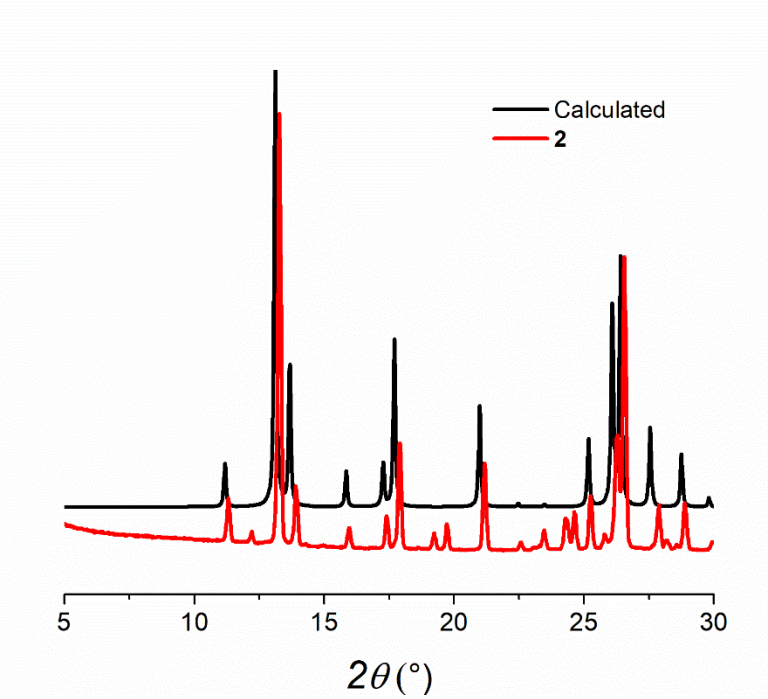

Figure 2.2 Powder x-ray diffraction pattern of **2** compared to the calculated spectra obtained from the crystal structure.

The original synthesis of **3** by Indrani Bhowmick was serendipitous and unable to be consistently reproduced. Reactions using the original synthesis repeatedly failed to precipitate or

crystallize any product, producing amorphous oils even when the solvent was left to slowly (or even quickly) evaporate. The addition of antisolvents was similarly unsuccessful. As a result, we developed an alternative synthetic route where the reaction was done in concentrated perchloric acid saturated with the Ni(II) starting material, enabling us to fully explore the magnetic properties of the compound. Oxidizing the Ni(II) starting material to the Ni(III) product greatly increased the solubility and allowed for more starting material to react, however not to the point of fully dissolving the solids. This allowed us to separate a solid (and not amorphous) product from the solution by filtration or centrifugation. The washings with THF and Et_2O removed residual perchloric acid, but did little to separate any remaining Ni(II) starting material from the Ni(III) product. DMSO was found to easily dissolve the Ni(III) product, while the Ni(II) starting material was sparingly soluble. As a result, the crude mixture produced from the THF/Et_2O washings was able to be purified by dissolving in DMSO, filtering, and then precipitating **3** as a powder with the addition of EtOAc. *I caution the reader to ensure there is no residual perchloric acid remaining after the THF Et_2O washes as DMSO and perchloric acid are explosively incompatible*. Vapor diffusions with the aforementioned solvents were attempted, however the solution turned from purple to green and suggested a change in the first coordination sphere, likely the coordination of DMSO. Recrystallization from this new green DMSO solution was attempted, however there was no crystal formation, and no further characterization was attempted. Nonetheless, this procedure produced a powder in good yield and purity, and whose powder x-ray diffraction pattern matched that of the crystal structure collected from the initial synthesis, as shown in Figure 2.3.

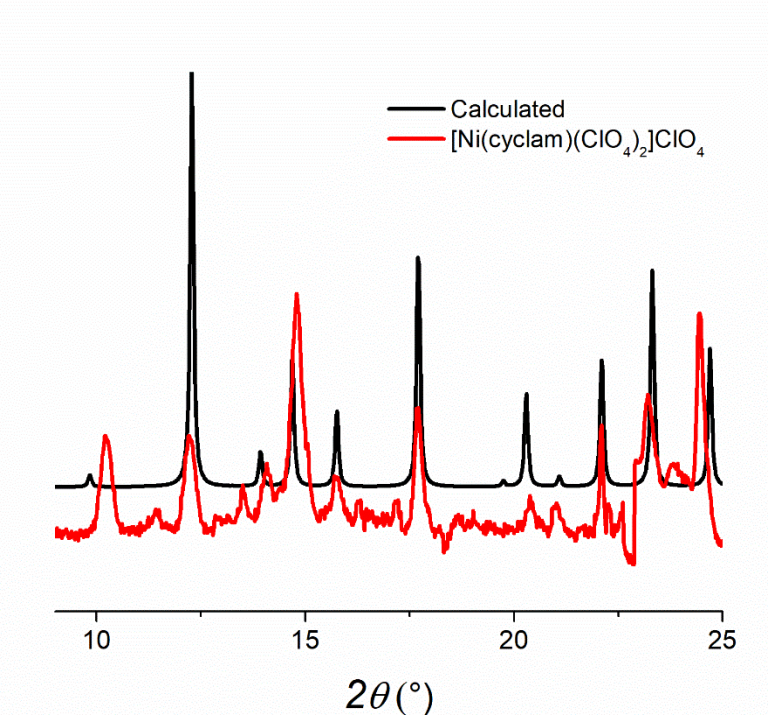

Figure 2.3 Powder x-ray diffraction pattern of **3** obtained from Method B and the calculated pattern from the crystal structure obtained from Method A.

2.4.2 X-ray Crystal Structures of Ni(III)cyclam complexes. Crystals of **1** suitable for x-ray analysis were unable to be obtained *via* the literature route, Method A, and so the modified route, Method B, was used instead. While polycrystalline samples were produced by the addition of HCl directly the solution, the rapid growth resulted in the crystals twinning and forming inclusions. In order to slow down the crystallization enough to form true single crystals, HCl was added to the solution through a vapor diffusion. While crystal formation was still rapid, forming within a few hours, the resulting crystals were of higher quality and the structure was able to be collected, Figure 2.4. Crystals of **2** were able to be obtained by the slow diffusion of Et_2O into a concentrated solution of **2** in methanol. Crystals of **3** serendipitously formed when the solution from Method A was allowed to rest for 2 days, Figure 2.5.

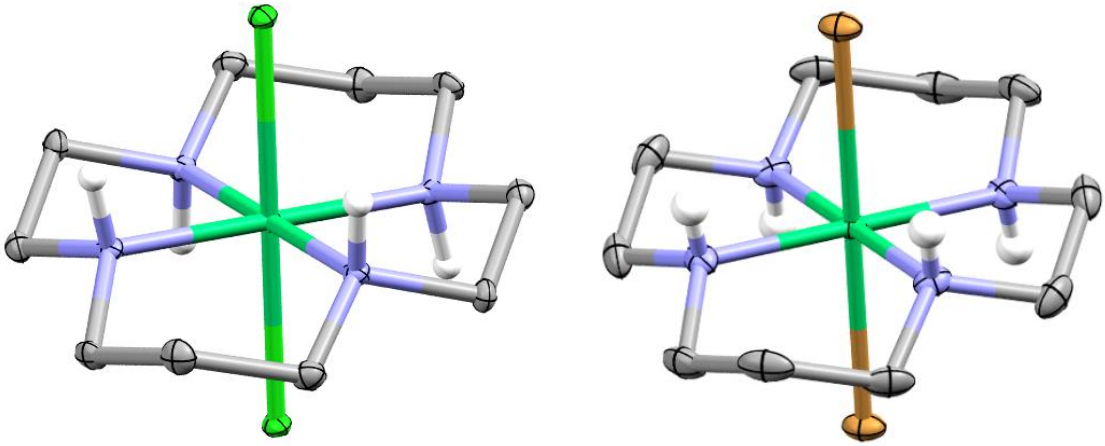

Figure 2.4 Crystal structure of **1** (left) and **2** (right) rendered with 50% ellipsoids. Gray, blue, brown, lime, and mint ellipsoids represent C, N, Br, Cl, and Ni atoms, respectively. White spheres represent H atoms. Non-amine hydrogen atoms and counter ions are omitted for clarity.

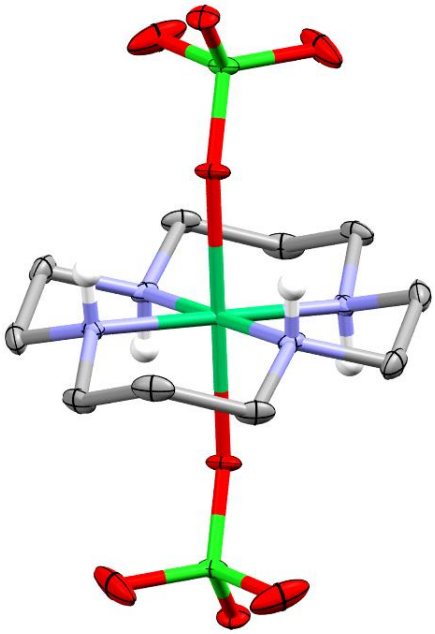

Figure 2.5 Crystal structure of **3** rendered with 50% ellipsoids. Gray, blue, red, lime, and mint ellipsoids represent C, N, O, Cl, and Ni atoms, respectively. White spheres represent H atoms. Non-amine hydrogen atoms and counter ions are omitted for clarity.

1 crystallizes in the $P2_1/n$ space group, but possesses severe solvent disorder. Solving the structured part of the system reveals that the Ni(III) center is ligated to cyclam in the typical R,S,S,R configuration with Cl in the axial positions. The outer-sphere Cl was also able to be located close to one of the amine H, 4.7 – 4.8 Å, supporting the Ni(III) oxidation state. After solving the structured part of the complex, the remaining solvent void comprised 33% of the volume of the unit cell. Squeezing the structure removes 156 electrons per unit cell, nominally corresponding to 12 H_2O molecules and 2 HCl molecules. The solvent voids can be seen in Figures A2.1 and A2.2 as orange channels throughout the unit cell.

Structural analyses of **2** and **3** reveal that both systems crystallize in $P4_2/m$. The molecular structure of **2** is very similar to that of **1**, with the difference in the Ni-X distances corresponding to the greater Van der Waal radius of Br. However, **2** does not possess the solvent channels that **1** has, nor does any solvent cocrystallize with the complex. Instead the structure is efficiently packed with Br^- ions separating the $[Ni(cyclam)Br_2]^+$ units. Each Br^- ion weakly hydrogen bonds to four different $[Ni(cyclam)Br_2]^+$ amines with a distance of 3.431(3) Å, much closer than that of **1**. The structure of **3** is similar, but the outer-sphere ClO_4^- is even closer to the cyclam amines with a distance of 2.980(2) Å.

Crystallographic analyses show that all three structures feature Ni(III) ions with comparable distorted octahedral coordination geometries. The halide-ligated **1** and **2** molecular structures are comparable to one another, although the closest Ni – Ni in **1** are much closer than those in **2**. The Ni-L distances are shown in Table 2.1 and are consistent with other published Ni(III)cyclam structures.

Table 2.1 Select distances for compounds $[Ni(cyclam)Cl_2]Cl\cdot 6H_2O\cdot HCl$ (**1**), $[Ni(cyclam)Br_2]Br$ (**2**), and $[Ni(cyclam)(ClO_4)_2]ClO_4$ (**3**).

	1	**2**	**3**
Ni – X (Å)	2.445(2)	2.6147(3) [a]	2.1572(13) [a]
	2.447(8)		
	2.444(8)		
	2.419(5)		
Ni – N (Å)	1.9802	1.9670(18) [a]	1.9634(11) [a]
	1.9851		
	1.9519		
	1.9815		
	1.9113		
	1.9597		
	2.0124		
	2.0452		
Ni – Ni, closest (Å)	6.3608	7.9044	8.7562

[a]Only one crystallographically unique bond.

Table 2.2 Crystallographic data for compounds $[Ni(cyclam)Cl_2]Cl\cdot 6H_2O\cdot HCl$ (**1**), $[Ni(cyclam)Br_2]Br$ (**2**), and $[Ni(cyclam)(ClO_4)_2]ClO_4$ (**3**).

	1	**2**	**3**
formula	$C_{10}H_{33}N_4O_4Cl_3Ni$	$C_{10}H_{24}N_4NiBr_3$	$C_{10}H_{24}N_4O_{12}Cl_3Ni$
fw (g/mol)	494.37	498.74	557.36
Color, habit	Orange needle	Red block	Purple block
T, K	100(2)	120(2)	120(2)
Space group	$P2_1/n$	$P4_2/m$	$P4_2/m$
Z	2	2	2
a, Å	9.7454(6)	7.9044(4)	8.9846(8)
b, Å	6.4003(4)	7.9044(4)	8.9846(8)
c, Å	16.3903(10)	12.9417(7)	12.0516(11)
α, deg	90	90	90
β, deg	107.019(3)	90	90
γ, deg	90	90	90
V, Å^3	977.55(11)	808.59(9)	972.84(19)
d_{calc}, g/cm^3	1.547	2.049	1.903
GOF	1.048	1.069	1.100
R_1[a] (wR_2[b]), %	8.56 (21.61)	2.11 (5.00)	2.13 (5.74)
R_1[a] (wR_2[b]), % all data	9.56 (22.45)	2.74 (5.14)	2.21 (5.79)

(a) $R_1 = \Sigma||F_o| - |F_c||/ \Sigma |F_o|$

(b) $wR_2 = [\Sigma [w(F_o^2-F_c^2)^2]/ \Sigma [w(F_o^2)^2]]^{½}$, $w = 1/[s^2(F_o^2) + (aP)^2 + bP]$, where $P = [\max(F_o^2 \text{ or } 0) + 2(F_c^2)]/3$

2.4.3 Electron Paramagnetic Resonance. Continuous wave electron paramagnetic resonance (EPR) were collected of **1**, **2**, and **3** of the powdered samples at room temperature in order to confirm the presence of the $S = ½$ Ni(III) ions and determine their magnetic anisotropy. The perchlorate containing **3** was also measured at 5 K, however the instrument's cryostat encountered issues before the low temperature data of **1** and **2** could be collected. Ideally, we would also see the super-hyperfine coupling to the axial halides, however the coupling is too small to be observable at room temperature. Fortunately the EPR of **1** and **2** at cryogenic temperatures (~77 K) have been previously reported in the literature, and do show the super-hyperfine coupling to the halide nuclear spin (a = 28 G, 39 G for **1** and **2**, respectively), unlike the isothiocyanate complex where the explicit coupling was not able to be observed.[17–19] We note that to the best of our knowledge, the EPR spectrum of **3** has not been previously reported.

From the room temperature data, Figure 2.6, it can be seen that the g values for **1** and **2** are extremely similar, but with **1** having far more inhomogeneous broadening than **2** due to the disordered part of the structure in **1**. Both halides feature an axial magnetic anisotropy, consistent with the literature and in contrast to the rhombic anisotropy of **3**, Figure 2.7.[17,18] The g values of all three complexes are within the normal range for Ni(III) $S = ½$ ions, 2.0 – 2.2, and are consistent with the literature with the exception of g_z in **3**, which is much higher at 2.31.[17]

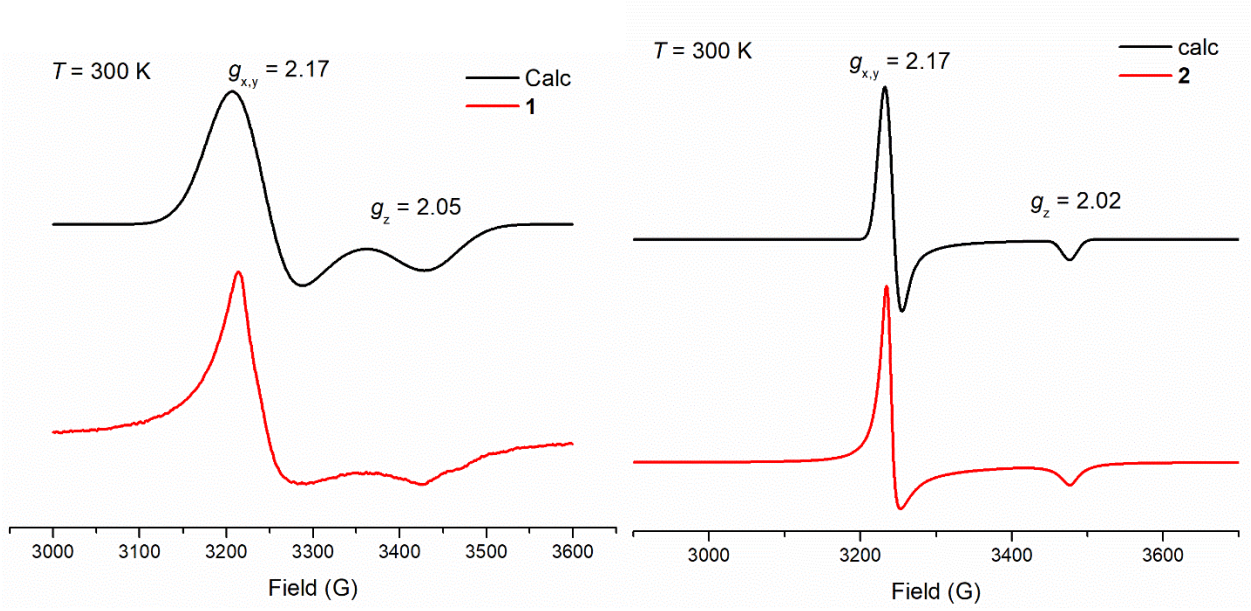

Figure 2.6 Left: EPR of **1** at 300 K with a microwave frequency of 9.817722 GHz. Right: EPR of **2** at 300 K with a microwave frequency of 9.834899 GHz.

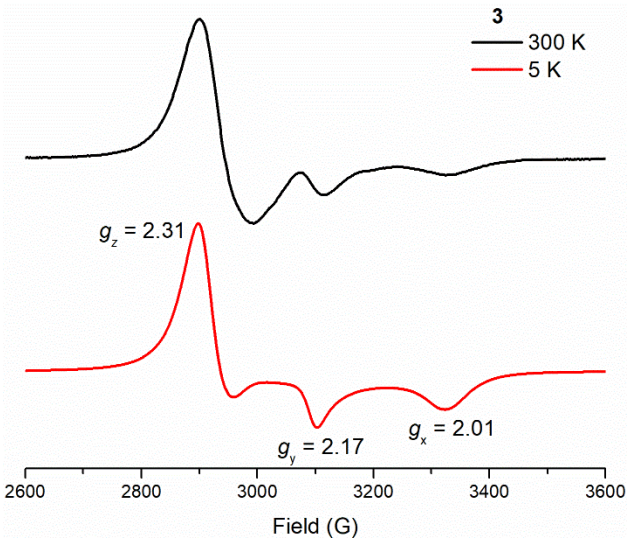

Figure 2.7 EPR of **3** at 5 K (9.835913 GHz) and at 300 K (9.829431 GHz).

2.4.4 Static (DC) magnetic properties. The temperature dependencies of the magnetic susceptibility-temperature products ($\chi_M T$) of ground samples of **1**, **2**, and **3** were collected between 2 K and 300 K with an applied DC field of 1 kOe and were fit using the program PHI, whose parameters are shown in Table 2.3. Figure 2.8 show that both complexes **1** and **2** possess $S = ½$

Ni(III) ions. **1** exhibits a $\chi_M T$ value of 0.41 cm^3 K mol^{-1} at 300 K, with the fit yielding a g_{iso} value of 2.06(1), slightly lower than that obtained by the EPR. Upon cooling, the magnetic susceptibility product decreases gradually at first, and then more rapidly below 20 K, to a minimum of 0.13 cm^3 K mol^{-1} at 2 K. This suggests a weak, through-space antiferromagnetic interaction, which is calculated to be -2.3(0) cm^{-1}. Similarly, **2** displays a room temperature $\chi_M T$ value of 0.41 cm^3 K mol^{-1}, with the fit yielding a g_{iso} value of 2.16(9), consistent with the EPR data.

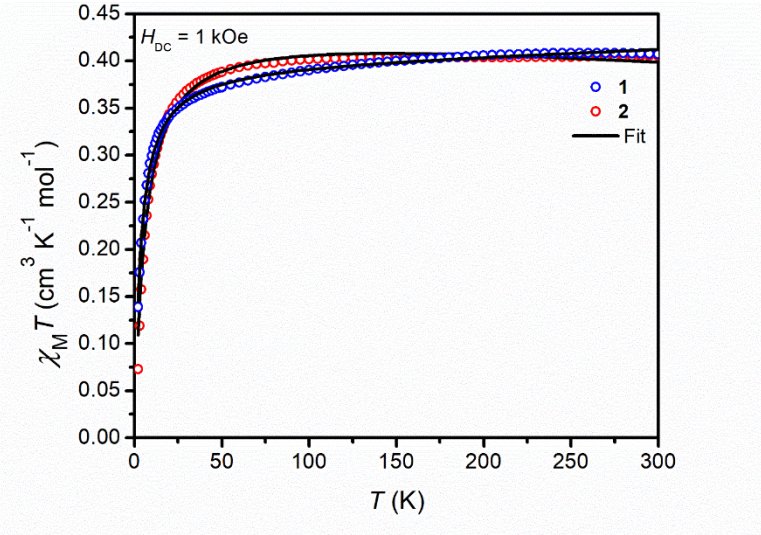

Figure 2.8 Temperature-susceptibility plot of **1** and **2** at 1 kOe from 2 – 300 K.

Table 2.3 Fit parameters of temperature-susceptibility data obtained from PHI.[15]

Complex	DC field (kOe)	g_{iso} value	zJ (cm^{-1})	χ_{TIP} (10^{-4} cm^3 mol^{-1})
1	1	2.06(1)	-2.3(0)	0.6(2)
2	1	2.16(9)	-3.6(1)	-1.1(7)[a]
3	1	2.20(4)	-0.5(3)	11.(01)
3	5	2.15(8)	-0.4(6)	1.2(5)

[a]Negative χ_{TIP} value possibly due to crystallite torquing.

Upon cooling, the $\chi_M T$ value decreases gradually in a similar fashion to **1** until reaching 0.07 cm^3 K mol^{-1} at 2 K. This weak antiferromagnetic interaction is calculated to be slightly stronger than that of **1**, -3.6(1) cm^{-1}. These results are consistent with the closest Ni – Ni distances from Table 2.1.

Unlike **1** and **2**, however, the temperature dependence of the magnetic susceptibility of **3** collected at 1 kOe shows a surprising amount of temperature independent paramagnetism (TIP), as shown in Figure 2.9 At 300 K the $\chi_M T$ value is 0.79 cm^3 K mol^{-1}, far higher than the expected value of 0.375 cm^3 K mol^{-1} for a $S = ½$, $g = 2$ system, but lesser than that of the 1.00 cm^3 K mol^{-1} expected for the $S = 1$, $g = 2$ Ni(II) decomposition product. The linear increase in the susceptibility is characteristic of TIP, and when the sample was measured at a higher field, 5 kOe, the susceptibility only reached a value of 0.46 cm^3 K mol^{-1} at 300 K, and the susceptibility was nearly constant in the range of 50 K – 300 K. From the fits obtained by PHI the contribution from TIP is almost ten times higher in the 1 kOe data compared to the 5 kOe data. In one way, this can be viewed as the higher field quenching the phenomenon responsible for the linear increase in the susceptibility, however this is incongruous with the magnetization vs field plot taken at 100 K, shown in Figure 2.10.

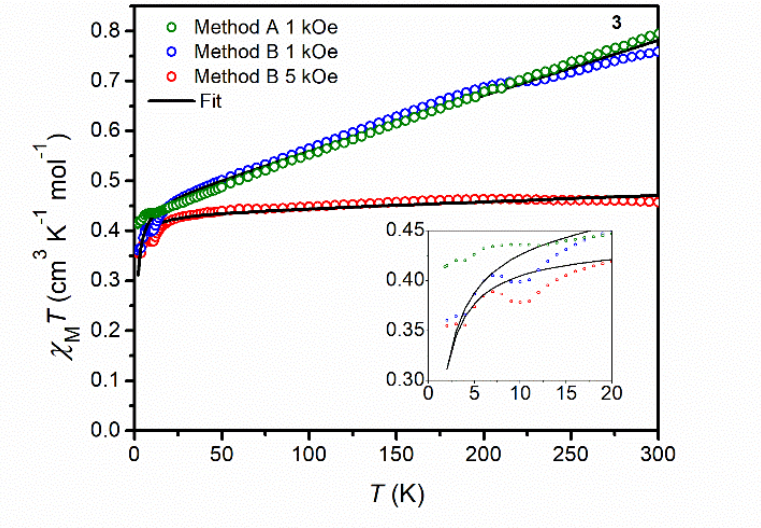

Figure 2.9 Temperature-susceptibility plot of **3** from the original serendipitous product resulting from Method A compared to the reproducible product from Method B. The data is for a static applied field of 1 kOe for both batches, with Method B also being collected at 5 kOe, from 2 – 300 K. The inset highlights the small bump at low temperatures, which can be seen in many Ni(cyclam) SMMs.

The *M* vs *H* plot of **3** is linear throughout the measurement, indicating the lack of ferromagnetic impurities that would result in significant curvature in the line. However, because it is linear, and the susceptibility is related to the magnetization divided by the field we would expect the susceptibility-temperature product at 100 K to be the same at 1 kOe and 5 kOe (and at all fields where the *M* vs *H* is linear). Figure 2.9 clearly shows that the susceptibilities are *significantly* different between the two fields measured. Comparing the raw data of from the *M* vs *H* plot to that of the $\chi_M T$ plots reveals that the 1 kOe temperature dependent data is approximately 3% higher at 100 K than the field-dependent data, which accounts for the difference after correcting for the sample holder and diamagnetism of the sample. This is in contrast to the 5 kOe temperature dependent data, which is only 0.4% lower than the field-dependent data at the same temperature. One possible explanation for this is the presence of a field-dependent phase transition that occurs for one field, but not the other, or perhaps more strongly for one over the other. Regardless, this field-dependence of the susceptibility requires further investigation.

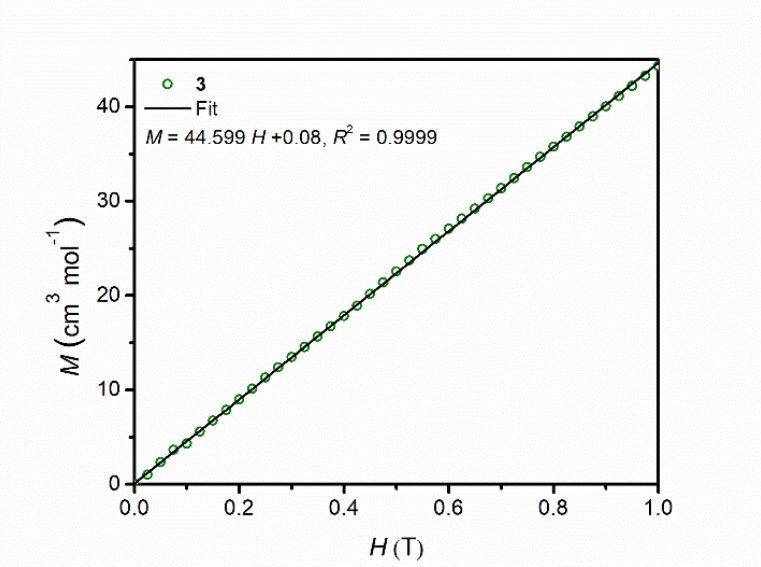

Figure 2.10 Magnetization of **3** (Method B) vs applied field at 100 K. Linearity in the plot indicates the lack of ferromagnetic impurities within the sample.

2.4.5 Dynamic (AC) magnetic properties. Consistent with our previous results, the nuclear-spin containing **1** and **2** did not show slow magnetic relaxation, however unlike the previous results these complexes exhibit anti-ferromagnetic interactions which effectively results in a $S = 0$ ground state, which also would not show slow magnetic relaxation. The nearly nuclear-spin free **3** was also consistent with the previous results and showed field induced slow magnetic relaxation. Figure A2.5 shows the in-phase and out-of-phase magnetic susceptibility of **1** from 0 – 2 kOe at 1.8 K, and Figure A2.6 shows the AC susceptibility of **2** from 0 – 8 kOe at 1.8 K. Because the magnetic susceptibility of **1** and **2** are so low at 1.8 K, consistent with their $\chi_M T$ plots, the 2 kOe data were retaken at 5 K, Figures A2.5 and A2.7, however slow magnetic relaxation was still not observable.

The field dependence of the AC susceptibility was studied for **3** at 2 K (Figure 2.11). Similar to the previously reported nitrate species, perchlorate-ligated **3** shows only a 'single' relaxation pathway which changes with applied field. There is no observable slow magnetic relaxation at zero

applied field, consistent with the majority of $S = ½$ SMMs, and applying a small magnetic field of 100 Oe is insufficient to induce slow magnetic relaxation. This rapid relaxation is likely due to the quantum tunneling of magnetization (QTM). Since **3** is $S = ½$ and contains no (obvious) barrier towards magnetic relaxation, QTM can contribute towards the relaxation simply by tunneling through the degenerate Kramers doublet. Increasing the applied DC field to 500 Oe strongly suppresses the QTM and moves the magnetic relaxation into frame, but the relaxation time τ remains faster than our instrumentation. By 1.0 kOe, the peak in the out-of-phase data moves into frame, and increasing the field up to 1.5 kOe slows the relaxation rate. Starting at 2.0 kOe, a second, slower relaxation pathway begins to appear at *ca.* 20 Hz, hereafter referred to as the 'high-field' relaxation pathway. Meanwhile, the original 'low-field' relaxation pathway gradually blends into the high-field pathway with the increasing field until 4.0 kOe, where it is indistinguishable from the tail of the high-field relaxation pathway. Further increasing the field slows the high-field relaxation pathway to a minimum of 0.2 Hz at 20.0 kOe.

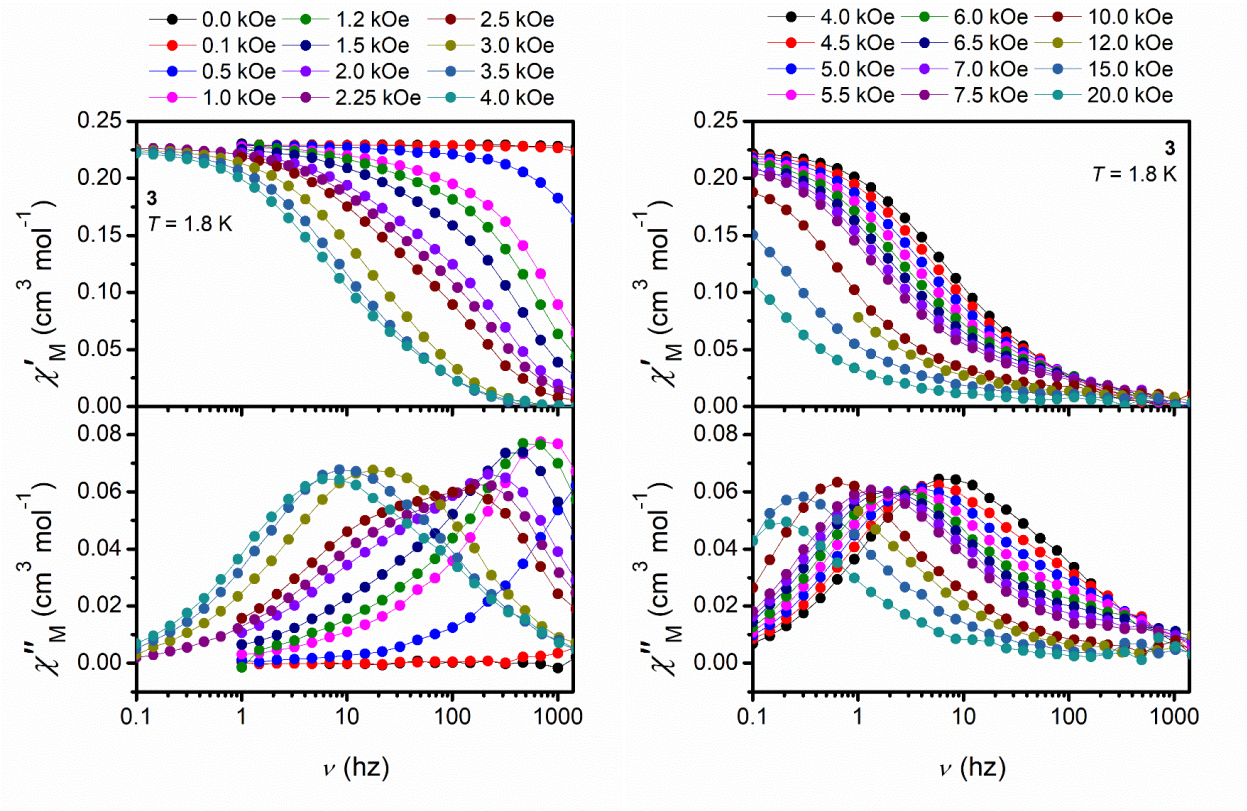

Figure 2.11 Field dependence of in-phase (top) and out-of-phase (bottom) magnetic susceptibility of **3** at 1.8 K from 0 – 4 kOe (left) and 4 – 20 kOe (right).

Extracting the relaxation rate, τ^{-1}, from the data using Equation 1.7 and plotting it against field highlights the similarities of the field dependence of the high- and low-field relaxation pathways, Figure 2.12. Plotting the data on a log-log plot reveals that the data can be modeled well with a linear fit, however such a line would suggest an H^3 dependence. Equation 2.1, reproduced below, describes the global relaxation rate as a function of the applied magnetic field, the first term represents the direct pathways, the second the quantum tunnelling of magnetization (QTM), and the third the phonon bottleneck effect (PBE), none of which has an H^3 dependence.

$$\tau^{-1} = AH^4T + \frac{b_1}{1+b_2H^2} + BT^2 \qquad \text{(Eq. 2.1)}$$

Therefore, we modeled the data as a combination of QTM and direct pathways, which also modeled the data well while being physically meaningful. We excluded the PBE from the fit of

the field-dependent data as its contribution at 1.8 K is negligibly small and the resulting fit was satisfactory. We note that a fourth term, representing Raman relaxation, is also commonly used in fitting the field dependence and takes the form $d(1+eH^2)T^n/(1+fH^2)$. However, when the field dependent data was fit including this term the Raman parameters refined to zero.

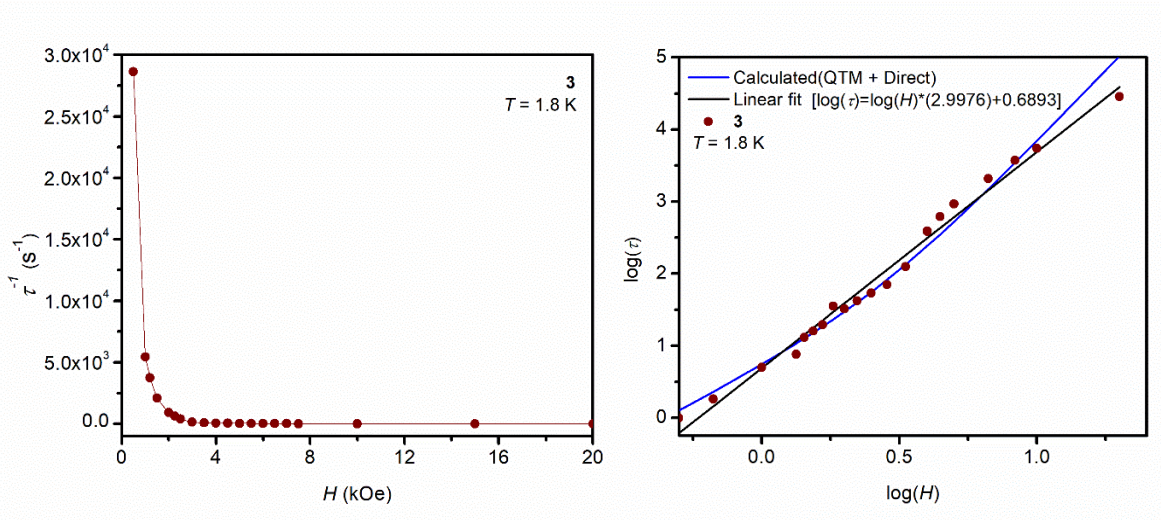

Figure 2.12 Field dependence of relaxation time of **3** from 0.5 – 20 kOe at 1.8 K with linear scaling (left) and logarithmic scaling (right). Black trace represents the linear fit of the data; blue trace represents the fit obtained from the QTM and direct relaxation pathways.

Table 2.4 Relaxation parameters extracted from AC magnetic data.

Data set	A (s^{-1} K^{-1} kOe^{-4})	b_1 (s^{-1})	b_2 (kOe^{-2})	QTM‡ (s^{-1})	B (s^{-1} K^{-2})
H dependence	0.359	1.66 x 10^5	3.39 x 10^4		
T dependence, 1.2 kOe	0.251			300	616
T dependence, 4.0 kOe	0.289			30.5	62.38

‡QTM term used in place of b_1 and b_2 for temperature dependent data to prevent overparameterization.

The temperature dependence of the AC susceptibility was investigated for **3** under a 1.2 kOe and 4.0 kOe applied DC field (Figure 2.12) to determine the mode of relaxation for the low- and high-field relaxation pathways. At 1.2 kOe the peak in the out-of-phase magnetic susceptibility is visible up to 2.5 K, after which only the tail is visible. At 4.0 kOe the peak is visible up to 10 K.

Extracting and plotting τ^{-1}, Figure 2.13, shows that the low-field relaxation pathway is far more sensitive towards temperature than the high-field relaxation pathway. A line of best fit reveals that the low-field pathway is linear with temperature, consistent with a direct relaxation pathway, however the *A* parameter extracted is orders of magnitude larger than the one extracted from the field dependent data as well as the one extracted from the high-field data (*vide infra*).

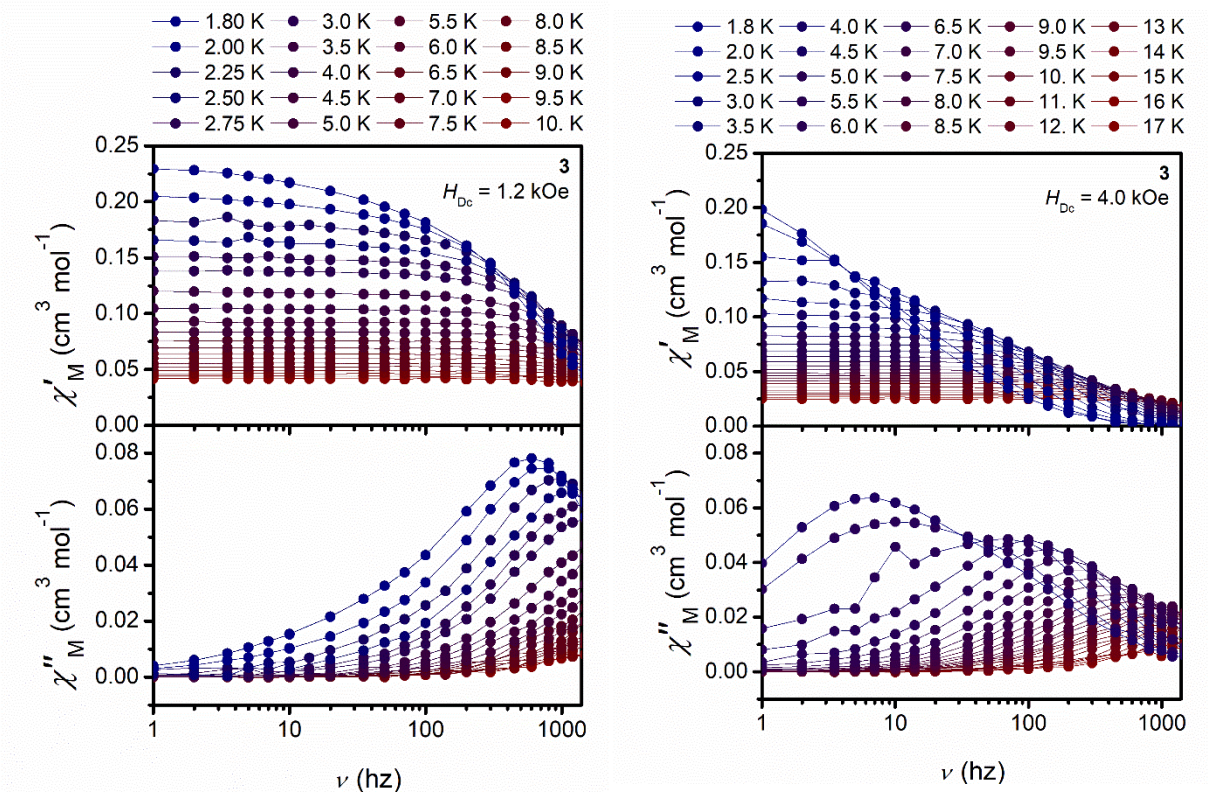

Figure 2.13 Temperature dependence of in-phase (top) and out-of-phase (bottom) magnetic susceptibility of **3** from 1.8 – 10 K at 1.2 kOe (left) and from 1.8 – 10 K at 4.0 kOe (right).

Additionally, such a fit suggests that magnetic relaxation would *stop completely* at approximately 1 K, an impossibility. However, a log-log plot can give better insight into the temperature dependence of the system. From the curvature in Figure 2.14 it is clear that the exponential temperature dependence is not consistent at all temperatures measured, and the slope of the line in the log-log plot is approximately 1.6, suggesting a combination of direct and phonon bottleneck

relaxation pathways, as well as QTM, though its contribution is negligible in comparison. As such, the data were fit using a combination of direct and phonon bottleneck relaxation pathways. We note that the $b_1/(1+b_2H^2)$ formulism for QTM was modeled as a single 'QTM' term to prevent overparameterization but is otherwise consistent with the expected values extracted from the field-dependent data.

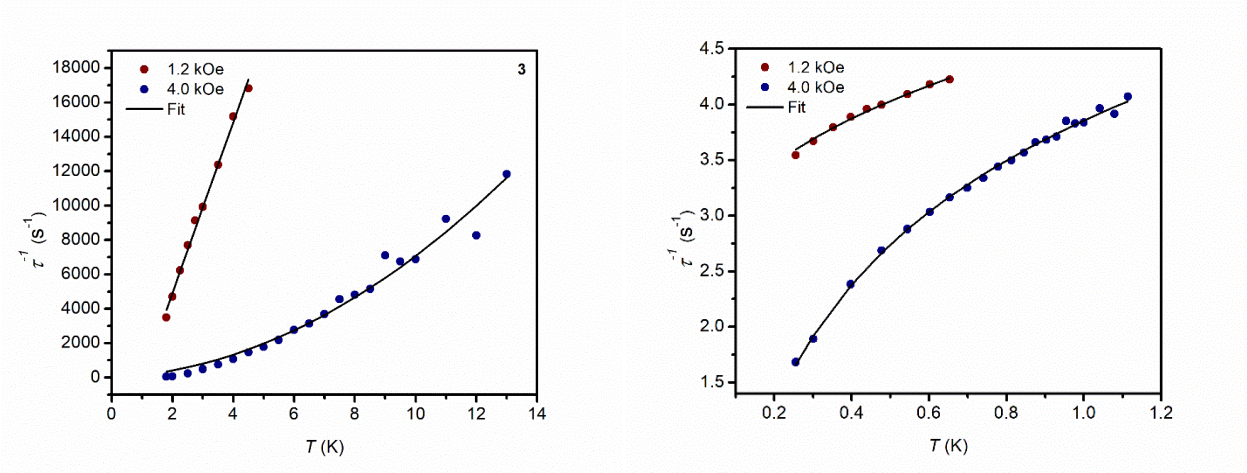

Figure 2.8 Temperature dependence of the relaxation rate of **3** with an applied magnetic field of 1.2 kOe and 4.0 kOe with a linear scaling (left) and logarithmic scaling (right).

The lower frequency of the high-field data allowed us to observe the peak in the χ'' data up to a much higher temperature than the low-field data, making the nonlinearity of the data much more obvious. This too was fit using a combination of direct, phonon bottleneck, and QTM pathways. The parameters extracted from the fits are self-consistent, where the parameters for all three data sets are similar enough to one another that it is likely to be the same process, involving the same (or similar) phonons.

2.5. Conclusion

We have prepared and measured the structural and magnetic properties of three additional Ni(III)cyclam type complexes, two featuring nuclear-spin containing halides and one essentially

nuclear-spin free perchlorate. Consistent with previous results, the halides **1** and **2** do not show slow magnetic relaxation at low temperatures, even with an applied magnetic field, whereas **3** shows slow magnetic relaxation characteristic of SMMs. Originally, we concluded from this that the presence of nuclear spin in the axial positions of these Ni(III) cyclam type complexes does preclude slow magnetic relaxation, which we postulated was the result of super-hyperfine coupling between the electronic- and nuclear-spins in the axial positions. However, in light of Yamashita's very recent publication showing $[Co_{0.9}Ni_{0.1}(cyclam)Cl_2]ClO_4$ undergoes slow magnetic relaxation, we believe that it is the antiferromagnetic interactions that preclude slow magnetic relaxation in **1** and **2**. Exploration of the temperature and field-dependence of the magnetic relaxation in **3** revealed a singular, direct relaxation pathway that was plagued with the phonon bottleneck effect, slowing the relaxation rates at the expense of complicating the system and likely reducing its ability to act as a qubit in application due to the random excitations associated with the phonon bottleneck effect.

2.6. References

(1) Guo, F. S.; Day, B. M.; Chen, Y. C.; Tong, M. L.; Mansikkamäki, A.; Layfield, R. A. Magnetic Hysteresis up to 80 Kelvin in a Dysprosium Metallocene Single-Molecule Magnet. *Science.* **2018**, *362* (6421), 1400–1403. https://doi.org/10.1126/science.aav0652.

(2) Gu, L.; Wu, R. Origins of Slow Magnetic Relaxation in Single-Molecule Magnets. *Phys. Rev. Lett.* **2020**, *125* (11), 117203. https://doi.org/10.1103/PHYSREVLETT.125.117203.

(3) Gu, L.; Wu, R. Origin of the Anomalously Low Raman Exponents in Single Molecule Magnets. *Phys. Rev. B* **2021**, *103* (1), 1–9. https://doi.org/10.1103/PhysRevB.103.014401.

(4) Escalera-Moreno, L.; Baldoví, J. J.; Gaita-Ariño, A.; Coronado, E. Spin States, Vibrations and Spin Relaxation in Molecular Nanomagnets and Spin Qubits: A Critical Perspective. *Chem. Sci.* **2018**, *9* (13), 3265–3275. https://doi.org/10.1039/c7sc05464e.

(5) Albino, A.; Benci, S.; Tesi, L.; Atzori, M.; Torre, R.; Sanvito, S.; Sessoli, R.; Lunghi, A. First-Principles Investigation of Spin-Phonon Coupling in Vanadium-Based Molecular Spin Quantum Bits. *Inorg. Chem.* **2019**, *58* (15), 10260–10268.

https://doi.org/10.1021/acs.inorgchem.9b01407.

(6) Moseley, D. H.; Stavretis, S. E.; Zhu, Z.; Guo, M.; Brown, C. M.; Ozerov, M.; Cheng, Y.; Daemen, L. L.; Richardson, R.; Knight, G.; Thirunavukkuarasu, K.; Ramirez-Cuesta, A. J.; Tang, J.; Xue, Z. L. Inter-Kramers Transitions and Spin-Phonon Couplings in a Lanthanide-Based Single-Molecule Magnet. *Inorg. Chem.* **2020**, *59* (7), 5218–5230. https://doi.org/10.1021/acs.inorgchem.0c00523.

(7) Bhowmick, I.; Roehl, A. J.; Neilson, J. R.; Rappé, A. K.; Shores, M. P. Slow Magnetic Relaxation in Octahedral Low-Spin Ni(III) Complexes. *Chem. Sci.* **2018**, *9* (31), 6564–6571. https://doi.org/10.1039/c7sc04482h.

(8) Toshima, K.; Sato, T.; Horii, Y.; Sato, K.; Sugisaki, K.; Breedlove, B. K.; Takaishi, S.; Li, Z. Y.; Yamashita, M. Slow Magnetic Relaxation of Ni(III) Complexes toward Molecular Spin Qubits. *Eur. J. Inorg. Chem.* **2023**. https://doi.org/10.1002/ejic.202300125.

(9) Prasad, L.; Nyburg, S. C. The Structure of Ni(Cyclam)(ClO4)2. *Acta Crystallogr.* **1987**, *C43*, 1038–1042. https://doi.org/10.1107/S0108270187093090.

(10) Taraszewska, J.; Sadło, J.; Michalik, J.; Korybut-Daszkiewicz, B. Stability and ESR Spectra of Ni(III) Tetraazamacrocyclic Complexes in Nitrate and Chloride Solutions. *Pol. J. Chem.* **2000**, *74* (6), 813–822.

(11) Bruker AXS inc. SAINT, v.8.38A. Madison, WI 2016.

(12) Sheldrick, G. M. SADABS, Version 2.03, Bruker Analytical X-Ray Systems, Inc., Madison, WI. Madison, WI 2000.

(13) Sheldrick, G. M. Crystal Structure Refinement with SHELXL. *Acta Crystallogr. Sect. C Struct. Chem.* **2015**, *71* (Md), 3–8. https://doi.org/10.1107/S2053229614024218.

(14) Bain, G. A.; Berry, J. F. Diamagnetic Corrections and Pascal's Constants. *J. Chem. Educ.* **2008**, *85* (4), 532–536. https://doi.org/10.1021/ed085p532.

(15) Chilton, N. F.; Anderson, R. P.; Turner, L. D.; Soncini, A.; Murray, K. S. PHI: A Powerful New Program for the Analysis of Anisotropic Monomeric and Exchange-Coupled Polynuclear d- and f-Block Complexes. *J. Comput. Chem.* **2013**, *34* (13), 1164–1175. https://doi.org/10.1002/jcc.23234.

(16) Stoll, S.; Schweiger, A. EasySpin, a Comprehensive Software Package for Spectral Simulation and Analysis in EPR. *J. Magn. Reson.* **2006**, *178* (1), 42–55. https://doi.org/10.1016/j.jmr.2005.08.013.

(17) Haines, R. I.; McAuley, A. Synthesis and Reactions of Nickel(III) Complexes. In *Coordination Chemistry Reviews,* **1981**; 39, 77–119. https://doi.org/10.1016/S0010-8545(00)80512-3.

(18) Desideri, A.; Raynor, J. B.; Chan, P. K.; Poon, C. K.; Dalton, J. C. S.; Goodman, B. A.; Raynor, J. B. Electron Spin Resonance Spectroscopy of Some Dianiono(1,4,8,1 I-Tetra-Azacyclotetradecane)-Iron (III) and-Nickel (III) Salts. *Dalt. Trans.* **1977**, 2051–2054. https://doi.org/10.1039/DT9770002051.

(19) Haines, R. I.; Mcauley, A. Kinetics of the Reaction of the (1, 4, 8, 11-Tetraazacyclotetradecane)Diaquonickel(III) Cation with Halide and Thiocyanate Ions in Aqueous Perchlorate Media. *Inorg. Chem.* **1980**, *19* (3), 719–723. https://doi.org/10.1021/ic50205a027.

Chapter 3: Crystallite Tuning of Magnetic Properties in $S = ½$ Ni(III) Cyclam (bi)Sulfate Complex Salts[1]

3.1 Introduction

Mononuclear single-molecule magnets (SMMs) are promising for exploitation in emerging information science technologies as potential quantum bits (qubits), high density data storage, and as gates for spin-polarized currents.[1–7] While lanthanide SMMs currently feature higher operating temperatures,[8] SMMs sourced from first-row transition metal ions are interesting due to their potential cost efficiency and increased sensitivity to local environments.[5] Thus far, a handful of 3d coordination complexes, featuring V(IV),[9–11] Mn(IV),[12] low spin Co(II),[13–15] Ni(I,III)[7,16], and Cu(II)[17,18] ions, has been shown to possess slow magnetic relaxation in the $S = ½$ state, providing an opportunity to design the smallest unit of molecular quantum computing.[19]

For SMMs with $S > ½$, there is an intrinsic (to the complex) barrier to transitions between microstates in the ground term; pathways for spin reorientation are governed by quantum tunneling through the barrier and/or energy absorption from various vibrations to go over the barrier. In contrast, for SMMs with $S = ½$ ground states, the physical underpinnings of the barrier, and pathways for slow magnetic relaxation, are less intuitive and may often arise from intermolecular interactions influenced by spin-phonon dynamics.

Previously, we reported the observation of slow magnetic relaxation in some low-spin ($S = ½$) and nearly nuclear spin-free (^{61}Ni, 1.1% abundant) Ni(III) cyclam complex salts.[7] We found that nitrate-ligated complexes showed slow magnetic relaxation, while the isothiocyanate-ligated species did not. The slow magnetic dynamics of the Ni(III) compounds appear to be governed by a combination of direct and Raman pathways. Computational studies suggested that the presence of nuclear spin (I) in the axial positions enabled a fast relaxation pathway, undetectable with

regular AC magnetometry. We hypothesized that the axial coordination of the nuclear spin-free atoms (^{16}O has $I = 0$) is required to observe slow magnetic relaxation in Ni(III) cyclam complexes. While hyperfine coupling is well known to quench slow magnetic relaxation with low to no applied field, the quenching effect via super-hyperfine coupling in the solid-state could offer a unique tool to manipulate the magnetic dynamics of Ni(III) cyclam systems. Overall, the results suggested that alteration of intermolecular interactions and nuclear spin could serve as synthetically adjustable parameters for control of slow relaxation in $S = ½$ systems.

SMM research has focused on understanding the role of vibrations, both intra- and inter-molecular (phonons), in recent years.[20–24] Understanding the role of connectivity, intermolecular interactions, and phonons is especially important for $S = ½$ systems as they lack the higher magnetic states that are typically considered the barrier towards magnetic relaxation. Furthermore, many $S = ½$ SMMs are affected by the phonon bottleneck effect (PBE), a phenomenon where the phonons emitted by the magnetic relaxation are inefficiently scattered and consequently reabsorbed.[12,25–30] While the PBE increases the spin-lattice relaxation time, a desirable quantity, it is typically considered detrimental as it complicates understanding the molecular relaxation pathways. Notwithstanding, the innate dependence of PBE on the chemical and structural environment may render it a valuable tool in elucidating the importance of different interactions for modulating slow relaxation of magnetization.

To study the effect of intra- and inter-molecular interactions on slow magnetic relaxation in Ni(III) cyclam complexes, we targeted several salts that would maintain the magnetically-productive N_4O_2 first coordination sphere, change anion geometry relative to previously-discussed nitrate complexes, potentially change overall complex charge to anionic species, and generate more extensive hydrogen bonding networks than the nitrato- and isothiocyanato-bound complexes

disclosed previously. Herein, we report the structural and magnetic properties of a sulfate-bridged Ni(III) cyclam chain compound, and the first example of bisulfate-bound Ni(III) cyclam complexes.

Scheme 3.1. Structural overview of polymeric **1** and molecular **2**, highlighting chemically tunable moieties. Exchangeable protons are shown explicitly. "X" generically refers to H-bond partner.

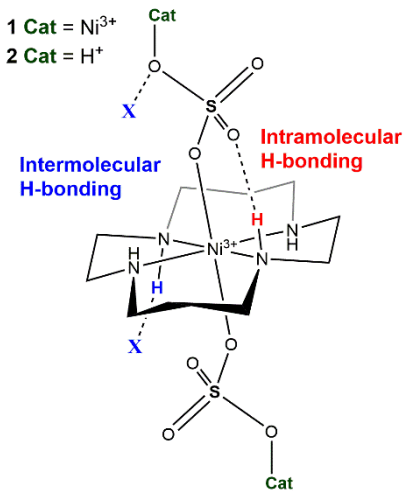

3.2 Division of Labor.

Tom Morrison synthesized, measured, and analyzed all materials presented. Dr. Indrani Bhowmick assisted with data analysis. Dr. Matt Shores assisted with visualization, conceptualization, methodology, and writing. We thank the ARC staff for their assistance with the collection of crystallographic, mass spectrometry, and magnetic data.

3.3 Experimental

3.3.1 Synthesis. Unless otherwise noted, compound syntheses and manipulations were performed at room temperature. The precursors $[Ni(cyclam)](ClO_4)_2$ and $[Ni(cyclam)Cl_2]Cl$ were

synthesized following literature procedures.[31,32] Unless specified, Millipore water was used, and all other reagents were obtained from commercial sources and used without further purification.

{[Ni(cyclam)(SO_4)]ClO_4·H_2O}$_n$ (1): This compound was synthesized by modifying the literature procedure[33] as follows: cyclam was used in place of tetramethylcyclam (TMC). A 20 mL scintillation vial was charged with solid [Ni(cyclam)](ClO_4)$_2$ (171 mg, 0.373 mmol) and dissolved in water (10 mL). To the yellow-colored solution, solid $Na_2S_2O_8$ (48.7 mg, 0.205 mmol) was added all at once and stirred for 30 minutes, whereupon the product precipitated as a light green powder. Anal. Calcd for $C_{10}H_{26}N_4O_9NiS$: C, 25.42; H, 5.55; N, 11.86; Found: C, 25.32; H, 5.39; N, 11.71. FT-IR (cm^{-1}) (Figure A3.2): 3550w, 3415w, 3221w, 3120w, 3044m, 2984w, 2961w, 2936w, 2869m, 2811w, 602m, 565m, 527m. 972m, 944w, 932w, 906m, 891m, 730w, 700w, 630m. Crystals suitable for single crystal x-ray diffraction analysis were synthesized by slowly removing the filtrate under vacuum over the course of one week, producing a mixture of dark green blocks of **1** and orange blocks of [Ni(cyclam)](ClO_4)$_2$.[34] The powder diffraction pattern of the green powder **1** was consistent with the calculated pattern of the collected crystal structure (Figure A3.4).

[Ni(cyclam)(HSO_4)$_2$]HSO_4·MeOH (2·MeOH): A 20 mL scintillation vial was charged with [Ni(cyclam)Cl_2]Cl (34.9 mg, 0.096 mmol), Ag_2SO_4 (45.5 mg, 0.146 mmol), and a 1:20 MeOH: conc. H_2SO_4 mixture (10 mL). The mixture was stirred for 30 minutes at room temperature and then filtered to remove the insoluble Ag(I) salts. A vapor diffusion of Et_2O into the MeOH:H_2SO_4 filtrate was performed, but there was no crystal formation after two days, whereupon $KClO_4$ (4.31 mg, 0.031 mmol) was added to the mother liquor to aid crystallization. After 3 days, the mother liquor became biphasic, composed of a green layer and a purple layer, with green and purple crystals coating the side of the vial in their respective layers. Single crystal x-ray diffraction

analyses revealed the crystals to be **1** (green) and **2·MeOH** (purple). Attempts to isolate **2·MeOH** as a pure bulk material were unsuccessful.

[Ni(cyclam)(HSO$_4$)$_2$]HSO$_4$ (2): A flame-dried 25 mL Schlenk flask was charged with [Ni(cyclam)Cl$_2$]Cl (59.5 mg, 0.163 mmol), and attached to a t-joint connected to a Schlenk line and base bath. The apparatus was flushed with N_2 gas, followed by the addition of concentrated sulfuric acid (500 μL); the mixture was stirred until all solids were dissolved and the solution stopped bubbling (*Caution! Produces HCl gas*), approximately 10 minutes. The red/brown solution was diluted with acetonitrile (20 mL), whereupon the solution color turned green, and filtered through a medium-porosity sintered glass frit. The filtrate was transferred to a scintillation vial, capped, and allowed to stand for 2 days at room temperature, whereupon the desired product formed as dark brown needles (29.9 mg, 0.054 mmol, 31 %). Anal. Calcd for $C_{10}H_{27}N_4O_{12}NiS_3$: C, 21.83; H, 4.95; N, 10.18; Found: C, 21.97; H, 4.91; N, 10.18. ESI-MS(+) (Figure A3.8) (*m*/*z*): 355.25, [Ni(II)(cyclam)(HSO$_4$)]$^+$; 452.17, [Ni(III)(cyclam)(HSO$_4$)$_2$]$^+$. FT-IR (cm^{-1}): 3372sh, 3160m, 3118m, 2864m, 2443w, 2348w, 1688w, 1592w, 1462m, 1453w, 1440m, 1426m, 1385w, 1367w, 1343w, 1335w, 1324w, 1293m, 1265w, 1245m, 1223m, 1208sh, 1157sh, 1142s, 1122sh, 1096sh, 1076sh, 1055sh, 1040sh, 1023s, 940w, 906w, 887s, 867s, 838s, 826sh, 766m, 724m, 604sh, 584sh, 568s, 526sh, 503m, 446m, 428m.

[Ni(d$_4$-cyclam)(DSO$_4$)$_2$]DSO$_4$ (2-d$_7$): An apparatus identical to the one described above was prepared and charged with [Ni(cyclam)Cl$_2$]Cl (31.6 mg, 0.087 mmol) and concentrated d_2 sulfuric acid (99% D, 500 μL). The mixture was stirred until all material was dissolved and the solution stopped bubbling, approximately 10 minutes. The red solution was diluted with d_3 acetonitrile (98% D, 2 mL) and filtered through a 0.2 μm nylon filter. The filtrate was transferred to a 1-dram shell vial, capped, and allowed to stand for 2 days at room temperature, whereupon the desired

product formed as dark brown needles (15.76 mg, 0.028 mmol, 32 %). A powder diffraction pattern and FTIR spectrum were collected to verify bulk purity and extent of deuteration. DART-MS(+) (Figures A3.9 and A3.10) (*m*/*z*): 230.23, $[Ni(d_4\text{-cyclam})(DSO_4)(D_2SO_4)]^{2+}$; 598.44, $[Ni(d_4\text{-cyclam})(DSO_4)_2 + D_2SO_4 + D_2O]^+$; +. FT-IR ($cm^{-1}$): 3372sh, 3137m, 3105m, 2871m, 2482m, 2348w, 1688w, 1592w, 1452w, 1436m, 1397w, 1382w, 1367sh, 1342m, 1321m, 1300m, 1267w, 1250 sh, 1235sh, 1218m, 1164sh, 1146s, 1122sh, 1094sh, 1068sh, 1015s, 940w, 906w, 879sh, 857s, 838s, 826sh, 766m, 736m, 604sh, 584sh, 564s, 526sh, 503m, 452m, 433m, 405w.

3.3.2 X-ray structure determinations. Crystals suitable for single-crystal x-ray analysis were coated with Paratone-N oil and supported on a Cryoloop before being mounted on a Bruker Kappa Apex II CCD diffractometer under a stream of N_2 gas. Data collections were performed at low temperature (100 K - 200 K, see Table S1) using a Siemens KFF Mo_2K-90 sealed tube (Mo Kα, λ = 0.71073 Å) x-ray source and a curved graphite monochromator, targeting complete coverage and 4-fold redundancy. Crystallographic data and metric parameters are presented in Table S1. Determination of unit cell parameters through refinement, data collection, reduction, and correction for Lorentz and polarization effects was performed using the SAINT software package.[35] Data were sorted, scaled, averaged, and corrected for semiempirical absorption affects with SADABS.[36] The structures were solved with the ShelXT structure solution program and refined with the ShelXL-2018/3 refinement package.[37] Unless otherwise noted, thermal parameters for all non-hydrogen atoms were refined anisotropically. Hydrogen atoms were added at calculated positions and were refined using a riding model. In the structure of **1**, the data were modeled as a two-component pseudo-merohedral twin; the refined fractional contribution of the minor component refined to 18%. In the structures of **2** and **2-d$_7$**, the outer-sphere bisulfate H atoms were found in the electron density difference maps, and DFIX and DANG restraints were used to

restrained them to chemically reasonable positions. In the structure of **2·MeOH**, the data were modeled as a two-component inversion twin; the refined fractional contribution of the minor component refined to 44%.

3.3.3 Magnetic measurements. Magnetic susceptibility data were collected using a Quantum Design MPMS XL magnetometer for **1** and a Quantum Design MPMS3 SQUID magnetometer for **2** and **2-d$_7$**. Samples were ground using a mortar and pestle and selected for different crystallite sizes by passing through size exclusion filters. Three crystallite size regimes were investigated, (a) "**crystalline**" is as-crystallized polycrystalline (particle size > 206 μm); (b) "**ground**" is lightly ground (106 μm < x < 206 μm); (c) "**100 μm**" is heavily ground (53 μm < x < 106 μm). The sifted samples were loaded into polyethylene bags and sealed, then the bags were inserted into drinking straws and inserted into the instrument. Ferromagnetic impurities were checked through a variable field analysis (0 to 10 kOe) of the magnetization at 100 K: overall linearity in the collected data for all three compounds indicated the lack of significant ferromagnetic impurities. Static (DC) magnetic susceptibility data for "ground" samples were collected at temperatures ranging from 3 K to 300 K at 1 kOe measuring field (see Appendix for other particle sizes). Alternating current (AC) magnetic susceptibility measurements were performed from 0.1 Hz to 700 Hz and from 1.8 K to 15 K with an alternating field of 4 Oe. Data were corrected for the magnetization of the sample holder by subtracting the susceptibility of an empty container, and for the diamagnetic contributions of the sample by using Pascal's constants.[38]

Temperature-dependent magnetic susceptibility data for **1** were modeled using a combination of a Bonner-Fisher component,[39–41] which modeled the susceptibility of an $S = ½$ infinite isotropic Heisenberg chain, and a Curie-Weiss-like component that modeled finite chain lengths with an odd number of Ni^{3+} spins, isolated Ni^{3+} spins, and/or other paramagnetic impurities. The resulting

exchange coupling is reported using $H = -S \cdot J \cdot S$ spin Hamiltonian formalism. See appendix 2.3 for details.

Temperature-dependent DC magnetic susceptibility data for **2** and **2-d$_7$** were modeled with the program PHI[42] to single-ion species with temperature independent paramagnetism, weakly interacting with the spin bath. See appendix for details.

The ac magnetic susceptibility data for several particle size-selected samples of **2** and **2-d$_7$** were fit to several multicomponent relaxation models. Using equation 3.1, the variables *A*, *B*, and *n* were allowed to refine freely.

$$\boldsymbol{\tau^{-1} = AT + BT^{n} + \tau_0 e^{\frac{-U_{eff}}{k_B T}}} \qquad \text{(Eq. 3.1)}$$

Here, the AT term represents the direct pathways, BT^n the Raman pathways, and $\tau_0\exp(-U_{eff}/k_BT)$ the Orbach pathway. Several models and temperature ranges were compared (Table A3.5 and Figures A3.28-29), and further details can be found in the appendix.

3.3.4 Other physical characterizations. Mass spectrometry experiments were performed on a Thermo-Finnigan LTQ LC/MS-MS ESI-MS instrument, where the sample was introduced via direct infusion using a syringe pump (rate 10 μL/s). The samples were dissolved in Millipore water, methanol, or acetonitrile at a concentration of 0.01 mg/mL. Electronic absorption spectra (Figure A3.13) were obtained using quartz cuvettes in an Agilent 8453 spectrometer. Complexes were dissolved in Millipore water. Diffuse reflectance data were obtained with a Thermo Scientific Evolution 300 UV-Vis spectrophotometer, using $BaSO_4$ for background. Infrared spectra were obtained using a Bruker Tensor II FT-IR spectrometer. Electron paramagnetic resonance spectra were obtained using a Bruker ESR-300 spectrometer equipped with an X-band microwave source, an ultra-high sensitivity resonator, and a liquid He cryostat with a quartz finger dewar. Data were collected with a 5 G modulation amplitude and 100 kHz frequency, and were simulated using Easy

Spin.[43] Thermal gravimetric analysis (TGA) was performed on a TA TGA Q500 Thermogravimetric Analyzer under a N_2 flow at a rate of 5 °C/min from room temperature to 100 °C and 10 °C/min thereafter. Powder X-ray diffraction data were collected at room temperature using a Scintag X-2 powder X-ray diffractometer equipped with Cu Kα radiation, Peltier detector and stationary sample stage, collecting diffraction angles between 5° and 30° 2θ. Elemental analyses were performed by Midwest Microlabs, Indianapolis, IN.

3.4 Results and Discussion

3.4.1 Syntheses and structures. To study the effect of intra- and inter-molecular interactions on slow magnetic relaxation in Ni(III) cyclam complexes, we synthesized several salts where the axial ligands contained tetrahedral SO_4(H) anions. Our initial attempts to synthesize sulfate-ligated Ni(III) cyclam salts through ion exchange reactions resulted in an inseparable mixture of crystalline Ni(cyclam)(SO_4)(ClO_4) (**1**) and [Ni(cyclam)(HSO_4)$_2$]HSO_4·MeOH (**2·MeOH**). We note that the nickel sulfate perchlorate compound has been synthesized previously, but not characterized crystallographically or had the temperature dependent magnetic susceptibility characterized; while **2·MeOH** represents a first example of a Ni(III) cyclam species bound by bisulfate ligands. To isolate pure products, we adapted a previously reported synthesis for [Ni(TMC)SO_4]ClO_4 for cyclam, producing **1** in good yield, and implemented an acid-base reaction, described in the experimental section, for synthesizing pure samples of **2.** From these procedures we isolated the chain compound {[Ni(cyclam)(μ_2-SO_4)]ClO_4·H_2O}$_n$ (**1**, Figure 3.1, left), the bisulfate-ligated complex [Ni(cyclam)(HSO_4)$_2$]HSO_4 (**2**, Figure 3.1, right), and its deuterated isotopologue **2-d$_7$**.

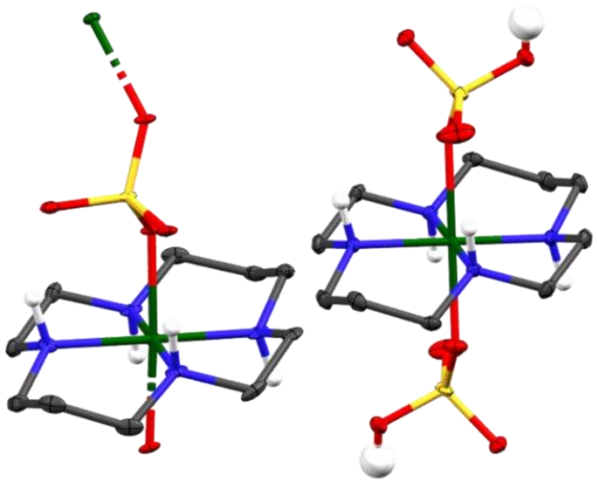

Figure 3.1 Crystal structures of sulfate-bridged chain **1** (left) and bisulfate-ligated molecular **2** (right) rendered with 50% thermal ellipsoids. Green, red, blue, yellow, and gray ellipsoids represent Ni, O, N, S, and C atoms, respectively, and white spheres represent H atoms involved in hydrogen bonding interactions. Solvent molecules, outer sphere anions, and H atoms not involved in hydrogen bonding are omitted for clarity.

Crystallographic analyses (Figure 3.1 and appendix) show that all four structures feature Ni(III) ions with comparable distorted octahedral coordination geometries. The sulfate-bridged chain featured in **1** is structurally comparable to a Mn-containing compound reported previously by Sessoli and coworkers.[44] The intra-chain Ni(III) centers are canted by 11.30(3)° and are separated by 6.280(1) Å, whereas the shortest inter-chain Ni-Ni distance is 8.536(1) Å. In comparison, the Mn analogue is canted by 15.6°, the closest intra-chain Mn-Mn distance is 6.362 Å, and the closest inter-chain Mn-Mn distance is 8.552 Å.[44] Meanwhile, compound **2** represents the first report of a Ni-bisulfate-ligated species, with a Ni-O distance of 2.1135(16) Å. The closest Ni-Ni distance is 7.838(2) Å.

Both **1** and **2** have different anion geometries and generate more extensive hydrogen bonding networks than the nitrato- and isothiocyanato-bound complexes disclosed previously.[7,45] Meanwhile, although **2** and **2·MeOH** have different hydrogen bonding networks while maintaining similar molecular environments, making them an ideal system to study the effect of

hydrogen bonding, we were unable to convert **2** into **2·MeOH** without reducing Ni(III) to Ni(II), and as a result we were unable to isolate pure bulk samples of **2·MeOH** for magnetic studies.

Hydrogen bonding in the structure of **1** is localized to each chain with no inter-chain H-bonding. Each sulfate in **1** makes three hydrogen bonds with the cyclam amines, with N···O distances of 2.82(7) Å, 2.86(6) Å, and 3.06(5) Å. The sulfate is also H-bonded to a co-crystallized H_2O molecule, 2.76(5) Å, which in turn is H-bonded to one outer-sphere perchlorate anion, 2.86(9) Å. In contrast, the structure of **2** features a more extensive network of hydrogen bonding interactions (Figure 3.2). The intramolecular N-H···OSO_3H distance in **2** is 2.878(2) Å and occurs once for each axial bisulfate moiety, which is also H-bonded to the outer-sphere bisulfate anion with a donor-acceptor distance of 2.521(3) Å. The two remaining amines H-bond to two other outer-sphere bisulfates with distances of 2.829(3) Å and 2.948(3) Å. The ligated HSO_4 anions in **2** also have a H-bond with another outer-sphere HSO_4^-, with a separation of only 2.466(4) Å. These interactions result in an extensive H-bonding network in **2**.

The solid-state structure of the deuterated isotopologue **2-d$_7$** was also determined through x-ray crystallography. It is isostructural with the protiated **2**, showing little change in the bond distances and crystal parameters. A powder diffraction of the material also shows little difference between isotopologues (Figure 3.3), indicating the lack of isotopic polymorphism.

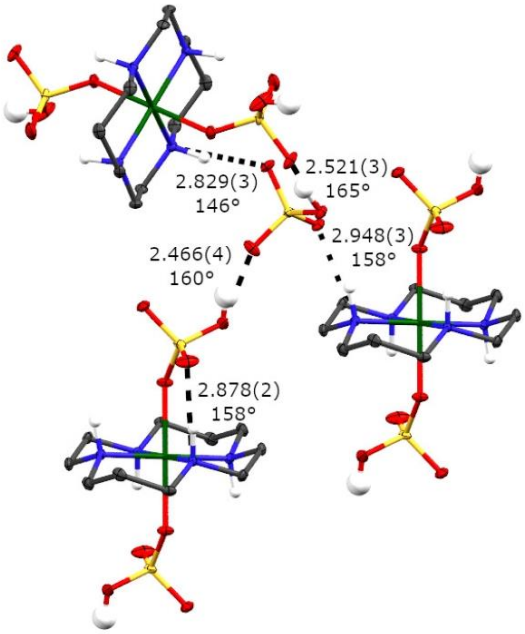

Figure 3.2 Unique hydrogen bonds in **2** given in Å; angles represent the donor-H-acceptor bond angle. Atom colors are as described in Figure 3.1. The outer sphere bisulfate moiety is disordered on an inversion center and only one position is shown for clarity.

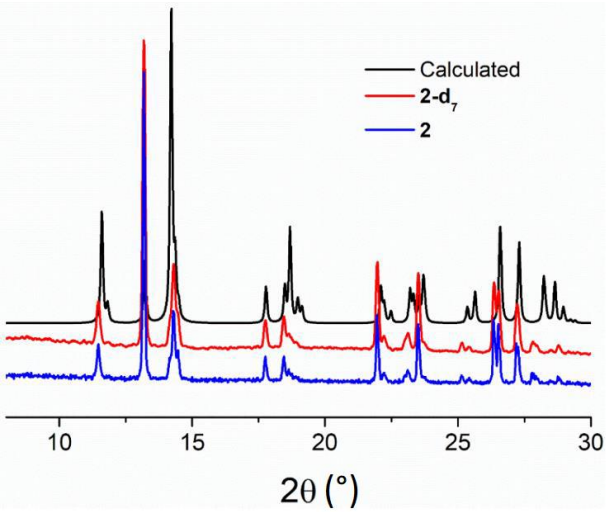

Figure 3.3 Powder XRD of a ground sample of **2** and **2-d$_7$**. The calculated trace is derived from single crystal data collected on **2**.

The IR spectra of **2** and **2-d$_7$** clearly show shifts in the bands involving the exchangeable protons (Figure 3.4), and the MS spectra confirm the d$_7$ assignment (Figures A3.9 and A3.10).

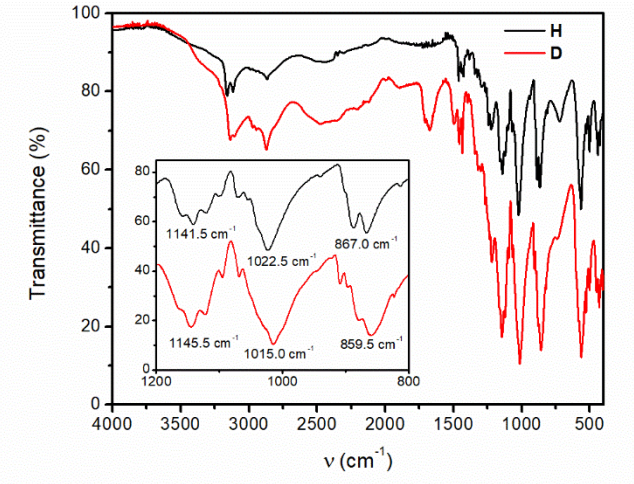

Figure 3.4 FTIR spectrum of **2** and **2-d$_7$** from 4000 cm^{-1} to 400 cm^{-1}. Inset corresponds to characteristic bisulfate bands shifted by deuteration.

We note that the MS spectrum for **2**, which used a liquid chromatographic introduction system, shows peaks consistent with Ni(II) *and* Ni(III) species, whereas the solid-state introduction system (DART) used for analyzing **2-d$_7$** only shows Ni(III) species. We attribute this difference to an artifact of the data collection method. Nevertheless, this highlights the importance of the proton inventory for the stability of the Ni(III) oxidation state, where the solution-phase introduction system is more likely than the solid-state introduction system to deprotonate the amines and initiate the reduction process.[46–49]

The structure of solvatomorph **2·MeOH** is like **2** in several ways, however the addition of methanolic H-bonds changes the symmetry significantly. The intramolecular N-H···OSO$_3$H distance is 2.878(8) Å for the bisulfate anion near the MeOH, and 2.823(8) Å for the other. The two remaining amines H-bond to the outer-sphere bisulfates with donor-acceptor distances of 2.799(7) Å and 3.007(8) Å, respectively. The inner-sphere bisulfate interacts with both the outer-sphere bisulfate, with distances of 2.625(8) Å and 2.888(8) Å, and with the methanol solvate at 2.552(8) Å. Methanol also hydrogen bonds to the outer-sphere HSO$_4^-$ at 2.70(1) Å. While **2** has shorter (and presumably stronger) H-bonds stronger than the **2·MeOH** solvatomorph, the

reduction in symmetry results in a greater number of unique H-bonds for **2·MeOH**, which in principle could influence magnetic relaxation properties.

3.4.2 Static (DC) magnetic properties. The temperature dependencies of the magnetic susceptibility-temperature products ($\chi_M T$) of ground samples of **1** and **2,** collected between 2 K and 300 K with an applied dc field of 1000 Oe (Figure 3.5), show that both complexes possess S = ½ Ni(III) ions, but interact with neighbors differently. The coordination polymer **1** shows a $\chi_M T$ value of 0.43 cm^3 K mol^{-1} at 300 K. Upon cooling, the magnetic susceptibility product decreases gradually at first, and then more rapidly below 75 K, to a minimum of 0.014 cm^3 K mol^{-1} at 2 K, consistent with an antiferromagnetic coupling within chains. The molecular bisulfate complex **2** displays a room temperature $\chi_M T$ value of 0.43 cm^3 K mol^{-1}. Upon cooling, the $\chi_M T$ value decreases gradually until reaching 0.402 cm^3 K mol^{-1} at 55 K, below which there is a pronounced downturn reaching a minimum of 0.36 cm^3 K mol^{-1} at 2 K.

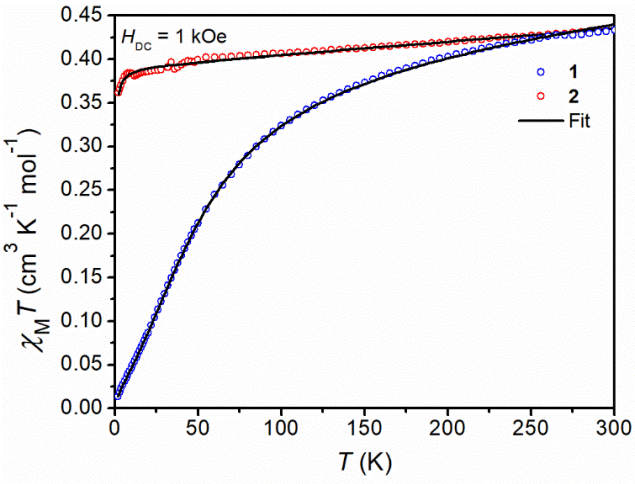

Figure 3.5 Static (DC) magnetic susceptibility of ground samples of **1** and **2** in a 1 kOe applied field from 1.8 K – 300 K. Fits are described in the appendix.

The susceptibility data for **1** are fit to a combination of the Bonner-Fisher model for chain compounds, a Curie-Weiss-like model, and a temperature-independent paramagnetism (χ_{TIP}) parameter (See appendix for details). The fit for **1** yields g = 2.20, consistent with the value

obtained via EPR ($g_{x,y}$ = 2.24, g_z = 2.04, see appendix). The strength of the antiferromagnetic coupling (-46.3 cm^{-1}) is much higher than that found for the Mn analogue measured by Sessoli and coworkers (-2.9 cm^{-1}),[44] but that is consistent with other literature examples where the metal ions have lower spin.[50] A similar Cr dimer complex, $[Cr(cyclam)(\mu\text{-}SO_4)_2Cr(cyclam)](ClO_4)_2$ similarly showed weak anti-ferromagnetic coupling, with J = (-)4.7 cm^{-1}.[51]

The plots of temperature dependence of $\chi_M T$ (Figure 3.5) and reduced field magnetization (Figure A3.17) support the S = ½ state and lack of substantial axial magnetic anisotropy for **2**. The susceptibility data were fit[42] to determine g, the mean-field intermolecular interaction zJ, and the contributions from χ_{TIP}. The fit for **2** yielded a slightly lower g value (g = 2.04) than the EPR (g_x = 2.23, g_y = 2.14, g_z = 2.09) but is still within reasonable agreement.

3.4.3 Dynamic (AC) magnetic properties. Dynamic magnetic properties were probed for **1** and **2**. Unsurprisingly, **1** shows no in-phase or out-of-phase AC susceptibility, owing to an overall singlet ground state arising from antiferromagnetic coupling of Ni(III) ions through sulfate and hydrogen-bonding networks. In contrast, bisulfate-bound **2** shows slow magnetic relaxation in an applied DC field, which is qualitatively distinct from the behavior previously reported for $[Ni(cyclam)(NO_3)_2]^+$.[7] The field dependence of the AC susceptibility was studied for **2** at 2 K (Figure A3.20). Bisulfate-ligated **2** shows a multi-mode relaxation profile, in contrast to the nitrate species. At low applied DC field, 1 kOe, only a single peak can be observed in the out-of-phase data, with a maximum susceptibility at 150 Hz. Increasing the applied DC field suppresses this high-frequency relaxation pathway, and a new low-frequency pathway centered at 1 Hz emerges at 6 kOe. The temperature dependence of the AC susceptibility was further investigated for **2** under a 6 kOe applied DC field (Figure A3.22), and it shows the peak in the out-of-phase signal rapidly

moving to higher frequencies up to 4 K, whereupon the increase with temperature slows substantially.

In an effort to deconvolute intra- and intermolecular contributions to the observed slow relaxation, we focus here on structural aspects of **2** that can be tuned synthetically, and measurement ranges where magnetic events can be captured as fully as possible. Particle size selection and deuteration represent distinct ways to alter intermolecular interactions while minimizing changes to local ligand field environment of Ni(III) ions. Our inspirations for the deuteration studies come from an example in solution-phase pulsed EPR spectroscopy where deuteration led to increased decoherence times for a V(IV) complex,[19] and a solid-state magnetic study on a Co(II) complex where deuteration was claimed to quench PBE and slow down molecular relaxation processes.[52] To study a magnetic relaxation event over a larger temperature and applied field regime, and because slower relaxations are more desirable in qubits, we focused our investigations on the low-frequency pathway identified above. From the temperature dependence data, the peak locations of the out-of-phase χ"(ν) maxima were found, and the relaxation times, τ, were extracted and plotted using logarithmic values. These data for several samples of **2** are collected in Figure 3.6, acquired under the conditions favoring the original low-frequency event.

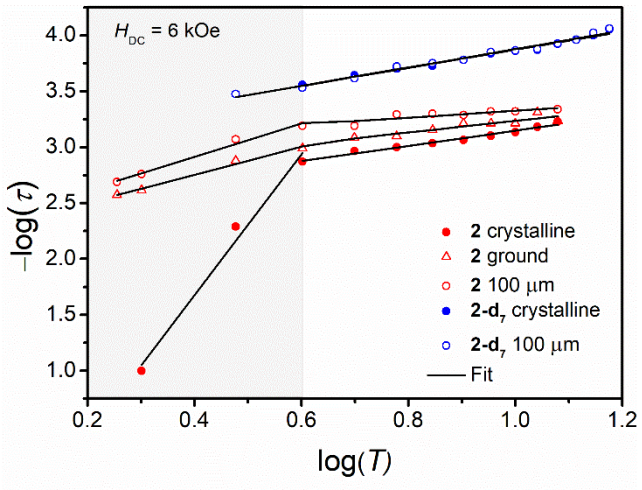

Figure 3.6 Crystallite size dependence of relaxation rates for several size-selected samples of **2** and **2-d$_7$**, as measured under a static DC field of 6 kOe. Size-selected samples of **2**: as-crystallized (**2 crystalline**, x > 206 µm), lightly ground (**2 ground**, 106 µm < x < 206 µm), and more finely ground (**2 100 µm**, 53 µm < x < 106 µm). Best fit lines are fit from the log-log data to the equation -log(τ) = n*log(T) + b, where b = 10^C .

For protiated samples of **2**, we identify two temperature-based regimes, < 4 K and > 4 K, where significant changes occur in the relaxation. The effect is most pronounced for the sample with the largest particle size (**2 crystalline**, x > 206 µm), but is also observed for the samples with smaller particle sizes (**2 ground**, 106 µm < x < 206 µm; and **2 100 µm**, 53 µm < x < 106 µm). Interestingly, the deuterated analogues **2-d$_7$ 100 crystalline** and **2-d$_7$ 100 µm** do not show differences in temperature dependence of relaxation times based on particle size.

Extracting magnetic relaxation mechanisms from the plots in Figure 3.6, we acknowledge that multiple pathways exist in **2** and can be accessed or suppressed under different environmental conditions. Notwithstanding, for self-consistency in the analysis, we treat the relaxation data and fits as if there is only one event to be modeled, and separate all samples into the two temperature ranges relevant to **2 crystalline**; thus, fit parameters presented in Table 3.1 should be regarded provisionally.

Table 3.1 Relaxation parameters for **2** and **2-d$_7$** at different particle sizes.

	B (s^{-1} T^{-n})	n
2 crystalline (LT)	0.143	6.3
2 crystalline (HT)	292.415	0.68
2 ground (LT)	179.102	1.25
2 ground (HT)	516.654	0.52
2 100 µm (LT)	207.682	1.49
2 100 µm (HT)	1027.596	0.32
2-d_7 crystalline	1148.682	0.81
2-d_7 100 µm	1136.842	0.82

In principle, when plotted as a double log plot, the slope of the line corresponds to the exponent of the temperature dependence for scenarios where one relaxation pathway is dominant. Building from equation 3.1, for a system with only the direct relaxation pathway operative, we would expect a linear temperature dependence, corresponding to a slope of $n = 1$, whereas for a system where the phonon bottleneck is operative, we would expect a temperature dependence of T^2 and a slope of $n = 2$, and Raman relaxation processes are often marked by larger slopes ($n > 2$). In systems with multiple relaxation pathways, we expect an n value between the pure systems and a slight deviation from linearity. For a $S = ½$ system without spin-orbit coupling, as evidenced by the DC magnetic measurements, an Orbach relaxation pathway is not realistic as there are only two available magnetic states, $m_s = + ½$ and $m_s = - ½$. As a result, the Orbach term was discarded (see appendix for fits to alternative models). Instead, only the Raman term was used in the final fits as the data in the log-log plots of relaxation times vs temperature gave nearly linear fits when constrained to the two temperature regimes.

We find interesting particle size-dependent relaxation dynamics for compound **2** both below and above 4 K. The as-crystallized sample (**2 crystallized**) shows a Raman-like temperature

dependence below 4 K (n = 6.3) and a temperature dependence roughly consistent with a direct pathway at higher temperatures. For the lightly ground sample of (**2 ground**) the parameter n =1.25 suggests a combination of direct and phonon bottleneck (PB) relaxation pathways at low temperatures. Above 4 K, the n parameter dops to 0.52, significantly lower than what is normally expected for Raman or Direct processes. The 100 μm size-selected sample similarly shows behavior provisionally interpreted as a combination of PB and direct processes at low temperature, with a switch an anomalously slow pathway above 4 K. Of the three samples, the largest and smallest particle sizes show significant changes in slope at 4 K, while the **2 ground** sample has a more gradual change with temperature. Meanwhile, the isostructural deuterated analogues **2-d$_7$ crystalline** and **2-d$_7$ 100 μm** show essentially the same temperature dependencies, with fit n values suggesting a direct relaxation pathway, similar to **2 100 μm**. The particle size dependence seems to have disappeared upon deuteration, from which we could infer that deuteration somehow quenches the PBE, leaving only the faster, molecular relaxation pathways.

Whereas the anomalous values of n extracted from the data do not enable unambiguous identification of PBE pathways, other chemical tuning can reveal those intermolecular effects. Assignment of the PBE is often supported by examining magnetic dilution with an analogous diamagnetic species, where relaxation rates should increase as the magnetic species becomes more dilute.[7] Unfortunately, we were unable to replace Ni(III) with diamagnetic ions Co(III), Al(III), or Ti(III) due to synthetic difficulties. Alternatively, studies by Sessoli, Mosser, and Yamashita have shown that the relaxation rate of PB increases with decreasing crystallite size as the increased surface area results in increased phonon scattering, hindering the bottleneck.[25,53,54] Relaxation profiles, collected in Figure 3.7 at one temperature and applied DC field, illustrate the increased rate of relaxation upon particle size reduction, at least for the protiated samples.

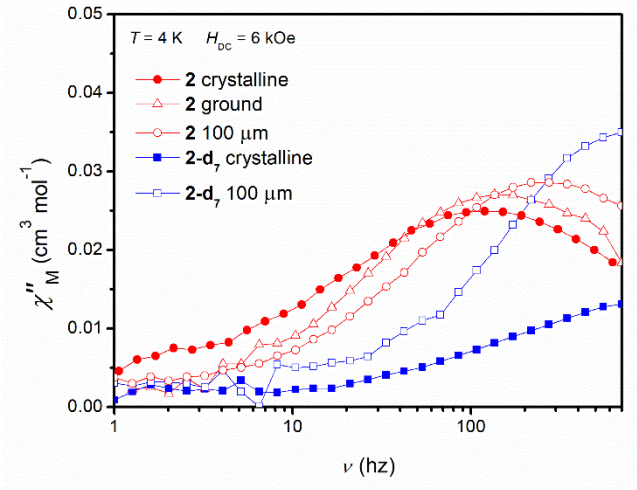

Figure 3.7 Particle size influences frequency dependence of out-of-phase magnetic susceptibilities of various forms of the bisulfate-containing **2**: crystalline, ground crystalline, and 100 µm sample of **2** and **2-d$_7$**, measured with a 6 kOe applied field at 4 K. Normalized data showing **2-d$_7$** samples overlap are provided in the appendix (Figure A3.31).

Both **2 ground** and **2 100 µm** samples show higher frequency relaxation events than the **2 crystalline** sample, consistent with the presence a phonon bottleneck-like effect. Interestingly, the relaxation event moves to even higher frequencies when the isotopologues are interrogated. We note that *slower* relaxation upon deuteration was observed by Song and coworkers for a structurally similar Co(II) complex,[52] and will discuss this in more detail below. We also note a large increase in the out-of-phase susceptibility value is observed after **2-d$_7$ crystalline** is ground to produce **2-d$_7$ 100 µm**, suggesting that a larger proportion of magnetic units are undergoing slow magnetic relaxation in the ground sample. This same effect is observed for the protiated analogues, albeit more subtly within the same particle size regime. Elucidating the origins of this effect require further investigation. The observation is not consistent with PBE, because larger crystals are less likely to scatter the phonons responsible for relaxation, and that would lead to larger signal. Instead, we speculate that intramolecular relaxation pathways are being revealed by the production of smaller particle sizes.

Although precise pathways for magnetic relaxation cannot be fully separated for **2**, we find that both particle size and deuteration clearly influence the dynamic magnetic properties, and these effects can be traced back to the hydrogen bonding network connecting $[Ni(cyclam)(HSO_4)_2]^+$ complexes. Deuteration-induced changes in H-bond strength have been studied in a wide variety of compounds with varying results. In some systems, such as oxalic acid dihydrate, deuteration changes H-bond strength by lengthening the donor–acceptor distance, whereas H-bonds involving deuterated phenol are generally stronger than the isotopologue, without structural changes.[55,56] For crystal structures of compound **2**, non-H/D atoms do not move upon deuteration, so any changes to bond strength would be related provisionally to dispersion. Regardless of the origin, we do know that the phonon energetics are changed by reference to the FT-IR spectra shown in Figure 3.4. The complexity of H/D-bond strength changes is especially relevant in **2**, as there are two general types of H-bonds: (1) between bisulfates, and (2) between the cyclam amines and inner- and outer-sphere bisulfates. In contrast, in the study reported by Song and coworkers, where deuteration of a Co(II) complex led to slower relaxation, the deuteration was localized to a ligated acetonitrile molecule, which did not participate in H-bonding.[52] Additionally, exchanging H for D also changes the nuclear spin on those sites from $I = ½$ to $I = 1$, which has been shown in pulsed EPR experiments to affect T_1.[10,57] Given the proximity of the spin changes to the Ni(III) center, and the complexity of the H-bonding framework, it perhaps should be expected that the relaxation dynamics of **2** would change drastically upon deuteration.

3.5 Conclusions

Overall, we report the magnetic relaxation dynamics of two Ni(III) salts of comparable first coordination spheres. Consistent with our predictions from our previous report,

$[Ni(cyclam)(HSO_4)_2]^+$ in **2** exhibits slow magnetic relaxation with axially coordinated oxygen atoms, whereas the antiferromagnetism in **1** precludes magnetic relaxation as a singlet ground state does not possess any magnetic moment available for relaxation. The magnetic dynamic measurements exhibit the presence of multiple relaxation pathways, the faster of which is quenched by applying a stronger magnetic field. The slower pathway is assigned as a mixture of Raman, PB, and direct pathways, where the relative contributions vary significantly with particle size and temperature regime. Deuteration of **2** reveals a faster relaxation pathway that does not change with particle size. We believe that by deuterating **2**, we quench the phonon bottleneck effect through altering the energetics of the H-bonding network. While isotopic influences on the phonon landscape are complicated and system dependent, the observation of significant magnetic dynamic changes upon deuteration suggests that further investigation of isotope effects on magnetostructural properties will be useful for the broader magnetism community, could serve as a synthetic tool for modulating magnetic frameworks.

3.6 References

(1) Martínez-Pérez, M. J.; Cardona-Serra, S.; Schlegel, C.; Moro, F.; Alonso, P. J.; Prima-García, H.; Clemente-Juan, J. M.; Evangelisti, M.; Gaita-Ariño, A.; Sesé, J.; Van Slageren, J.; Coronado, E.; Luis, F. Gd-Based Single-Ion Magnets with Tunable Magnetic Anisotropy: Molecular Design of Spin Qubits. *Phys. Rev. Lett.* **2012**, *108* (24), 1–5. https://doi.org/10.1103/PhysRevLett.108.247213.

(2) Brunet, G.; Safin, D. A.; Jover, J.; Ruiz, E.; Murugesu, M. Single-Molecule Magnetism Arising from Cobalt(II) Nodes of a Crystalline Sponge. *J. Mater. Chem. C* **2017**, *5* (4), 835–841. https://doi.org/10.1039/c6tc04703c.

(3) Mannini, M.; Pineider, F.; Sainctavit, P.; Danieli, C.; Otero, E.; Sciancalepore, C.; Talarico, A. M.; Arrio, M. A.; Cornia, A.; Gatteschi, D.; Sessoli, R. Magnetic Memory of a Single-Molecule Quantum Magnet Wired to a Gold Surface. *Nat. Mater.* **2009**, *8* (3), 194–197. https://doi.org/10.1038/nmat2374.

(4) Aromí, G.; Aguilà, D.; Gamez, P.; Luis, F.; Roubeau, O. Design of Magnetic

Coordination Complexes for Quantum Computing. *Chemical Society Reviews*. 2012, pp 537–546. https://doi.org/10.1039/c1cs15115k.

(5) Frost, J. M.; Harriman, K. L. M.; Murugesu, M. The Rise of 3-d Single-Ion Magnets in Molecular Magnetism: Towards Materials from Molecules? *Chem. Sci.* **2016**, *7* (4), 2470–2491. https://doi.org/10.1039/c5sc03224e.

(6) Craig, G. A.; Murrie, M. 3D Single-Ion Magnets. *Chem. Soc. Rev.* **2015**, *44* (8), 2135–2147. https://doi.org/10.1039/c4cs00439f.

(7) Bhowmick, I.; Roehl, A. J.; Neilson, J. R.; Rappé, A. K.; Shores, M. P. Slow Magnetic Relaxation in Octahedral Low-Spin Ni(III) Complexes. *Chem. Sci.* **2018**, *9* (31), 6564–6571. https://doi.org/10.1039/c7sc04482h.

(8) Woodruff, D. N.; Winpenny, R. E. P.; Layfield, R. A. Lanthanide Single-Molecule Magnets. *Chem. Rev.* **2013**, *113* (7), 5110–5148. https://doi.org/10.1021/cr400018q.

(9) Stinghen, D.; Atzori, M.; Fernandes, C. M.; Ribeiro, R. R.; De Sá, E. L.; Back, D. F.; Giese, S. O. K.; Hughes, D. L.; Nunes, G. G.; Morra, E.; Chiesa, M.; Sessoli, R.; Soares, J. F. A Rare Example of Four-Coordinate Nonoxido Vanadium(IV) Alkoxide in the Solid State: Structure, Spectroscopy, and Magnetization Dynamics. *Inorg. Chem.* **2018**, *57* (18), 11393–11403. https://doi.org/10.1021/acs.inorgchem.8b01117.

(10) Tesi, L.; Lucaccini, E.; Cimatti, I.; Perfetti, M.; Mannini, M.; Atzori, M.; Morra, E.; Chiesa, M.; Caneschi, A.; Sorace, L.; Sessoli, R. Quantum Coherence in a Processable Vanadyl Complex: New Tools for the Search of Molecular Spin Qubits. *Chem. Sci.* **2016**, *7* (3), 2074–2083. https://doi.org/10.1039/c5sc04295j.

(11) Albino, A.; Benci, S.; Tesi, L.; Atzori, M.; Torre, R.; Sanvito, S.; Sessoli, R.; Lunghi, A. First-Principles Investigation of Spin-Phonon Coupling in Vanadium-Based Molecular Spin Quantum Bits. *Inorg. Chem.* **2019**, *58* (15), 10260–10268. https://doi.org/10.1021/acs.inorgchem.9b01407.

(12) Ding, M.; Cutsail, G. E.; Aravena, D.; Amoza, M.; Rouzières, M.; Dechambenoit, P.; Losovyj, Y.; Pink, M.; Ruiz, E.; Clérac, R.; Smith, J. M. A Low Spin Manganese(IV) Nitride Single Molecule Magnet. *Chem. Sci.* **2016**, *7* (9), 6132–6140. https://doi.org/10.1039/c6sc01469k.

(13) Cui, H. H.; Sun, T. M.; Wang, M.; Chen, L.; Tang, Y. F. Bulky Anion Supported a Five-Coordinate Spin-Crossover Cobalt(II) Complex with Slow Magnetic Relaxation. *J. Solid State Chem.* **2020**, *289* (June), 121535. https://doi.org/10.1016/j.jssc.2020.121535.

(14) Chen, L.; Song, J.; Zhao, W.; Yi, G.; Zhou, Z.; Yuan, A.; Song, Y.; Wang, Z.; Ouyang, Z. W. A Mononuclear Five-Coordinate Co(II) Single Molecule Magnet with a Spin Crossover between the $S = 1/2$ and 3/2 States. *Dalt. Trans.* **2018**, *47* (46), 16596–16602. https://doi.org/10.1039/C8DT03783C.

(15) Bhowmick, I.; Shaffer, D. W.; Shaffer, D. W.; Yang, J. Y.; Shores, M. P. Single Molecule Magnet Behaviour in a Square Planar: $S = 1/2$ Co(II) Complex and Spin-State Assignment of Multiple Relaxation Modes. *Chem. Commun.* **2020**, *56* (49), 6711–6714. https://doi.org/10.1039/d0cc01854f.

(16) Lin, W.; Bodenstein, T.; Mereacre, V.; Fink, K.; Eichhöfer, A. Field-Induced Slow Magnetic Relaxation in the Ni(I) Complexes $[NiCl(PPh_3)_2]\cdot C_4H_8O$ and $[Ni(N(SiMe_3)_2)(PPh_3)_2]$. *Inorg. Chem.* **2016**, *55* (5), 2091–2100. https://doi.org/10.1021/acs.inorgchem.5b02497.

(17) Boča, R.; Rajnák, C.; Titiš, J.; Valigura, D. Field Supported Slow Magnetic Relaxation in a Mononuclear Cu(II) Complex. *Inorg. Chem.* **2017**, *56* (3), 1478–1482. https://doi.org/10.1021/acs.inorgchem.6b02535.

(18) Cui, H. H.; Lv, W.; Tong, W.; Chen, X. T.; Xue, Z. L. Slow Magnetic Relaxation in a Mononuclear Five-Coordinate Cu(II) Complex. *Eur. J. Inorg. Chem.* **2019**, *2019* (43), 4653–4659. https://doi.org/10.1002/ejic.201900942.

(19) Yu, C. J.; Graham, M. J.; Zadrozny, J. M.; Niklas, J.; Krzyaniak, M. D.; Wasielewski, M. R.; Poluektov, O. G.; Freedman, D. E. Long Coherence Times in Nuclear Spin-Free Vanadyl Qubits. *J. Am. Chem. Soc.* **2016**, *138* (44), 14678–14685. https://doi.org/10.1021/jacs.6b08467.

(20) Cremer, D.; Kraka, E. From Molecular Vibrations to Bonding, Chemical Reactions, and Reaction Mechanism. *Curr. Org. Chem.* **2010**, *14* (15), 1524–1560. https://doi.org/10.2174/138527210793563233.

(21) Gu, L.; Wu, R. Origin of the Anomalously Low Raman Exponents in Single Molecule Magnets. *Phys. Rev. B* **2021**, *103* (1), 1–9. https://doi.org/10.1103/PhysRevB.103.014401.

(22) Lunghi, A.; Sanvito, S. Spin-Phonon Relaxation in Molecular Qubits from First Principles Spin Dynamics. **2019**.

(23) Mautner, F. A.; Bierbaumer, F.; Fischer, R. C.; Tubau, À.; Speed, S.; Ruiz, E.; Massoud, S. S.; Vicente, R.; Gómez-Coca, S. Insights into the Spin Dynamics of Mononuclear Cerium(III) Single-Molecule Magnets. *Inorg. Chem.* **2022**, *61* (29), 11124–11136. https://doi.org/10.1021/acs.inorgchem.2c00958.

(24) Escalera-Moreno, L.; Suaud, N.; Gaita-Ariño, A.; Coronado, E. Determining Key Local Vibrations in the Relaxation of Molecular Spin Qubits and Single-Molecule Magnets. *J. Phys. Chem. Lett.* **2017**, *8* (7), 1695–1700. https://doi.org/10.1021/acs.jpclett.7b00479.

(25) Tesi, L.; Lunghi, A.; Atzori, M.; Lucaccini, E.; Sorace, L.; Totti, F.; Sessoli, R. Giant Spin-Phonon Bottleneck Effects in Evaporable Vanadyl-Based Molecules with Long Spin Coherence. *Dalt. Trans.* **2016**, *45* (42), 16635–16643. https://doi.org/10.1039/c6dt02559e.

(26) Nash, F. R. Electron Spin Relaxation in Copper Tutton Salts at Low Temperatures. *Phys. Rev.* **1965**, *138* (5A). https://doi.org/10.1103/PhysRev.138.A1500.

(27) Bartolomé, E.; Arauzo, A.; Luzón, J.; Melnic, S.; Shova, S.; Prodius, D.; Nlebedim, I. C.; Bartolomé, F.; Bartolomé, J. High Relaxation Barrier in Neodymium Furoate-Based Field-Induced SMMs. *Dalt. Trans.* **2019**, *48* (41), 15386–15396. https://doi.org/10.1039/c9dt02047k.

(28) Pedersen, K. S.; Dreiser, J.; Weihe, H.; Sibille, R.; Johannesen, H. V.; Sørensen, M. A.; Nielsen, B. E.; Sigrist, M.; Mutka, H.; Rols, S.; Bendix, J.; Piligkos, S. Design of Single-Molecule Magnets: Insufficiency of the Anisotropy Barrier as the Sole Criterion. *Inorg.*

Chem. **2015**, *54* (15), 7600–7606. https://doi.org/10.1021/acs.inorgchem.5b01209.

(29) Lopez, N.; Prosvirin, A. V.; Zhao, H.; Wernsdorfer, W.; Dunbar, K. R. Heterospin Single-Molecule Magnets Based on Terbium Ions and $TCNQF_4$ Radicals: Interplay between Single-Molecule Magnet and Phonon Bottleneck Phenomena Investigated by Dilution Studies. *Chem. - A Eur. J.* **2009**, *15* (42), 11390–11400. https://doi.org/10.1002/chem.200900629.

(30) Wu, S. Q.; Miyazaki, Y.; Nakano, M.; Su, S. Q.; Yao, Z. S.; Kou, H. Z.; Sato, O. Slow Magnetic Relaxation in a Mononuclear Ruthenium(III) Complex. *Chem. - A Eur. J.* **2017**, *23* (42), 10028–10033. https://doi.org/10.1002/chem.201702047.

(31) Taraszewska, J.; Sadło, J.; Michalik, J.; Korybut-Daszkiewicz, B. Stability and ESR Spectra of Ni(III) Tetraazamacrocyclic Complexes in Nitrate and Chloride Solutions. *Pol. J. Chem.* **2000**, *74* (6), 813–822.

(32) Barefield, E. K. A New Synthesis of 1,4,8,11-Tetraazacyclotetradecane (Cyclam) via the Nickel(II) Complex. *Inorganic Chemistry*. 1972, pp 2273–2274. https://doi.org/10.1021/ic50115a065.

(33) Gore, E. S.; Busch, D. H. Stable Octahedral, Low-Spin Nickel(III) Complexes of a Tetradentate Macrocyclic Ligand Having Saturated Nitrogen Donors. *Inorg. Chem.* **1973**, *12* (1), 1–3. https://doi.org/10.1021/ic50119a001.

(34) Prasad, L.; Nyburg, S. C. The Structure of $Ni(Cyclam)(ClO_4)_2$. *Acta Crystallogr.* **1987**, *C43*, 1038–1042. https://doi.org/10.1107/S0108270187093090.

(35) Bruker AXS inc. SAINT, v.8.38A. Madison, WI 2016.

(36) Sheldrick, G. M. SADABS, Version 2.03, Bruker Analytical X-Ray Systems, Inc., Madison, WI. Madison, WI 2000.

(37) Sheldrick, G. M. Crystal Structure Refinement with SHELXL. *Acta Crystallogr. Sect. C Struct. Chem.* **2015**, *71* (Md), 3–8. https://doi.org/10.1107/S2053229614024218.

(38) Bain, G. A.; Berry, J. F. Diamagnetic Corrections and Pascal's Constants. *J. Chem. Educ.* **2008**, *85* (4), 532–536. https://doi.org/10.1021/ed085p532.

(39) Ami, T.; Crawford, M. K.; Harlow, R. L.; Wang, Z. R.; Johnston, D. C.; Huang, Q.; Erwin, R. W. Magnetic Susceptibility and Low-Temperature Structure of the Linear Chain Cuprate Sr_2CuO_3. *Phys. Rev. B* **1995**, *51* (9), 5994–6001. https://doi.org/10.1103/PhysRevB.51.5994.

(40) Bonner, J. C.; Fisher, M. E. Linear Magnetic Chains with Anisotropic Coupling. *Phys. Rev.* **1964**, *135* (3A). https://doi.org/10.1103/PhysRev.135.A640.

(41) Duffy, W.; Barr, K. Alternating Antiferromagnetic Heisenberg Linear Chains. *J. Appl. Phys.* **1968**, *39* (2), 969. https://doi.org/10.1063/1.1656348.

(42) Chilton, N. F.; Anderson, R. P.; Turner, L. D.; Soncini, A.; Murray, K. S. PHI: A Powerful New Program for the Analysis of Anisotropic Monomeric and Exchange-Coupled Polynuclear d- and f-Block Complexes. *J. Comput. Chem.* **2013**, *34* (13), 1164–

1175. https://doi.org/10.1002/jcc.23234.

(43) Stoll, S.; Schweiger, A. EasySpin, a Comprehensive Software Package for Spectral Simulation and Analysis in EPR. *J. Magn. Reson.* **2006**, *178* (1), 42–55. https://doi.org/10.1016/j.jmr.2005.08.013.

(44) Mossin, S.; Weihe, H.; Osholm Sørensen, H.; Lima, N.; Sessoli, R. Rationalisation of Weak Ferromagnetism in Manganese(III) Chains: The Relation between Structure and Ordering Phenomena. *J. Chem. Soc. Dalt. Trans.* **2004**, *4* (4), 632–639. https://doi.org/10.1039/b314355d.

(45) Yamashita, M.; Toriumi, K.; Ito, T. Structure of Bis(Isothiocyanato)(1,4,8,1 l-Tetraazacyclotetradecane)Nickel(III) Perchlorate. *Acta* **1985**, *C41*, 1607–1609.

(46) Bossu, F. P.; Margerum, D. W. The Stabilization of Trivalent Nickel in Deprotonated-Peptide Complexes. *J. Am. Chem. Soc.* **1976**, *98* (13), 4003–4004. https://doi.org/10.1021/ja00429a047.

(47) Zilbermann, I.; Maimon, E.; Cohen, H.; Meyerstein, D. Redox Chemistry of Nickel Complexes in Aqueous Solutions. *Chem. Rev.* **2005**, *105* (6), 2609–2625. https://doi.org/10.1021/cr030717f.

(48) Shamir, D.; Zilbermann, I.; Maimon, E.; Shames, A. I.; Cohen, H.; Meyerstein, D. Anions as Stabilizing Ligands for Ni(III)(Cyclam) in Aqueous Solutions. *Inorganica Chim. Acta* **2010**, *363* (12), 2819–2823. https://doi.org/10.1016/j.ica.2010.03.057.

(49) Haines, R. I.; McAuley, A. Synthesis and Reactions of Nickel(III) Complexes. In *Coordination Chemistry Reviews,* 1981; 39, 77–119. https://doi.org/10.1016/S0010-8545(00)80512-3.

(50) Keene, D. T.; Zimmermann, I.; Neels, A.; Sereda, O.; Hauser, J.; Bonin, M.; Hursthouse, B. M.; Price, J. D.; Decurtins, S. Heterocyclic Amine Directed Synthesis of Metal(II)-Oxalates: Investigating the Magnetic Properties of Two Complete Series of Chains with S = 5/2 to S = 1/2. *Dalt. Trans.* **2010**, *39* (20), 4937–4950. https://doi.org/10.1039/b927522c.

(51) Glerup, J.; Goodson, P. A.; Hodgson, D. J.; Masood, M. A.; Michelsen, K. Syntheses and Characterization of Novel Binuclear Chromium (III) Complexes of 1,4,8,11-Tetraazacyclotetradecane (Cyclam). *Inorganica Chim. Acta* **2005**, *358* (2), 295–302. https://doi.org/10.1016/j.ica.2004.07.055.

(52) Li, J.; Xiong, S.-J.; Li, C.; Jin, B.; Zhang, Y.-Q.; Jiang, S.-D.; Ouyang, Z.-W.; Wang, Z.; Wu, X.-L.; van Tol, J.; Song, Y. Manipulation of Molecular Qubits by Isotope Effect on Spin Dynamics. *CCS Chem.* **2020**, 2548–2556. https://doi.org/10.31635/ccschem.020.202000384.

(53) Petukhov, K.; Bahr, S.; Wernsdorfer, W.; Barra, A. L.; Mosser, V. Magnetization Dynamics in the Single-Molecule Magnet Fe8 under Pulsed Microwave Irradiation. *Phys. Rev. B - Condens. Matter Mater. Phys.* **2007**, *75* (6), 1–12. https://doi.org/10.1103/PhysRevB.75.064408.

(54) Horii, Y.; Katoh, K.; Miyazaki, Y.; Damjanović, M.; Sato, T.; Ungur, L.; Chibotaru, L. F.;

Breedlove, B. K.; Nakano, M.; Wernsdorfer, W.; Yamashita, M. Coexistence of Spin–Lattice Relaxation and Phonon-Bottleneck Processes in Gd^{III}–Phthlocyaninato Triple-Decker Complexes under Highly Diluted Conditions. *Chem. - A Eur. J.* **2020**, *26* (36), 8076–8082. https://doi.org/10.1002/chem.201905796.

(55) Delaplane, R. G.; Ibers, J. A. Direct Determination of the Effect of Isotopic Substitution on Bond Lengths in Solid Oxalic Acid Dihydrate. *J. Chem. Phys.* **1966**, *45* (9), 3450–3451. https://doi.org/10.1063/1.1728130.

(56) Rao, C. N. R. Effect of Deuteration on Hydrogen Bonds. *J. Chem. Soc. Faraday Trans. 1 Phys. Chem. Condens. Phases* **1975**, *71*, 980–983. https://doi.org/10.1039/F19757100980.

(57) Eaton, G. R.; Eaton, S. S. Solvent and Temperature Dependence of Spin Echo Dephasing for Chromium(V) and Vanadyl Complexes in Glassy Solution. *J. Magn. Reson.* **1999**, *136* (1), 63–68. https://doi.org/10.1006/jmre.1998.1610.

Chapter 4: Investigating the Role of Complex Charge in Ni(III) Cyclam Magnetic Relaxation

4.1 Introduction

Individual molecules that exhibit a barrier towards magnetic reversal, called single molecule magnets (SMMs), have garnered intense research for the past three decades. Many SMMs focus on the metal center as the dominant moiety in determining the complexes' ability to undergo slow magnetic relaxation.[1–4] So far the vast majority of the leading SMMs, which have high operating temperatures with observable relaxation at liquid nitrogen temperatures, utilize Dy centers in low coordinate environments.[5–8] These specially designed materials attempt to maximize the magnetic anisotropy, spin, and orbital contributions in order to push the operating temperature ever higher, and have achieved great success. However, the field is approaching an upper limit, with better materials showing very small improvements on these figures of merit.[9,10] In order for the next generation of SMMs to be developed a more holistic approach towards magnetic relaxation is required.

In the Dy SMMs, the combination of high spin, magnetic anisotropy, and orbital contributions complicates the analysis of the magnetic properties. A $S = ½$ system, without orbital contributions, may serve as an excellent model system for understanding the effects beyond the metal center and zero-field splitting. Previously we have reported on the magnetic properties of Ni(III) cyclam materials, which show field-induced slow magnetic relaxation despite being a two-level system. In our group's first report, we investigated the effect of nuclear spin in the axial positions,[11] where the lone pair electron resides, and found that nuclear spin in these positions rapidly sped up magnetic relaxation. Nuclear spin has long been known to affect the magnetic

relaxation dynamics in single molecule magnets, however it is usually the nuclear spin of the spin center. This hyper-fine interaction splits the magnetic states, increasing the number of low-lying magnetic states and decreasing the separation between states, ultimately increasing the relaxation times, particularly the quantum tunneling of magnetization. For most cases, the further away the nuclear spin is away from the electronic spin, the smaller the interaction. This makes the strong on/off effect of the nuclear spin in the axial positions in Bhowmick *et al.* 2018 paper and those discussed in Chapter 2 very interesting. [11]

We hypothesized that since the electronic spin on the Ni center was coupling to the nuclear spin in the axial positions, then contracting the dz^2 orbital by introducing neutral ligands and increasing the complex charge may reduce the nuclear spin dependence of the system. Furthermore, solution-phase EPR spectra of $[Ni(cyclam)]^{3+}$ systems in acetonitrile, which was believed to be ligated, has been studied previously and no evidence of super-hyperfine coupling has been shown.[12,13] Herein we report on the structural and magnetic properties of $[Ni(cyclam)(MeCN)_2]X$ AN (X = triflate, perchlorate, or tetrafluoroborate) and $[Ni(cyclam)(BN)_2]OTf_3$ (BN = butyronitrile).

4.2 Division of Labor

Maddie Roach assisted with the collection of mass spectrometry data. Dr. Indrani Bhowmick and the ARC assisted with magnetic data collection. The analyses and all other data collection were performed by Tom Morrison.

4.3 Experimental

4.3.1 Preparation of compounds. Unless noted otherwise, all manipulations were performed in air and with Millipore deionized water.

[Ni(cyclam)$(MeCN)_2$]OTf_3 AN (**1a**): Two syntheses that resulted in the same material were used. Method A: concentrated triflic acid (*ca.* 2 mL) was added *via* syringe to [Ni(cyclam)Cl_2]Cl (80 mg) in a round bottom flask (*caution! Produces HCl gas!*) that was constantly flushed with nitrogen into a base bath. The solution was stirred for 30 minutes, diluted with 20 mL acetonitrile, and then filtered to remove the insoluble chloride starting material. The solution was then concentrated by rotary evaporation, redissolved into the minimum amount of acetonitrile, *ca.* 5 mL, and then filtered again. Large green block crystals of **1** were grown by a vapor diffusion of Et_2O into the filtered acetonitrile solution; the crystals were collected by vacuum filtration, washed with Et_2O, and were stored in a desiccator. Anal. Calcd for $C_{19}H_{33}N_7F_9O_9S_3Ni$: C, 25.90; H, 3.84; N, 10.66; Found: C, 24.65; H, 3.84; N, 9.57. (Anal. Calc for $C_{19}H_{33}N_7O_9F_9S_3Ni + 3H_2O$: C, 24.25; H, 4.28; 9.98).

Method B: cyclam (100.3 mg) and $NiOTf_2$ (179.2 mg) were refluxed in 20 mL acetonitrile for 1 hour, producing a yellow solution. The solution was then cooled to room temperature and acidified with HOTf (*ca*. 1 mL), then H_2O_2 (30% w/w, 10 uL) was added, immediately turning the solution green. The solution was then stirred for 2 hours, filtered, and used in the vapor diffusion process to produce green blocks identical to those produced by Method A.

[Co(cyclam)$(MeCN)_2$]OTf_3 AN (**1b**): The synthesis of the Co(III) analog was identical to Method B described for **1a**, replacing $CoOTf_2$ for $NiOTf_2$, except the oxidant used was air bubbling through the solution.

$[Ni_{0.06}Co_{0.94}(cyclam)(MeCN)_2]OTf_3$ (**1c**): Acetonitrile solutions of **1a** and **1b** were mixed in a 1:19 ratio and crystallized through a vapor diffusion of Et_2O to yield orange blocks. The percent metal composition was determined through UV-Vis experiments, which coincided with the values obtained through magnetic measurements.

$[Ni(cyclam)(BN)_2]OTf_3$ (**2**): **1a** (44.2 mg) was dissolved in butyronitrile (10 mL) and a small (< 0.1 mL) amount of HOTf for stabilization, filtered through a sintered glass frit, and then recrystallized through a vapor diffusion of Et_2O. Anal. Calcd for $C_{21}H_{38}F_9O_9N_6NiS_3$: C, 29.88; H, 4.51; N, 9.66; Found: C, 27.50; H, 4.15; N, 9.04. (Anal. Calc for $C_{21}H_{38}F_9O_9N_6NiS_3$+ 3.8 H_2O: C, 27.63; H, 5.01; N, 9.04).

$[Ni(cyclam)(MeCN)_2](BF_4)_3$ (**3**): A modified procedure of Method B from the synthesis of **1** was used: $Ni(BF_4)_2$ hydrate (185.8 mg) was refluxed in MeCN with cyclam (108.7 mg) until fully dissolved, then cooled to room temperature. Ethereal HBF_4 (50%, 1 mL) was added to the solution, stirred, and then H_2O_2 (30% w/w, 10 uL) was added, immediately turning the solution green. The solution was then stirred for 2 hours, filtered, and used in the vapor diffusion process to produce green blocks that were washed with 3:1 Et_2O:MeCN.

$[Ni(cyclam)(MeCN)_2](ClO_4)_3$ (**4**): A modified procedure of Method B from the synthesis of **1** was used: $Ni(ClO_4)_2$ hydrate (145.1 mg) was refluxed in MeCN with cyclam (100.1 mg) until fully dissolved, then cooled to room temperature. $HClO_4$ (70%, 1 mL) was added to the solution, stirred, and then H_2O_2 (30% w/w, 10 uL) was added, immediately turning the solution green. The solution was then stirred for 2 hours, filtered, and used in the vapor diffusion process to produce green blocks.

4.3.2 X-ray structure determinations. Crystals suitable for single-crystal x-ray analysis were coated with Paratone-N oil and supported on a Cryoloop before being mounted on a Bruker Kappa Apex II CCD diffractometer under a stream of N_2 gas. Data collections were performed at low temperature (100 K - 170 K, see Table 4.1) using a Siemens KFF Mo_2K-90 sealed tube (Mo Kα, λ = 0.71073 Å) x-ray source and a curved graphite monochromator, targeting complete coverage and 4-fold redundancy. Crystallographic data and metric parameters are presented in Table 4.1. Determination of unit cell parameters through refinement, data collection, reduction, and correction for Lorentz and polarization effects was performed using the SAINT software package.[14] Data were sorted, scaled, averaged, and corrected for semiempirical absorption effects with SADABS.[15] The structures were solved with the ShelXT structure solution program and refined with the ShelXL-2018/3 refinement package.[16] Unless otherwise noted, thermal parameters for all non-hydrogen atoms were refined anisotropically. Hydrogen atoms were added at calculated positions and were refined using a riding model.

4.3.3 Magnetic measurements. Magnetic susceptibility data were collected using a Quantum Design MPMS3 SQUID magnetometer. The samples were loaded into polyethylene bags and sealed, then the bags were inserted into drinking straws and inserted into the instrument. Ferromagnetic impurities were checked through a variable field analysis (0 to 10 kOe) of the magnetization at 100 K: overall linearity in the collected data for all compounds indicated the lack of significant ferromagnetic impurities. Static (DC) magnetic susceptibility data were collected at temperatures ranging from 2 K to 300 K at 1 kOe and 5 kOe. Alternating current (AC) magnetic susceptibility measurements were performed from 1 Hz to 700 Hz and from 1.8 K to 30 K with an alternating field of 4 Oe. Data were corrected for the magnetization of the sample holder by

subtracting the susceptibility of an empty container, and for the diamagnetic contributions of the sample by using Pascal's constants.[17]

Temperature-dependent DC magnetic susceptibility data were modeled with the program PHI[18] to single-ion species with temperature independent paramagnetism, weakly interacting with the spin bath. Using equation 4.1, the variables *A*, *B*, and *n* were allowed to refine freely.

$$\boldsymbol{\tau^{-1} = AT + BT^{n}} \qquad \text{(Eq. 4.1)}$$

Here, the *AT* term represents the direct relaxation pathway and the BT^n term represents the Raman relaxation pathway.

4.3.4 Other physical characterizations. Mass spectrometry experiments were performed on a Thermo-Finnigan LTQ LC/MS-MS ESI-MS instrument, where the sample was introduced via direct infusion using a syringe pump (rate 10 μL/s). The samples were dissolved in Millipore water, methanol, or acetonitrile at a concentration of 0.01 mg/mL. Electronic absorption spectra were obtained using quartz cuvettes in an Agilent 8453 spectrometer. Infrared spectra were obtained using a Bruker Tensor II FT-IR spectrometer. Electron paramagnetic resonance spectra were obtained using a Bruker ESR-300 spectrometer equipped with an X-band microwave source, an ultra-high sensitivity resonator, and a liquid He cryostat with a quartz finger dewar. Data were collected with a 5 G modulation amplitude and 100 kHz frequency, and were simulated using Easy Spin.[19] Powder X-ray diffraction data were collected at room temperature using a Scintag X-2 powder X-ray diffractometer equipped with Cu Kα radiation, Peltier detector and stationary sample stage, collecting diffraction angles between 5° and 30° 2θ. Elemental analyses were performed by Midwest Microlabs, Indianapolis, IN.

4.4 Results and Discussion

From the results of the 2018 paper and from Chapter 2, we had tentatively concluded that Ni(III) cyclam complexes would only exhibit slow magnetic relaxation in the absence of nuclear spin in the axial positions. Notwithstanding, we recognized that replacing the anionic ligands with neutral ligands might enable contraction of the dz^2 orbital in which the unpaired electron resides, reducing the overlap with the ligands in the axial positions and therefore the super-hyperfine interaction that quenches slow magnetic relaxation. Furthermore, unlike the HSO_4 complex discussed in Chapter 3, a Co analogue of **1a** was able to be synthesized, allowing for a more traditional method of circumventing the phonon bottleneck effect that appears in many of these systems. Additionally, because we were able to exchange the charge balancing ions in **1a** with ClO_4 and BF_4 (**3** and **4**, respectively), which have extremely similar crystal structures to one another, but different than that of **1**. From this we were able to study the influence of the differences in the hydrogen bonding between **3** and **4** on the magnetic properties. From **2** we are able to conclude that acetonitrile is not unique in its properties, although the true purpose of studying **2** was to investigate the solution-phase properties discussed in Chapter 5, *vide infra*, and compare them to the solid-state properties.

4.4.1 Synthesis and characterization of Ni(III) cyclam complexes. The initial synthesis of **1a** was carried out using a similar procedure to the HSO_4 species from Chapter 3, using triflic acid in place of sulfuric acid, Scheme 4.1. The reaction was performed under N_2 gas and produced caustic HCl gas, which was bubbled through a base bath. Once the reaction stopped off gassing HCl, the solvent, acetonitrile in this case, was added and the reaction was stirred. The insoluble starting material was removed by filtration and the filtrate concentrated by rotary evaporation, and X-ray quality crystals were produced by vapor diffusion with Et_2O. After confirming the structure

by X-ray diffraction, the safer, alternative method, method B, was developed and found to produce the same material. Examples of triflate ligating directly to metal centers are rare, making it a good counterion for studying the role of neutral ligands in the axial positions. **2** was able to be synthesized directly by dissolving **1a** in butyronitrile, but not by a procedure analogous to method B. Attempts at exchanging the counterion by introducing new ions to the acetonitrile solution to produce **3** and **4** was inconsistent, producing mixtures of **1a** and the new materials. As a result, they were synthesized directly in order to increase the scope of the acetonitrile study and investigate the role(s) of the counter ion in magnetic relaxation processes.

Scheme 4.1. General synthetic route for **1a** and **2-4**.

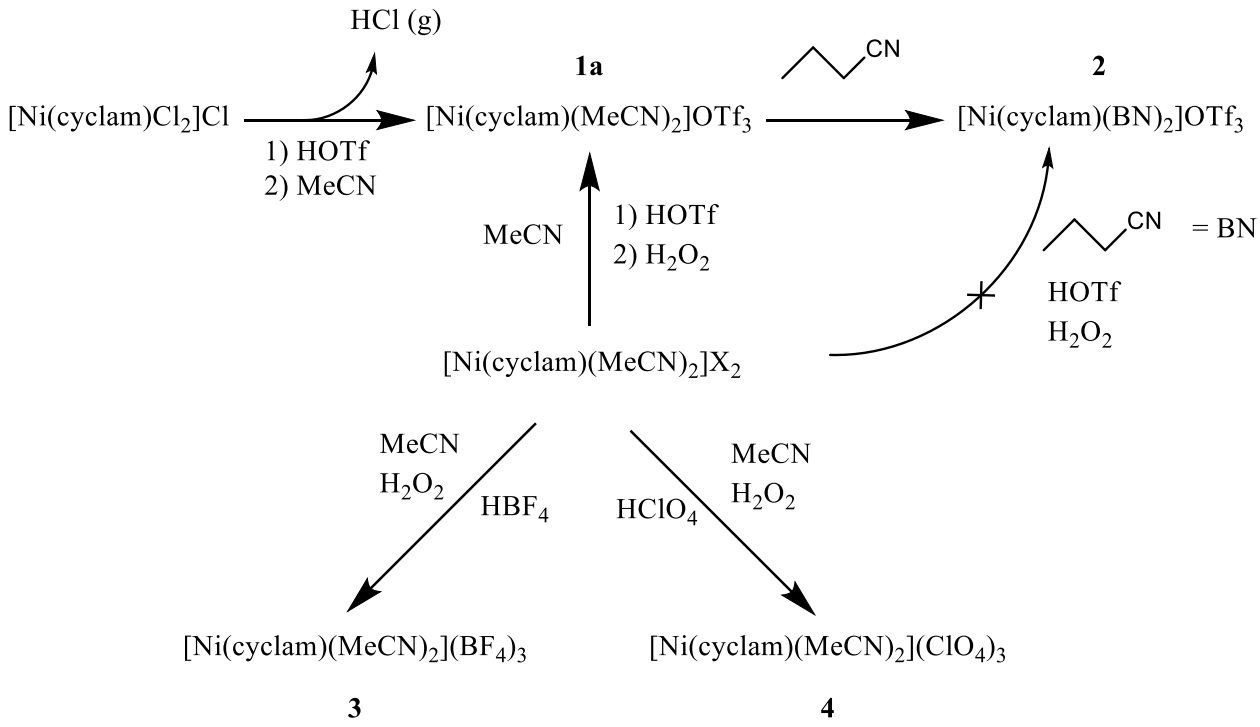

The diamagnetic Co(III) analogue to **1a**, **1b**, was synthesized in order to perform a magnetic dilution of **1a**. The stochiometric mixing of acetonitrile solutions of **1a** and **1b** and crystallizing by vapor diffusion successfully produced the magnetically diluted **1c**, which was

confirmed to be isostructural with **1a** (and **1b**, as they too are isostructural) by powder X-ray diffraction (Figure 4.1).

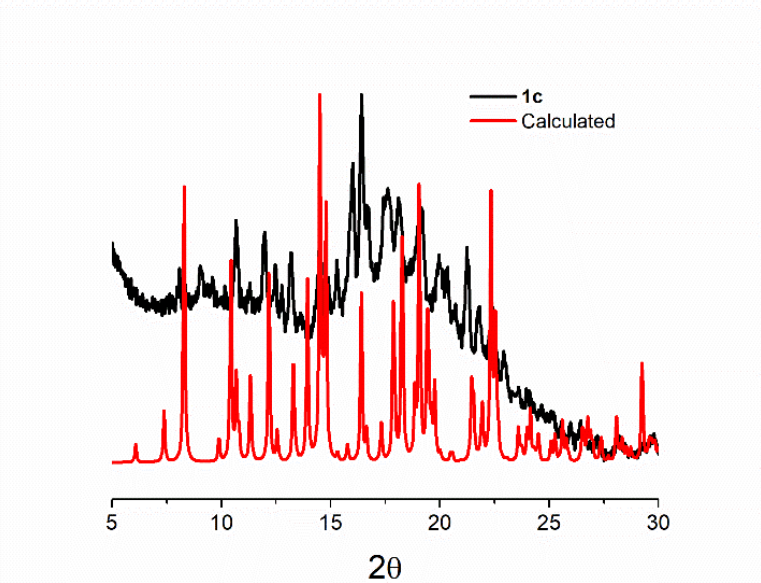

Figure 4.1 Powder x-ray diffraction pattern of **1c** compared to the calculated spectra obtained from the crystal structure of **1a**.

A portion of **1c** was then redissolved in acetonitrile and the molar absorptivity measured. The percent Ni content was determined by fitting the data as a linear combination of the molar absorptivity of **1a** and **1b** (Figure 4.2). It was found that the sample contained 6% Ni, slightly higher than the target value of 5% Ni.

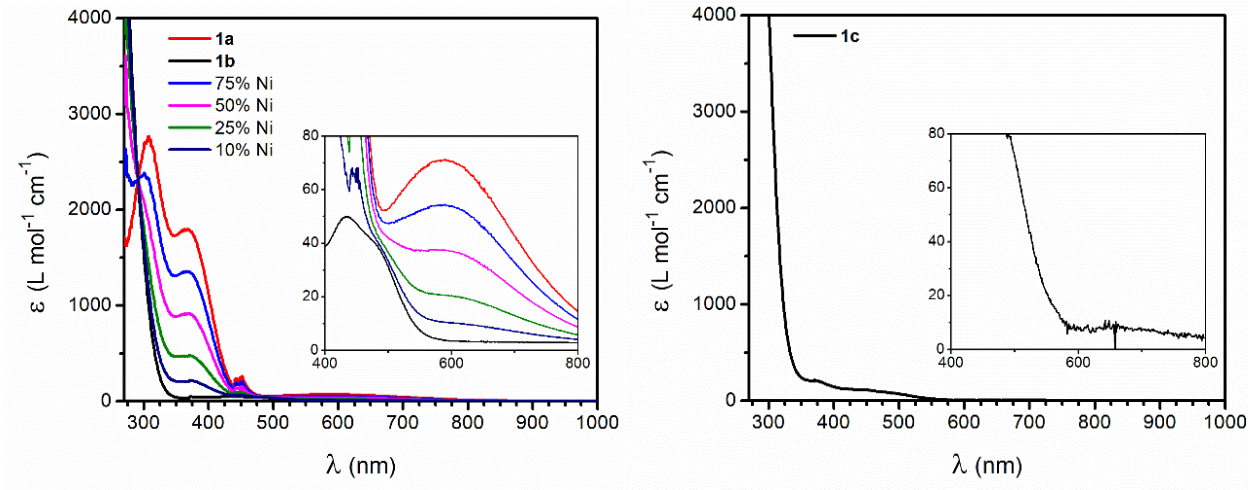

Figure 4.2 Left: Molar absorptivity of **1a** and **1b** in acetonitrile, with calculated linear combinations of the two at different ratios. Right: Molar absorptivity of **1c** in acetonitrile.

Due to the poor residuals of the crystallographic data for **3** and **4** and their propensity for twinning, powder X-ray diffraction patterns of the two materials were taken in order to confirm their structural similarities. Figure 4.3 shows that they are extremely similar to one another and both patterns closely match the calculated pattern for **4**.

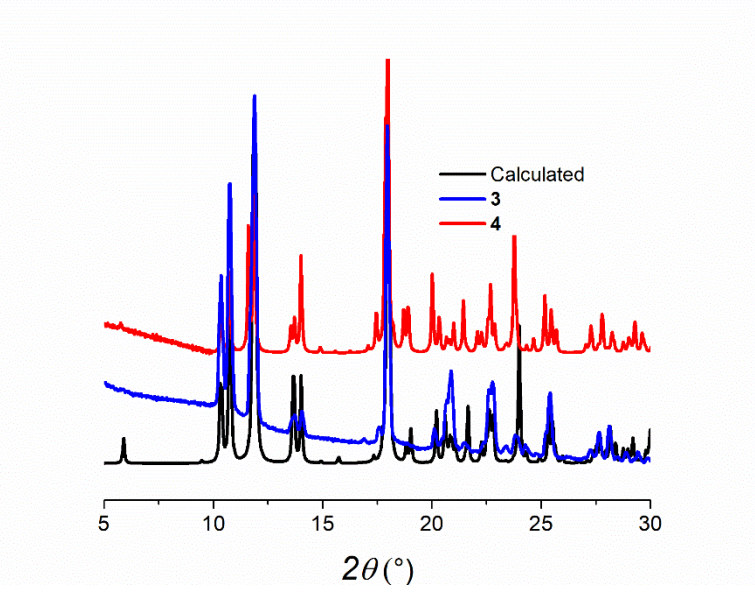

Figure 4.3 Powder x-ray diffraction pattern of **3** and **4** compared to the calculated spectra obtained from the crystal structure of **4**.

4.4.2 X-ray Crystal Structures Crystals of **1a** and **1b** suitable for X-ray analysis were obtained by vapor diffusion of Et_2O into an acetonitrile solution of the compounds. Crystals of **2** were able to be obtained by vapor diffusion of Et_2O into a solution of **1a** in butyronitrile. X-ray quality crystals of **3** and **4** were able to be obtained by the vapor diffusion of Et_2O into acetonitrile solutions of the compounds, but diffracted weakly and were often twinned or polycrystalline. While the structures of **3** and **4** were able to be determined and true single crystals were isolated, the weak diffraction resulted in poor data quality.

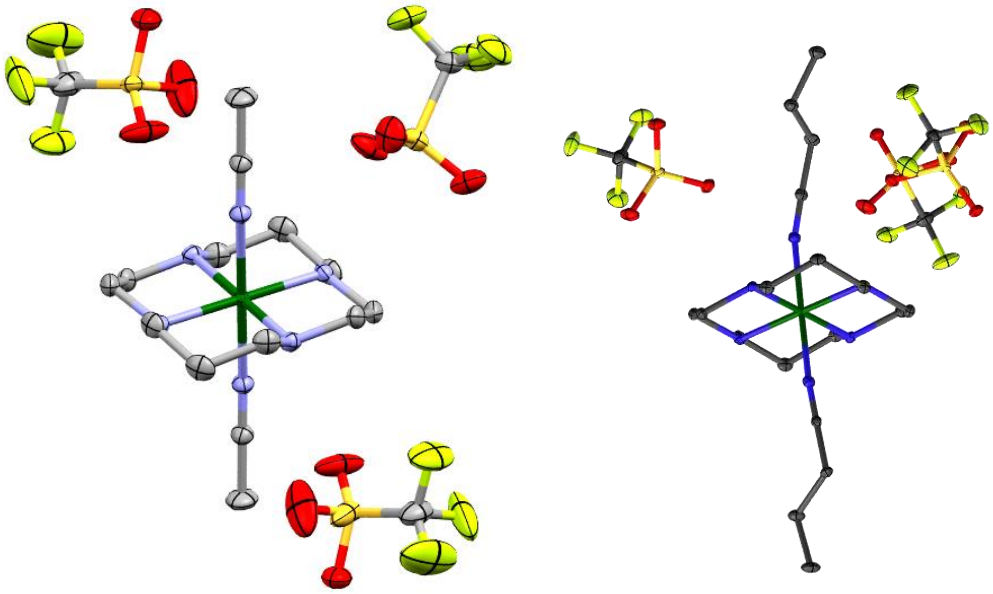

Figure 4.4 Crystal structures of **1a** (left) **2** (right) rendered with 50% thermal ellipsoids. Green, red, blue, yellow, lime, and gray ellipsoids represent Ni, O, N, S, F, and C atoms, respectively. Solvent molecules and H atoms not involved in hydrogen bonding are omitted for clarity.

The crystal structures of **1a** (and **1b**) are solved in $P\bar{1}$ and show two unique Ni centers and a co-crystallized acetonitrile molecule. The first coordination spheres show similar Ni-N distances, shown in Table 4.2. The Ni-N cyclam distances are shorter than those in $[Ni(cyclam)(MeCN)_2]OTf_2$ (2.068 Å – 2.0831 Å) consistent with the increased oxidation state,

however the Ni-N acetonitrile distances are nearly unchanged (2.125 Å and 2.145 Å). The three triflate ions found per metal center support the Ni(III) oxidation state and H-bond with the cyclam amines. The number of H-bonds each triflate molecule forms is dependent on which Ni center it is nearest to; Each Ni2 amine forms a H-bond to a triflate molecule that H-bonds to another, adjacent Ni2 cyclam amine, forming a 1-dimensional chain of **1a** as shown in Figure 4.5. In contrast, each Ni1 amine H-bonds to a lone triflate ion, which does not hydrogen bond to any other units. As a result, the crystal structure is organized of H-bonded chains of Ni2 centers separated by the molecular Ni1 units that functionally balance the charge of the chains.

Table 4.1 Crystallographic data for $[Ni(cyclam)(MeCN)_2]OTf_3 \cdot AN$ (**1a**), ,$[Ni(cyclam)(MeCN)_2]OTf_3 \cdot AN$ (**2a**), $[Ni(cyclam)(BN)_2]OTf_3$ (**2**), $[Ni(cyclam)(MeCN)_2](BF_4)_3$ (**3**), and $[Ni(cyclam)(MeCN)_2](ClO_4)_3$ (**4**).

	1a	**1b**	**2**	**3**	**4**
formula	$C_{19}H_{33}N_7F_9NiO_9S_3$	$C_{19}H_{32}N_7CoF_9O_9S_3$	$C_{21}H_{38}N_6F_9NiO_9S_3$	$C_{14}H_{30}N_6B_3F_{12}Ni$	$C_{14}H_{30}N_6Cl_3NiO_{12}$
fw (g/mol)	829.41	828.62	844.46	611.93	639.50
Color, habit	Green blocks	Orange blocks	Green blocks	Green needles	Green needles
T, K	168(2)	120(2)	108(2)	103(2)	100(2)
Space group	$P\bar{1}$	$P\bar{1}$	$P2_1/n$	*Pnma*	*Pnma*
Z	2	2	4	8	8
a, Å	9.3539(5)	9.9030	10.0796(3)	17.1530(2)	17.0688(14)
b, Å	12.64151(6)	11.9850	20.2143(7)	29.9690(3)	30.467(3)
c, Å	15.5352(8)	15.4270	17.1894(6)	9.8060(7)	9.8662(9)
α, deg	72.825(2)	98.070	90	90	90
β, deg	74.422(2)	101.350	101.8390(10)	90	90
γ, deg	76.819(2)	108.020	90	90	90
V, Å^3	16668.86(15)	1666.9	3427.9(2)	5040.9(1)	5130.7(8)
d_{calc}, g/cm^3	1.651	1.649	1.636	1.613	1.656
GOF	1.064	1.028	1.027	1.072	1.093
R_1[a] (wR_2[b]), %	3.66 (8.75)	6.97 (18.59)	3.34 (6.67)	9.21 (19.20)	10.43 (19.11)
R_1[a] (wR_2[b]), % all data	4.57 (9.47)	7.78 (19.55)	5.44 (7.37)	20.96 (24.44)	18.61 (23.99)

(a) $R_1 = \Sigma||F_o| - |F_c||/ \Sigma |F_o|$

(b) $wR_2 = [\Sigma [w(F_o^2-F_c^2)^2]/ \Sigma [w(F_o^2)^2]]^{½}$, $w = 1/[s^2(F_o^2) + (aP)^2 + bP]$, where $P = [\max(F_o^2 \text{ or } 0) + 2(F_c^2)]/3$

Complex **2** crystallizes in the $P2_1/c$ space group and has only a single unique Ni center and no cocrystallized solvent molecules. The first coordination sphere is similar to **1a**, but the hydrogen bonding network is vastly different, Figure 4.6. Each cyclam amine hydrogen bonds to a triflate ion, of which there are two unique types. The first triflate ion does not hydrogen bond to any other molecule, similar to the Ni1 unit in **1a**, however the second triflate ion does hydrogen bond to a nearby cyclam. The result is a fully charge balanced H-bonded chain where the Ni ions are canted by 44.40°.

Both **3** and **4** crystallize in the space group *Pnma*, and while they are not technically isostructural, they are incredibly similar to one another, Figure 4.7. These similarities are not only in their crystallographic structures, but also extend to the quality of their diffraction and their propensity towards twinning. Both structures have similar first coordination spheres to **1a** and **2**, and like **1** they have two crystallographically unique Ni centers. Each cyclam amine hydrogen bonds to one outer-sphere ion, which in turn hydrogen bonds to neighboring cyclam. This results in a much more connected H-bonding network than in the other nitrile systems.

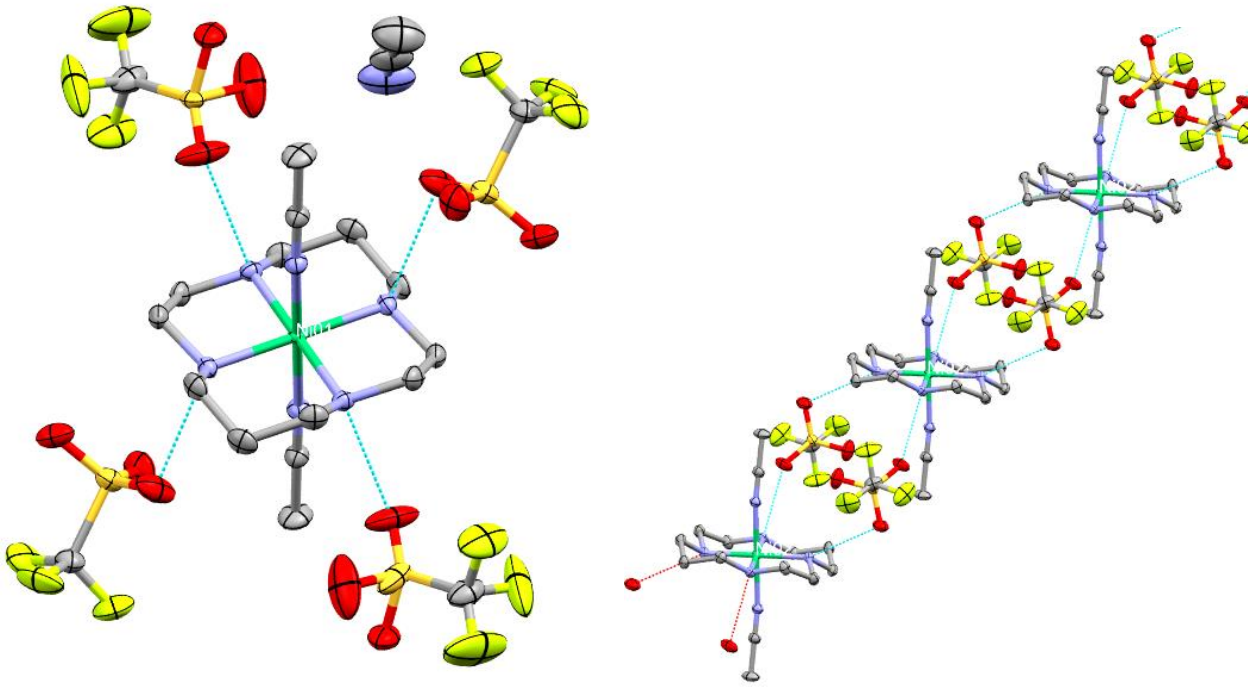

Figure 4.5 View of the hydrogen bonding network of **1a** involving the Ni1 site (left) and the Ni2 site (right).

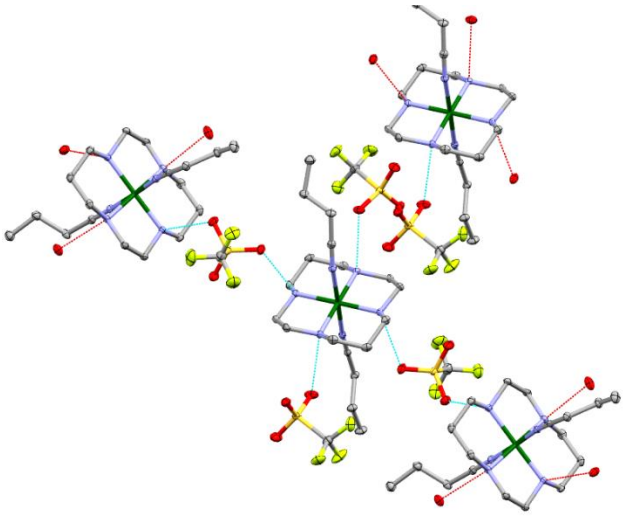

Figure 4.6 View of the hydrogen bonding network of **2**.

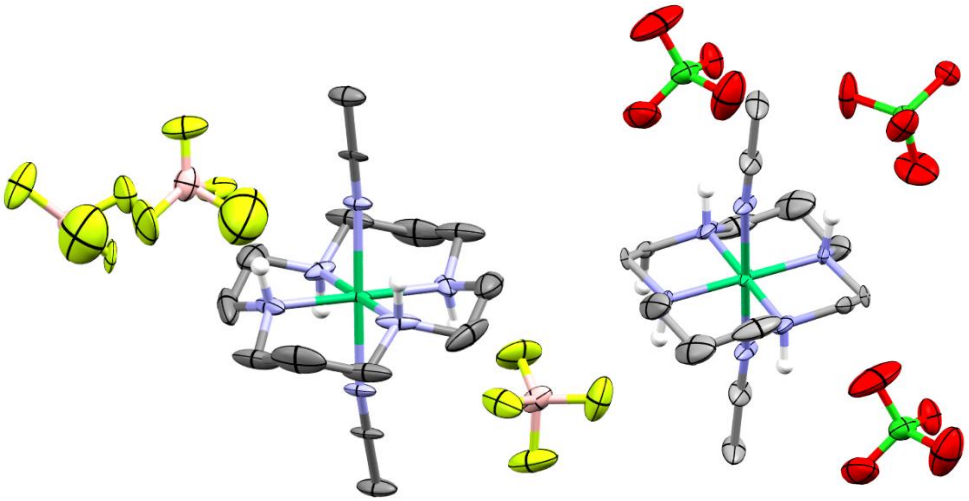

Figure 4.7 Crystal structures of **3** (left) **4** (right) rendered with 50% thermal ellipsoids. Green, red, blue, pink, lime, mint, and gray ellipsoids represent Ni, O, N, B, F, Cl, and C atoms, respectively, and white spheres represent H atoms involved in hydrogen bonding interactions. H atoms not involved in hydrogen bonding are omitted for clarity.

Table 4.2 Select metal-ligand bond distances.

Bond distance	**1a**	**2**	**3**	**4**
Ni-N (cyclam) (Å)	1.974	1.971	1.985	1.971
	1.976	1.977	1.981	1.990
	1.971		1.970	1.977
	1.975		1.965	1.970
Ni-N (nitrile, Å) (Å)	2.098	2.082	2.080	2.090
	2.125		2.090	2.080
			2.110	2.102

In order to quantify and compare the intermolecular interactions between the structures, Hirshfeld surface plots were generated and the fingerprint plots are shown in Figure 4.8. Comparing **1a** to **2**, the latter shows stronger H-bonding interactions (as smaller distances d_i v. d_e distances). Comparing **3** to **4**, whose crystal structures are nearly identical, shows how the H-bonding networks are nearly identical between the two structures. However, while the H-X distances are nearly the same, the BF_4 ions in **3** are much closer to the acetonitrile ligands than the ClO_4 ions in **4** are, which is shown as the gray tail.

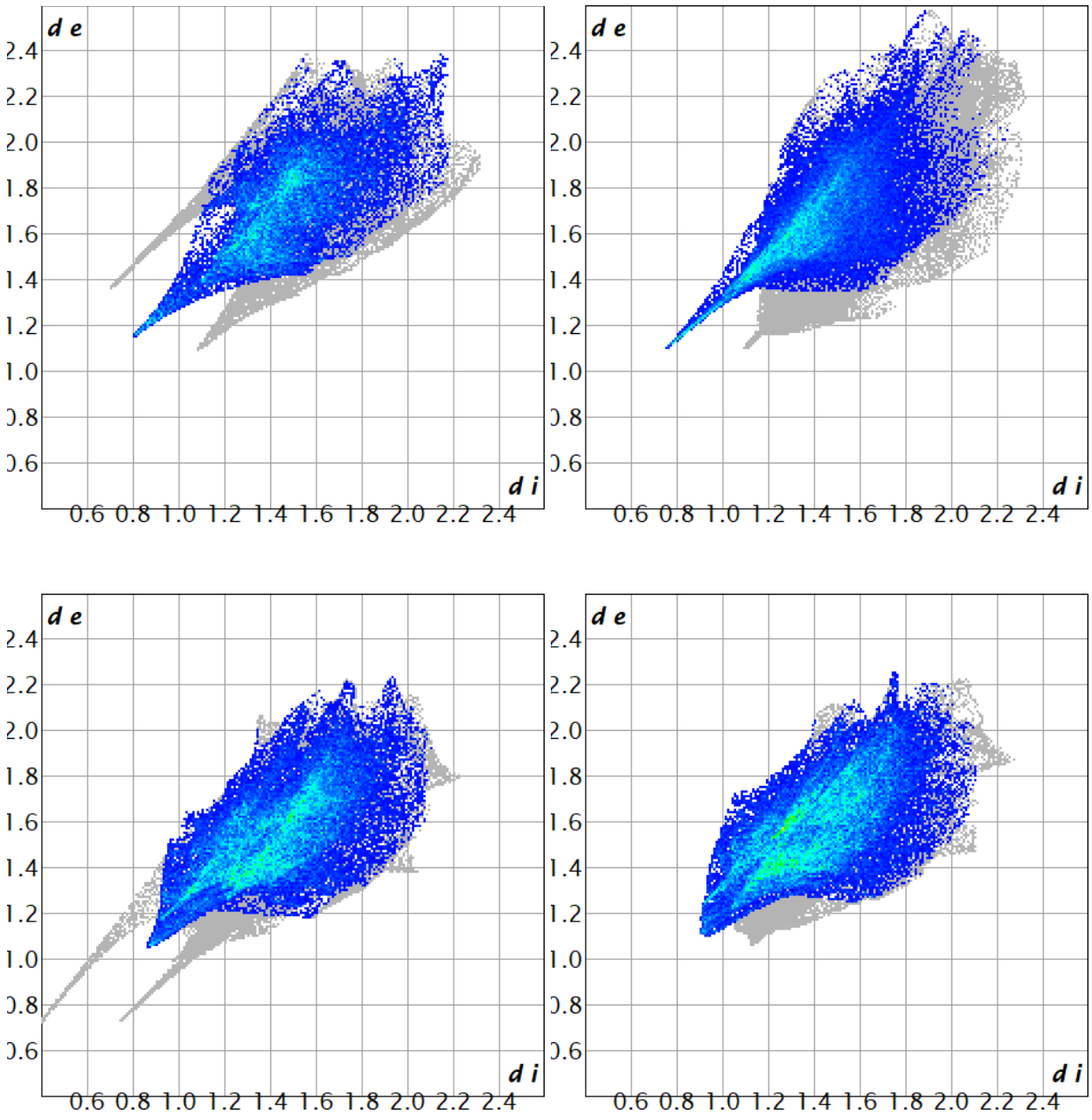

Figure 4.8 Fingerprint plots of **1a** (top left), **2** (top right), **3** (bottom left), and **4** (bottom right) showing the intermolecular interactions of the $[Ni(cyclam)L_2]^{3+}$ units. The highlighted regions are H-X (X = O, F) distances, with all other distances shown in gray.

4.4.3 Electron Paramagnetic Resonance. Continuous wave electron paramagnetic resonance (EPR) spectra were collected for **1a** and **2**-**4** as solids at room temperature in order to

confirm the presence of the $S = ½$ Ni(III) ions and determine their magnetic anisotropies, and are shown in Figure 4.9. All four species show signals consistent with a $S = ½$ systems with axial anisotropy, and the g values extracted from Easyspin are shown in Table 4.3.

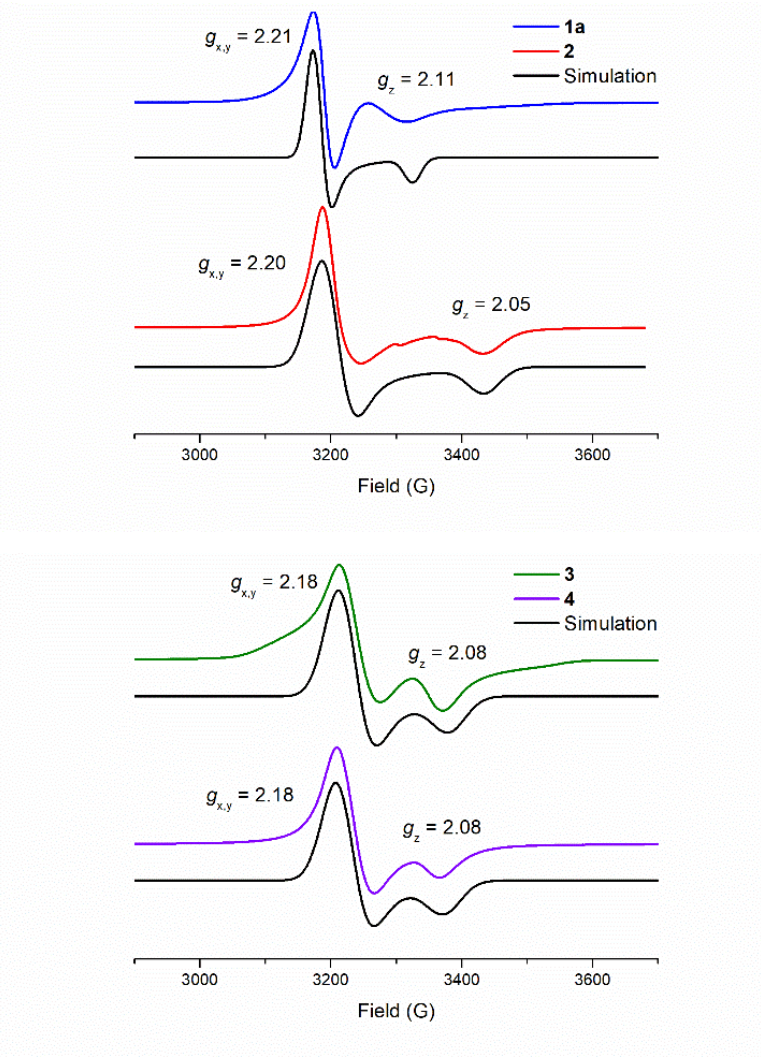

Figure 4.9 Room temperature X-band EPR spectra of Top: **1a** and **2** with microwave frequencies of 9.835506 GHz and 9.846924 GHz, respectively; Bottom: **3** and **4** with microwave frequencies of 9.841493 GHz and 9.826822 GHz, respectively.

Table 4.3 List of *g* values extracted from the room temperature, X-band EPR spectra.

Complex	$g_{x,y}$	g_z
1a	2.21	2.11
2	2.20	2.05
3	2.18	2.08
4	2.18	2.08

All three of the acetonitrile complexes, **1a**, **3**, and **4**, unsurprisingly show very similar spectra, with **3** and **4** being nearly identical, and none of which show any explicit fine structure. The EPR spectra of **2** is closely related to **1a**, but the g_z component is less than any of the acetonitrile-ligated systems. This suggests that the magnetic moment in the *z* direction is less sensitive to changes in the magnetic field (in the z direction) than the acetonitrile systems, but the difference is small. In 1980 Haines and McAuley reported on the frozen-solution phase EPR spectra of nominally $[Ni(cyclam)(MeCN)_2]^{3+}$ and found $g_{x,y} = 2.2148$ and $g_z = 2.0250$.[12,13] While the solution-phase spectrum is likely to differ from the solid-state, it is curious the range is so much greater than that of the acetonitrile materials presented here. This may be, in part, due to the difference sample preparation. Haines and McAuley measured a 1 M perchloric acid solution of $[Ni(cyclam)X_2]ClO_4$ (X = Cl or Br, with no mention of which anion was being used), with no mention of where or how the acetonitrile was introduced.

4.4.4 Static (DC) magnetic properties. The $\chi_M T$ plots of **1a** and **2-4** show that all complexes are $S = ½$, consistent with the Ni(III) oxidation state and the *M* vs *H* plots (Fig. A.4.1-4) at 100 K are linear, indicating a lack of ferromagnetic impurities that might interfere with the AC measurements. Figure 4.10 shows that at 300 K and with an applied field of 1 kOe **1a** has a $\chi_M T$ value of 0.407 cm^3 K mol^{-1} and remains nearly constant as the temperature decreases, reaching a minimum of 0.394 cm^3 K mol^{-1} at 22 K before increasing back to a maximum of 0.407 cm^3 K mol^{-1} at 2 K. The susceptibility at 5 kOe applied field is similar. Fitting the susceptibility data with

the program PHI (Table 4.4) results in a very slight ferromagnetic through-space interaction (zJ) of +0.03 cm^{-1}, which is unlike all other Ni(cyclam) systems reported herein. The magnetic dilution with Co(III), **1c**, very clearly removes these ferromagnetic interactions, however. The susceptibility for the dilution is commensurately low with the dilution factor, consistent with the UV-Vis data, and results in a small signal with large error. The $\chi_M T$ value at 300 K is of 0.020 cm^3 K mol^{-1} (4.9% that of **1a**) and remains approximately constant as the temperature decreases, reaching a minimum of 0.0166 cm^3 K mol^{-1} at 2 K. We note that the irregularity from 135 K – 185 K is due to the sample transitioning from mostly paramagnetic to mostly diamagnetic, resulting in large error in the waveform used to extract the susceptibility.

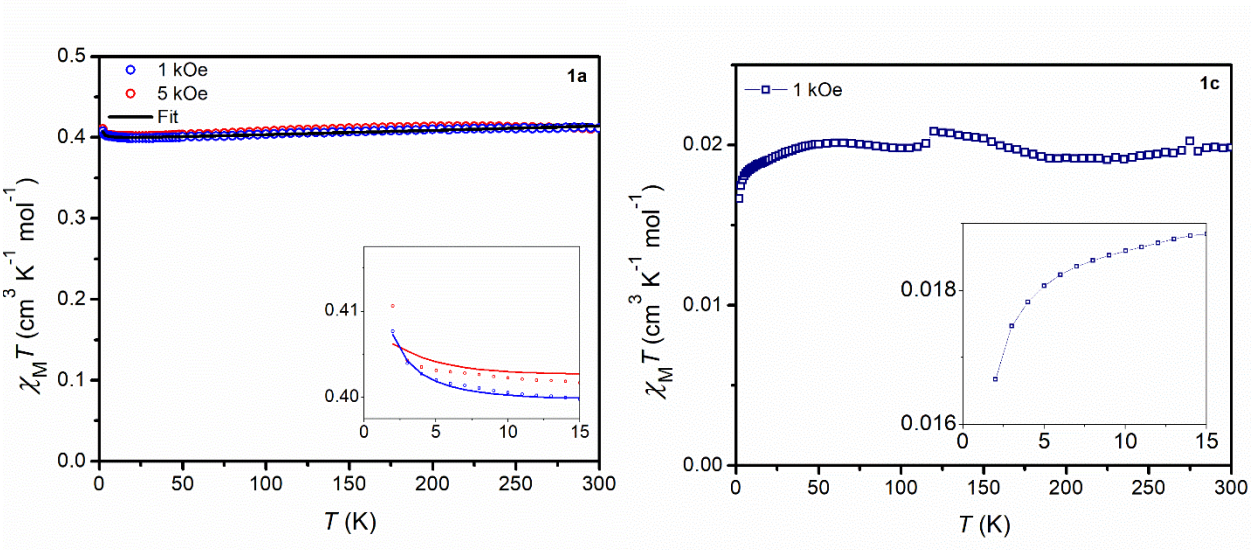

Figure 4.10 DC susceptibility of **1a** (left) and **1c** (right) at 1 kOe and 5 kOe from 2 K – 300 K. Inset: Enhanced view of the low temperature magnetic susceptibility-temperature product. Note: The deviation from linearity from *ca.* 100 K – 175 K in the susceptibility of **1c** is an artifact of the waveform of the sample transitioning from paramagnetic to diamagnetic. Lines are to guide the eye.

Table 4.4 Fit parameters of temperature-susceptibility data obtained from PHI.[18]

Complex	DC field (kOe)	g_{iso} value	zJ (cm^{-1})	χ_{TIP} (10^{-6} cm^3 mol^{-1})

1a	1	2.059(6)	+0.03(1)	54.(3)
1a	5	2.067(1)	+0.03(0)	5(3)
2	1	2.21(1)	-0.4(1)	-7(5)
$\mathbf{2}_{LT}$	1	2.19(3)	-0.36(4)	79.(9)
2	5	2.19(5)	-0.40(8)	-6(2)
$\mathbf{2}_{LT}$	5	2.17(8)	-0.36(3)	12.(8)
3	1	2.05(4)	-0.08(8)	10(5)
3	5	2.05(4)	-0.04(9)	10(9)
4	1	2.14(5)	-0.21(9)	36(8)
4	5	2.14(1)	-0.19(8)	37(7)

In comparison, **2** has a $\chi_M T$ value of 0.431 cm^3 K mol^{-1} at 300 K and 1 kOe which increases to 0.467 cm^3 K mol^{-1} at 235 K before decreasing to 0.429 cm^3 K mol^{-1} at 9 K, and then more rapidly to a minimum of 0.328 cm^3 K mol^{-1} at 2 K. Fitting the data using PHI results in a g value of 2.20, slightly higher than that obtained by EPR, with a modest, but curiously negative, χ_{TIP} of -6.9 x 10^{-5} cm^3 mol^{-1} (averaged between the two fields measured), however there is visible disagreement between the fit and data due to the irregular change in slope at 235 K. Initially we thought that this might be indicative of a structural rearrangement, however the powder diffraction pattern, which is collected at room temperature, very closely matches the structure collected by single crystal X-ray diffraction at 108.2 K. While this behavior is poorly modeled by the fit by PHI, our primary interest is in the low temperature AC magnetometry and the data below 235 K is very much what we expect for a $S = ½$ system, including the slight anti-ferromagnetic through-space interactions typical for Ni(III) cyclams. Excluding the data from 235 K – 300 K from the fit, $\mathbf{2}_{LT}$, very slightly decreases the g value and zJ, however the χ_{TIP} refines to a much more agreeable value of +8.0 x 10^{-5} cm^3 mol^{-1} at 1 kOe and +1.3 x 10^{-5} cm^3 mol^{-1} at 5 kOe.

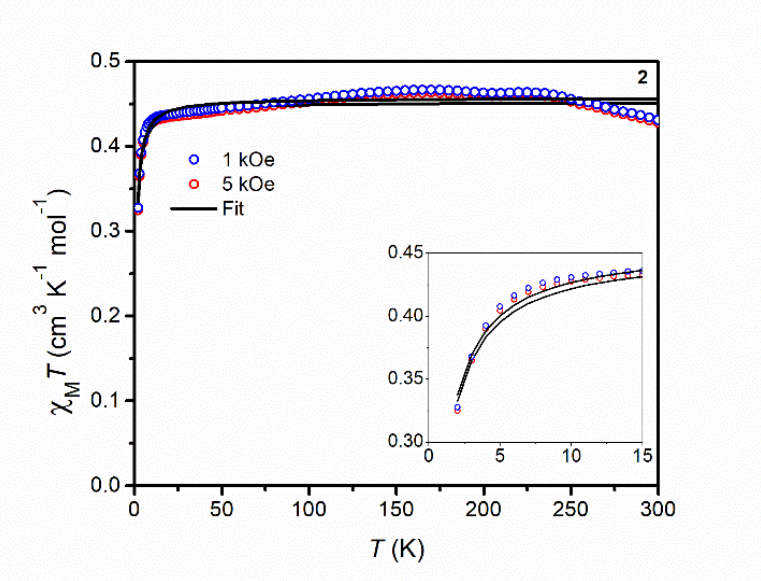

Figure 4.11 DC susceptibility of **2** in the solid-state at 1 kOe and 5 kOe from 2 K – 300 K. Fits shown are for the full temperature data set. Inset: Enhanced view of the low temperature magnetic susceptibility-temperature product.

Next, **3** almost perfectly represents the expected susceptibility for Ni(III) cyclam systems, and without complications. It has a $\chi_M T$ value of 0.426 cm^3 K mol^{-1} at 300 K and 1 kOe, which decreases to 0.394 cm^3 K mol^{-1} at 4 K before decreasing more rapidly to a minimum of 0.369 cm^3 K mol^{-1} at 2 K. Fitting the data using PHI models the data well and with extremely slight antiferromagnetic interactions and χ_{TIP}, although the g value obtained is less than that obtained by EPR. Structurally similar **4** shows temperature dependence of $\chi_M T$ that is unsurprisingly similar, except with significant χ_{TIP} contributions like the ClO_4 species discussed in Chapter 2. The $\chi_M T$ value at 300 K is 0.541 cm^3 K mol^{-1}, which decreases to 0.418 cm^3 K mol^{-1} at 7 K before decreasing more rapidly to a minimum of 0.352 cm^3 K mol^{-1} at 2 K, and the susceptibility profile obtained at 5 kOe is similar.

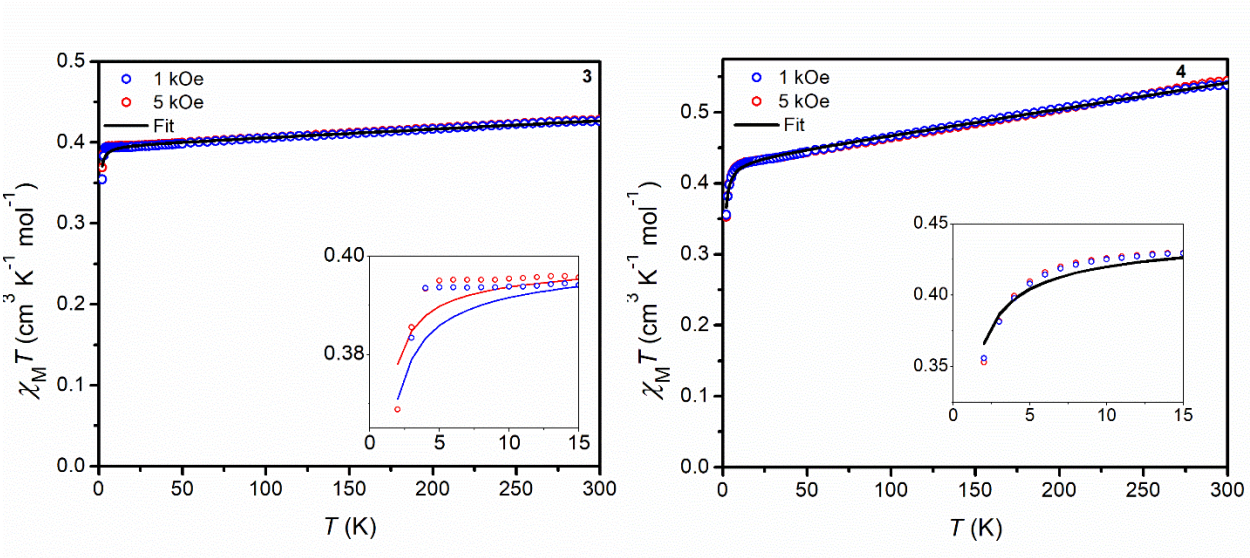

Figure 4.12 DC susceptibility of **3** (left) and **4** (right) in the solid-state at 1 kOe and 5 kOe from 2 K – 300 K. Inset: Enhanced view of the low temperature magnetic susceptibility-temperature product.

While **2-4** all showed similar temperature dependence in their susceptibilities and with very slight anti-ferromagnetic interactions, **1a** was unique with slight ferromagnetic through-space interactions. Thus far, this is the only system to show such interactions, although they are thoroughly quenched by the magnetic dilution with diamagnetic Co(III) in **1c**. We hypothesize that this might be due to the unique H-bonding chain within the system allowing for easier alignments of the magnetic moments. While **1** and **2** share the same triflate counter ions, it is difficult to elucidate the effect of exchanging acetonitrile with butyronitrile on the magnetic properties as they are crystallographically distinct, which plays a very large role in the magnetic properties of these superparamagnets. However, **3** and **4** *do* share an extremely similar structure, and it is interesting to note that the ClO_4 containing **4** has such large contributions from χ_{TIP} while **3** does not. Given that $[Ni(cyclam)(ClO_4)_2]ClO_4$ in Chapter **2** also had large χ_{TIP} contributions, it is possible that ClO_4 has unique interactions with the magnetic excited states that the other counter ions do not, such as

charge transfer, resulting in more accessible excited states that can mix with the ground state. It is unclear, however, specifically why ClO_4 is unique and further research into the electronic structure of the perchlorate containing complexes is required.

4.4.5 Dynamic (AC) magnetic properties. Unlike the halides discussed in Chapter 2 and the isothiocyanate complex in the 2018 study, all of the nitrile containing species presented here show field-induced slow magnetic relaxation, despite the presence of nuclear spin on the axial ligand sites. The field dependencies of the AC susceptibility data were studied at 1.8 K for **1a** and **1c** (Figure 4.13), **2** (Figure 4.15), **3** (Figure 4.17), and **4** (Figure 4.21). The temperature dependence of the AC susceptibility was also measured at 2 kOe from 1.8 – 15 K for all undiluted complexes, with **1a** being extended to 30 K. The BF_4 containing **3** was also measured at 1.2 kOe from 2 – 15 K due to complications in the 2 kOe data (*vide infra*).

For the undiluted **1a**, slow magnetic relaxation can be seen with an applied field as little as 500 Oe, but increasing the field to 1 kOe shows how the system has a multi-mode relaxation profile as a peak at *ca.* 7 Hz begins to grow in while the peak at *ca*. 400 Hz remains nearly unchanged. Further increasing the field to 1.5 kOe appears to slow the faster peak to *ca.* 80 Hz, and by 2 kOe is completely subsumed by the slower peak. Further increases to the field very slightly decrease the peak but do not show any separation of the two events. The magnetically diluted **1c** is strikingly similar to the deuterated sample from Chapter 3, [Ni(d_4-cyclam)$(DSO_4)_2$]DSO_4, showing only one (obvious) relaxation event, though its maxima are outside the frame. The stark contrast between the two systems is good evidence for the existence of the phonon bottleneck effect in **1a**, which is quenched in **1c**, leaving only the molecular relaxation.

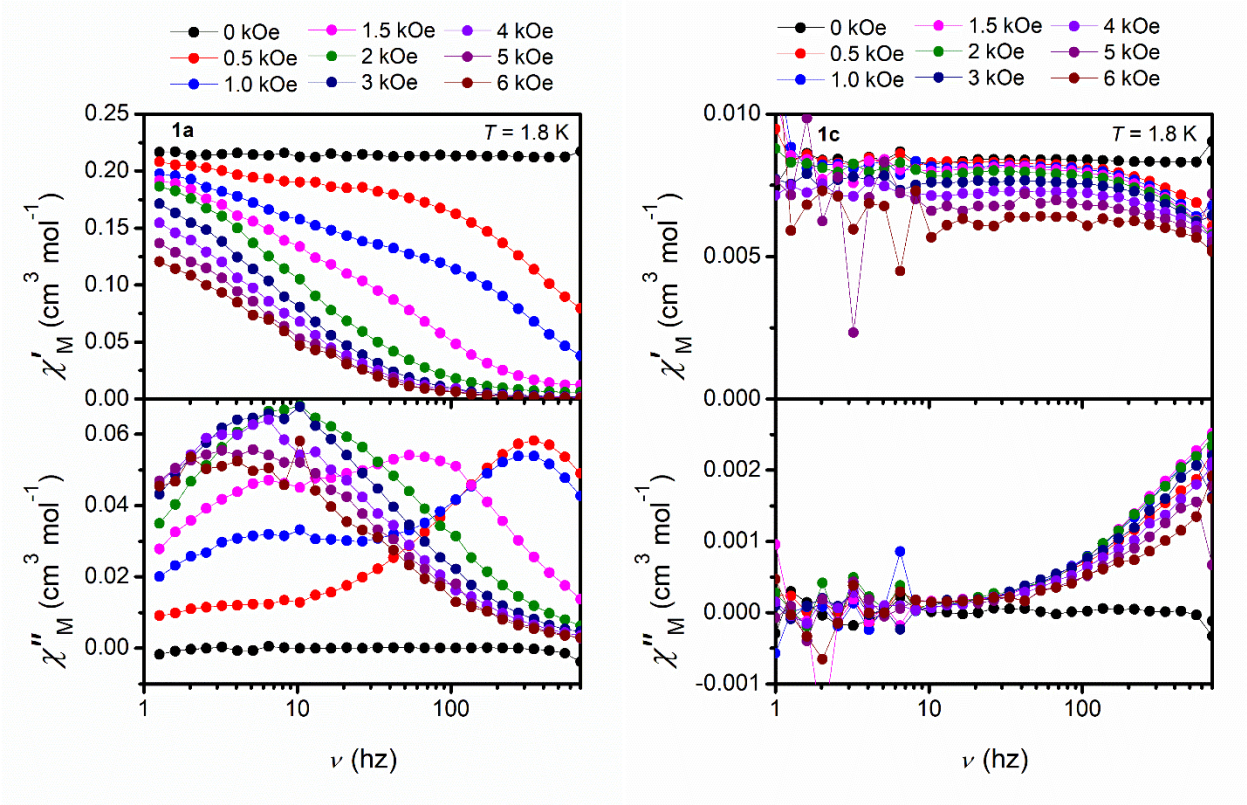

Figure 4.13 Field dependence of in-phase (top) and out-of-phase (bottom) magnetic susceptibility of **1a** (left) and **1c** (right) from 0 – 6 kOe.

The temperature dependence of **1a** was investigated from 1.8 K – 30 K at 2 kOe, where only a single relaxation mechanism was visible and further increases to the field had diminishing effects on the relaxation times. The data were fit to equation 1.7 and the relaxation rates, τ^{-1}, were extracted. Plotting the relaxation rates as a log-log plot, Figure 4.14, shows that the relaxation rates are similar to the Ni(III) cyclams reported in the previous chapters; At low temperatures, below 4 K, the relaxation rates increased rapidly, consistent with a Raman relaxation pathway. At *circa* 4 K the rate of increase begins to slow, consistent with the phonon bottleneck effect, and in a similar manner to the HSO_4 complex discussed in Chapter 3. Looking at the slopes of the log-log plot above and below 4 K, 2.70 and 1.64, respectively, suggest a combination of a Raman relaxation pathway with a phonon bottleneck.

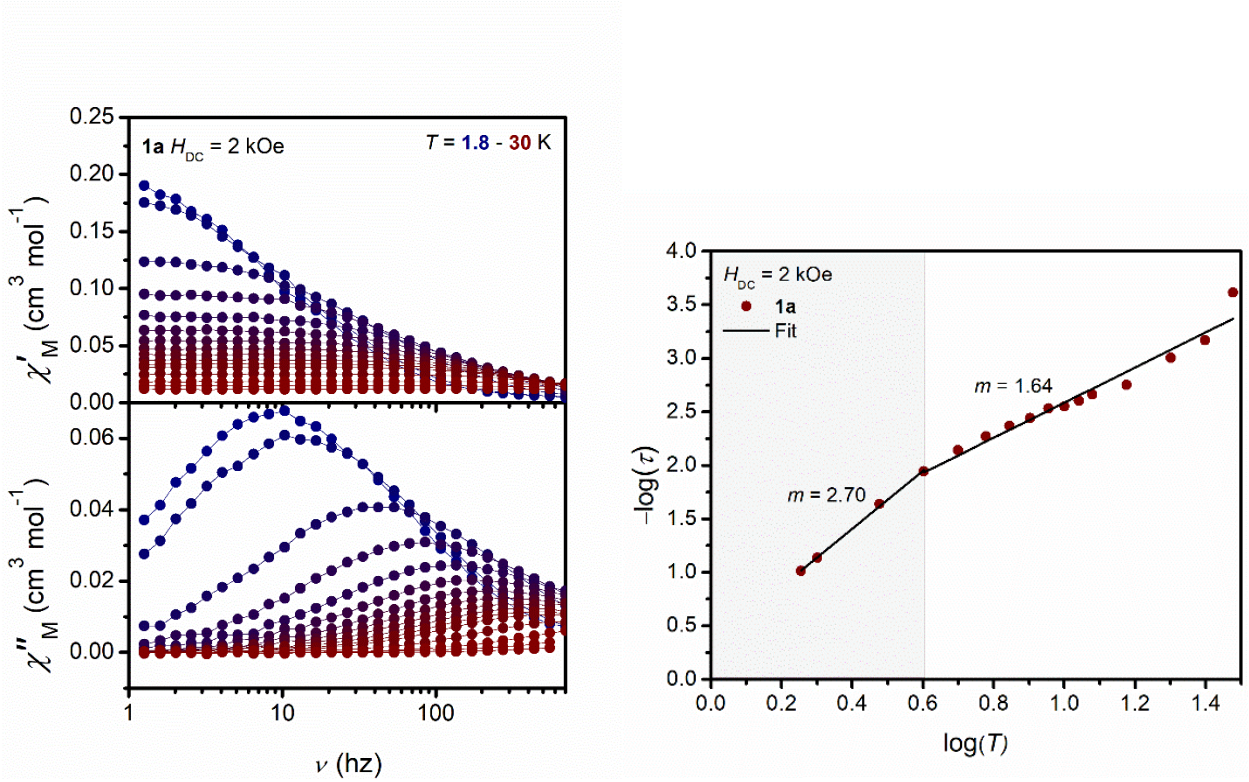

Figure 4.14 Left: In-phase (top) and out-of-phase (bottom) AC magnetic susceptibility of **1a** at 2 kOe from 1.8 K – 30 K. Right: log-log plot of relaxation rates extracted as a function of temperature; lines represent slope of log-log plot.

The field dependent AC susceptibility of **2** is similar to that of **1a**, despite the similar first coordination spheres. As with all Ni(III) cyclam complexes measured, the AC susceptibility does not show any slow magnetic relaxation at zero applied field, but at 500 Oe a multi-mode relaxation profile is observed. The first pathway occurs at *ca*. 8 Hz and the second pathway at *ca*. 100 Hz, but further increases to the magnetic field increase the first event and decreases the second instead of shifting the second event to lower frequencies, as seen in **1a**. By 2 kOe the second pathway is completely indistinguishable from the tail of the first relaxation pathway. Interestingly, at all non-zero field measured the system has incomplete relaxation, as evident by the in-phase (χ') susceptibility saturating at approximately 0.065 cm^3 mol^{-1} instead of zero. This corresponds to

only 60% of the spins within the system undergoing slow relaxation. The crystal structure of **2** only possesses one crystallographically unique Ni site, unlike **1a** which possesses two unique sites unrelated by symmetry, and so the source of this incomplete relaxation is unlikely to be solely due to crystallographic reasons. However, we do note that half of the Ni centers align along the (21 36- 19, h k l) plane and the other half along the (16 30 12) plane. This split in co-linearity of Ni centers is not unique to **2**, but present in nearly all Ni(III) cyclams, and without an in-depth analysis of the phonon dispersion diagram we cannot comment on the significance of this in **2**.

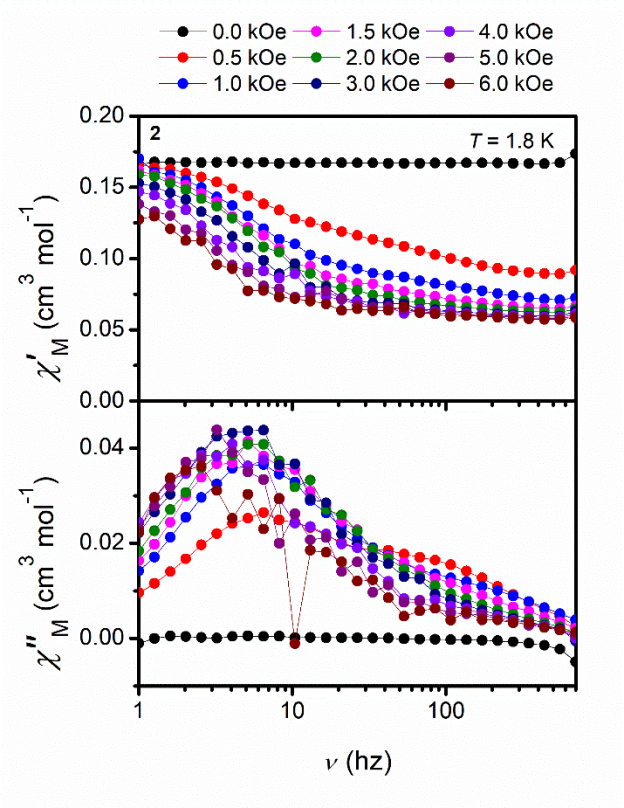

Figure 4.15 In-phase (top) and out-of-phase (bottom) AC magnetic susceptibility of **2** at 1.8 K, ranging from 0 kOe – 6 kOe.

The temperature dependence of the AC susceptibility of **2** was measured at 2 kOe (Figure 4.16) and is qualitatively similar to the other systems measured, with the exception of the

incomplete relaxation. Initially the relaxation rate of **2** is less than that of **1a**, but the greater slope (3.52) overtakes it by 4 K ($\log_{10}(4) = 0.6$), after which the phonon bottleneck effect begins to block the relaxation. This results in the increase in the relaxation rates being approximately the same after 4 K (m = 1.60), although **2** is consistently faster than **1a** at all temperatures past 4 K.

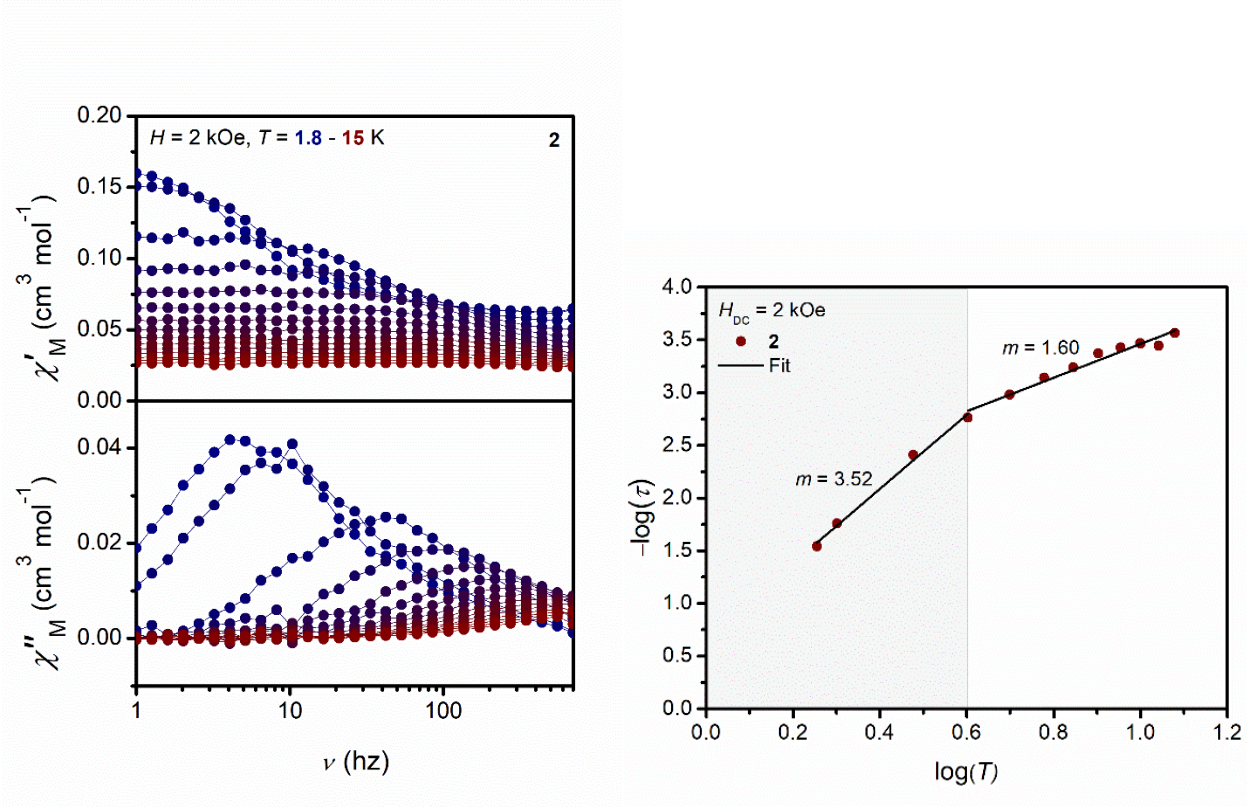

Figure 4.16 Left: In-phase (top) and out-of-phase (bottom) AC magnetic susceptibility of **2** at 2 kOe from 1.8 – 15 K. Right: log-log plot of relaxation rates extracted as a function of temperature; lines represent slope of log-log plot.

The field dependence of the AC susceptibility of **3** is again similar to that of the others, but interestingly the two processes at low field are at approximately the same intensity. At 500 Oe the first pathway occurs at *ca*. 8 Hz and the second pathway at *ca*. 200 Hz. In order to investigate this further the low-field dependence was extended by collecting at DC fields ranging from 100 Oe to

400 Oe. This data shows that the intensity of both relaxation pathways increases at a similar rate but does not appear to significantly shift with the field. After 500 Oe the increase in field does appear to shift the second relaxation pathway to lower frequencies, but at 1.0 and 1.5 kOe the second pathway can only be vaguely seen as a shoulder of the first. By 2 kOe the second pathway is nearly indistinguishable from the tail of the first relaxation pathway.

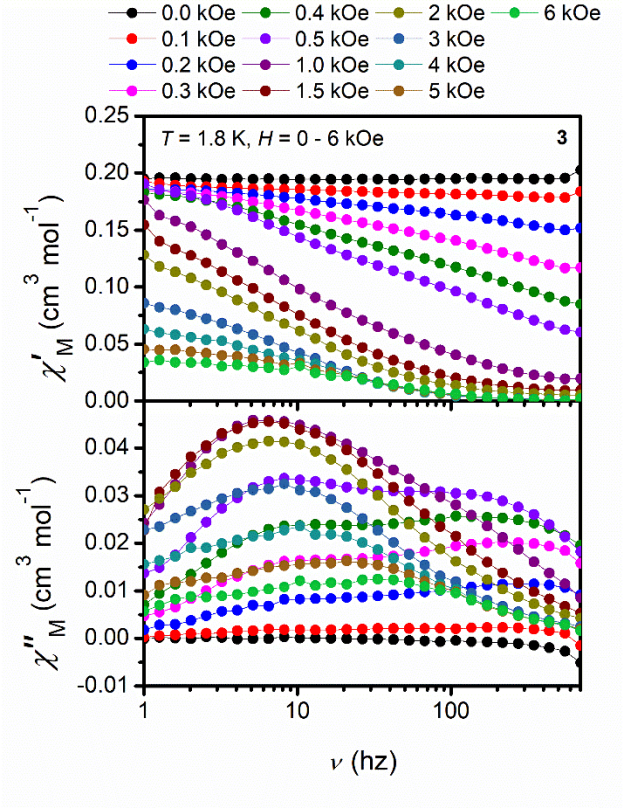

Figure 4.17 In-phase (top) and out-of-phase (bottom) AC magnetic susceptibility of **3** at 1.8 K from 0 kOe – 6 kOe.

Fitting the 2 kOe data to equation 1.7, which accounts for only a single operative relaxation pathway, systematically overestimated the relaxation rates. As a result, the data were fit using a linear combination of two operative pathways. The resulting fits were far better in modeling the behavior, and an example is shown in Figure 4.18. In-phase (top) and out-of-phase (bottom) AC

magnetic susceptibility of **3** at 1.2 kOe (left) and 2 kOe (right) from 1.8 K – 15 K. Because the 2 kOe data was composed of two pathways the temperature dependence was also measured at 1.2 kOe where it was easier to separate the two events. See Table A4.2 for the fits of the full data sets.

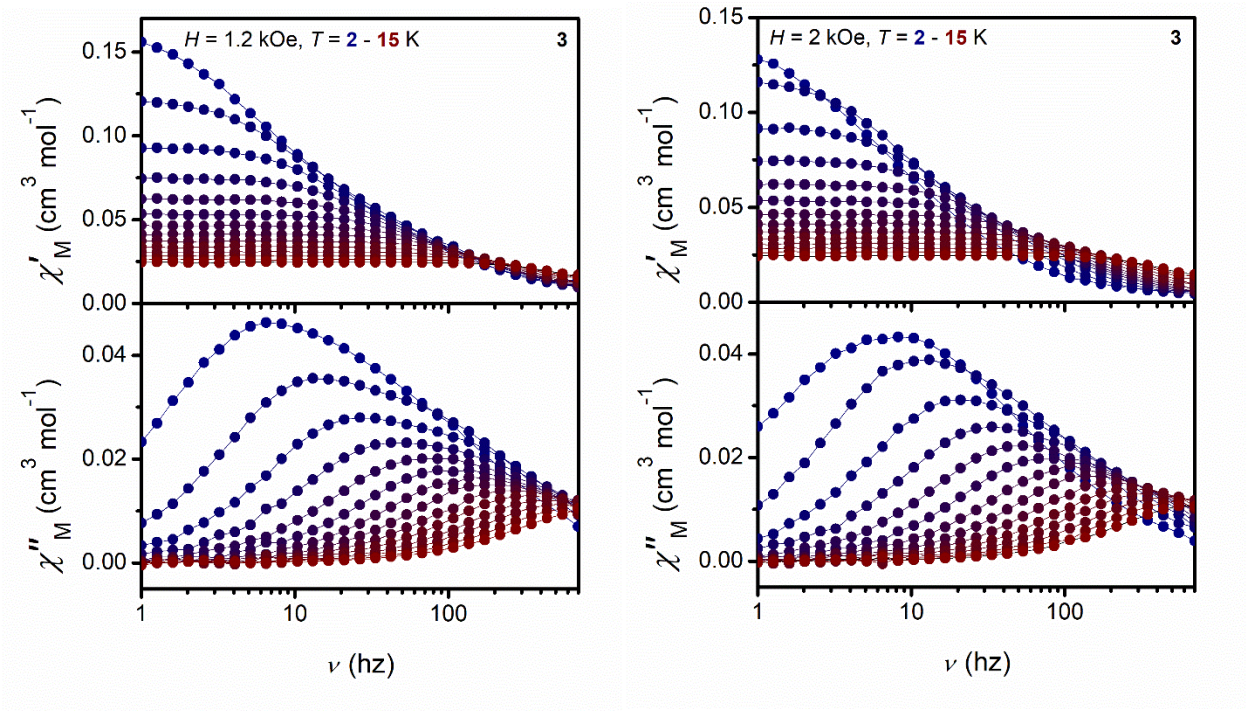

Figure 4.18 In-phase (top) and out-of-phase (bottom) AC magnetic susceptibility of **3** at 1.2 kOe (left) and 2 kOe (right) from 1.8 K – 15 K.

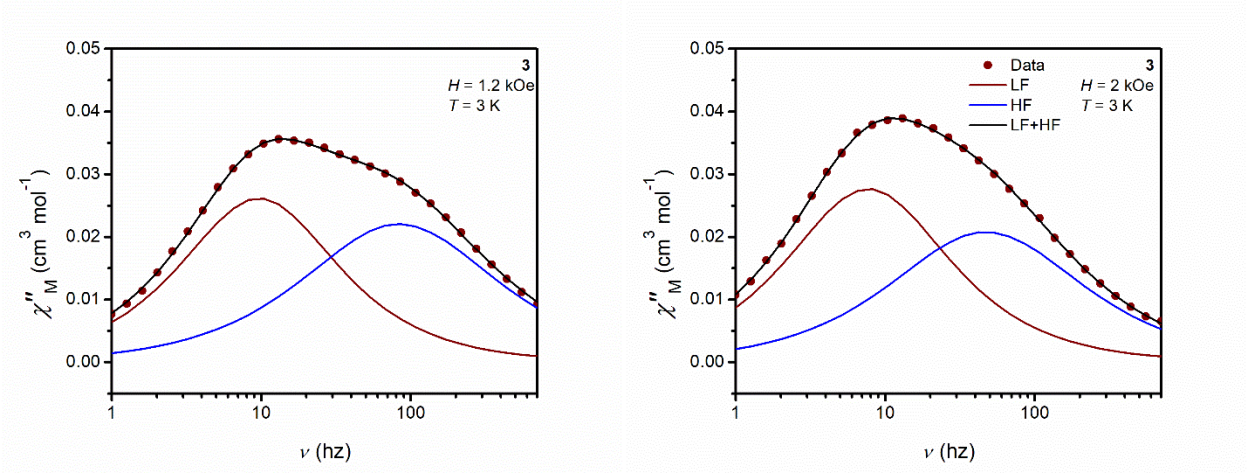

Figure 4.19 Examples of fits obtained for **3** by modeling two events. See Appendix for the full set of fits.

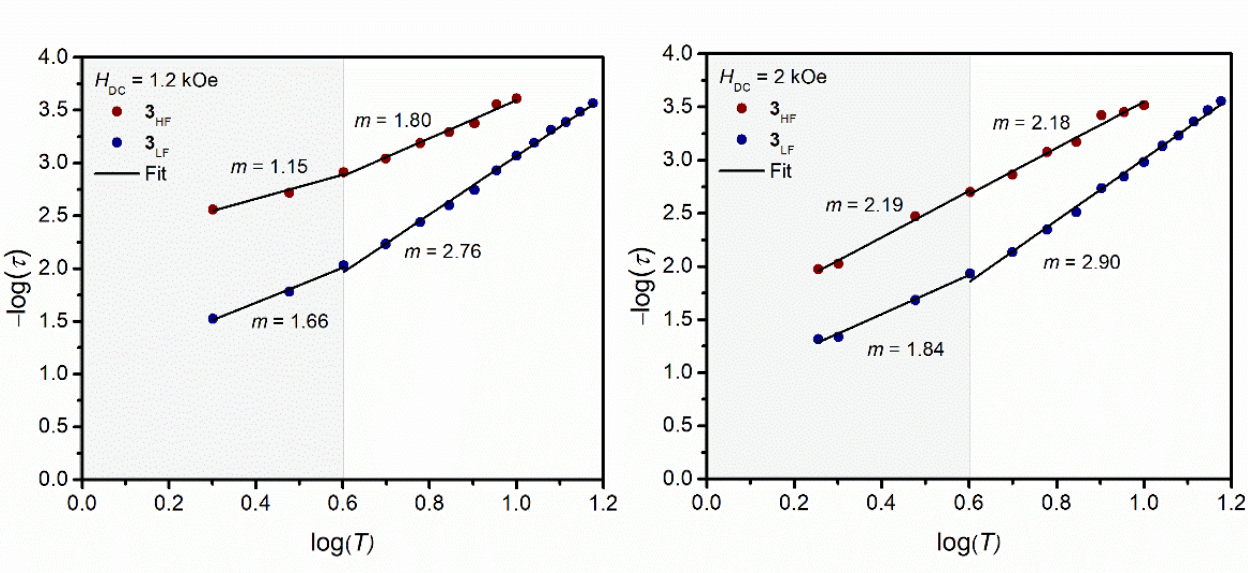

Figure 4.20 Log-log plot of relaxation rates for **3** extracted as a function of temperature at 1.2 kOe (left) and 2.0 kOe (right); lines represent slope of log-log plot.

Unsurprisingly, the field dependence of the AC susceptibility of **4** is most similar to **3** but is shifted to higher frequencies. However, unlike **3**, **4** does appear to have incomplete relaxation, though not to the same extent as **2** with 80% of the spins undergoing relaxation. At 500 Oe the first pathway occurs at *ca*. 20 Hz and the second pathway at *ca*. 300 Hz. At 1.0 and 1.5 kOe the second pathway can again only be vaguely seen as a shoulder of the first. By 2 kOe the second pathway is again indistinguishable from the tail of the first relaxation pathway.

The temperature dependence of the AC susceptibility of **4** was measured at 2 kOe (Figure 4.22) and is qualitatively similar to the other systems measured, again with the exception of the incomplete relaxation.

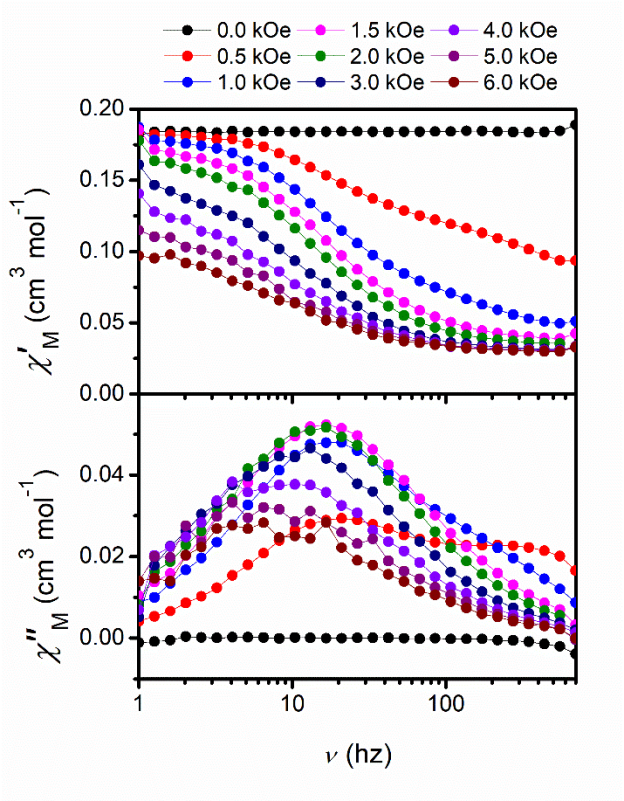

Figure 4.21 In-phase (top) and out-of-phase (bottom) AC magnetic susceptibility of **4** at 1.8 K from 0 kOe – 6 kOe.

Comparing the relaxation rates of **1a** and **2-4** (Figure 4.23) we can see that the phonon bottleneck effect that is present in all four complexes differs slightly in its onset temperature, but by 4 K seemingly affects all systems in a similar manner. This fact, along with the differences in the H-bonding network, suggests that the onset temperature of the phonon bottleneck effect is

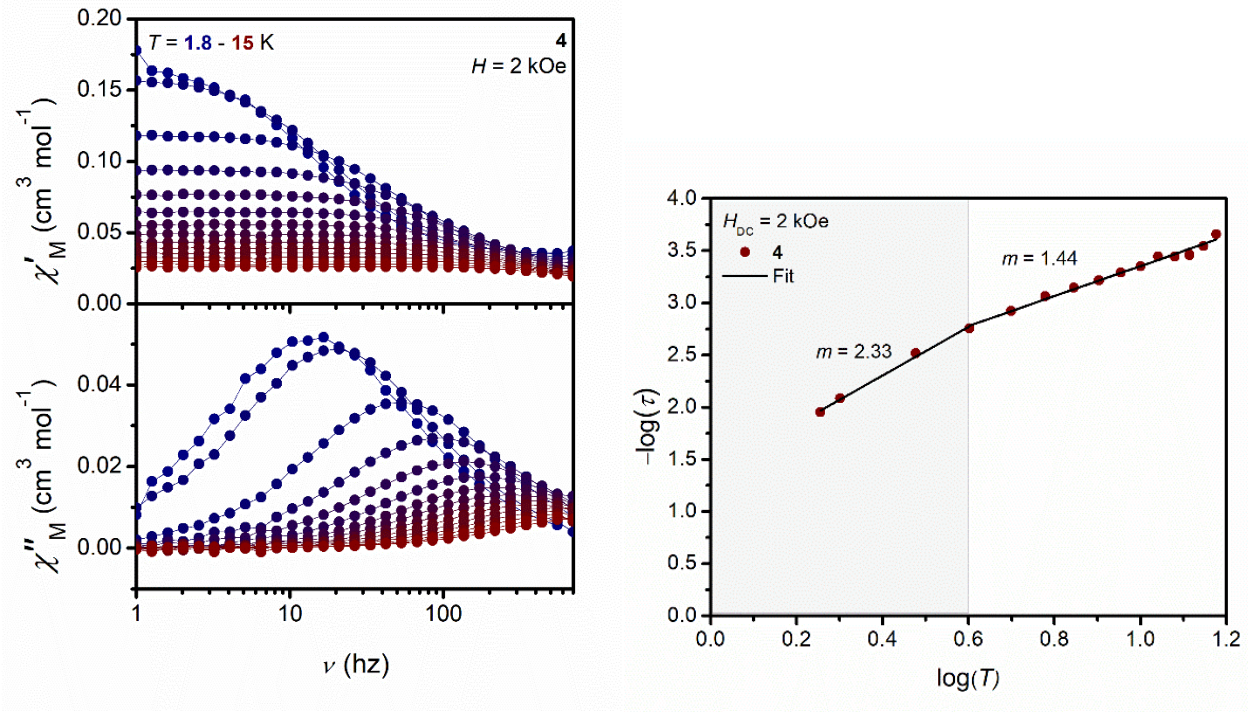

Figure 4.22 Left: In-phase (top) and out-of-phase (bottom) AC magnetic susceptibility of **4** at 2 kOe from 1.8 – 15 K. Right: log-log plot of relaxation rates extracted as a function of temperature; lines represent slope of log-log plot.

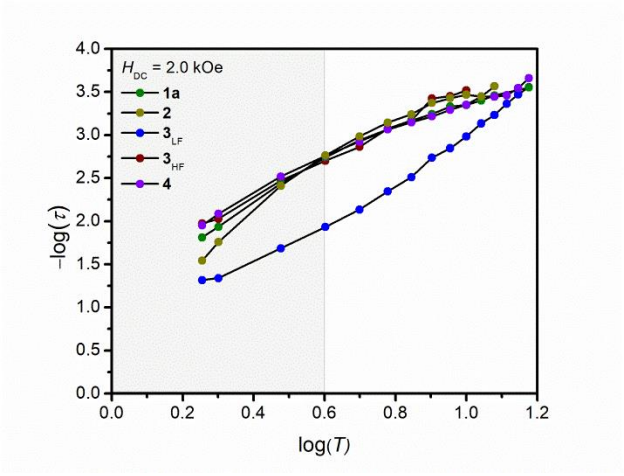

Figure 4.23 Log-log plot of relaxation rates extracted as a function of temperature for all complexes measured here at 2.0 kOe. Lines are to guide the eye.

affected by the H-bonding network, which can be explained by considering the heat capacity of the lattice. Changes to the H-bonding network result in changes in the heat capacity of the lattice

and of the material, in addition to changes in the energy of the phonons. The phonon bottleneck effect was originally derived thermodynamically by Stoneham in 1965 from the perspective of the heat capacity of the spins and the lattice.[20] From his work he arrived at equation 4.2,

$$\tau_{obs} = \tau_0 + \frac{C_S}{C_L}\tau_{ph} \qquad \text{(Equation. 4.2)}$$

where τ_{obs} is the observed relaxation *time*, τ_0 is the molecular relaxation time, τ_{ph} is the phonon lifetime, C_S is the heat capacity of the spins, and C_L is the heat capacity of the lattice. Essentially, this states that the observed relaxation time is the molecular relaxation time plus a fraction of the phonon lifetime, as the heat capacity of the spins is far below that of the lattice. This second term can also be considered as the probability of reabsorption of the phonon by another magnetic center. The heat capacity of the spins for all the materials measured here are unlikely to differ significantly, but this is especially true for **3** and **4** as they are nearly isostructural. Similarly, the differences in the counterions in **3** and **4** are likely to differ by a small amount. If τ_{ph} is sufficiently long, such that the second term in Eqn 4.2 is greater than that of τ_0 then τ_{obs} will be approximately the same for all of the complexes measured. We propose that the changes in the molecular relaxation rates are related to the changes in the cyclam amine H-bonding, which only comprise a small part of the overall heat capacity of the lattice, resulting in a similar τ_{obs} for all of the materials.

4.5 Conclusions

Four Ni(III) cyclam nitrile complexes were magnetically and crystallographically characterized. The neutral nitriles showed magnetic relaxation on par with the HSO_4^- system previously reported, despite the presence of nuclear spin in the axial position, which is predominantly I = 1. We conclude that the neutral ligands, which increase complex charge over the anionic ligands, contract

the dz^2 orbital and sufficiently reduce the interaction strength between nuclear and electronic spins to allow for slow magnetic relaxation. Investigations of the field and temperature dependence of the slow magnetic relaxation reveal that all four complexes show two relaxation pathways, a molecular pathway of either Raman or direct character, and an intermolecular phonon bottleneck effect pathway. While exchanging tetrafluroborate for perchlorate resulted in very little change in the crystal structure, the H-bonding network, and the *g* values of the Ni center, the exchange significantly affects the field dependence of the relaxation rates. Exchanging butyronitrile for acetonitrile in the triflate structures also significantly affected the field dependence of the relaxation, nearly eliminating the molecular pathway, which is only visible at 500 Oe. The similarities in the phonon bottleneck effect for all complexes, but difference in onset temperature and the temperature dependence at low temperature leads us to believe that the changes in the molecular relaxation rates are related to the changes in the cyclam amine H-bonding, which only comprise a small part of the overall heat capacity of the lattice, resulting in a similar phonon bottleneck effect for all of the materials.

4.6. References

(1) Habib, F.; Murugesu, M. Lessons Learned from Dinuclear Lanthanide Nano-Magnets. *Chemical Society Reviews*. **2013**, pp 3278–3288. https://doi.org/10.1039/c2cs35361j.

(2) Bar, A. K.; Pichon, C.; Sutter, J. P. Magnetic Anisotropy in Two- to Eight-Coordinated Transition–Metal Complexes: Recent Developments in Molecular Magnetism. *Coordination Chemistry Reviews*. Elsevier B.V. **2016**, pp 346–380. https://doi.org/10.1016/j.ccr.2015.06.013.

(3) Benelli, C.; Gatteschi, D. SMM with Lanthanides. In *Introduction to Molecular Magnetism*, **2015**, 239–249. https://doi.org/10.1002/9783527690541.ch14.

(4) Alexandropoulos, D. I.; Vignesh, K. R.; Stamatatos, T. C.; Dunbar, K. R. Rare "Janus"-Faced Single-Molecule Magnet Exhibiting Intramolecular Ferromagnetic Interactions.

Chem. Sci. **2018**, *10* (6), 1626–1633. https://doi.org/10.1039/c8sc04384a.

(5) Guo, F. S.; Day, B. M.; Chen, Y. C.; Tong, M. L.; Mansikkamäki, A.; Layfield, R. A. A Dysprosium Metallocene Single-Molecule Magnet Functioning at the Axial Limit. *Angew. Chemie - Int. Ed.* **2017**, *56* (38), 11445–11449. https://doi.org/10.1002/anie.201705426.

(6) Guo, F. S.; Day, B. M.; Chen, Y. C.; Tong, M. L.; Mansikkamäki, A.; Layfield, R. A. Magnetic Hysteresis up to 80 Kelvin in a Dysprosium Metallocene Single-Molecule Magnet. *Science.* **2018**, *362* (6421), 1400–1403. https://doi.org/10.1126/science.aav0652.

(7) He, M.; Guo, F. S.; Tang, J.; Mansikkamäki, A.; Layfield, R. A. Synthesis and Single-Molecule Magnet Properties of a Trimetallic Dysprosium Metallocene Cation. *Chem. Commun.* **2021**, *57* (52), 6396–6399. https://doi.org/10.1039/d1cc02139g.

(8) Ding, Y. S.; Yu, K. X.; Reta, D.; Ortu, F.; Winpenny, R. E. P.; Zheng, Y. Z.; Chilton, N. F. Field- and Temperature-Dependent Quantum Tunnelling of the Magnetisation in a Large Barrier Single-Molecule Magnet. *Nat. Commun.* **2018**, *9* (1), 1–10. https://doi.org/10.1038/s41467-018-05587-6.

(9) Dong, H.-M.; Liu, Z.-Y.; Tang, H.-M.; Yang, E.-C.; Zhang, Y.-Q.; Zhao, X.-J. Slow Relaxations of Dy(III) Single-Ion Magnets Dominated by Simultaneous Binding of Chelating Ligands in Low-Symmetry Ligand-Fields. *Dalt. Trans.* **2022**. https://doi.org/10.1039/d1dt03637h.

(10) Rasamsetty, A.; Mehta, S.; Ansari, K. U.; Kumar, P.; Mondal, A.; Shanmugam, M. Six-Coordinated Dinuclear Lanthanide(III) Amide Complexes: Investigation of Magnetization Relaxation Dynamics and Their Electronic Structures . *Dalt. Trans.* **2022**, *51* (1), 63–68. https://doi.org/10.1039/d1dt03708k.

(11) Bhowmick, I.; Roehl, A. J.; Neilson, J. R.; Rappé, A. K.; Shores, M. P. Slow Magnetic Relaxation in Octahedral Low-Spin Ni(III) Complexes. *Chem. Sci.* **2018**, *9* (31), 6564–6571. https://doi.org/10.1039/c7sc04482h.

(12) Haines, R. I.; Mcauley, A. Kinetics of the Reaction of the (1, 4, 8, 11-Tetraazacyclotetradecane)Diaquonickel(III) Cation with Halide and Thiocyanate Ions in Aqueous Perchlorate Media. *Inorg. Chem.* **1980**, *19* (3), 719–723. https://doi.org/10.1021/ic50205a027.

(13) Haines, R. I.; McAuley, A. Synthesis and Reactions of Nickel(III) Complexes. In *Coordination Chemistry Reviews,* **1981**, 39, 77–119. https://doi.org/10.1016/S0010-8545(00)80512-3.

(14) Bruker AXS inc. SAINT, v.8.38A. Madison, WI 2016.

(15) Sheldrick, G. M. SADABS, Version 2.03, Bruker Analytical X-Ray Systems, Inc., Madison, WI. Madison, WI 2000.

(16) Sheldrick, G. M. Crystal Structure Refinement with SHELXL. *Acta Crystallogr. Sect. C Struct. Chem.* **2015**, *71* (Md), 3–8. https://doi.org/10.1107/S2053229614024218.

(17) Bain, G. A.; Berry, J. F. Diamagnetic Corrections and Pascal's Constants. *J. Chem. Educ.* **2008**, *85* (4), 532–536. https://doi.org/10.1021/ed085p532.

(18) Chilton, N. F.; Anderson, R. P.; Turner, L. D.; Soncini, A.; Murray, K. S. PHI: A Powerful New Program for the Analysis of Anisotropic Monomeric and Exchange-Coupled Polynuclear d- and f-Block Complexes. *J. Comput. Chem.* **2013**, *34* (13), 1164–1175. https://doi.org/10.1002/jcc.23234.

(19) Stoll, S.; Schweiger, A. EasySpin, a Comprehensive Software Package for Spectral Simulation and Analysis in EPR. *J. Magn. Reson.* **2006**, *178* (1), 42–55. https://doi.org/10.1016/j.jmr.2005.08.013.

(20) Stoneham, A. M. The Phonon Bottleneck in Paramagnetic Crystals. *Proc. Phys. Soc.* **1965**, *86* (6), 1163–1177. https://doi.org/10.1088/0370-1328/86/6/302.

Chapter 5: Solution Phase Magnetic Relaxation of Ni(III) Cyclam Complexes and the Role of Glassy and Non-Glassy Solvents

5.1 Introduction

Choosing a glassy or non-glassy solvent for magnetic measurements has important implications in how phonons are transmitted within the material and has been shown in the pulsed EPR community to have a substantial effect on magnetic relaxation times, however the impact of solvent choice on single molecule magnets in AC susceptometry is less often reported.[1–3] In the Ni(III)cyclam systems studied thus far, the role of phonons have been critical to the magnetic relaxation properties, and the propagation of phonons differs between crystalline (non-glassy) and amorphous (glassy) solids. In crystalline solids, which have well-defined and periodic atomic arrangements, phonons propagate as coherent waves, which can travel long distances without significant scattering or loss of energy. This is one reason why the phonon bottleneck effect is possible in the solid-state samples discussed previously. In amorphous solids, however, there is no long-range order and periodicity, manifesting as significant disorder. This disorder disrupts the coherent propagation of phonons and leads to strong phonon scattering and lack of well-defined phonon modes present in crystalline materials.[4–6]

In frozen solutions the distribution of substrate molecules depends on many factors, such as the freezing rate, solute concentration, and solute-solvent interactions. During the freezing process, the formation of crystalline frozen domains can lead to the exclusion of solute molecules from the lattice; this cage effect increases the concentration of solute molecules in the remaining liquid regions between ice crystals.[7–9] Rapidly cooling solvents limits the time available for solute molecules to be excluded from the solid parts of the system, creating a more homogenous and even

distribution of solute molecules. In glassy solvents, however, the viscous nature of the solvent innately works against the exclusion of solute molecules, similar to the effect rapidly cooling the solutions but to even greater effect.[10,11] This results in frozen solutions of non-glassy solvents producing inhomogeneous regions of high and low concentrations of solute molecules, which can be reduced, but not eliminated, by increasing the freezing rate. The most extreme cases can be considered as microcrystals of the substrates with the interstitial spaces filled by crystalline solvent, creating interfaces between the materials. Meanwhile, frozen glassy solvents are more homogenous regardless of the freezing rate, with large distances between solute molecules.

In chapters two and four we discussed the solid-state magnetic properties for $[Ni(cyclam)Cl_2]Cl$ and $[Ni(cyclam)L_2]OTf_3$ (L = acetonitrile or butyronitrile), respectively. The literature has suggested that when the Cl-ligated system is dissolved in water (or dilute HCl) the chlorides exchange for water, forming the hydrated complex $[Ni(cyclam)(OH_2)_n]^{3+}$ (n = 1, 2) *in situ*, which would lack the nuclear spin that precludes slow magnetic relaxation.[12–14] However, while the Cl system is ambiguous in the ligands ligated in solution, the nitrile containing systems present a good opportunity to study the effect of solvent choice while removing such ambiguity. Acetonitrile and butyronitrile are extremely similar to one another in most ways, however the properties of their frozen solutions are very different. Acetonitrile is a non-glassy solvent that forms a crystalline lattice when frozen, giving the structure a clearly defined regularity. Butyronitrile, however, is a glassy solvent that is amorphous when frozen.[15,16] Furthermore, the successful conversion from acetonitrile to butyronitrile in Chapter 4 suggests that it is possible to study systems with other solvent molecules ligated, but are unable to be isolated through crystallization. As a result, solutions of tetrahydrofuran, a non-glassy solvent, and 2-methyltetrahydrofuran, its glassy analogue, were also investigated.

5.2. Division of Labor

All of the data collection and analyses were performed by Tom Morrison. The ARC staff and Dr. Indrani Bhowmick assisted with magnetic data collection.

5.3 Experimental.

5.3.1. Preparation of compounds. All manipulations were performed in air and with Millipore deionized water unless noted otherwise. The synthesis of $[Ni(cyclam)(MeCN)_2]OTf_3$ MeCN (**1a**), $[Ni(cyclam)(BN)_2]OTf_3$ (**2**, BN = butyronitrile), and $[Ni(cyclam)Cl_2]Cl$ (**3**) measured here are described in chapters 2 and 4 (**1a** and **2** are numbered consistently with Chapter 4, **3** was previously numbered **1** in chapter 2).

5.3.2 Magnetic measurements. Magnetic susceptibility data were collected using a Quantum Design MPMS3 SQUID magnetometer. The sample solutions were loaded into polyethylene bags and sealed, then the bags were inserted into drinking straws, frozen by submerging the straw in liquid N_2 for approximately 30 seconds, and then quickly inserted into the instrument. Ferromagnetic impurities were checked through a variable field analysis (0 to 10 kOe) of the magnetization at 100 K: overall linearity in the collected data for all compounds indicated the lack of significant ferromagnetic impurities. Static (DC) magnetic susceptibility data were collected at temperatures ranging from 2 K to 300 K at 1 kOe and 5 kOe. Alternating current (AC) magnetic susceptibility measurements were performed from 1 Hz to 700 Hz and from 1.8 K to 30 K with an alternating field of 4 Oe. Data were corrected for the magnetization of the sample holder by subtracting the susceptibility of an empty container, and for the diamagnetic contributions of the sample by using Pascal's constants.[17] Due to the instability of the Ni(III) oxidation state in

solution the data were collected in the following order in order to prevent sample decomposition: Magnetization (*M* v *H*) at 100 K, AC susceptibility in the temperature range 1.8 K – 15 K, and DC susceptibility from 2 K to 300 K.

4.3.3 Other physical characterizations. Electronic absorption spectra were obtained using quartz cuvettes in an Agilent 8453 spectrometer. Electron paramagnetic resonance spectra were obtained using a Bruker ESR-300 spectrometer equipped with an X-band microwave source, an ultra-high sensitivity resonator, and a liquid He cryostat with a quartz finger Dewar. Data were collected with a 5 G modulation amplitude and 100 kHz frequency.

5.4 Results and discussion

5.4.1 General Results. The existence of Ni(III) cyclam complexes bound by neutral nitrile ligands (Chapter 4) provided an excellent opportunity to explore the solution phase properties of species that might otherwise be unable to be isolated through ligand exchange, as well as give us an understanding of how the glassy and non-glassy solution magnetic properties differ from the solid-state properties. The electronic absorbance spectra of **1a** in MeCN was measured in the presence of NBu_4X (X = Cl, Br, I, PF_6, and OAc) and are shown in Figure 5.1. Addition of NBu_4Cl resulted in the precipitation of [Ni(cyclam)Cl_2]Cl, which was confirmed by powder X-ray diffraction and UV-Vis in water.

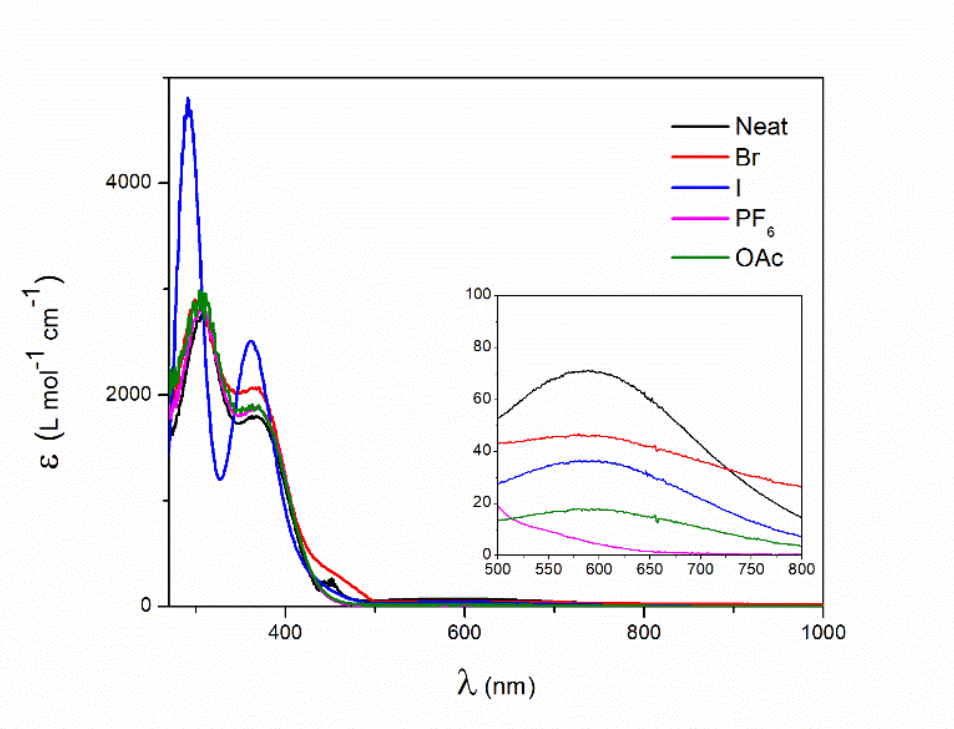

Figure 5.1 Absorptivity of **1a** in MeCN and with 10 equivalents NBu_4X salts (X = Br, I, PF_6, OAc)

Table 5.1 List of peaks in electronic absorption spectra of **1a** in acetonitrile with the addition of Bu_4NX (X = Br, I, PF_6, OAc).

	Charge transfer λ_{max} (nm)	*d-d* λ_{max} (nm)
Neat **1a**	308, 368	590
+ Br^-	304, 370	589
+ I^-	291, 362	590
+ PF_6^-	307, 370	570‡
+ OAc^-	306, 370	594

‡ *d-d* transition not clearly defined and appears as a shoulder.

Qualitatively there is little difference in the λ_{max} of electronic absorption spectra of **1a** upon the addition of the various salts, suggesting that the ligated acetonitrile ligand was not exchanged in the presence of these ions, unlike the insoluble Cl species. The neat **1a** solution has charge transfers centered at 308 nm and 368 nm, as well as the *d-d* transition at 590 nm. The addition of the salts slightly blue shift the 308 nm charge transfer according to Table 5.1. The charge 368 nm

charge transfer was slightly red shifted for all of the salts except for iodide, which was significantly blue shifted in comparison.

While the additions of the various NBu_4 salts did not show the significant changes in the electronic absorbance we would expect if the acetonitrile were exchanged, with the possible exception of NBu_4PF_6, exchanging the solvents did. Figure 5.2. shows the absorbance spectra of **1a** in dilute HOTf (*aq*), MeCN, BN, 2-MeTHF, MeOH, $MeNO_2$, and in THF over the course of two hours. The dilute HOTf, MeOH, and $MeNO_2$ spectra show a similar difference in the *d-d* transition, suggesting the MeCN ligand was successfully exchanged with the O-donating solvents. While **1a** had good solubility in these solvents, it had limited solubility in THF and 2-MeTHF and the *d-d* transition was unable to be observed. Figure 5.2 shows the most concentrated solution of **1a** obtained, 0.45 mM, and is significantly different from the other solutions.

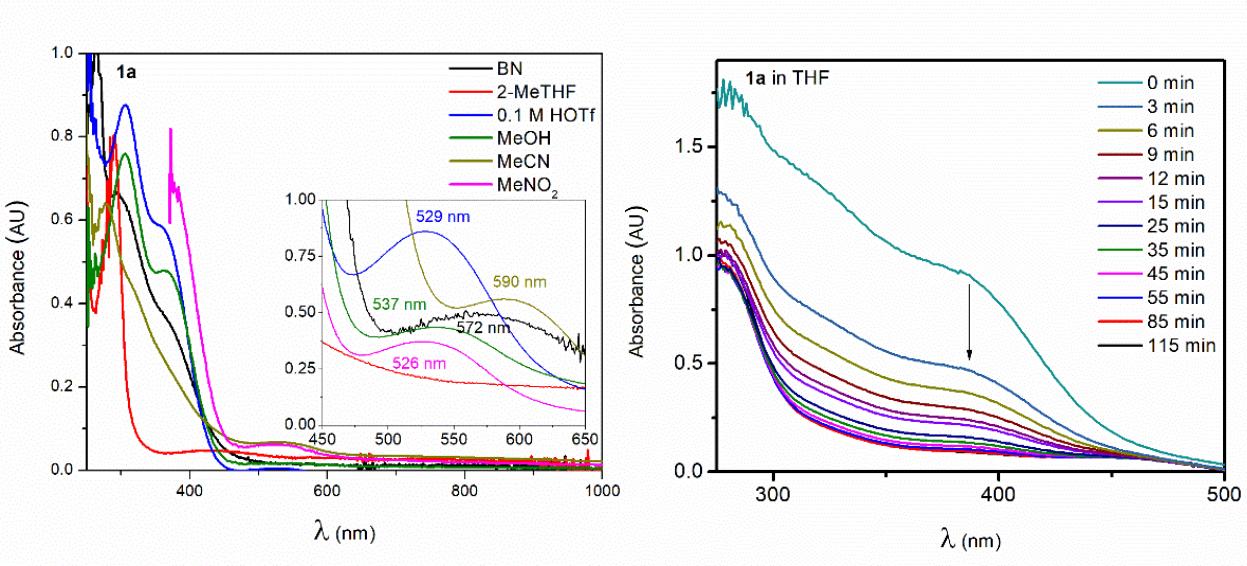

Figure 5.2 Left: Absorbance spectra of **1a** in 0.1 M HOTf (*aq*), neat MeCN, BN, 2-MeTHF, MeOH, and $MeNO_2$. Inset shows an enhanced view of a more concentrated solution. Spectra in $MeNO_2$ truncated at 370 nm for clarity. Right: Decay in absorbance of **1a** in THF over two hours.

While adding acid to the solutions of the Ni(III) complexes greatly increased the stability of the oxidation state, using such solutions for the magnetic measurements was undesirable as small leaks could ruin the instruments. Solutions of **1a** and **2** in acetonitrile and butyronitrile, respectively, were stable for days, whereas aqueous and methanolic solutions resulted in decomposition within minutes without adding acids. $MeNO_2$ was slightly better, showing complete decomposition within half an hour, but THF was stable for over an hour. As a result, the stability of the Ni(III) oxidation state of **1a** in THF was studied without additional acid in order to determine its suitability for solution-phase magnetic measurements. Fitting to a second order rate of decay yielded a half-life of 4.4 min at the concentration measured (k = 504 M^{-1} min^{-1}), Figure 5.3.

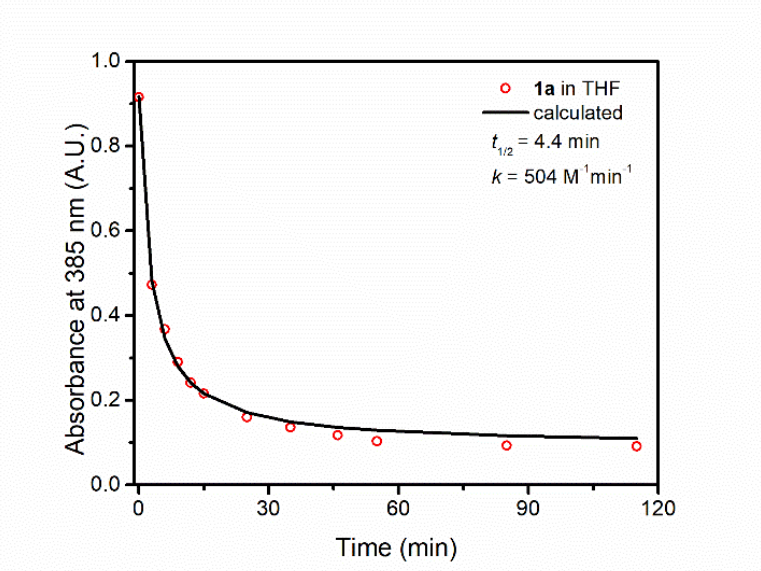

Figure 5.3 Absorbance of **1a** in THF over two hours as the Ni(III) material decays into the Ni(II) product. Calculated line is a fit of the data to a second order reaction rate with k = 504 $M^{-1}min^{-1}$ with an initial concentration of 0.45 mM.

5.4.2 Electron Paramagnetic Resonance. The continuous wave EPR spectra were collected of **1a** in solution at room temperature and are shown in Figure 5.4. All *g* values lie within the expected range for Ni(III) cyclam systems, and are shown in Table 5.2. Firstly, **1a** shows a stark change in the EPR spectra when dissolved in acetonitrile when compared to THF. In acetonitrile the spectrum becomes isotropic with only a single *g* value observed. However, when dissolved in THF the spectra unexpectedly show *four g* values. One *g* value is similar to the isotropic acetonitrile solution *g* value of 2.12, while another is very similar to the solid state $g_{x,y}$ value of **1a** at 2.20. The last two peaks correspond to *g* values of 2.65 and 2.03. Unlike **1a**, **2** is very similar in solution to its solid-state counterpart. The spectrum shows easy-plane anisotropy with *g* values of 2.19 and 2.04, very slightly lower than the solid-state *g* values of 2.20 and 2.05.

The EPR spectra of **1a** in 2-MeTHF could not be taken as the sample decomposed before it was able to be measured, and **3** in 1.0 M HCl (*aq*) was also unable to be collected due to the strong absorption of the solvent.

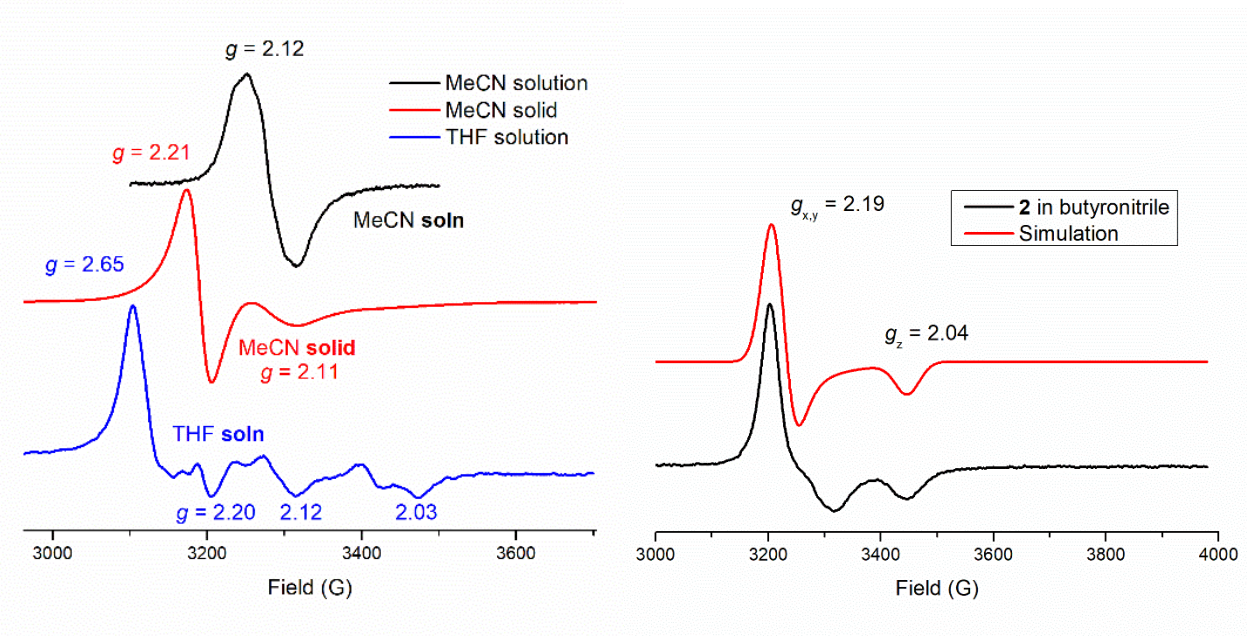

Figure 5.4 Left: EPR spectrum of **1a** in MeCN and THF solutions compared to the solid **1a** spectrum. All spectra were collected at room temperature. Microwave frequencies of 9.851271 GHz, 9.846956 GHz, and 9.835506 GHz, respectively. Right: EPR spectrum of **2** in butyronitrile. Microwave frequency of 9.852507 GHz.

Table 5.2 EPR *g* values of **1a** and **2** in MeCN, THF, and BN solutions.

Complex	Solvent	*g* value
1a	MeCN	2.12
	THF	2.65, 2.20, 2.12, 2.03
2	BN	2.19, 2.04

5.4.3 DC Magnetism. The temperature dependencies of the magnetic susceptibility of **1a** dissolved in MeCN and THF, respectively, are shown in Figure 5.5, and the magnetic susceptibility of **2** in butyronitrile and **1a** in 2-MeTHF are shown in Figure 5.6. The susceptibility at 2 K for frozen solutions of **1a** in MeCN and THF is 0.35 cm^3 K mol^{-1} for both solutions, and reaches approximately 0.375 cm^3 K^{-1} mol^{-1}, the expected value for the S = ½ system, by 5 K. The susceptibility drifts away from this expected value as the temperature approaches the melting point, drifting higher for the MeCN solution and lower for the THF solution.

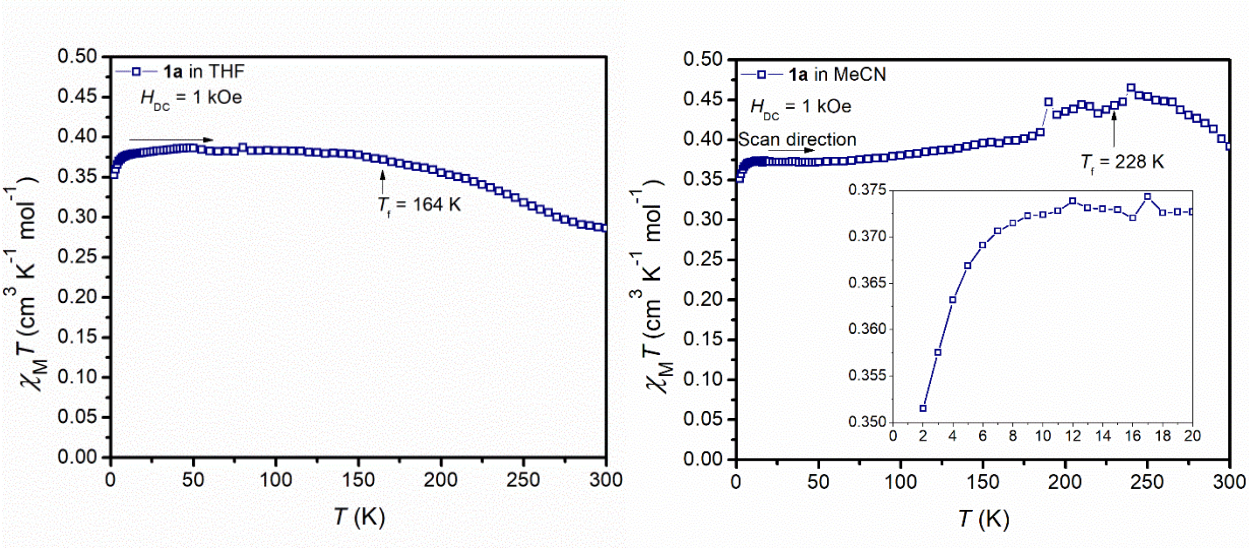

Figure 5.5 DC susceptibility of **1a** in a tetrahydrofuran solution (left) and acetonitrile solution (right) at 1 kOe from 2 K – 300 K. Inset: Enhanced view of the low temperature magnetic susceptibility-temperature product. The T_f corresponds to the freezing point of tetrahydrofuran (164 K) and acetonitrile (228 K).

The susceptibility for **2** in butyronitrile, measured at 1 kOe, is far less regular than that for **1a**. At 2 K the susceptibility is at a minimum of 0.28 cm^3 K mol^{-1}, which increases to approximately 0.4 by 12 K but has a large monotonic increase up to approximately 50 K. This increase appears to be due to significant temperature independent paramagnetism (TIP), however the shape of the data through the whole temperature range measured makes this assignment difficult. After 50 K the susceptibility increases sharply to approximately 0.65 cm^3 K mol^{-1} and remains somewhat constant up through the melting point of butyronitrile (T_f = 160 K) before decreasing as the solution melts. The susceptibility reaches a minima at 250 K and 0.38 cm^3 K mol^{-1} before increasing back to approximately 0.65 cm^3 K mol^{-1} at 300 K. This increase is not linear, as the low temperature increase was, and appears to be due to the Ni(III) ions (S = ½, $\chi_M T$ ≈ 0.375) decomposing into the Ni(II) product (S = 1, $\chi_M T$ ≈ 1). Stronger evidence for decomposition in solution can be seen in the 2-MeTHF solution. At 2 K the $\chi_M T$ is at a minimum

of 0.15 cm^3 K mol^{-1}, which increases to 0.40 cm^3 K mol^{-1} by 15 K. The susceptibility remains mostly constant up to 100 K before drifting lower to 0.38 cm^3 K mol^{-1}, where it then remains constant until the temperature reaches 250 K. After 250 K the susceptibility rapidly increases to 1.1 at 300 K, close to the expected value for the Ni(II) decomposition product. This decomposition was confirmed by a second scan at 5 kOe, which showed a susceptibility consistent with a $S = 1$ Ni(II) system, albeit very noisy, Figure A5.6. Interestingly, both glassy solvents show greater antiferromagnetic interactions than their non-glassy counterparts.

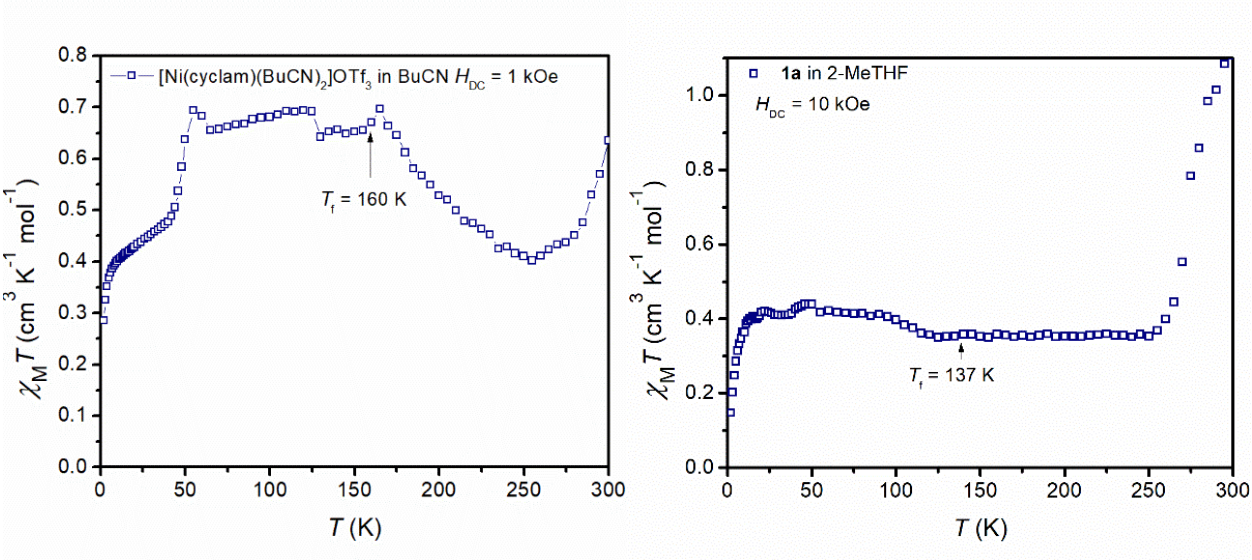

Figure 5.6 DC susceptibility of **2** in a butyronitrile solution at 1 kOe (left) and 2-MeTHF solution at 10 kOe (right) from 2 K – 300 K. The T_f corresponds to the freezing point of butyronitrile (160 K).

The shapes of the low temperature data are reminiscent of anti-ferromagnetic interactions, which is surprising given the low concentrations, approximately 2.2 mM in butyronitrile and 0.3 mM in 2-MeTHF. The sharp increase in the butyronitrile solution from 50 K is possibly from the sample changing from a mostly paramagnetic signal to a mostly diamagnetic signal, which significantly increases the error associated with the measurement. The elevated susceptibility of

the sample up to 170 K is abnormal, and while it is possible that this increase is due to decomposition of the Ni(III) ions producing Ni(II) ions, the decrease after the melting point followed by the increase after 250 K, which also occurs in 2-MeTHF, does not support this hypothesis.

The last solution measured, **3** in 1.0 M HCl (*aq*), was also consistent with the Ni(III) oxidation state. At 2 K the susceptibility is at a minimum of 0.33 cm^3 mol^{-1} K, which quickly reaches a maximum of 0.47 cm^3 K mol^{-1} at 7 K before decreasing to 0.38 cm^3 mol^{-1} K by 10 K. This hump was similar to the ClO_4 and HSO_4 systems investigated previously, and the susceptibility shows a very small increase as the temperature increases further until reaching the freezing point of the solution, whereupon the susceptibility once again decreased. The lack of significant antiferromagnetic interactions at low temperatures was promising that the ligated Cl ions were exchanged for water molecules, which we predicted will show slow magnetic relaxation due to the findings from chapters two and four. Furthermore, the hump in centered at 7 K appears in several of the other Ni(III)cyclam SMMs.

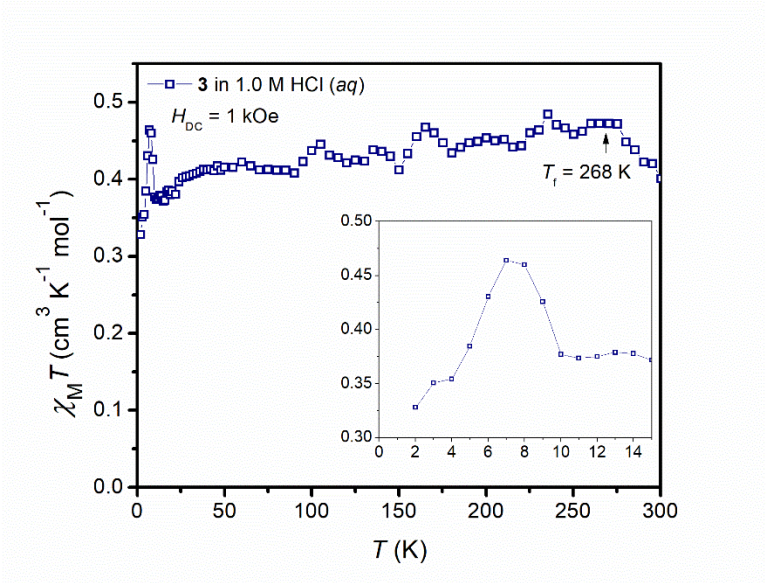

Figure 5.7 DC susceptibility of **3** in a 1.0 M HCl (*aq*) solution at 1 kOe from 2 K – 300 K.

5.4.4 AC Magnetism. The AC magnetic susceptibility of the solutions were first measured at 1.8 K from 0 – 6 kOe, Figure 5.8, then from 1.8 – 15 K, Figure 5.9. **1a** in MeCN shows slow magnetic relaxation with an applied field as low as 500 Oe, but the peak isn't visible until the applied field reaches 3 kOe. This behavior is similar to the magnetic dilution presented in chapter 4 (**1c**) but is slightly slower as the peak in the magnetic dilution was never visible. The THF solution, in comparison, shows a much slower relaxation rate with the peak being visible even at 500 Oe. As the field is increased the relaxation rate decreases in a similar manner to the solid-state data presented in Chapter 4, where the rate only slightly changes up to 1500 Oe, then slows significantly from 2 kOe to 3 kOe, where the relaxation rate then plateaus. At the higher applied fields the shape of the relaxation rates is irregular, suggesting multiple relaxation rates or possibly multiple species present in solution, however only a single peak is visible at any point, unlike in the solid-state data where multiple peaks are clearly visible.

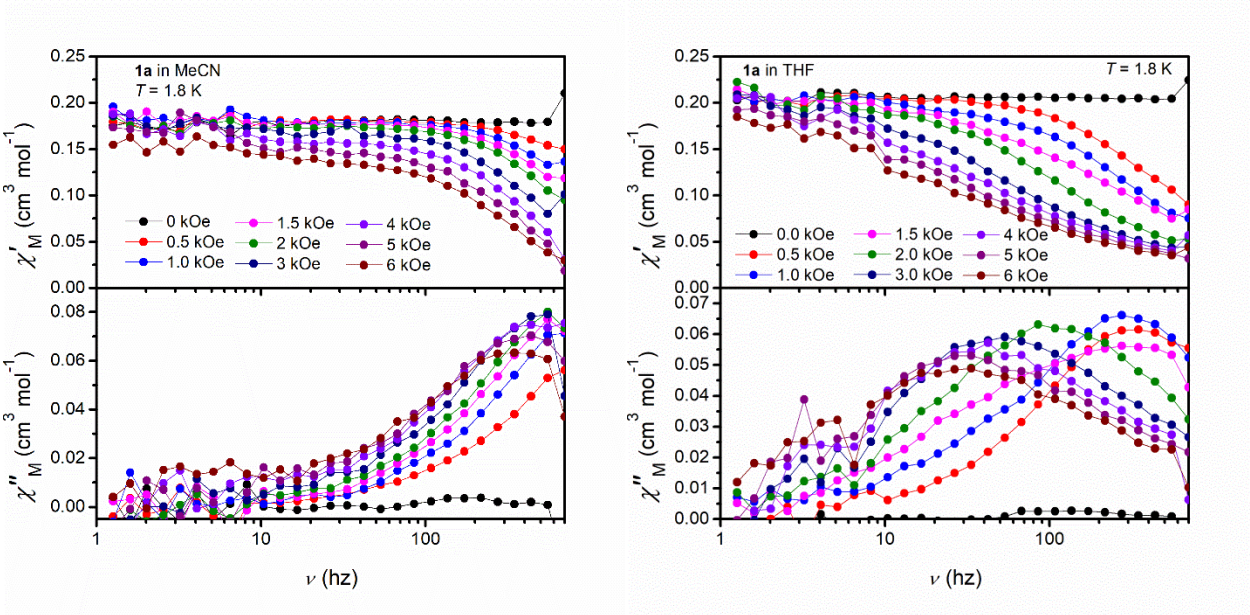

Figure 5.8 In-phase (top) and out-of-phase (bottom) AC magnetic susceptibility of **1a** in a frozen acetonitrile (left) or THF (right) solution at 1.8 K from 0 kOe – 6 kOe.

The temperature dependence of **1a** in MeCN, measured at 2 kOe, shows that the magnetic relaxation is no longer visible by 3 K. In contrast, in THF at 4 kOe (the optimal field for the system, where further increases to the field had diminishing effects) the peak is visible up to 4 K and magnetic relaxation up to 9 K. Plotting the relaxation rates as a log-log plot of these solutions and comparing them to the solid-state data presented in Chapter 4, Figure 5.10, shows that the acetonitrile solution has a much steeper slope for the two data points visible. The THF solution, on the other hand, is far more reminiscent of the solid-state data, but shifted to higher relaxation rates. This suggests that the acetonitrile solution may not undergo a phonon-bottleneck like relaxation pathway while the THF solution does.

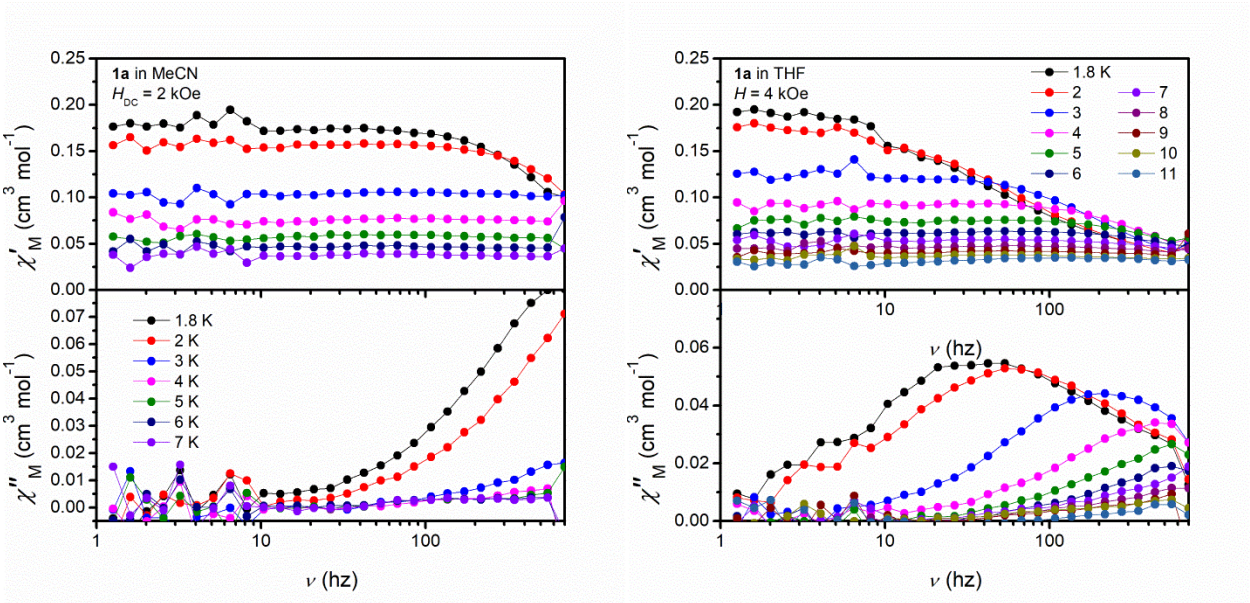

Figure 5.9 In-phase (top) and out-of-phase (bottom) AC magnetic susceptibility of **1a** in a frozen acetonitrile (left) solution at 2 kOe from 1.8 K – 7 K and a THF (right) solution at 4 kOe from 1.8 K – 11 K.

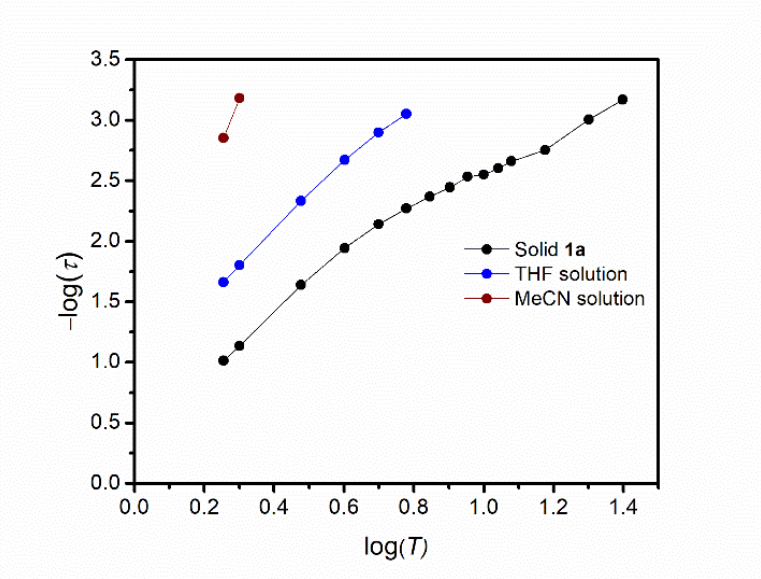

Figure 5.10 log-log plot of relaxation rates extracted from solutions of **1a** in MeCN (H_{dc} = 2 kOe) and THF (H_{DC} = 4 kOe) compared to the solid-state data presented in chapter 4.

Next, the magnetic relaxation of **1a** and **2** were measured in the glassy solvents 2-MeTHF and butyronitrile, Figure 5.11. We remind the reader that AC susceptibility measurements were obtained prior to DC susceptibility measurements, and the subsequent sample decomposition. Contrary to our expectations, both solutions do not show slow magnetic relaxation, unlike in their non-glassy analogues. Given the results from Yamashita's $[Co_{0.9}Ni_{0.1}(cyclam)Cl_2]ClO_4$ study and from Chapter 2,[18] it is like that the antiferromagnetic interactions seen in the DC susceptibility are preventing slow magnetic relaxation. However, it is also possible that the crystalline lattice of the non-glassy solvents is required for magnetic relaxation to be observable as the amorphous nature greatly affects the phonon lifetimes.

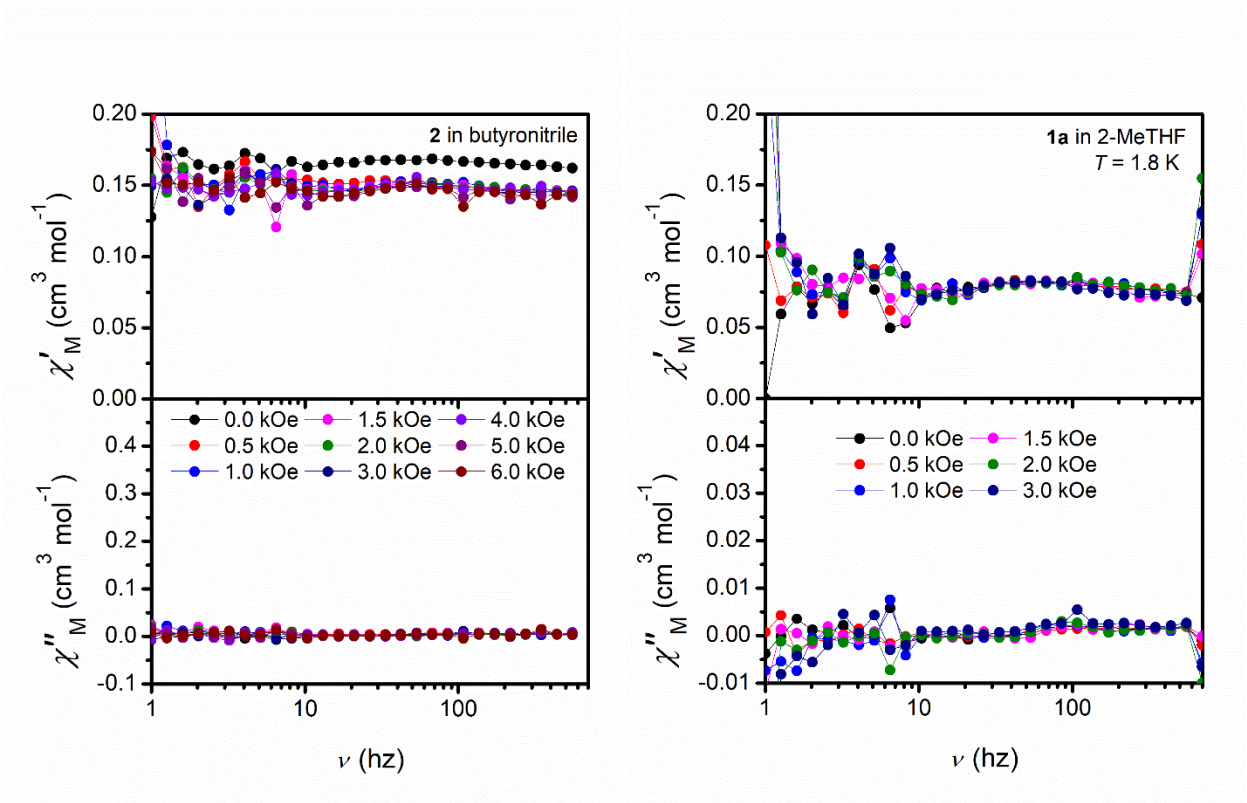

Figure 5.11 AC susceptibility of a butyronitrile solution of **2** at 1.8 K from 0 – 6 kOe (left) and of a 2-MeTHF solution at 1.8 K from 0 – 3 kOe (right).

For acidic aqueous solutions of **3**, considering the lack of significant anti-ferromagnetic interactions in the low-temperature DC susceptibility, we had hoped that the solution-phase would show slow magnetic relaxation, especially if the ligated chlorides were replaced by water molecules. Unfortunately, Figure 5.12 shows that the solution-phase AC susceptibility did not show any slow magnetic relaxation under any of the conditions measured.

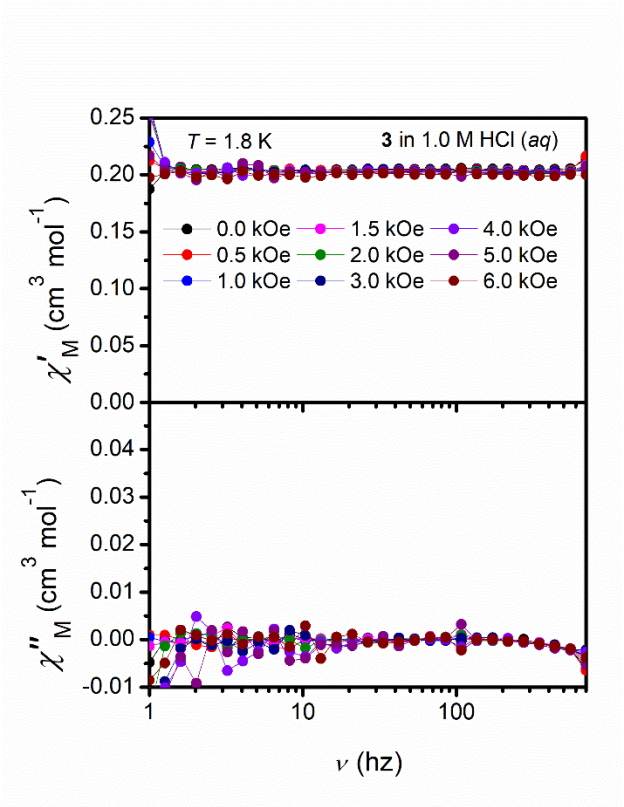

Figure 5.12 AC susceptibility of **3** in 1.0 M HCl (*aq*). Left: From 0.0 – 6.0 kOe at 1.8 K. Right: From 1.8 – 15 K at 2.0 kOe.

5.5 Conclusions

The solution-phase magnetic properties of **1a**, **2**, and **3** were investigated in a variety of solvents. Substitution of the ligated solvent molecules in **1a** was shown to be possible through the conversion to **2**, and the electronic absorption spectra of **1a** in different solvents showed significant differences in the *d-d* transition when in N-donating solvents (acetonitrile and butyronitrile) compared to O-donating solvents (MeOH, THF, 2-MeTHF, and $MeNO_2$). Furthermore, addition of NBu_4X salts to the acetonitrile solutions only showed small changes in the UV-Vis, suggesting no changes in the first coordination sphere, with the exception of NBu_4Cl, which precipitated the insoluble **3**, and NBu_4PF_6, where the *d-d* transition appeared as a shoulder and was shifted significantly more than expected. This showed that investigating the magnetic relaxation of

$[Ni(cyclam)X_2]^+$ species generated *in situ* is likely not viable, however exchanging the neutral ligated solvents for other neutral solvents is possible. Magnetic measurements of **1a** in the non-glassy solvents showed magnetic relaxation similar to the solid-state properties of solid **1a**, with a phonon-bottleneck effect-like relaxation mechanism apparent from the narrow window where the peak was visible. Unexpectedly, when the glassy solvents butyronitrile and 2-MeTHF were used no slow magnetic relaxation was observable. We propose that the PBE in the non-glassy solvents are due to the solute molecules aggregate during the freezing process, forming. In contrast, the glassy solvents show antiferromagnetic interactions that likely interfere with the magnetic relaxation. The glassy solutions also produce much more homogenous solutions with large distances between solute molecules, and the disordered nature of the glassy solvents scatter the phonons generated from the magnetic relaxation process before they can be reabsorbed by other, nearby magnetic units. It is unclear which reason, if either, is responsible for the lack of slow magnetic relaxation in the glassy solvents, however. This implies that the $[Ni(cyclam)L_2]^{3+}$ (L = BN, 2-MeTHF) molecular units might not show true *single molecule* slow magnetic relaxation but are a product of the extended material. However, it is also possible that the magnetic relaxation is simply outside the narrow region of detection of the instrument.

5.6 References

(1) Kogut, E.; Wiencko, H. L.; Zhang, L.; Cordeau, D. E.; Warren, T. H. A Terminal Ni(III)-Imide with Diverse Reactivity Pathways. *J. Am. Chem. Soc.* **2005**, *127* (32), 11248–11249. https://doi.org/10.1021/ja0533186.

(2) Aubin, S. M. J.; Wemple, M. W.; Adams, D. M.; Tsai, H. L.; Christou, G.; Hendrickson, D. N. Distorted $Mn(IV)Mn(III)_3$ Cubane Complexes as Single-Molecule Magnets. *J. Am. Chem. Soc.* **1996**, *118* (33), 7746–7754. https://doi.org/10.1021/ja960970f.

(3) Ishikawa, N.; Sugita, M.; Ishikawa, T.; Koshihara, S. Y.; Kaizu, Y. Lanthanide Double-

Decker Complexes Functioning as Magnets at the Single-Molecular Level. *J. Am. Chem. Soc.* **2003**, *125* (29), 8694–8695. https://doi.org/10.1021/ja029629n.

(4) Kittel, C. Interpretation of the Thermal Conductivity of Glasses. *Phys. Rev.* **1949**, *75* (6), 972–974. https://doi.org/10.1103/PhysRev.75.972.

(5) Graebner, J. E.; Golding, B. Phonon Echoes in a Glass at Low Temperatures. *Phys. Rev. B* **1979**, *19* (2), 964–975. https://doi.org/https://doi.org/10.1103/PhysRevB.19.964.

(6) Golding, B.; Graebner, J. E. Phonon Echoes in Glass. *Phys. Rev. Lett.* **1976**, *37* (13), 852–855. https://doi.org/https://doi.org/10.1103/PhysRevLett.37.852.

(7) Eckert, T.; Bartsch, E. Re-Entrant Glass Transition in a Colloid-Polymer Mixture with Depletion Attractions. *Phys. Rev. Lett.* **2002**, *89* (12), 20–23. https://doi.org/10.1103/PhysRevLett.89.125701.

(8) Bennemann, C.; Baschnagel, J.; Paul, W.; Binder, K. Molecular-Dynamics Simulation of a Glassy Polymer Melt: Rouse Model and Cage Effect. *Comput. Theor. Polym. Sci.* **1999**, *9* (3–4), 217–226. https://doi.org/10.1016/S1089-3156(99)00008-2.

(9) An, L.-Y.; Dai, Z.; Xu, L.-L. Advances in Cryochemistry: Mechanisms, Reactions, and Applications. *Molecules* **2021**, *26*, 750. https://doi.org/https://doi.org/10.3390/molecules26030750.

(10) Doliwa, B.; Heuer, A. Cage Effect, Local Anisotropies, and Dynamic Heterogeneities at the Glass Transition: A Computer Study of Hard Spheres. *Phys. Rev. Lett.* **1998**, *80* (22), 4915–4918. https://doi.org/10.1103/PhysRevLett.80.4915.

(11) Weeks, E. R.; Weitz, D. A. Subdiffusion and the Cage Effect Studied near the Colloidal Glass Transition. *Chem. Phys.* **2002**, *284* (1–2), 361–367. https://doi.org/10.1016/S0301-0104(02)00667-5.

(12) Haines, R. I.; Mcauley, A. Kinetics of the Reaction of the (1, 4, 8, 11-Tetraazacyclotetradecane)Diaquonickel(III) Cation with Halide and Thiocyanate Ions in Aqueous Perchlorate Media. *Inorg. Chem.* **1980**, *19* (3), 719–723. https://doi.org/10.1021/ic50205a027.

(13) Haines, R. I.; McAuley, A. Synthesis and Reactions of Nickel(III) Complexes. In *Coordination Chemistry Reviews,* **1981**, 39, pp 77–119. https://doi.org/10.1016/S0010-8545(00)80512-3.

(14) Shamir, D.; Zilbermann, I.; Maimon, E.; Shames, A. I.; Cohen, H.; Meyerstein, D. Anions as Stabilizing Ligands for Ni(III)(Cyclam) in Aqueous Solutions. *Inorganica Chim. Acta* **2010**, *363* (12), 2819–2823. https://doi.org/10.1016/j.ica.2010.03.057.

(15) Renge, I.; Mauring, K.; Avarmaa, R. Site-Selection Optical Spectra of Bacteriochlorophyll and Bacteriopheophytin in Frozen Solutions. *J. Lumin.* **1987**, *37* (4), 207–214. https://doi.org/10.1016/0022-2313(87)90161-X.

(16) Yip, H.; Cheng, L.; Cheung, K.; Che, C. Luminescent Platinum(II) Complexes. Electronic Spectroscopy of Platinum(II) Complexes of 2,2':6',2''-Terpyridine (Terpy) and p-Substituded Phenylterpyridines and Crystal Structure of [Pt(Terpy)Cl][CF_3SO_3]. *J. Chem.*

Soc., Dalt. Trans. **1993**, *2* (11), 2933–2938. https://doi.org/https://doi.org/10.1039/DT9930002933.

(17) Bain, G. A.; Berry, J. F. Diamagnetic Corrections and Pascal's Constants. *J. Chem. Educ.* **2008**, *85* (4), 532–536. https://doi.org/10.1021/ed085p532.

(18) Toshima, K.; Sato, T.; Horii, Y.; Sato, K.; Sugisaki, K.; Breedlove, B. K.; Takaishi, S.; Li, Z. Y.; Yamashita, M. Slow Magnetic Relaxation of Ni(III) Complexes toward Molecular Spin Qubits. *Eur. J. Inorg. Chem.* **2023**. https://doi.org/10.1002/ejic.202300125.

Chapter 6: Summary and Outlook of the Slow Magnetic Relaxation of $S = ½$ Ni(III)cyclams

Several novel Ni(III)cyclam systems have been synthesized and magnetically characterized in this dissertation. In Chapter 2, the role of nuclear spin of the ligated anions in the axial position in $[Ni(cyclam)X_2]^+$ systems was further investigated beyond the first reported Ni(III) SMM, $[Ni(cyclam)(NO_3)_2]X$ (X = NO_3^-, ClO_4^-), and the rapidly relaxing $[Ni(cyclam)(NCS)_2]ClO_4$.[1] The findings were that for the complexes with halide ligands Br^- and Cl^-, which have previously been shown to exhibit superhyperfine coupling to the Ni(III) electronic spin *via* EPR, slow magnetic relaxation was not observed, but the nearly nuclear-spin free ClO_4^- ligand very clearly showed slow magnetic relaxation, supporting the hypothesis that anions in axial position possessing nuclear spin speeds up magnetic relaxation. However, Yamashita's recent publication of the magnetic properties $[Co_{0.9}Ni_{0.1}(cyclam)Cl_2]ClO_4$ suggest that in the absence of antiferromagnetic interactions, the $[Ni(cyclam)Cl_2]^+$ core does show slow magnetic relaxation.[2] In Chapter 3, a novel HSO_4^- system was developed and allowed for the study of the deuterated isotopologue, which quenched the phonon bottleneck effect that was present in the protiated sample, suggesting the importance of the vibrational landscape of the system and phonon landscape to the magnetic relaxation.

In Chapter 4, a series of $[Ni(cyclam)(MeCN)_2]X$ (X = OTf^-, ClO_4^-, BF_4^-) and $[Ni(cyclam)(BN)_2]OTf_3$ (BN = butyronitrile) was investigated and found to possess slow magnetic relaxation, despite the presence of nuclear spin in the axial positions. This result shows that exchanging the anionic ligands for neutral ligands opens up a more comprehensive library of

potential Ni(III) SMMs than previously thought, which we attribute to the contraction of the d orbitals that result from the increased complex charge and reduce the superhyperfine coupling between the electronic and nuclear spins. Furthermore, the ClO_4^- and BF_4^- species are isostructural but show slightly different relaxation rates and magnetic relaxation behavior, demonstrating the importance of intermolecular interactions in the magnetic properties. In Chapter 5, we investigated the solution-phase properties of the triflate species, focusing on the role of glassy versus non-glassy solvents. The result was that the crystalline, non-glassy solvents MeCN and THF showed similar magnetic relaxation, albeit faster than what was observed in the solid state. In contrast, samples dissolved in the glassy solvents butyronitrile and 2-MeTHF did not show slow magnetic relaxation, which was attributed to a combination of the antiferromagnetic interactions seen in the DC susceptibility and the poor phonon propagation in the homogenous but disordered glassy solvents.

While there are potentially an infinite number of Ni(III)cyclam SMMs waiting to be discovered, particularly ones utilizing chalcogen-donating ligands such as *p*-toluenesulfonic acid, thioacetic acid, and trifluoroacetic acid, further spectroscopic studies into the magneto-vibrational properties of the systems may yield more information into where the barrier towards magnetic relaxation originates and guide a more targeted approach to interesting synthetic molecules. For example, should the vibrations of the N-H bonds play a role in magnetic relaxation, then substituting cyclam for tetramethyl cyclam may show interesting magnetic properties. Additionally, the pH sensitivity of the Ni(III) cyclams limits the scope of ligands able to be studied Magnetic field-dependent Raman and IR spectroscopy are experimentally viable in determining which vibrational modes are magnetically correlated.[3–5] These specific vibrational modes interact with the magnetic states, and by identifying critical motifs in these modes, we may be able to

synthetically target new ligands or functionalize the cyclam molecule, such as by affixing pendant R groups to the amines, that greatly extend the SMM figures of merit. However, as we have seen, molecular vibrations are only one part of the story, and one must take a holistic approach to consider the extended lattice effects and phonons to more thoroughly understand the magnetic relaxation of the materials, including the origin of the barrier. One method is to utilize neutron scattering techniques to determine the phonon dispersion diagram and investigate how it changes with the applied magnetic field. Because the phonons involved with magnetic relaxation are so low in energy but can be circumvented through two-phonon processes, understanding the complete phonon dispersion diagram, and investigating both acoustic and optical phonons, may be required. Ideally, calculations of the intra- and intermolecular vibrations and their interactions with the magnetic states will corroborate these spectroscopic experiments and further our understanding of spin-phonon interactions in superparamagnetic single molecule magnets.

6.1 References

(1) Bhowmick, I.; Roehl, A. J.; Neilson, J. R.; Rappé, A. K.; Shores, M. P. Slow Magnetic Relaxation in Octahedral Low-Spin Ni(III) Complexes. *Chem. Sci.* **2018**, *9* (31), 6564–6571. https://doi.org/10.1039/c7sc04482h.

(2) Toshima, K.; Sato, T.; Horii, Y.; Sato, K.; Sugisaki, K.; Breedlove, B. K.; Takaishi, S.; Li, Z. Y.; Yamashita, M. Slow Magnetic Relaxation of Ni(III) Complexes toward Molecular Spin Qubits. *Eur. J. Inorg. Chem.* **2023**. https://doi.org/10.1002/ejic.202300125.

(3) Moseley, D. H.; Stavretis, S. E.; Thirunavukkuarasu, K.; Ozerov, M.; Cheng, Y.; Daemen, L. L.; Ludwig, J.; Lu, Z.; Smirnov, D.; Brown, C. M.; Pandey, A.; Ramirez-Cuesta, A. J.; Lamb, A. C.; Atanasov, M.; Bill, E.; Neese, F.; Xue, Z. L. Spin-Phonon Couplings in Transition Metal Complexes with Slow Magnetic Relaxation. *Nat. Commun.* **2018**, *9* (1), 1–11. https://doi.org/10.1038/s41467-018-04896-0.

(4) Moseley, D. H.; Stavretis, S. E.; Zhu, Z.; Guo, M.; Brown, C. M.; Ozerov, M.; Cheng, Y.; Daemen, L. L.; Richardson, R.; Knight, G.; Thirunavukkuarasu, K.; Ramirez-Cuesta, A. J.; Tang, J.; Xue, Z. L. Inter-Kramers Transitions and Spin-Phonon Couplings in a

Lanthanide-Based Single-Molecule Magnet. *Inorg. Chem.* **2020**, *59* (7), 5218–5230. https://doi.org/10.1021/acs.inorgchem.0c00523.

(5) Toulouse, C.; Martin, C.; Measson, M. A.; Gallais, Y.; Sacuto, A.; Cazayous, M. Magnetic Transitions in $CaMn_7O_{12}$: Raman Observation of Spin-Phonon Couplings. *Phys. Rev. B* **2019**, *99* (2), 1–5. https://doi.org/10.1103/PhysRevB.99.024303.

Chapter 7: Tuning First Coordination Sphere Geometry Through Intra-molecular π- π Interactions

7.1 Introduction

Coordination geometry plays a pivotal role in the fundamental properties and reactivity of metal complexes. Traditionally, the tuning of coordination sphere geometry has been achieved through modifications of the ligand structure and coordination number.[1] However, recent research results have suggested that intramolecular π-π interactions can serve as a powerful and versatile tool for modulating the first coordination sphere geometry.[2] Intramolecular π-π interactions involve noncovalent interactions between aromatic or conjugated moieties within a ligand. These interactions are known for their ability to influence molecular conformation, electronic structure, and intermolecular associations.[1] By utilizing the influence of intramolecular π-π interactions, we aim to expand the toolbox available for fine-tuning the coordination chemistry, and through the precise manipulation of the first coordination sphere geometry *via* intramolecular π-π interactions, it becomes possible to design and optimize metal complexes with enhanced properties and tailored reactivity.

The original aim of this study focused on searching for Fe(II) hexadentate complexes that underwent spin crossover, SCO, where a change in temperature results in a change from high spin to low spin. The tris(2-aminoethyl)amine (tren)-based iminopyridine ligands were targeted as they might allow for SCO after tuning the electronic structure of the ligand through substituent effects. Unfortunately, all of the complexes measured were low spin at all temperatures. However, one structure with pendant thiophenols showed intraligand π-π stacking between the three arms of the ligand. From this I postulated that by modulating the π-π strength I could torque the ligand, and

therefore the metal center geometry. Because π-π interactions are so prevalent in nature, much research has been devoted into better understanding what affects these interactions, including heteroatom substitution, substituent effects, aromaticity, and the number of fused rings.[1,3–5] Using these principles I sought to design a series of modular complexes that would allow for the fine tuning of the coordination geometry and the resulting properties. Herein I report the synthesis and characterization of $[Ni(tren(PySPh\text{-}H)_3)](BF_4)_2$ (**SPh-H**) and its Co analogue $[Co(tren(PySPh\text{-}H)_3)](BF_4)_2$ (**CoSPh-H**), $[Ni(tren(PySPh\text{-}Me)_3)](BF_4)_2$ (**SPh-Me**), $[Ni(tren(PySPh\text{-}OMe)_3)](BF_4)_2$ (**SPh-OMe**), and $[Ni(tren(PySNaph)_3)](BF_4)_2$ (**SNaph**), all of which were able to be studied crystallographically. Furthermore, the sulfoxide and sulfone complexes $[Ni(tren(PySOPh)_3)](BF_4)_2$ (**SOPh**), $[Ni(tren(PySONaph)_3)](BF_4)_2$ (**SONaph**), and $[Ni(tren(PySO_2Ph\text{-}H)_3)](BF_4)_2$ (**SO_2Ph**) were also synthesized, but unable to be studied crystallographically.

7.2 Division of Labor

The original synthesis of the parent ligand was developed by Dr. Tarik Ozumerzifon, and adapted to the other ligands by Tom Morrison. Sam DalCais assisted in synthesizing the parent NiSPh-H complexes, and all other materials were synthesized by Tom Morrison. Morrison was also responsible for all measurements and structures reported herein. We thank the ARC staff for their assistance with the collection of crystallographic and magnetic data.

7.3 Experimental

7.3.1 Preparation of compounds. Unless noted otherwise, all manipulations were performed in air. The synthesis of all ligands followed the same general synthetic procedures,

detailed in Schemes 7.1-7.3. The starting material 5-bromo-2-(1,3-dioxolan-2-yl)pyridine was added to a flame-dried round bottom flask and charged with 1,4-dioxane. The flask was capped, and the solution was then sparged with N_2 gas for 30 minutes, after which $Pd_2(dba)_3$ (dba = dibenzylideneacetone), xantphos, and *i*-Pr_2NEt were added to the solution. A flame-dried condenser was then added to the apparatus and the headspace was replaced with N_2 gas, followed by the quick addition of the volatile thiols. The reaction mixture was then refluxed for 16 – 40 h, after which TLC analysis indicated complete consumption of the starting material. The reaction mixture was then filtered through Celite, concentrated by rotary evaporation, and purified *via* flash column chromatography (3:1 Hexanes:EtOAc eluent) to yield the purified thioether acetals.

Scheme 7.1 General synthetic procedure for producing thiophenol acetals.

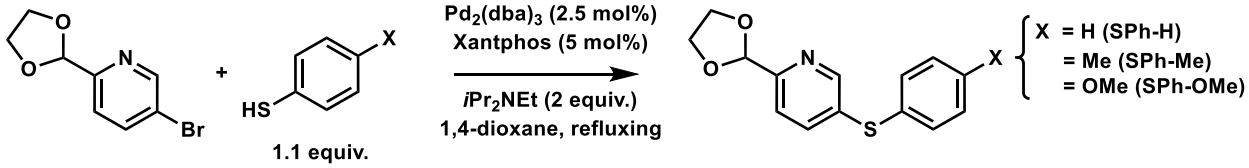

A portion of the purified thioethers were then oxidized through the dropwise addition of a solution of *m*PBCA in CH_2Cl_2 to cold (0 °C) CH_2Cl_2 solutions of the thioethers, using 1.1 and 2.2 equivalents of oxidant to form the sulfoxide and sulfone, respectively. While the oxidation of the parent thiophenol and thionaphthalene was successful, oxidation of the X = Me and OMe thiophenols were unsuccessful.

Next, the acetal was removed through by refluxing in a 4:1 MeCN:H_2O solution containing pyridinium p-toluenesulfonate (PPTS) for 16 hours. The resulting solution was then basified with saturated $NaHCO_3$, extracted with EtOAc, washed with brine, dried over $MgSO_4$, filtered, and purified through flash column chromatography with a 3:1 Hexanes:EtOAc eluent when necessary.

The resulting aldehydes were then condensed with tris(2-aminoethyl)amine (tren) by refluxing the reagents in dry acetonitrile. The solutions were then dried over $MgSO_4$, filtered, and then dried *in vacuo* to form the target ligands.

Scheme 7.2 General synthetic procedure for the oxidation of thioethers to sulfoxides and sulfones

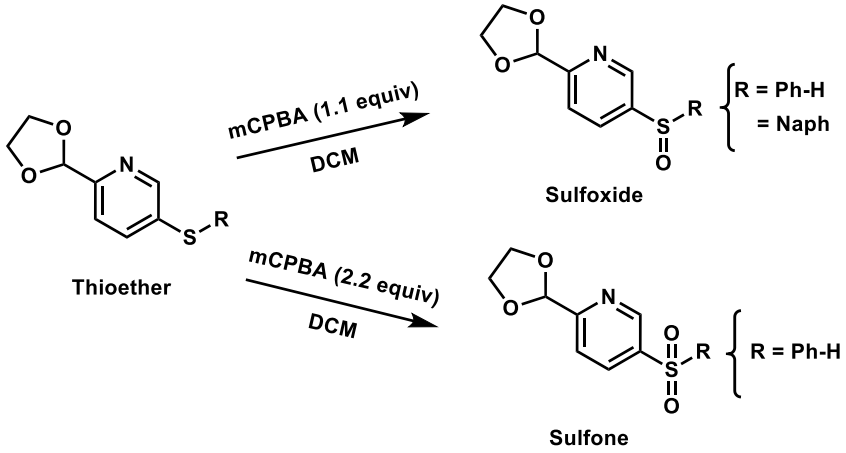

Scheme 7.3 Generate synthetic procedure for the deprotection of thio-acetals and condensation with tren to produce the target ligands.

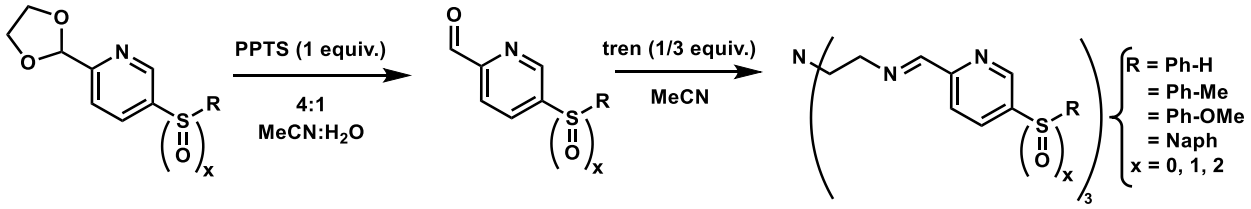

The ligands were then complexed with $Ni(BF_4)_2 \cdot 6\ H_2O$ by dissolving the starting materials in acetonitrile and refluxing for 1 hour. The solutions were then concentrated *in vacuo* and X-ray quality single crystals were obtained by the vapor diffusion of Et_2O into the concentrated acetonitrile solutions, forming $[Ni(tren(PySPh\text{-}H)_3](BF_4)_2$ (**SPh-H**), $[Ni(tren(PySPh\text{-}Me)_3](BF_4)_2$ (**SPh-Me**), $[Ni(tren(PySPh\text{-}OMe)_3](BF_4)_2$ (**SPh-OMe**), and $[Ni(tren(PySNaph)_3](BF_4)_2$ (**SNaph**). Crystallization of the sulfoxone and sulfoxide complexes **SOPh, SO_2Ph**, and **SONaph** were unsuccessful, producing amorphous solids and oils that did not diffract. Unfortunately, the

remaining sulfoxides and sulfones could not be synthesized. The complex [Co(tren(PySPh-H)$_3$](BF$_4$)$_2$ (**CoSPh-H**) was synthesized in an analogous way to the Ni analogue. Hereafter, unless otherwise specified, all spectra reported are for the Ni complexes.

7.3.2 X-ray structure determinations. Crystals suitable for single-crystal x-ray analysis were coated with Paratone-N oil and supported on a Cryoloop before being mounted on a Bruker Kappa Apex II CCD diffractometer under a stream of N_2 gas. Data collections were performed at low temperature (100 K - 170 K, see Table 7.1) using a Siemens KFF Mo_2K-90 sealed tube (Mo Kα, λ = 0.71073 Å) x-ray source and a curved graphite monochromator, targeting complete coverage and 4-fold redundancy. Crystallographic data and metric parameters are presented in Table 7.1. Determination of unit cell parameters through refinement, data collection, reduction, and correction for Lorentz and polarization effects was performed using the SAINT software package.[6] Data were sorted, scaled, averaged, and corrected for semiempirical absorption effects with SADABS.[7] The structures were solved with the ShelXT structure solution program and refined with the ShelXL-2018/3 refinement package.[8] Unless otherwise noted, thermal parameters for all non-hydrogen atoms were refined anisotropically. **SNaph** was refined isotropically and as a two-component twin due to poor resolution. Hydrogen atoms were added at calculated positions and were refined using a riding model.

4.3.3 Magnetic measurements. Magnetic susceptibility data were collected using a Quantum Design MPMS3 SQUID magnetometer. The powdered samples were loaded into polyethylene bags and sealed, then the bags were inserted into drinking straws and inserted into the instrument. Ferromagnetic impurities were checked through a variable field analysis (0 to 10 kOe) of the magnetization at 100 K: overall linearity in the collected data for all compounds indicated the lack of significant ferromagnetic impurities. Static (DC) magnetic susceptibility data were collected at

temperatures ranging from 2 K to 300 K at 1 kOe. Alternating current (AC) magnetic susceptibility measurements were performed from 1 Hz to 1000 Hz and at 1.8 K with an alternating field of 4 Oe. Data were corrected for the magnetization of the sample holder by subtracting the susceptibility of an empty container, and for the diamagnetic contributions of the sample by using Pascal's constants.[9]

7.3.4 Other physical characterizations. ^{1}H NMR spectra were obtained on a Bruker Ascend 400 MHz spectrometer and are reported relative to $SiMe_4$ (δ 0.00). All NMR reported were taken in $CDCl_3$. Electronic absorption spectra were obtained using quartz cuvettes in an Agilent 8453 spectrometer. Infrared spectra were obtained using a Bruker Tensor II FT-IR spectrometer. Electrochemical experiments were performed in 0.1 M NBu_4PF_6 MeCN solutions. All voltammograms were recorded on a Gamry Instruments Reference 600 potentiostat using a 0.785 mm^2 glassy carbon working electrode, a silver wire pseudo-reference electrode, and a platinum wire counter electrode. Scans were measured at 100 mV/s and all potentials are reported versus the ferrocene/ferrocenium redox couple, which was measured by adding a small amount of ferrocene on the last scan of the experiment as an internal standard.

7.4 Results and Discussions

7.4.1 X-ray Crystallography. X-ray quality single-crystals of **SPh-H, SPh-Me, SPh-OMe,** and **SNaph** were able to be grown by vapor diffusion of Et_2O into acetonitrile solutions of the complexes. Many of the resulting crystals were amorphous, weakly diffracting, or significantly twinned, resulting in poor quality crystallographic data. **SNaph** was particularly weakly diffracting and was only able to be solved using isotropic parameters. The crystal structures of each structure are shown in Figure 7.1 and 7.2. Each structure shows two BF_4^- ions per metal center, supporting

the Ni(II) oxidation state, and all three thioether pendants of each structure π-stack with the pyridine ring of an adjacent arm, forming helical structures.

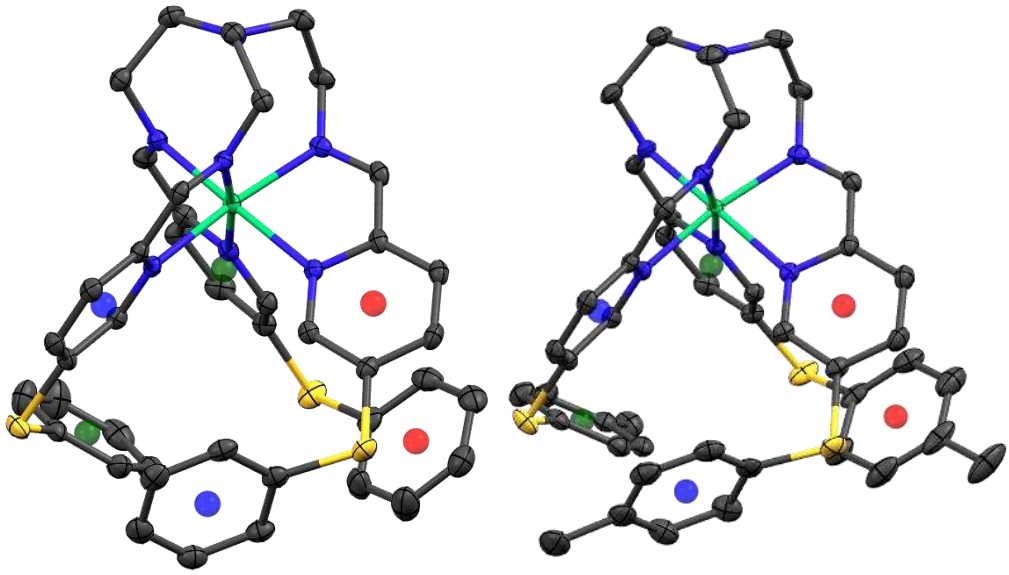

Figure 7.1 Crystal structures of **SPh-H** (left) **SPh-Me** (right) rendered with 50% thermal ellipsoids. Green, blue, yellow, and gray ellipsoids represent Ni, N, S, and C atoms, respectively. Counter ions and H atoms not involved in hydrogen bonding are omitted for clarity. Blue, red, and green translucent spheres represent centroids of aromatic systems, pairs matched by color.

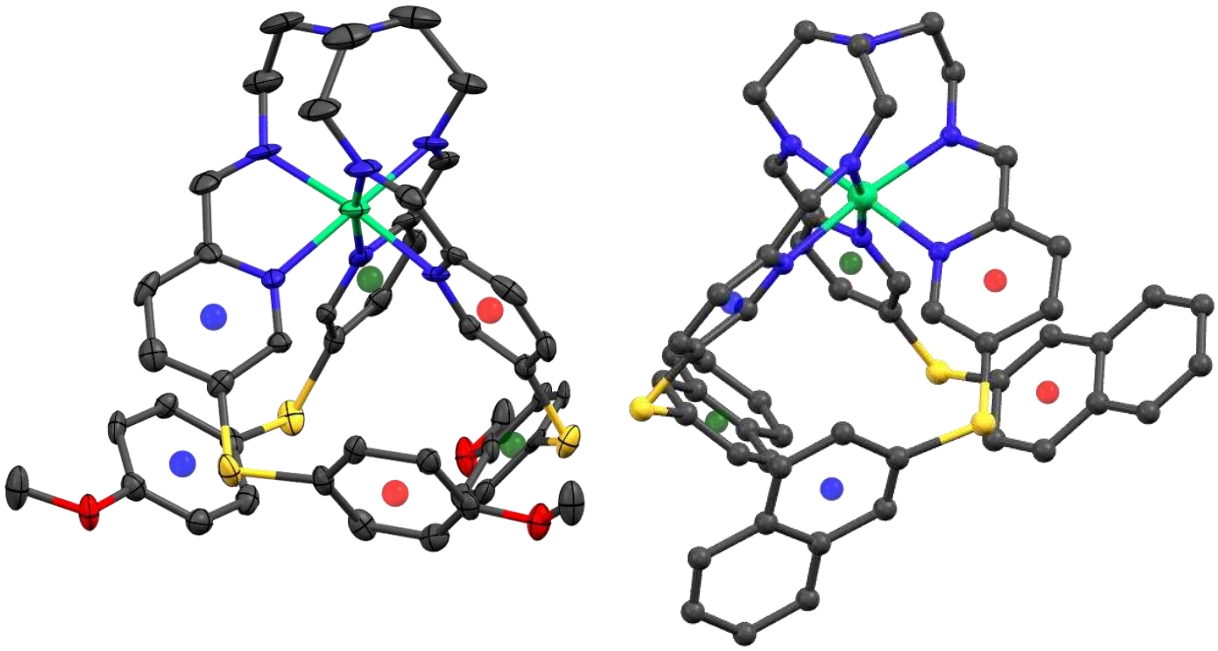

Figure 7.2 Crystal structures of **SPh-OMe** (left) **SNaph** (right) rendered with 50% thermal ellipsoids. Green, red, blue, yellow, and gray ellipsoids represent Ni, O, N, S, and C atoms, respectively. H atoms not involved in hydrogen bonding are omitted for clarity. Blue, red, and green translucent spheres represent centroids of aromatic systems, pairs matched by color.

The π-stacking for each structure can be seen in Figure 7.3 and shows that the angle between the two aromatic systems remains mostly constant, but the distances between the centroids varies. The parent **SPh-H** complex has the longest centroid π- π centroid distance, followed by **SPh-Me**, then **SPh-OMe**, and **SNaph** has the shortest distance. Predictions of the π-π interactions depend on several factors, including aromaticity, heteroatom substitution, substituent identity, and the relative orientation of the π-systems.[3,5,10,11] This makes these intra-ligand π- π interactions complicated, as they possess different substituents, heteroatom substitutions, and the sulfides connects the aromatic pyridine with the pendent benzene and naphthalene, changing the aromaticity of the system. Fortunately, the differences between the systems are limited to the substituents in the phenyls and the aromaticity between phenyl and naphthalene. Research has shown that the

Table 7.1 Crystallographic parameters for **SPh-H**, **SPh-Me**, **SPh-OMe**, and **SNaph**.

	SPh-H	**SPh-Me**	**SPh-OMe**	**SNaph**
formula	$C_{42}H_{39}B_2F_8N_7NiS_3$	$C_{49}H_{53}B_2F_8N_8NiO_{0.50}S_3$	$C_{96}H_{99}B_4F_{16}N_{17}Ni_2O_6S_6$	$C_{54}H_{44}B_2F_8N_7NiS_3$
fw (g/mol)	970.31	1090.50	2243.94	1119.97
Color, habit	Orange blocks	Orange blocks	Orange blocks	Orange blocks
T, K	100(2)	100(2)	100(2)	101(2)
Space group	$P\bar{1}$	*C*2/*c*	$R\bar{3}$	$P2_1$
Z	2	8	6	4
a, Å	10.6638(5)	22.4958(9)	14.2336(9)	17.0811(17)
b, Å	11.8194(5)	12.3486(5)	14.2336(9)	14.4899(15)
c, Å	18.5676(8)	37.4532(15)	90.482(9)	21.188(2)
α, deg	79.366(2)	90	90	90
β, deg	87.576(2)	96.028(2)	90	103.266(6)
γ, deg	68.8230(10)	90	120	90
V, Å^3	2143.98(17)	10346.7(7)	15875(3)	5104.3(9)
d_{calc}, g/cm^3	1.503	1.400	1.408	1.457
GOF	1.102	1.134	0.912	1.041
R_1[a] (wR_2[b]), %	5.07 (12.39)	5.32 (12.98)	6.49 (14.64)	12.27 (28.90)
R_1[a] (wR_2[b]), % all data	6.94 (14.53)	6.04 (12.98)	14.75 (17.43)	16.95 (33.30)

(a) $R_1 = \Sigma||F_o| - |F_c||/ \Sigma |F_o|$

(b) $wR_2 = [\Sigma [w(F_o^2-F_c^2)^2]/ \Sigma [w(F_o^2)^2]]^{½}$, $w = 1/[s^2(F_o^2) + (aP)^2 + bP]$, where $P = [\max(F_o^2 \text{ or } 0) + 2(F_c^2)]/3$

multiple substituents on the pyridine are unlikely to cause issues in the comparisons as substituent effects are predicted to affect the system independently, so long as they are not in close proximity.[3,12] A study by Wheeler showed that substituent effect on the interaction are correlated with the Hammet parameter σ_m, and that substituents with $0 > \sigma_m$, such as -Me ($\sigma_m = -0.069$), have stronger interactions than substituents with $0 < \sigma_m$, such as -OMe ($\sigma_m = +0.115$).[12] However, that same study found that *both* substituents are more stabilizing than the parent -H. This trend is then consistent with the crystallography of **SPh-H**, **SPh-Me**, and **SPh-OMe**. Another study by Wheeler

showed that polyaromatic hydrocarbons, like naphthalene, enhance π-π interactions due to the increased overlap of the π-systems, which is consistent with the crystal structure of **SNaph**.[13]

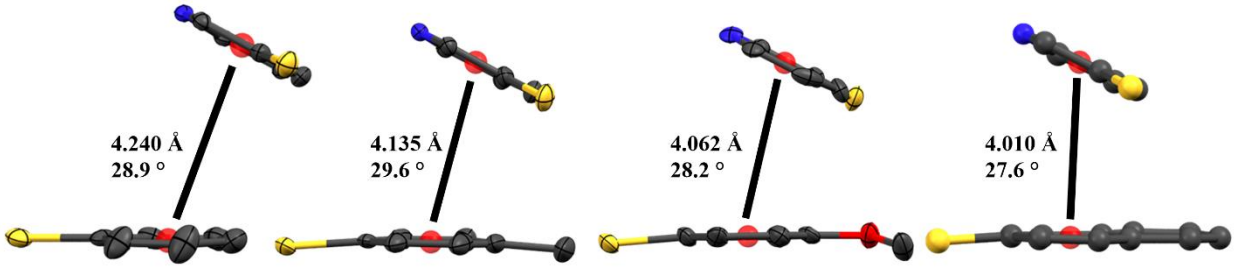

Figure 7.3 π-π stacking of **SPh-H**, **SPh-Me**, **SPh-OMe**, and **SNaph**. °

7.4.2 Electronic absorbance. The electronic absorbance spectra of **SPh-H**, **SPh-Me**, **SPh-OMe**, and **SNaph** were taken in acetonitrile in order to investigate the d-d transition and therefore the *Dq* value, representing the ligand field strength. As a d^8 system with approximately octahedral splitting, there are three spin allowed transitions for these complexes, $^3T_{2g} \leftarrow {}^3A_{2g}$ (F, ν_1), $^3T_{1g} \leftarrow {}^3A_{2g}$ (F, ν_2), and $^3T_{1g} \leftarrow {}^3A_{2g}$ (P, ν_3). Of these, the lowest energy transition, ν_1, is equal to the 10*Dq* value, making the analysis simple. Figure 7.4. shows the electronic absorbance of the aforementioned complexes, and from the d-d transitions centered at *ca.* 880 nm we can see that the *Dq* values increase from **SPh-H**, **SPh-Me**, **SPh-OMe**, to **SNaph**. The electronic absorbance of the oxidized complexes **SOPh-H**, **SO_2Ph-H**, and **SONaph** show an increased *Dq* value for the sulfoxides compared to their parent species, but the sulfone **SO_2Ph-H** did not show any d-d transitions, even when the solution was concentrated. Above 1000 nm, close to the edge of the detection limit for the instrument, a very broad peak begins to emerge which may be the d-d transitions, and if so would represent a very substantial decrease in *Dq*.

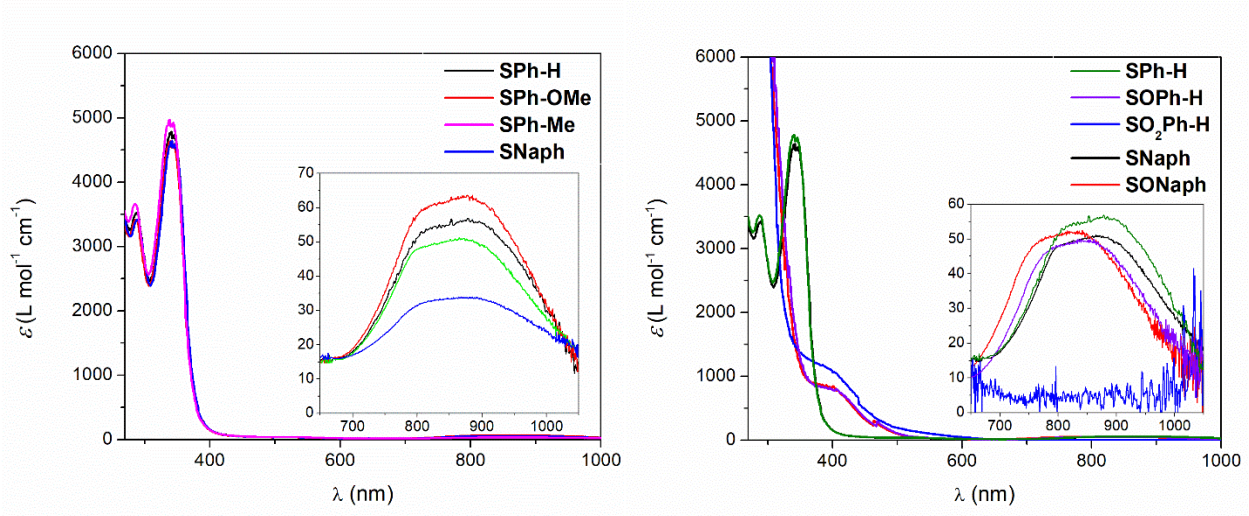

Figure 7.4 Left: Electronic absorption spectra of **SPh-H**, **SPh-Me**, **SPh-OMe**, and **SNaph** in acetonitrile. Right: Electronic absorption spectra of **SOPh-H**, **SO_2Ph-H**, and **SONaph**, compared to their parent species.

7.4.3 Geometry calculations. In order to accurately determine the structures' first coordination sphere geometry the program Shape was used. Shape uses the coordinates of the first coordination sphere and compares the angular distortional distance between the structure and a reference polyhedral, providing a quantitative assessment of the metal center's coordination. These calculations yield the Shape scores S_{Oh} and S_{Trp}, the likeness of the structure to an octahedral and a trigonal prismatic polyhedral, respectively, where $S = 0.000$ would be a perfect polyhedral. The Shape scores for the complexes are shown in Table 7.2. Comparing the S_{Oh} to the π- π distance we can see that by increasing the π-π stacking strength (and decreasing the distances between the systems) we are able to distort the geometry away from octahedral and towards trigonal prismatic. Furthermore, this is also reflected in the *Dq* values obtained from the d-d transitions in the electronic absorption spectra. These relationships can be seen in Figure 7.5 and are approximately linear. Comparing the π-π distance to the average M-L distance, Figure 7.6, shows that there are essentially two pairs of points. **SPh-H** and **SPh-Me** both have similar 1st coordination sphere

distances, at approximately 2.095 Å, while **SPh-OMe** and **SNaph** are at 2.080 Å. In general, the shorter π-π distances seem to result in shorter M-L distances and greater distortion away from an octahedral geometry, although the changes are minor. However, in the context of the original premise, Fe(II) SCO, these minor changes may be the tipping point and introduce SCO to the family of complexes and require further investigation.

Table 7.2 Select crystallographic values and Shape scores of complexes.

	SPh-H	**SPh-Me**	**SPh-OMe**	**SNaph**
π-π distance (Å)	4.240	4.135	4.062	4.010
Ni – N distance (Å)	2.096	2.095	2.079	2.081
Dq (cm^{-1})	1111	1136	1140	1156
S_{Oh}	0.975	1.048	1.039	1.246
S_{Trp}	15.922	15.571	15.215	14.199

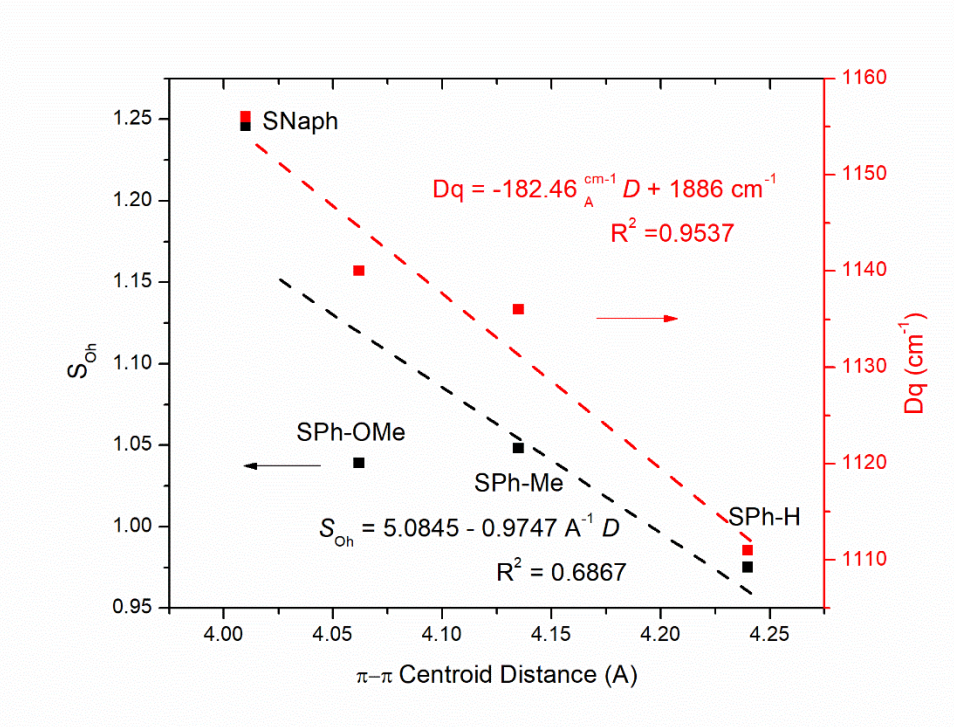

Figure 7.5 Correlation plot of centroid distance, octahedral Shape score S_{Oh}, and *Dq*.

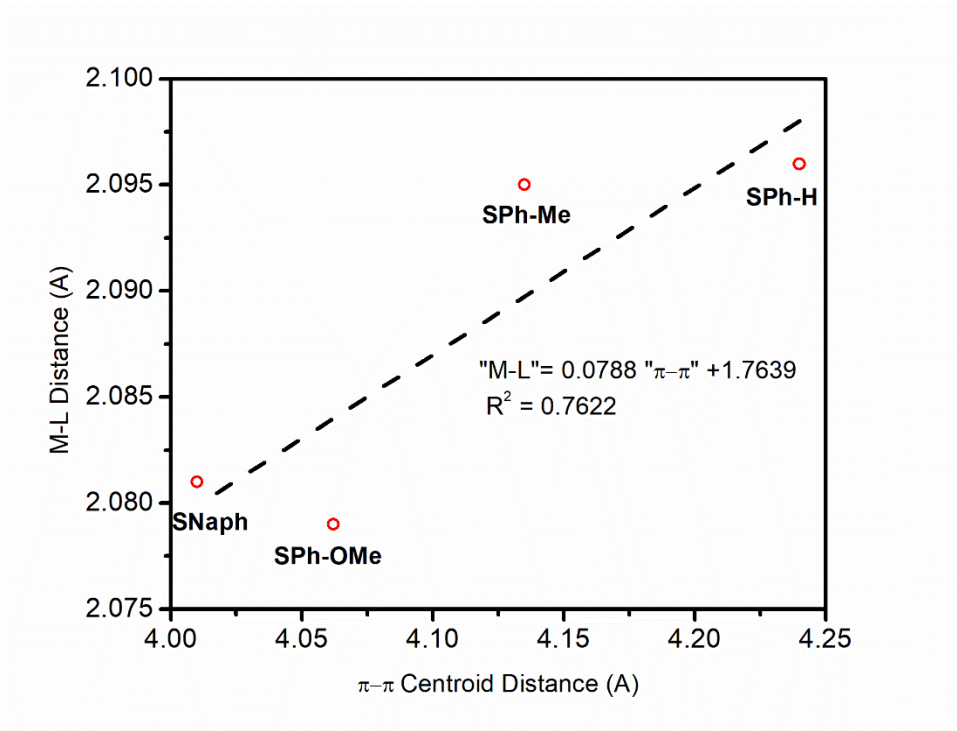

Figure 7.6 Correlation plot of centroid distance and M-L distances.

7.4.4 Electrochemistry. In order to determine the complexes ability to support the Ni(III) oxidation state, cyclic and square wave voltammograms of **SPh-H** were measured, Figure 7.7. Unfortunately, the oxidation to Ni(III) was irreversible in the square-wave voltammogram, suggesting that a ligand transformation occurred. Given Ni(III)'s rarity and propensity to be involved in ligand-noninnocence, it is likely that the oxidation formed a ligand-stabilized radical instead. Attempts to electrochemically synthesize and isolate this "Ni(III)" species proved unsuccessful. Chemical oxidation of the species also proved unsuccessful. The electrochemical properties of the other complexes were assumed to be similar and were not investigated.

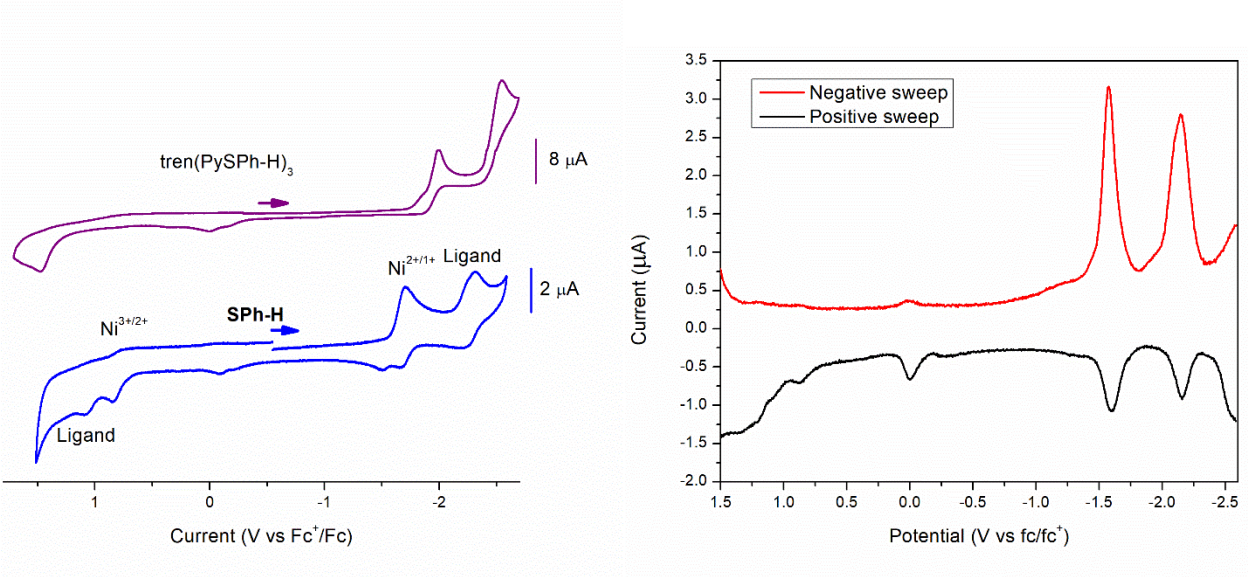

Figure 7.7 Left: Cyclic voltammogram of metalated **SPh-H** and the unmetalated ligand, tren(PySPh-H)$_3$. Right: Square wave voltammogram of **SPh-H.** Measurements in a 0.1 M NBu_4BF_4 acetonitrile solution. Potentials referenced using a fc/fc$^+$ internal standard. A glassy carbon working electrode, platinum wire counter electrode, and a silver wire refence electrode were used.

7.4.5 Cobalt Magnetism. As a result of the Ni(III) oxidation state being inaccessible, a Co(II) analogue of **SPh-H**, **CoSPh** was synthesized and measured. The Co(II) oxidation state is frequently encountered in research on single molecule magnets (SMMs), to the point that it is almost ubiquitous with 3d transition metal SMMs. Therefore, we investigated the magnetic properties of **CoSPh**. The $\chi_M T$ versus T plot (Figure 7.8) of **CoSPh** shows that the complex ground spin state is $S = 3/2$, consistent with the Co(II) oxidation state. The M vs H plot at 100 K is linear, indicating a lack of ferromagnetic impurities that might interfere with the AC measurements. At 300 K and an applied field of 1 kOe, **CoSPh** has a $\chi_M T$ value of 2.21 cm^3 K mol^{-1} and stays constant as the temperature decreases until 15 K, where the susceptibility decreases before reaching a minimum of 1.58 cm^3 K mol^{-1} at 2 K. A fit of the data yields a g value of 2.17 and a zero-field splitting, D, of +2.00 cm^{-1}, although the sign of D is unreliably determined from susceptibility data

alone. The AC susceptibility was also investigated at 1.8 K from 0 – 6 kOe, Figure 7.9, but no frequency dependence was found, and thus magnetic relaxation was not slow under the conditions applied.

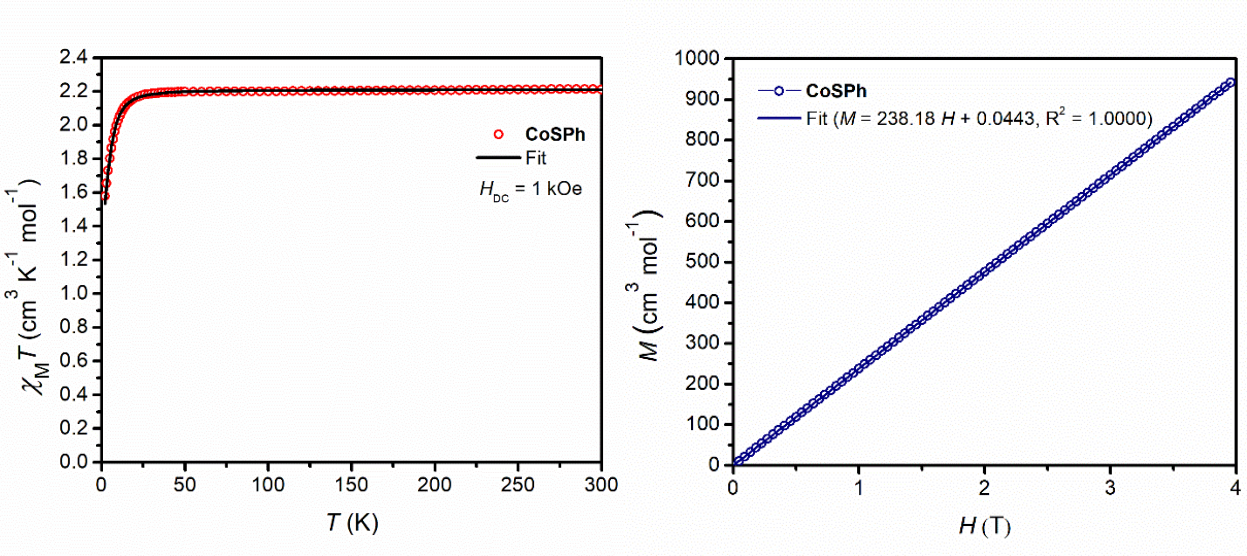

Figure 7.8 Left: Temperature dependence of DC susceptibility of **CoSPh** from 2 – 300 K with H_{DC} = 1 kOe. Right: Field dependence of magnetization from 0 – 4 T at 100 K. Linearity in the plot demonstrates the lack of ferromagnetic impurities.

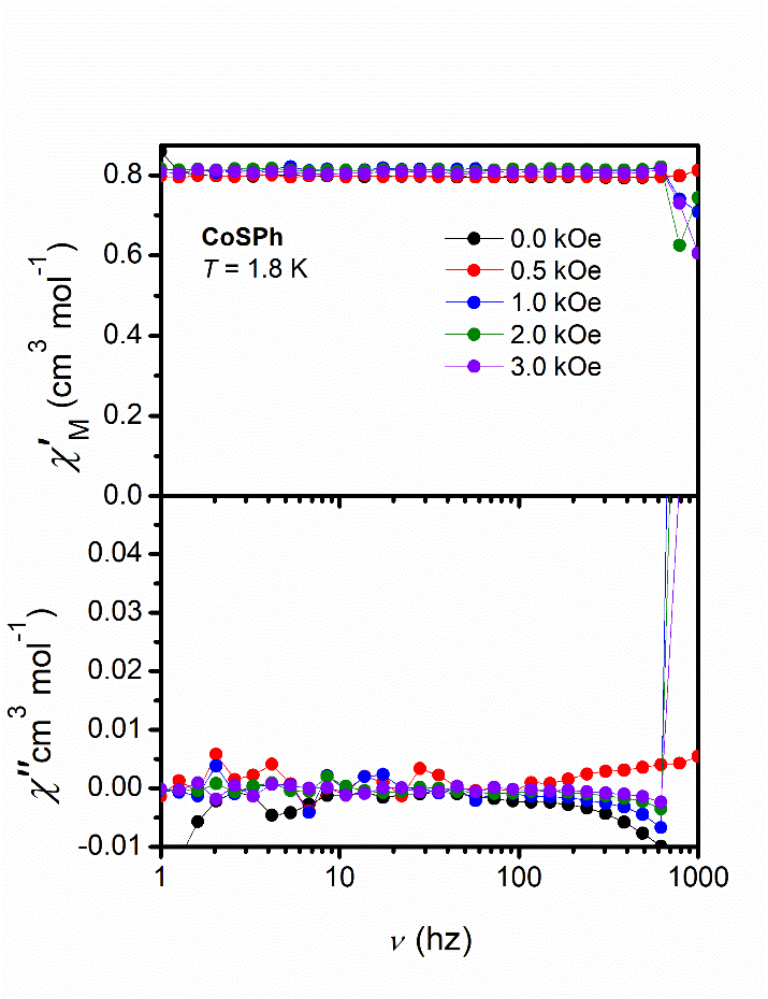

Figure 7.9 AC susceptibility of **CoSPh** at 1.8 K from 0 – 3 kOe.

7.5 Conclusions

In summary, six Ni(II) complexes with intra-ligand π-π stacking were synthesized and characterized. Of the six complexes, crystallographic data was able to be obtained for only the four sulfide species **SPh-H**, **SPh-Me**, **SPh-OMe**, and **SNaph**. The sulfoxide species **SOPh-H** and **SONaph**, and the sulfone species **SO_2Ph** were unable to be crystallized, allowing only for electronic absorption data to be collected. Intra-ligand π-π stacking strength, as determined by the centroid distance of the π-systems, was found to be strongly correlated with the distortion away from octahedral, S_{Oh}, and with the resulting ligand field strength, *Dq*. The strength of the π-π

stacking was consistent with the trends seen from *ab initio* calculations performed for other systems, and the stronger π-π stacking resulted in distorting the structure towards trigonal prismatic. Electronic absorption experiments showed that the structures with greater π-π strength showed an increase in ligand field strength. Extrapolating from this, the sulfoxides, which could not be crystallized, would show the greatest amount of distortion and strongest π-π stacking. While the synthesis of the ligands is lengthy and non-trivial, cumulatively taking several days and rounds of purification, once synthesized this family of complexes might prove to be a good candidate for exercising fine control over the geometry of the metal center, inducing SCO in Fe(II) complexes, and in studying π-π interactions.

7.6 Individual Syntheses.

All syntheses presented here follow the generalized procedure outlined above unless otherwise specified. All solvents were dried and degassed prior to use, with the exception of Millipore water. All products purified as described above. PPTS = pyridinium *p*-tolunesulfonate.

2-(1,3-dioxolan-2-yl)-5-(phenylthio)pyridine. 2.09763 mg of 5-bromo-2-(1,3-dioxolan-2-yl)pyridine was added to a 50 mL round bottom flask with 1 mL *i*-Pr_2EtN, 203.43 mg $Pd_2(dba)_3$, 261.73 mg xantphos, 1.78 mL benzenethiol, and 25 mL 1,4-dioxane and refluxed under N_2 for 16 hours. 30% yield. ^1H NMR in $CDCl_3$: 4.02, m; 5.76, s; 7.11, m; 7.22, m; 7.78, d; 8.62, s.

5-(phenylthio)picolinaldehyde. 450 mg 2-(1,3-dioxolan-2-yl)-5-(phenylthio)pyridine was added to a 50 mL round bottom flask with 43.55 mg PPTS, 9 mL MeCN, and 2.5 mL water and refluxed for 24 hours. 50% yield. ^1H NMR in $CDCl_3$: 7.43, m; 7.46, m; 7.70, d; 8.43, s; 9.91, s.

tren(PySPh-H)$_3$. 353.4 mg 5-(phenylthio)picolinaldehyde was added to a 50 mL round bottom flask with 81.56 mg tren and refluxed for 24 hours. 95% yield. ^{1}H NMR in $CDCl_3$: 2.98, t; 3.37, t; 7.37, d; 7.45, d; 7.54, d; 7.80, d; 8.28, s; 8.47, s.

SPh-H. 33.38 mg tren(PySPh-H)$_3$ was added to a 5 mL solution of 14.05 mg $Ni(BF_4)_2$ $6H_2O$ in MeCN and stirred for 24 hours. 93% yield.

CoSPh-H. In a glovebox with a N_2 atmosphere anhydrous $Co(BF_4)_2$ (9.98 mg) was added to a 5 mL solution of tren(PySPh-H)$_3$ (31.60 mg) in acetonitrile in a 20 mL scintillation vial and stirred for 24 hours. Et_2O was added to the solution and a red-orange precipitate formed, which was washed 3 x 5 mL with 2:1 Et_2O:MeCN and dried *in vacuo*.

2-(1,3-dioxolan-2-yl)-5-(phenylsulfinyl)pyridine. 188.25 mg 2-(1,3-dioxolan-2-yl)-5-(phenylthio)pyridine was dissolved in 10 mL CH_2Cl_2 in a 25 mL round bottom flask and placed into an ice bath. *m*CPBA (172.88 mg, 81.2%) was also dissolved into a separate 10 mL CH_2Cl_2 solution and then added dropwise *via* addition funnel. 91% yield. ^{1}H NMR in $CDCl_3$: 4.06, m; 5.81, s; 7.46, t; 7.62, d; 7.90, d; 8.20, d.

5-(phenylsulfinyl)picolinaldehyde. 165.40 mg 2-(1,3-dioxolan-2-yl)-5-(phenylsulfinyl)pyridine was added to a 25 mL round bottom flask with 21.32 mg PPTS, 8 mL MeCN, and 2 mL water, and refluxed for 18 hours. 43% yield. ^{1}H NMR in $CDCl_3$: 7.46, s; 7.63, s; 7.96, d; 8.10, d; 8.87, s; 10.01, s.

Tren(PySOPh)$_3$. 40.76 mg 5-(phenylsulfinyl)picolinaldehyde was added to a 20 mL scintillation vial with 8.76 μL tren and stirred for 16 hours in 10 mL MeCN. 87% yield. ^{1}H NMR in $CDCl_3$: 2.46, t; 2.69, t; 5.80, s; 7.46, d; 7.54, d; 7.61, d; 7.87, d; 8.19, d; 9.04, s.

SOPh. 31.75 mg tren(PySOPh)$_3$ was dissolved in 10 mL MeCN with 14.11 mg mg Ni(BF$_4$)$_2$ 6H$_2$O and refluxed for 24 hours. 83% yield.

2-(1,3-dioxolan-2-yl)-5-(phenylsulfonyl)pyridine. 412.06 mg 2-(1,3-dioxolan-2-yl)-5-(phenylthio)pyridine was dissolved in 15 mL CH_2Cl_2 in a 50 mL round bottom flask and placed into an ice bath. *m*CPBA (772.08 mg, 81.2%) was also dissolved into a separate 10 mL CH_2Cl_2 solution and then added dropwise *via* addition funnel. 55% yield. ^{1}H NMR in $CDCl_3$: 4.10, m; 5.88, s; 7.55, d; 7.61, d; 7.95, d; 8.27, d; 9.13, s.

5-(phenylsulfonyl)picolinaldehyde. 382.09 mg 2-(1,3-dioxolan-2-yl)-5-(phenylsulfonyl)pyridine was added to a 50 mL round bottom flask with 39.33 mg PPTS, 20 mL MeCN and 5 mL water, and refluxed for 16 hours. 33% yield. ^{1}H NMR in $CDCl_3$: 7.51, m; 7.58, m; 8.31, d; 9.21, s; 10.02, s.

Tren(SO$_2$Ph)$_3$. 108.61 mg 5-(p-tolylthio)picolinaldehyde was added to a 20 mL scintillation vial with 20 mg tren and stirred for 16 hours in 10 mL MeCN. 94% yield. ^{1}H NMR in $CDCl_3$: 2.95, t; 3.72, t; 7.56; m; 8.00, m; 8.19, m; 8.27, d; 9.07, s.

SO$_2$Ph. 190.76 mg tren(SO$_2$Ph)$_3$ was dissolved in 10 mL MeCN with 77.82 mg Ni(BF$_4$)$_2$ 6H$_2$O and refluxed for 24 hours. 66% yield.

2-(1,3-dioxolan-2-yl)-5-(p-tolylthio)pyridine. 1.05732 g of 5-bromo-2-(1,3-dioxolan-2-yl)pyridine was added to a 50 mL round bottom flask with 1.5 mL *i*-Pr$_2$EtN, 103.5 mg Pd$_2$(dba)$_3$, 139.27 mg xantphos, 579.69 mg 4-methylbenzenethiol, and 25 mL 1,4-dioxane and refluxed under N_2 for 16 hours. 70% yield. ^{1}H NMR in $CDCl_3$: 2.28, s; 4.09, m; 5.75, s; 7.10, d; 7.24, d; 7.34, d; 7.46, d; 8.41, s.

5-(p-tolylthio)picolinaldehyde. 382.09 mg 2-(1,3-dioxolan-2-yl)-5-(p-tolylthio)pyridine was added to a 50 mL round bottom flask with 39.33 mg PPTS, 20 mL MeCN and 5 mL water, and refluxed for 16 hours. 33% yield. ^{1}H NMR in $CDCl_3$: 7.51, m; 7.58, m; 8.31, d; 9.21, s; 10.02, s. ^{1}H NMR in $CDCl_3$. 3.87, s; 7.00, s; 7.49, d; 7.50, d; 7.78 8.44, s; 9.98, s.

Tren(PySPh-Me)$_3$. 105.18 mg 5-(p-tolylthio)picolinaldehyde was added to a 20 mL scintillation vial with 21.8 µL tren and stirred for 16 hours in 10 mL MeCN. 81% yield.

2-(1,3-dioxolan-2-yl)-5-((4-methoxyphenyl)thio)pyridine. 530.08 mg of 5-bromo-2-(1,3-dioxolan-2-yl)pyridine was added to a 25 mL round bottom flask with 750 µL *i*-Pr$_2$EtN, 54.54 mg $Pd_2(dba)_3$, 72.33 mg xantphos, 450 µL 4-methoxybenzenethiol and 9 mL 1,4-dioxane and refluxed under N_2 for 16 hours. 36% yield. ^{1}H NMR in $CDCl_3$: 3.76, s; 4.05, m; 5.76, s; 6.88, d; 7.59, d; 7.79, d; 8.17, d; 9.01, s.

5-((4-methoxyphenyl)thio)picolinaldehyde. 215.40 mg 2-(1,3-dioxolan-2-yl)-5-((4-methoxyphenyl)thio)pyridine was added to a 50 mL round bottom flask with 23.25 mg PPTS, 16 mL MeCN and 4 mL water. 88% yield. ^{1}H NMR in $CDCl_3$: 2.41, t; 7.26, s (not $CDCl_3$); 7.28, s; 7.44, m; 7.78, d; 8.48, s; 9.98, s.

Tren(PySPh-OMe)$_3$. 97.99 mg 5-((4-methoxyphenyl)thio)picolinaldehyde was added to a 25 mL round bottom flask with 17.65 mg tren in 8 mL MeCN and stirred for 20 h. 86% yield.

SPh-OMe. 40.83 mg tren(PySPh-OMe)$_3$ was added to a 25 mL round bottom flask with 17.02 mg $Ni(BF_4)_2$ $6H_2O$. 91% yield.

2-(1,3-dioxolan-2-yl)-5-(naphthalen-2-ylsulfinyl)pyridine. 236.06 mg of 5-bromo-2-(1,3-dioxolan-2-yl)pyridine was added to a 25 mL round bottom flask with 375 µL *i*-Pr$_2$EtN, 26.19 mg $Pd_2(dba)_3$, 35.65 mg xantphos, 170.6 mg 2-naphthalene-2-thiol, and 9 mL 1,4-dioxane and

refluxed under N_2 for 24 hours. 51% yield. ^{1}H NMR in $CDCl_3$: 4.08, m; 5.75, s; 6.18, s; 6.57, d; 6.95, d; 7.37, m; 7.62, d; 7.81, d; 8.62, s.

5-(naphthalen-2-ylthio)picolinaldehyde. 106.68 mg 2-(1,3-dioxolan-2-yl)-5-(naphthalen-2-ylsulfinyl)pyridine was added to a 50 mL round bottom flask with 10.98 mg PPTS, 10 mL MeCN and 2.5 mL water. 98% yield. ^{1}H NMR in $CDCl_3$: 7.50, m; 7.71, d; 7.76, d; 7.82, m; 8.03 s; 8.49, s; 9.93 s.

Tren(PySNaph)$_3$. 118.5 mg 5-(naphthalen-2-ylthio)picolinaldehyde was added to 22.22 µL tren and 10 mL MeCN in a 20 mL scintillation vial. ^{1}H NMR in $CDCl_3$: 2.94, t; 3.74, t; 7.40, d; 7.51, m; 7.81, d; 7.93, m; 8.26, s; 8.49, s.

SNaph. 50.03 mg $Ni(BF_4)_2$ $6H_2O$ and 130.52 mg tren(PySNaph)$_3$ were added to a 50 mL round bottom flask with 20 mL MeCN. The solution was refluxed for 2 hours and then dried by rotary evaporation. 91% yield.

2-(1,3-dioxolan-2-yl)-5-(naphthalen-2-ylsulfinyl)pyridine. 395.82 mg 2-(1,3-dioxolan-2-yl)-5-(naphthalen-2-ylsulfinyl)pyridine was dissolved in 10 mL CH_2Cl_2 in a 25 mL round bottom flask and placed into an ice bath. *m*CPBA (249.73 mg, 75%) was also dissolved into a separate 10 mL CH_2Cl_2 solution and then added dropwise *via* addition funnel. 50% yield. ^{1}H NMR in $CDCl_3$: 4.11, m; 5.87, s; 7.67, q; 7.89, d; 7.95, d; 8.31; 8.56, s; 9.20, d.

5-(naphthalen-2-ylsulfinyl)picolinaldehyde. 183.17 mg of 2-(1,3-dioxolan-2-yl)-5-(naphthalen-2-ylsulfinyl)pyridine was added to a 50 mL round bottom flask with 20.10 mg PPTS, 20 mL MeCN and 5 mL water. 61% yield. ^{1}H NMR in $CDCl_3$: 7.52, t; 7.57, m; 7.78, d; 7.92 m; 8.10, s; 10.00, s

Tren(SONaph)$_3$. 39.89 mg 5-(naphthalen-2-ylthio)picolinaldehyde was added to 7.33 mg tren and 5 mL MeCN in a 20 mL scintillation vial. Note: Product was sparingly soluble in MeCN. 71% yield.

SONaph. 15.16 mg $Ni(BF_4)_2$ $6H_2O$ and 41.63 mg tren(PySONaph)$_3$ were added to a 25 mL round bottom flask with 10 mL MeCN. The solution was refluxed for 2 hours and then dried by rotary evaporation. Note: Product was far more soluble than the pure ligand. 91% yield.

7.7 References

(1) Tiekink, E. R. T.; Zukerman-Schpector, J. *The Importance of Pi-Interactions in Crystal Engineering: Frontiers in Crystal Engineering*; **2012**. https://doi.org/10.1002/9781119945888.

(2) Ozumerzifon, T. J. Efforts Towards Controlling Magnetic Properties of Cobalt and Iron Coordination Complexes, Colorado State University, **2017**.

(3) Wheeler, S. E. Understanding Substituent Effects in Noncovalent Interactions Involving Aromatic Rings. *Acc. Chem. Res.* **2013**, *46* (4), 1029–1038. https://doi.org/10.1021/ar300109n.

(4) Martinez, C. R.; Iverson, B. L. Rethinking the Term "Pi-Stacking." *Chem. Sci.* **2012**, *3* (7), 2191–2201. https://doi.org/10.1039/c2sc20045g.

(5) Bootsma, A. N.; Doney, A. C.; Wheeler, S. E. Predicting the Strength of Stacking Interactions between Heterocycles and Aromatic Amino Acid Side Chains. *J. Am. Chem. Soc.* **2019**, *141* (28), 11027–11035. https://doi.org/10.1021/jacs.9b00936.

(6) Bruker AXS inc. SAINT, v.8.38A. Madison, WI 2016.

(7) Sheldrick, G. M. SADABS, Version 2.03, Bruker Analytical X-Ray Systems, Inc., Madison, WI. Madison, WI 2000.

(8) Sheldrick, G. M. Crystal Structure Refinement with SHELXL. *Acta Crystallogr. Sect. C Struct. Chem.* **2015**, *71* (Md), 3–8. https://doi.org/10.1107/S2053229614024218.

(9) Bain, G. A.; Berry, J. F. Diamagnetic Corrections and Pascal's Constants. *J. Chem. Educ.* **2008**, *85* (4), 532–536. https://doi.org/10.1021/ed085p532.

(10) Mishra, B. K.; Sathyamurthy, N. π-π Interaction in Pyridine. *J. Phys. Chem. A* **2005**, *109* (1), 6–8. https://doi.org/10.1021/jp045218c.

(11) Headen, T. F.; Cullen, P. L.; Patel, R.; Taylor, A.; Skipper, N. T. The Structures of Liquid Pyridine and Naphthalene: The Effects of Heteroatoms and Core Size on Aromatic Interactions. *Phys. Chem. Chem. Phys.* **2018**, *20* (4), 2704–2715. https://doi.org/10.1039/c7cp06689a.

(12) Wheeler, S. E.; Houk, K. N. Substituent Effects in the Benzene Dimer Are Due to Direct Interactions of the Substituents with the Unsubstituted Benzene. *J. Am. Chem. Soc.* **2008**, *130* (33), 10854–10855. https://doi.org/10.1021/ja802849j.

(13) Bloom, J. W. G.; Wheeler, S. E. Taking the Aromaticity out of Aromatic Interactions. *Angew. Chemie - Int. Ed.* **2011**, *50* (34), 7847–7849. https://doi.org/10.1002/anie.201102982.

Appendix

Chapter 2 Appendix

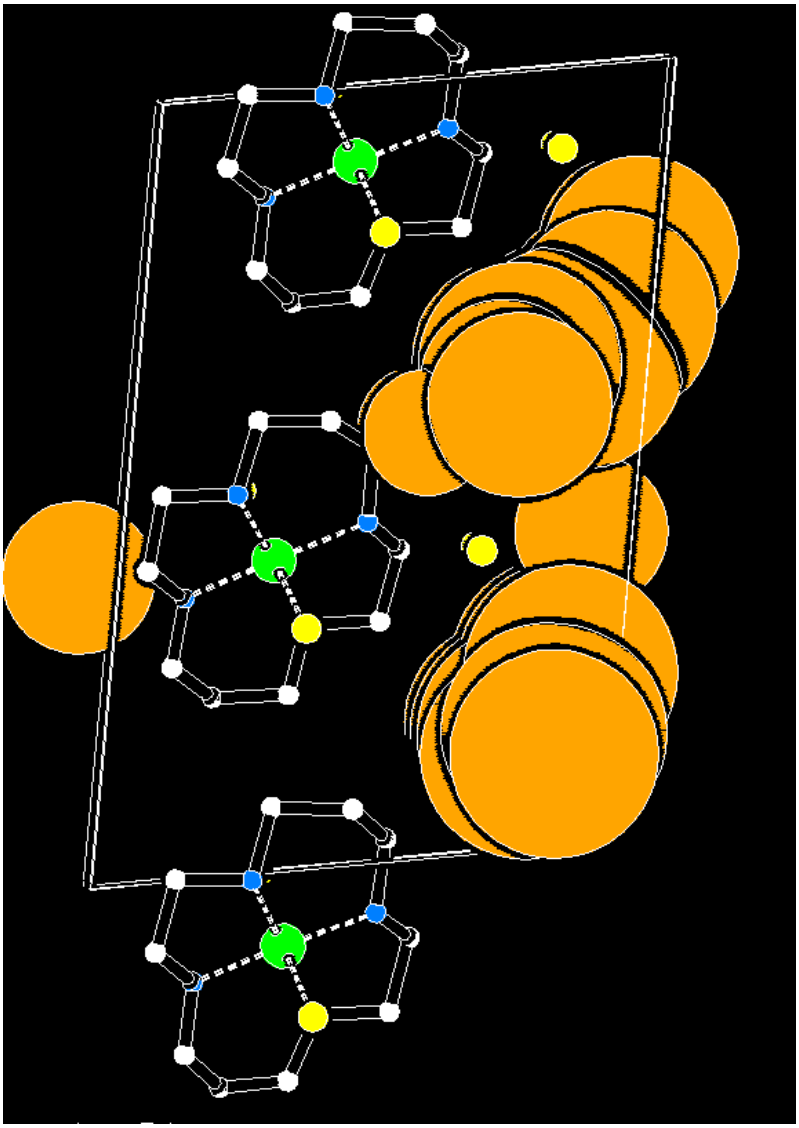

Figure A1.1 View of the solvents voids (orange) in **1** down the a axis.

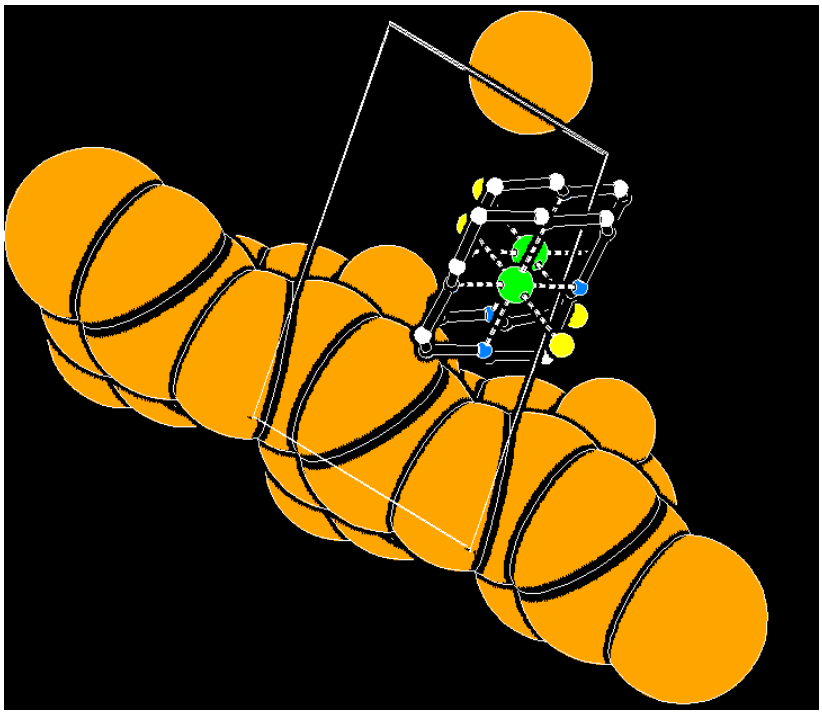

Figure A2.2 View of the solvent voids (orange) in **1** down the c axis.

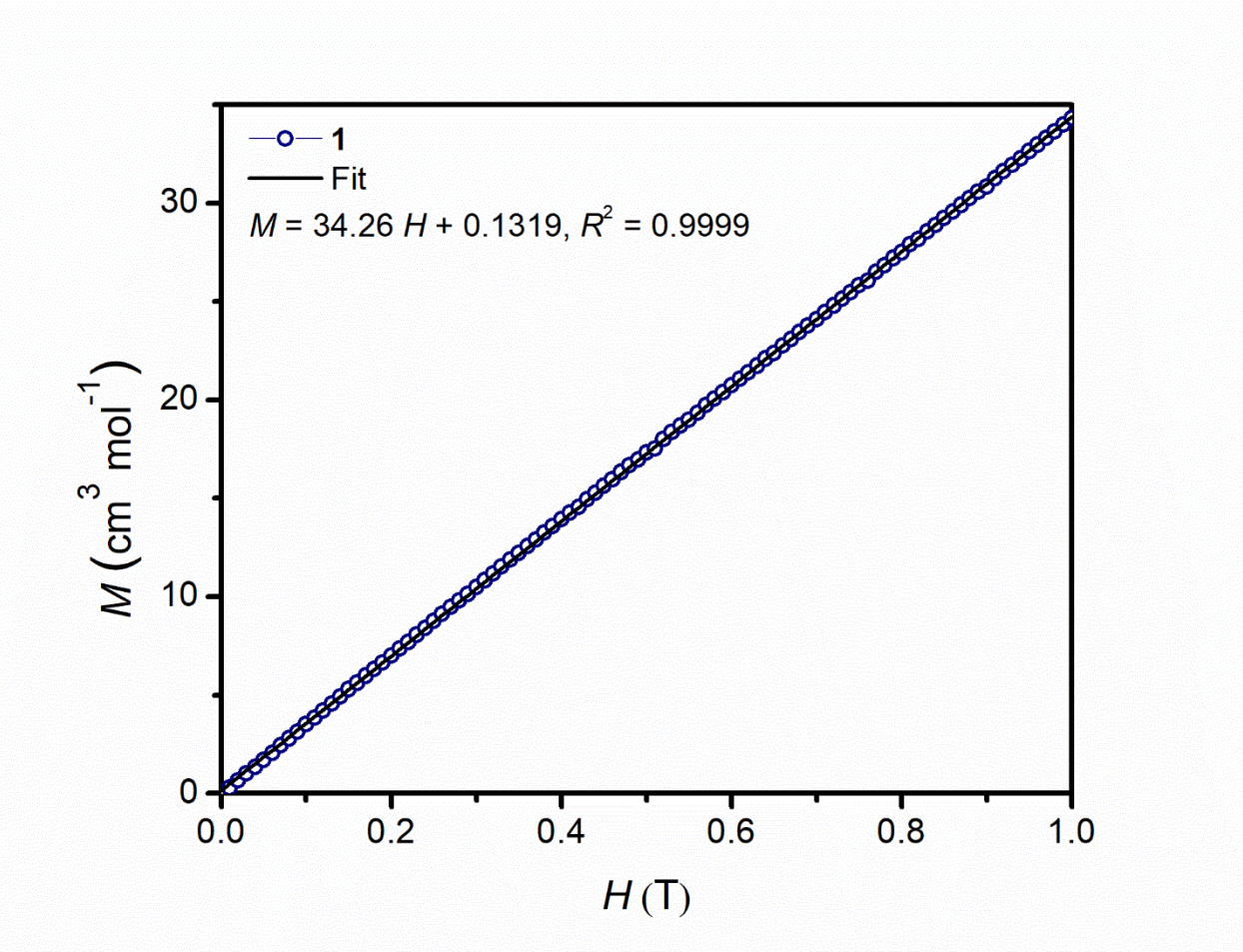

Figure A2.3 Magnetization of **1** vs. applied magnetic field at 100 K. Linearity in the plot indicates the lack of ferromagnetic impurities.

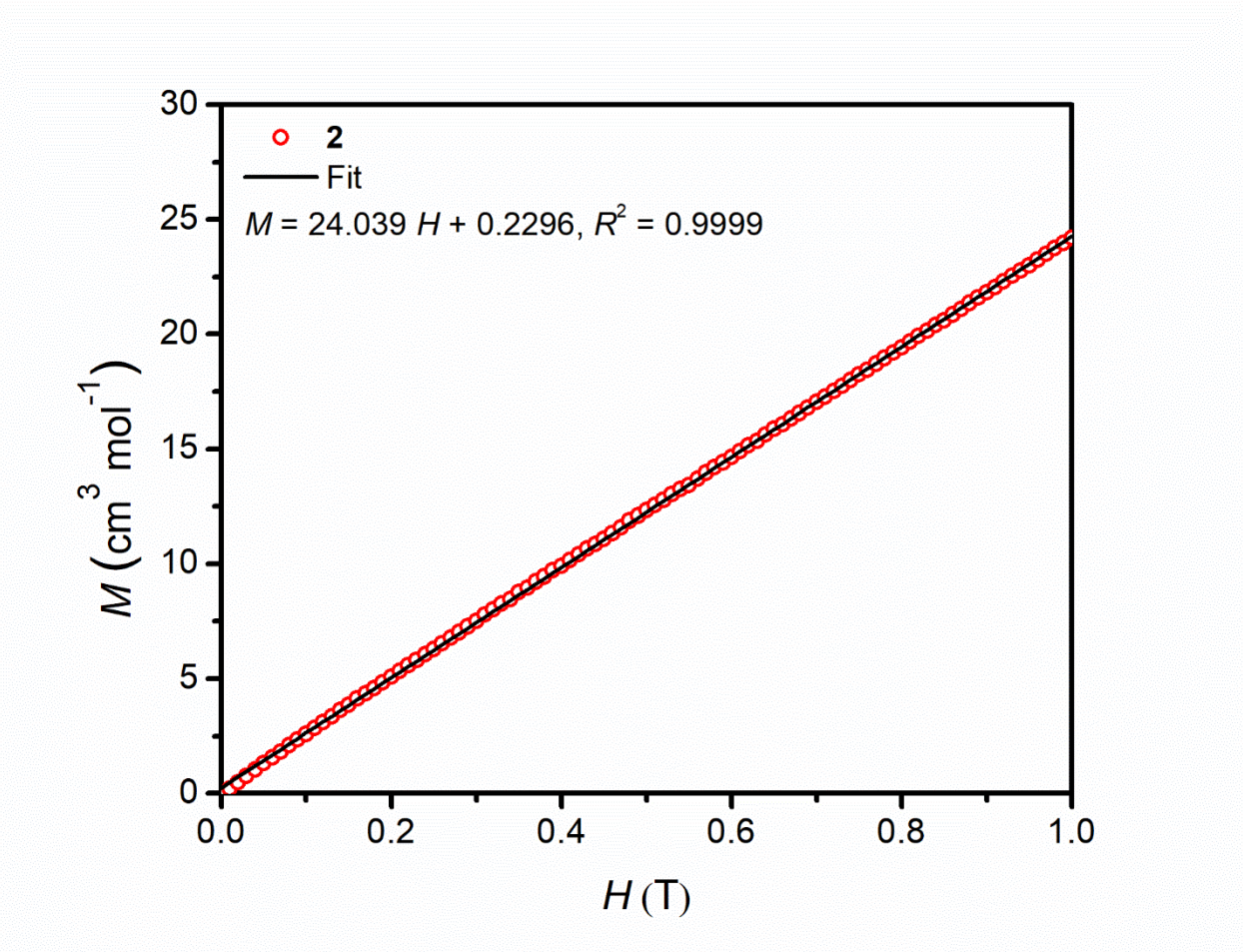

Figure A2.4 Magnetization of **2** vs applied magnetic field at 100 K. Linearity in the plot indicates the lack of ferromagnetic impurities.

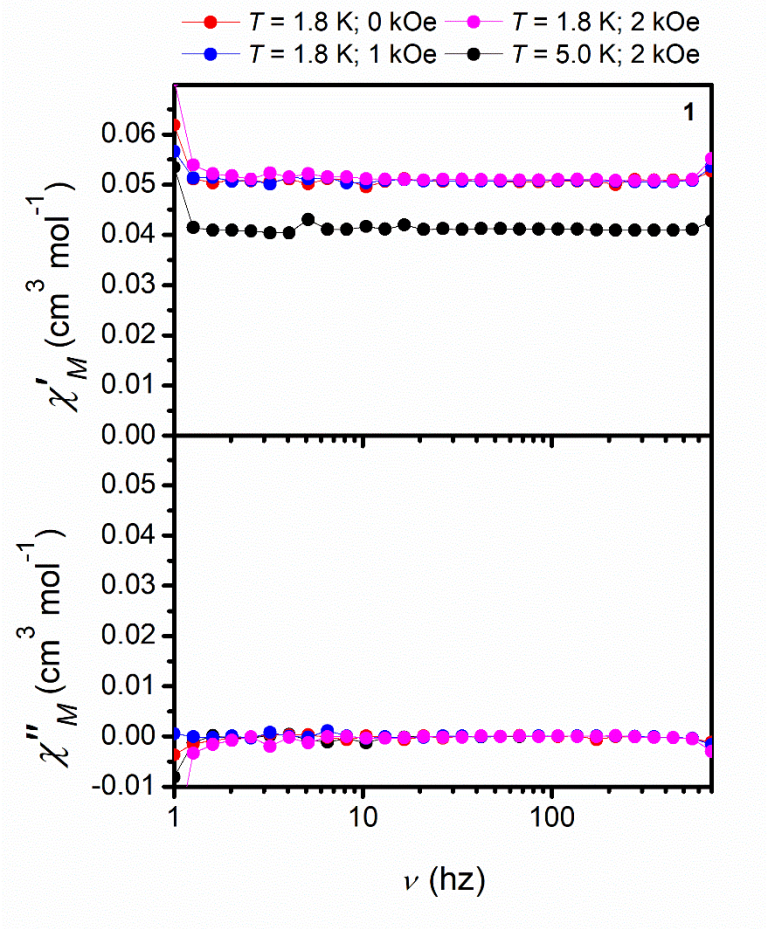

Figure A2.5 In-phase (top) and out-of-phase (bottom) magnetic susceptibility of **1** at 1.8 K from 0 – 2 kOe and at 5 K and 2 kOe.

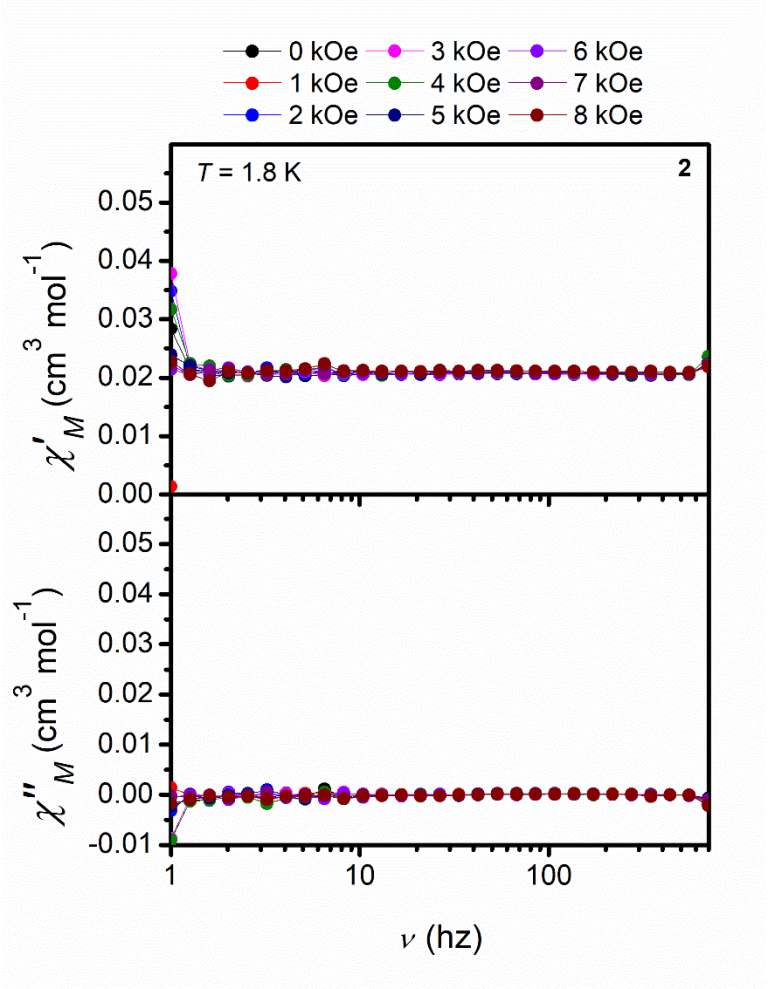

Figure A2.6 In-phase (top) and out-of-phase (bottom) magnetic susceptibility of **2** at 1.8 K with an applied field of 0 – 8 kOe.

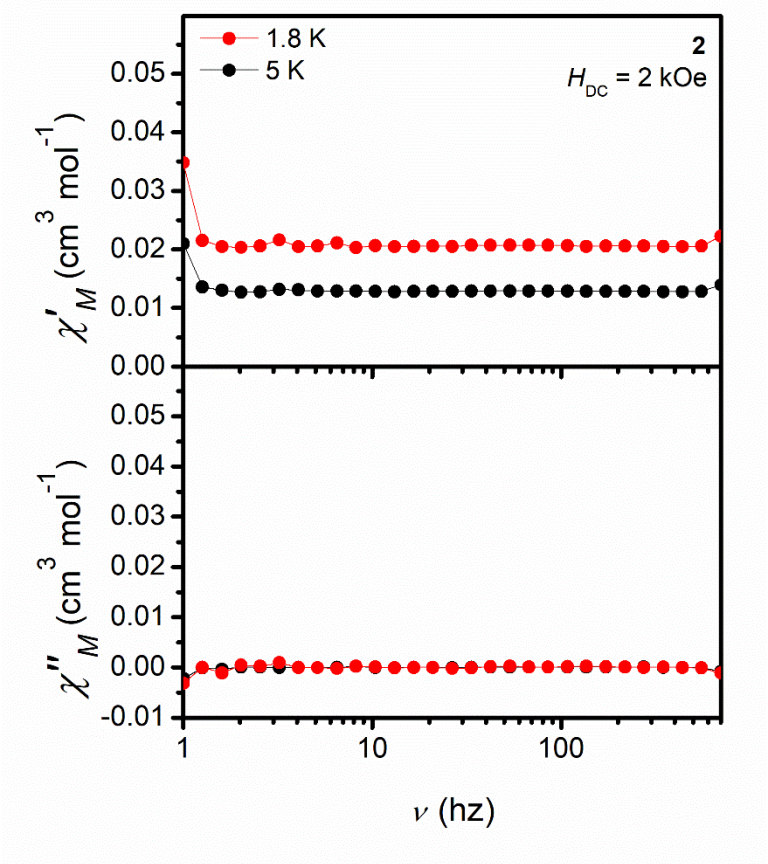

Figure A2.7 In-phase (top) and out-of-phase (bottom) magnetic susceptibility of **2** at 1.8 K and 5.0 K with an applied magnetic field of 2 kOe.

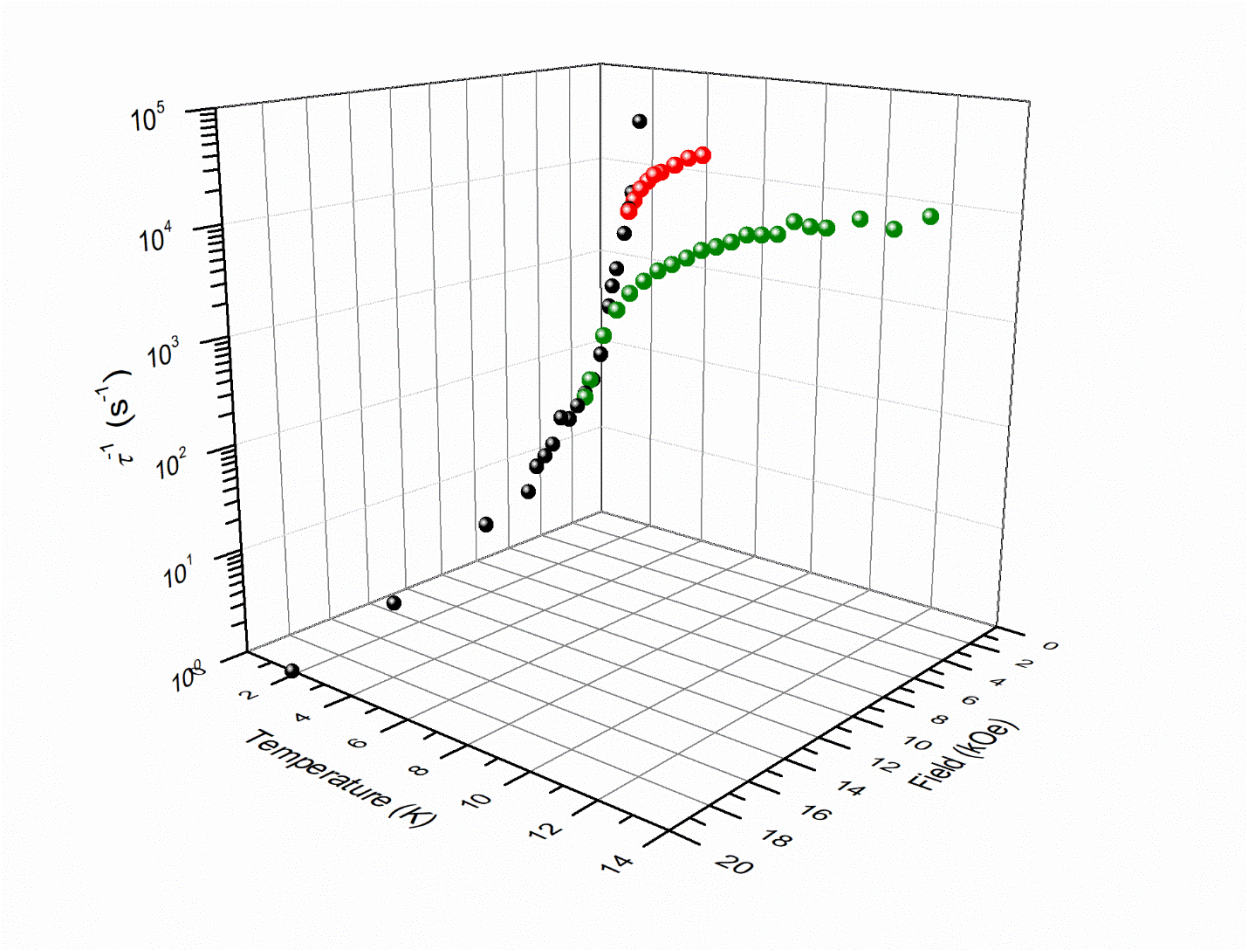

Figure A2.8 Full field-temperature space of the relaxation rates of **3**. The black spheres represent the magnetic field sweep at 1.8 K, the red spheres the temperature sweep at 1.2 kOe from 1.8 – 4.5 K, and the green spheres the temperature sweep at 4.0 kOe from 1.8 – 13 K.

Chapter 3 Appendix

Table A3.1 Single crystal X-ray diffraction parameters for compounds in this study: {[Ni(cyclam)(SO_4)]ClO_4·H_2O}n (**1**), [Ni(cyclam)(HSO_4)$_2$]HSO_4 (**2**), [Ni(cyclam)(HSO_4)$_2$]HSO_4·MeOH (**2·MeOH**), and [Ni(d_4-cyclam)(DSO_4)$_2$]DSO_4 (**2-d_7**).

	1	**2**	**2·MeOH**	**2-d_7**
CCDC Number	2216214	2216213	2216215	2216212
Empirical formula	$C_{10}H_{25}ClN_4NiO_9S$	$C_{10}H_{27}N_4NiO_{12}S_3$	$C_{11}H_{31}N_4NiO_{13}S_3$	$C_{10}D_7H_{20}N_4NiO_{12}S_3$
FW (g/mol)	471.44	550.23	582.29	550.23
Temperature (K)	100(2)	122(2)	100(2)	200(0)
Wavelength (Å)	0.71073	0.71076	0.71073	0.71073
Crystal size (mm)	0.045 × 0.058 × 0.087	0.137 × 0.178 × 0.264	0.086 x 0.078 x 0.047	0.202 x 0.083 x 0.069
Crystal habit	Translucent green blocks	Translucent light brown needles	Translucent violet blocks	Translucent light brown needles
Crystal system	orthorhombic	Monoclinic	Monoclinic	Monoclinic
Space group	$P2_12_12_1$	C_2/c	P_n	C_2/c
a (Å)	10.9069(6)	9.796(6)	8.2624(3)	9.8609(5)
b (Å)	12.4366(7)	13.377(8)	10.6104(4)	13.3678(7)
c (Å)	13.1197(7)	15.677(9)	12.4936(5)	15.6882(7)
β (°)	90	107.42(2)	102.684(2)	107.516(2)
Volume (Å^3)	1779.62(17)	1960.(2)	1068.55(7)	1972.11(17)
Z	4	4	2	4
Density (g/cm^3)	1.760	1.865	1.810	1.853
Abs. coeff. (mm^{-1})	1.412	1.381	1.275	1.372
$F_{(000)}$	984	1148	610	1148
N_{ref}	4087	1931	5263	3010
GOF on F^2	1.021	1.050	1.043	1.043
Completeness (%)	100.0	96.1	100.0	99.7
R [$I>2\sigma(I)$]: R_1[a]	0.0617	0.0282	0.0550	0.0335
(wR$_2$[b])	(0.1307)	(0.0712)	(0.1011)	(0.0833)
R (all data): R_1[a]	0.1024	0.0304	0.0772	0.0472
(wR$_2$[b])	(0.1468)	(0.0730)	(0.1199)	(0.0833)

(a) $R_1 = \Sigma||F_o| - |F_c||/ \Sigma |F_o|$

(b) $wR_2 = [\Sigma [w(F_o^2-F_c^2)^2]/ \Sigma [w(F_o^2)^2]]^{½}$, $w = 1/[s^2(F_o^2) + (aP)^2 + bP]$, where $P = [\max(F_o^2 \text{ or } 0) + 2(F_c^2)]/3$

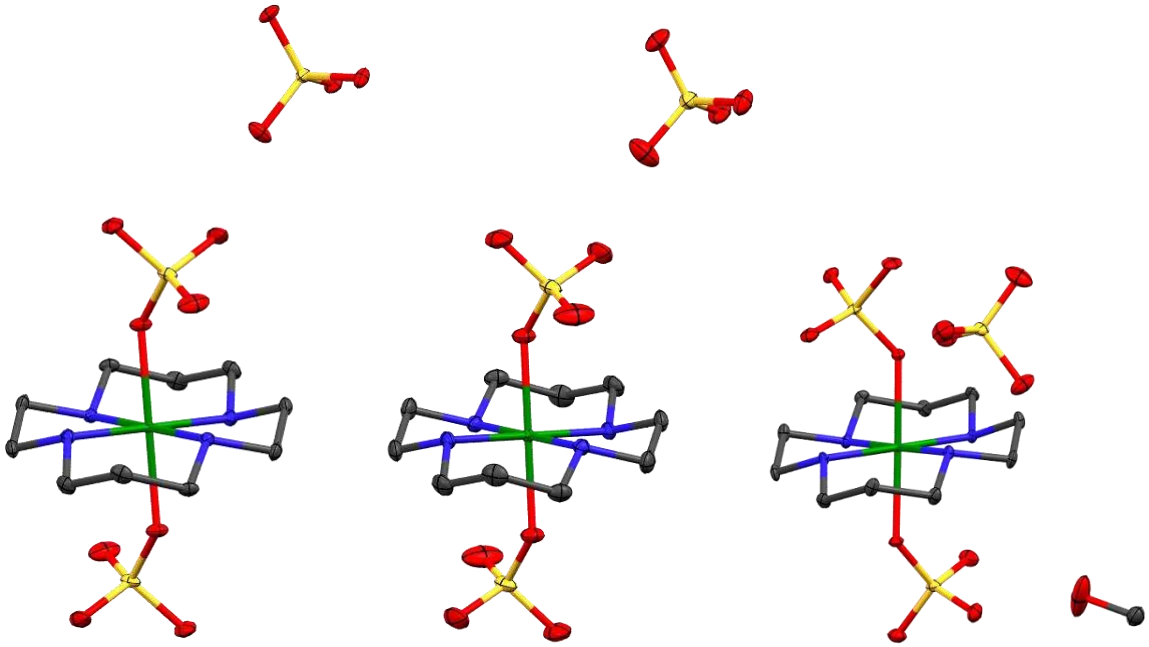

Figure A3.1 Crystal structures of [Ni(cyclam)$(HSO_4)_2$]HSO_4 (100 K; left), [Ni(d_4-cyclam)$(DSO_4)_2$]DSO_4 (200 K; center), and [Ni(cyclam)$(HSO_4)_2$]HSO_4 MeOH (120 K, right), with thermal ellipsoids set at 50% probability level. Green, yellow, red, blue, and black colors represent Ni, S, O, N, and C atoms, respectively. Hydrogen and deuteron atoms omitted for clarity.

Table A3.2 Select interatomic distances (Å) for structures containing the Ni(III) cyclam bisulfate complex.

	[Ni(cyclam)$(HSO_4)_2$]HSO_4 (**2**)	[Ni(d_4-cyclam)$(DSO_4)_2$]DSO_4 (**2-d$_7$**)	[Ni(cyclam)$(HSO_4)_2$]HSO_4 MeOH (**2-MeOH**)
Ni-N	1.961(2)	1.962(3)	1.964(6)
	1.979(7)	1.972(8)	1.965(6)
	1.961(2)	1.962(3)	1.969(5)
	1.979(7)	1.972(8)	1.970(5)
Ni-O	2.114(16)	2.113(2)	2.099(5)
	2.114(16)	2.113(2)	2.166(5)
O(H)···O †	2.467(4)	2.496(5)	2.608(8)
N(H)···O ‡	2.878(2)	2.878(3)	2.833(7)
O(H)···OMe	N/A	N/A	2.540(8)

†H-bond from inner-sphere HSO_4 to outer-sphere HSO_4. ‡ H-bond from amine to inner-sphere HSO_4.

Other physical characterizations

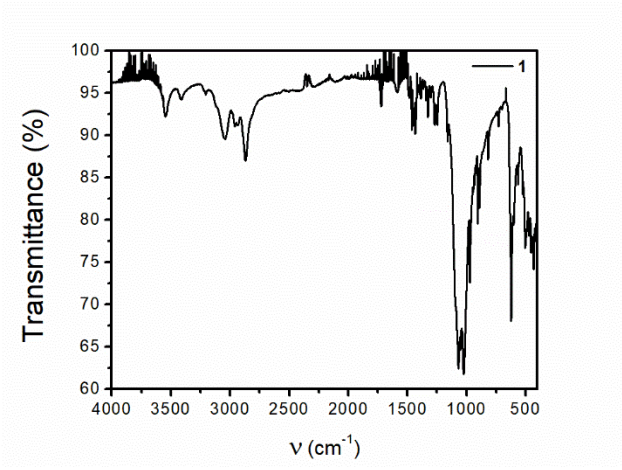

Figure A3.2 FTIR spectrum of **1** from 4000 cm^{-1} to 400 cm^{-1}.

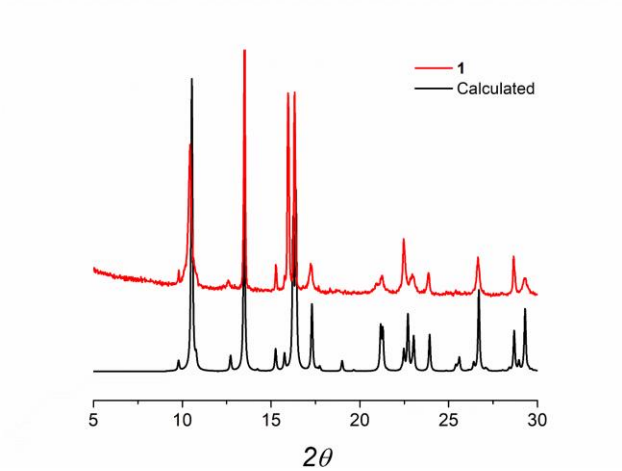

Figure A3.3 Powder XRD of **1**, compared to calculated data from single crystal structure of **1**.

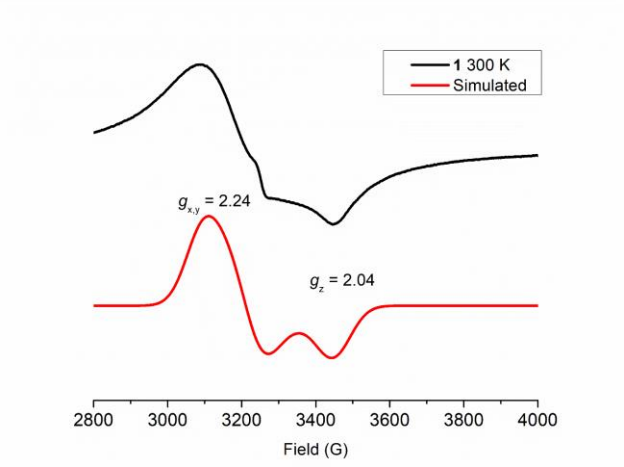

Figure A3.4 EPR spectrum of **1**, collected at 300 K; microwave frequency of 9.818563 GHz. The *g* values are consistent with those reported by Chechik *et al.*[1]

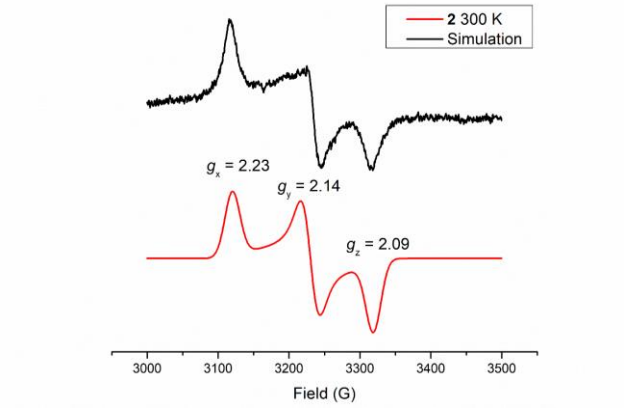

Figure A3.0.5 EPR spectrum of **2**, collected at 300 K; microwave frequency of 9.813376 GHz.

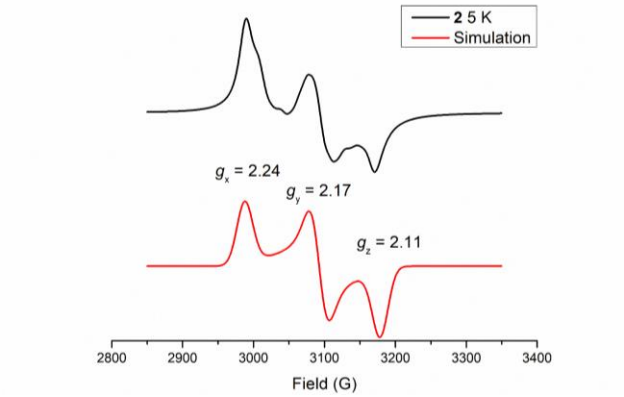

Figure A3.6 EPR spectrum of **2**, collected at 5 K; microwave frequency of 9.376704 GHz.

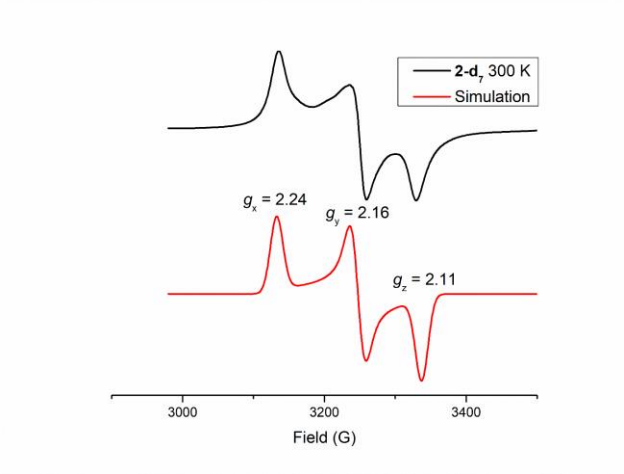

Figure A3.7 EPR spectrum of **2-d$_7$** collected at 300 K; microwave frequency of 9.839884 GHz.

Table A3.3 List of *g*-values.

	T (K)	g_{iso}‡	g_x†	g_y†	g_x†
1	300	2.17	2.24	2.24	2.04
1	1.8-300	2.20			
2	300	2.15	2.23	2.14	2.09
2	5	2.17	2.24	2.17	2.11
2 ground	1.8-300	2.04			
2-d$_7$ crystalline	3-300	2.08			
2-d$_7$ 100 µm	3-300	2.05			
2-d$_7$ crystalline	300	2.17	2.24	2.16	2.11

†Value obtained by simulation of EPR data. ‡Value obtained by fits to DC susceptibility data.

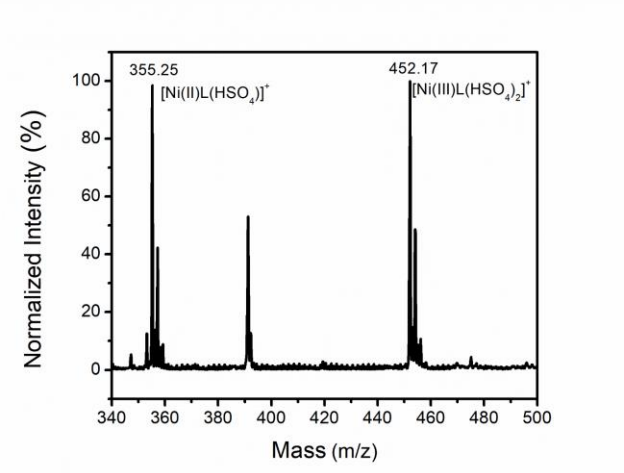

Figure A3.8 ESI-MS spectrum of **2** in H_2O in positive (+) ion mode. The presence of equal amounts of Ni(II) and Ni(III) material shows the instability in non-acidic media. L = cyclam, $C_{10}N_4H_{24}$. Note: the peak at 391 *m/z* corresponds to a plasticizer (diisooctyl phthalate + H) that is present in the blank spectrum.

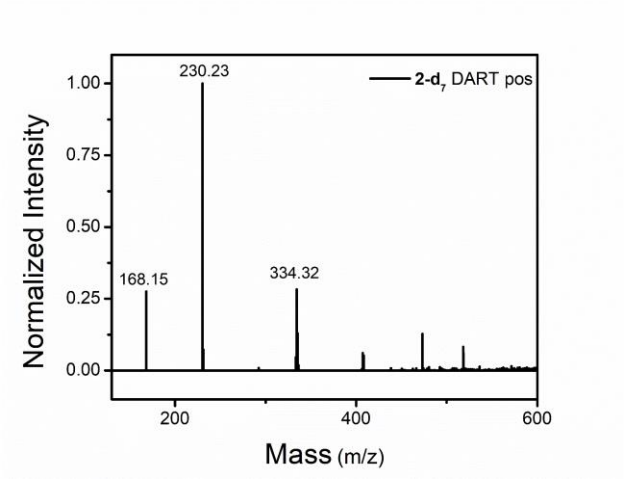

Figure A3.9 DART-MS of **2-d7** at 300°C in positive (+) ion mode with a solid-state introduction method. 230.23 m/z assigned to $[Ni(III)(d\text{-}4\ cyclam)(DSO4)(D2SO4)]^{2+}$.

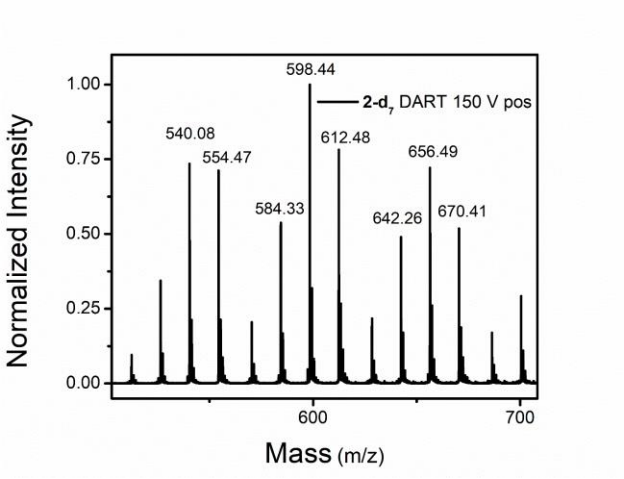

Figure A3.10 Fragmentation DART-MS of **2-d7** at 300°C in positive (+) ion mode with a solid-state introduction method. 598.44 m/z assigned to [Ni(III)(d-4 cyclam)(DSO4)2 + D2SO4 + 2 D2O]. 656.49 m/z assigned to [Ni(III)(d-4 cyclam)(DSO4)2 + 2D2SO4]+. Satellite peaks of ± 14 m/z assigned to the gain/loss $\cdot CH_2$.

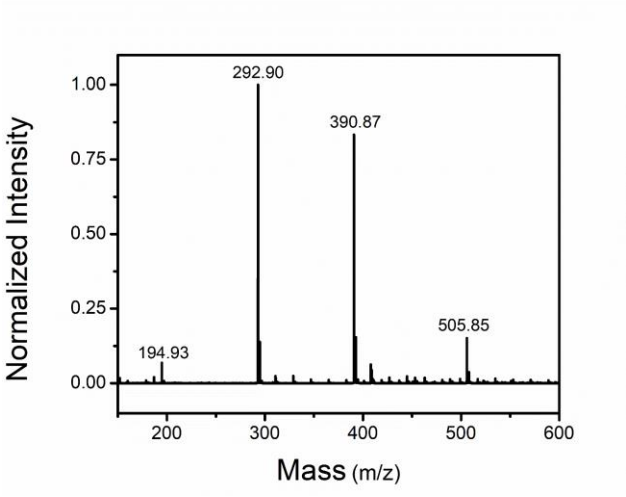

Figure A3.11 DART-MS of **2-d$_7$** at 300°C in negative (-) ion mode with a solid-state introduction method. 194.93 m/z assigned to (H2SO4 + HSO4)-. 292.90 m/z assigned to (2H2SO4 + HSO4)-. 390.87 m/z assigned to $(3H2SO4 + HSO_4)^-$.

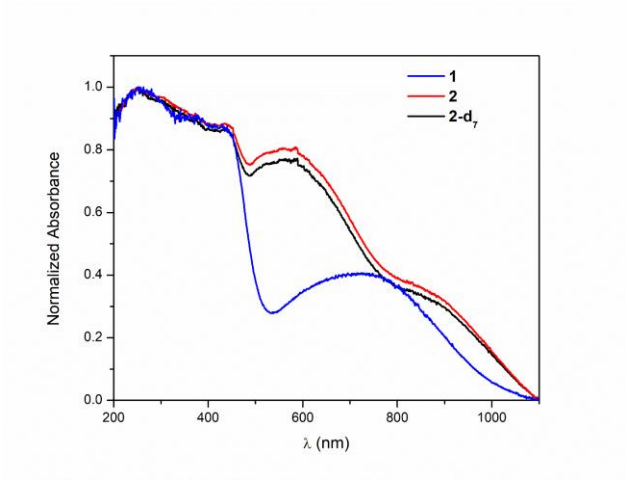

Figure A3.12 Normalized diffuse reflectance spectra of **1**, **2**, and **2-d$_7$**, collected at room temperature from 200 nm to 1100 nm with a BaSO4 background. Data are normalized to the peak at ca. 225 nm.

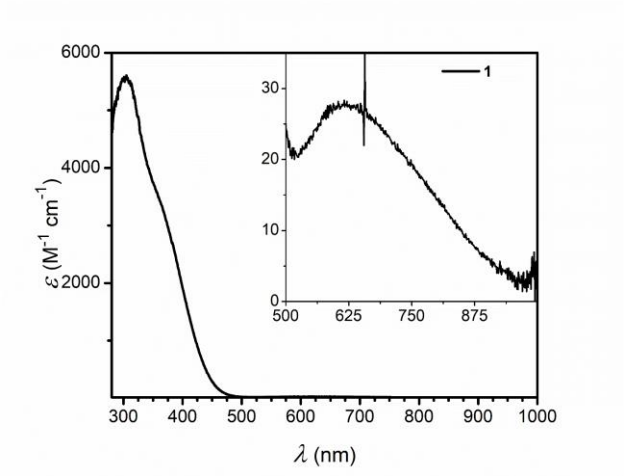

Figure A3.13 Electronic absorption spectrum of **1** dissolved in Millipore water. The feature at ca. 650 nm is an artifact due to switching lamps.

Magnetic property characterizations

Checks for ferromagnetic impurities

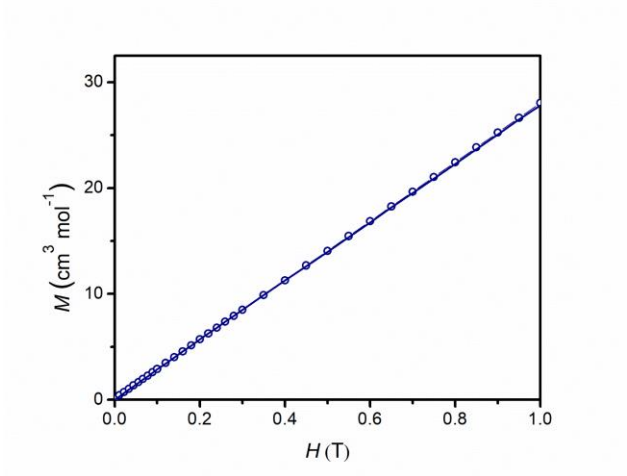

Figure A3.14 Field dependence of magnetization of **1** at 100 K. Line represents the line of best fit, M = 27.79(H) + 0.0857 R^2 = 1.000

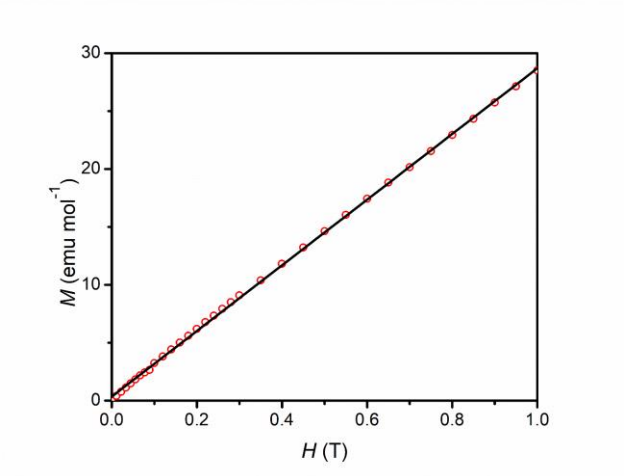

Figure A3.15 Field dependence of magnetization of **2** at 100 K. Line represents the line of best fit, M = 28.34(H) + 0.35. R2 = 0.9997.

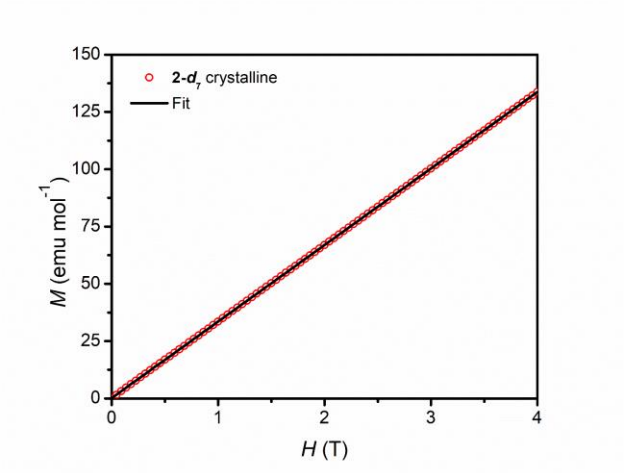

Figure A3.16 Field dependence of magnetization of **2-d$_7$** at 100 K. Line represents the line of best fit, M = 33.39(*H*) + 0.1506. R^2 = 1.000

DC susceptibility data for 1 & 2

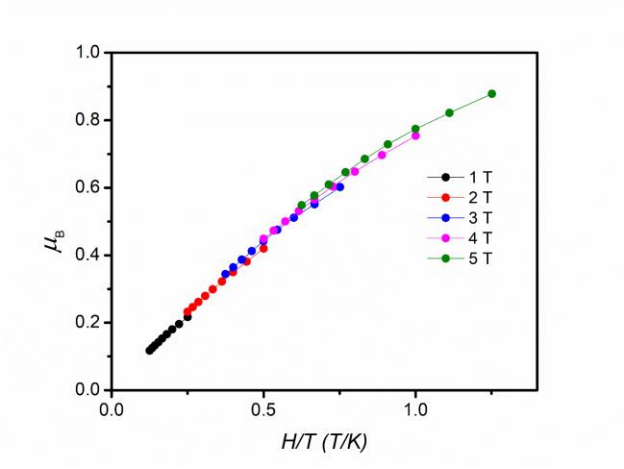

Figure A3.17 Reduced field magnetization plot of a ground sample of **2** from 1 T to 5 T and 4 K to 8 K in 0.5 K increments.

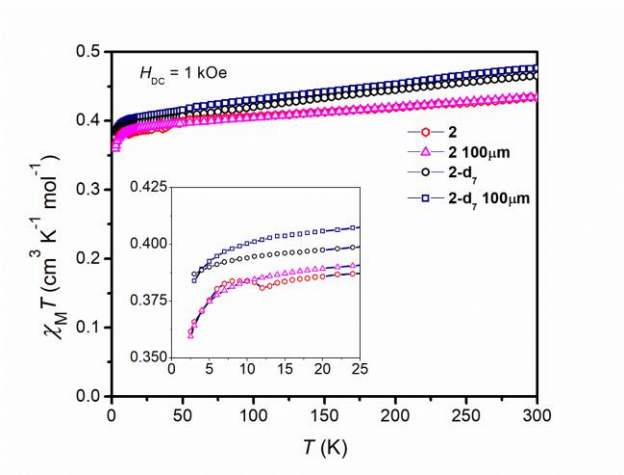

Figure A3.18 Static (DC) susceptibility of a crystalline and powdered sample of **2** and **2-d$_7$** at 1 kOe from 3 K – 300 K for 2-d7 and 1.8 K to 300 K for 2.

Temperature-dependent magnetic susceptibility data for **1** were modeled using a combination of a Bonner-Fisher component, which modeled the susceptibility of an $S = ½$ infinite isotropic Heisenberg chain, and a Curie-Weiss-like component that modeled finite chain lengths with an odd number of Ni^{3+} spins, isolated Ni^{3+} spins, and/or other paramagnetic impurities (Eq. A3.1). The coefficient ρ represents the effect level, N is Avogadro's number, μ_B is the Bohr magneton, T is the temperature, k_B is the Boltzmann constant, χ_{TIP} is the temperature independent paramagnetism, and $x = |J|/k_BT$. We note that there are no analytical solutions for the magnetic susceptibility of Heisenberg chains, but that the polynomial expression below given by the Bonner-Fisher model is a useful approximation.

$$\chi = \rho \frac{Ng^2\mu_B^2}{k_BT}\left(\frac{0.25+0.14995x+0.30094x^2}{1+1.9862x+0.68854x^2+6.0626x^3}\right) + (1-\rho)\frac{Ng^2\mu_B^2 S(S+1)}{3k_B(T-\Theta)} + \chi_{TIP} \quad \text{(Eq. A3.1)}$$

Temperature-dependent DC magnetic susceptibility data were modeled with the program PHI (Eq. A3.2).[2]

$$\hat{H} = \mu_B g\hat{\vec{S}} - \sum_{i<j}^{i,j\in N} \hat{\vec{S}}_1 \cdot \bar{\bar{J}} \cdot \hat{\vec{S}}_2 \quad \text{(Eq. A3.2)}$$

$$\chi_{TIP} = \chi_{calc} + TIP \quad \text{(Eq. A3.3)}$$

$$\chi_{zJ} = \frac{\chi_{TIP}}{1-(\frac{zJ}{N_A\mu_B^2})\chi_{TIP}} \quad \text{(Eq. A3.4)}$$

Table A3.4 Fit parameters of temperature dependence of static magnetic susceptibility.

	g_{iso}	c_{TIP} ($cm^3\ mol^{-1}$)	J (cm^{-1})	zJ (cm^{-1})	Θ (K)	ρ	Residual
1	2.20	1.71 x 10^{-4}	-46.3		-3.0	0.928	0.0001817
2 ground	2.04	1.50 x 10^{-4}		-1.433			0.0003994
2 100 µm	2.05	1.56 x 10^{-4}		-0.039			0.0001457
2-d_7	2.08	2.45 x 10^{-4}		-0.118			0.0000728
2-d_7 100 µm	2.05	2.44 x 10^{-4}		-0.055			0.0001011

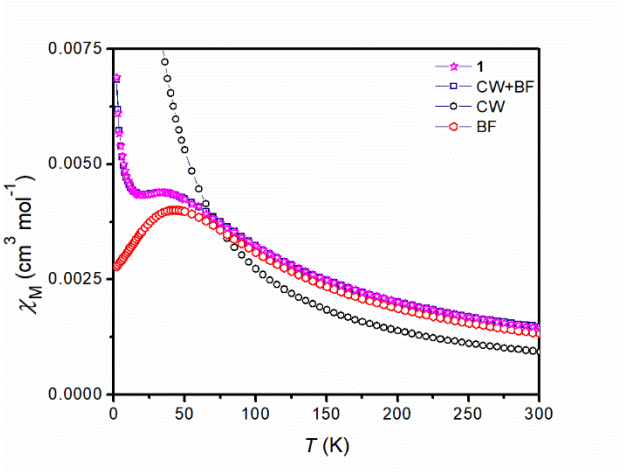

Figure A3.19 Static (DC) magnetic susceptibility of ground samples of **1**, measured in a 1 kOe applied field from 1.8 K – 300 K. Fits from the Curie-Weiss-like model, Bonner-Fisher model, and their sum using $\rho = 0.928$ are shown (see above for details).

AC susceptibility data for **2**

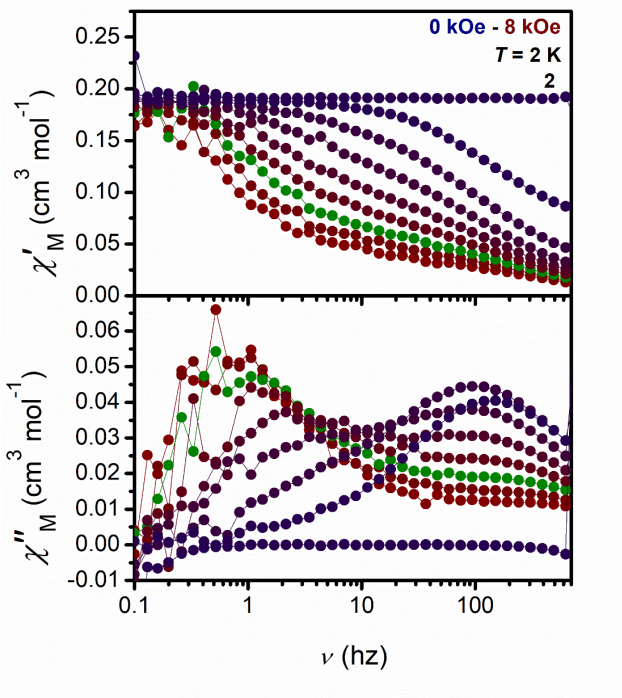

Figure A3.20 Frequency dependence of in-phase (top) and out-of-phase (bottom) AC susceptibility of a crystalline sample of **2** at 2 K with applied DC field ranging from from 0 kOe to 8 kOe in 1 kOe steps. The data collected at 6 kOe are highlighted in green.

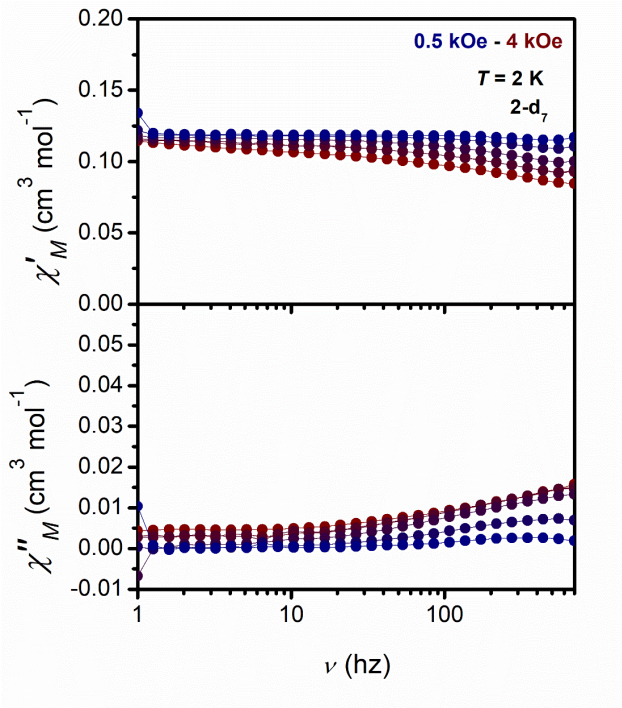

Figure A3.21 Frequency dependence of in-phase (top) and out-of-phase (bottom) AC susceptibility of a crystalline sample of **2-d$_7$**, measured at 2 K at 0.5 kOe and 1 kOe – 4 kOe in 1 kOe steps.

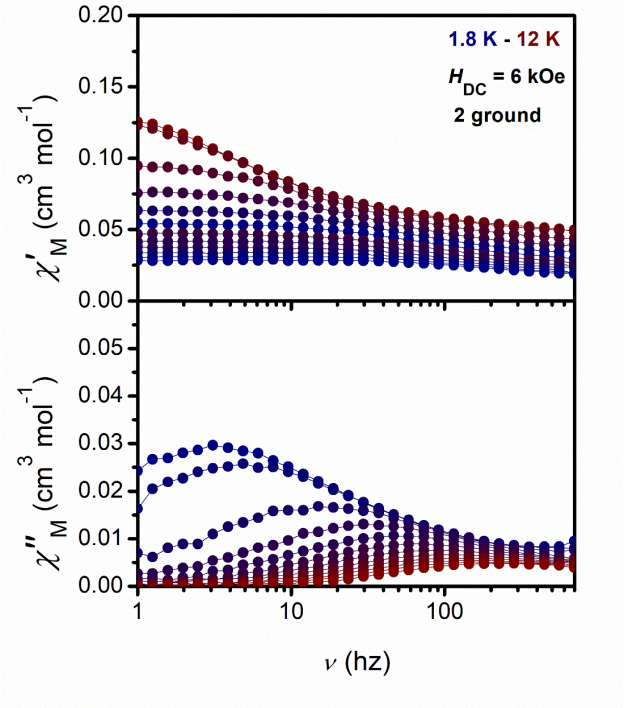

Figure A3.22 Frequency dependence of in-phase (top) and out-of-phase (bottom) AC susceptibility of a ground sample of **2**, measured at 6 kOe from 1.8 K to 12 K in 1 K steps starting at 2 K.

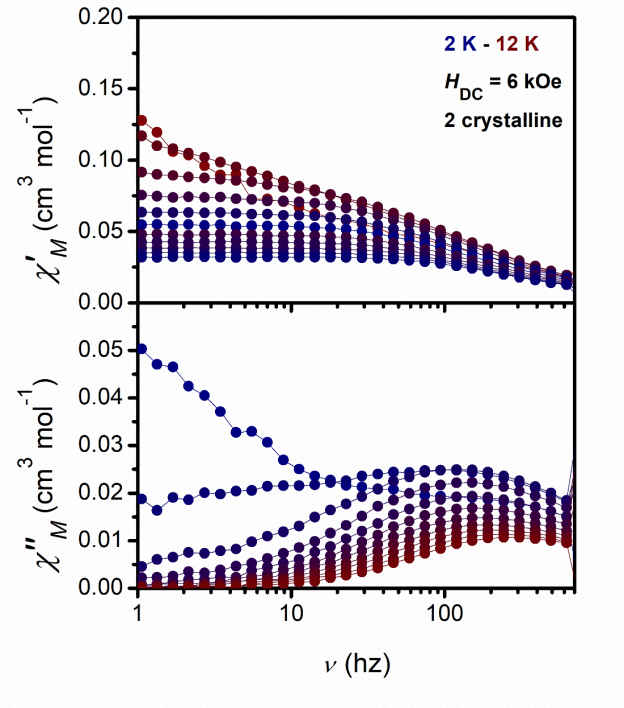

Figure A3.23 Frequency dependence of in-phase (top) and out-of-phase (bottom) AC susceptibility of a crystalline sample of **2**, measured at 6 kOe from 2 K to 12 K in 1 K steps.

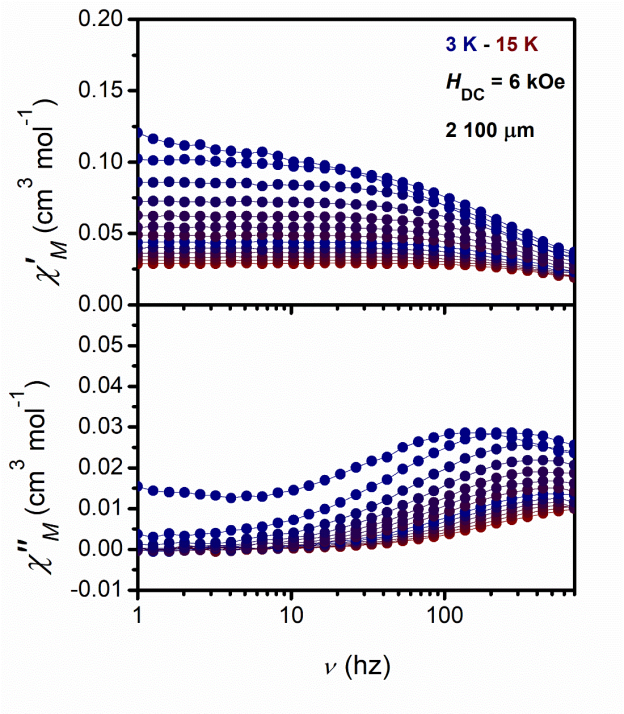

Figure A3.24 Frequency dependence of in-phase (top) and out-of-phase (bottom) AC susceptibility of a powdered sample of **2** with particle sizes between 53 μm and 106 μm, measured at 6 kOe from 3 K to 15 K in 1 K steps.

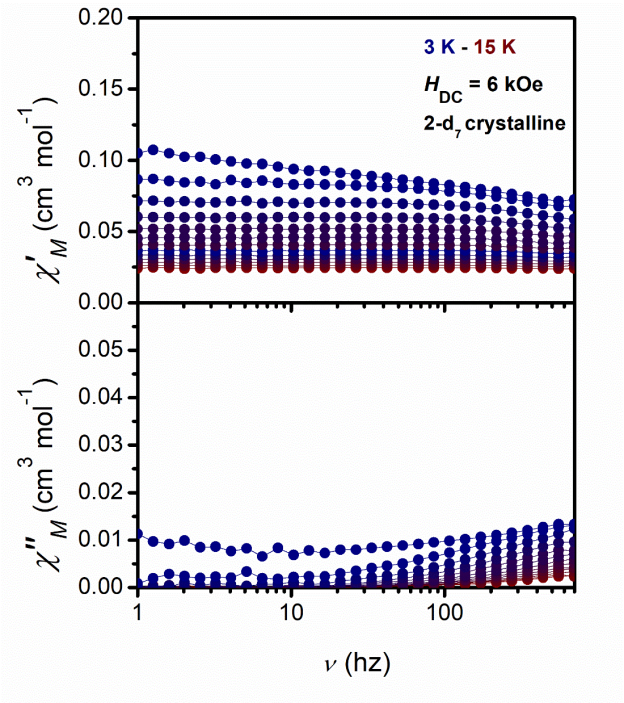

Figure A3.25 Frequency dependence of in-phase AC susceptibility of a crystalline sample of **2-d$_7$** with particle sizes as crystallized, measured from 3 K to 15 K in 1 K increments.

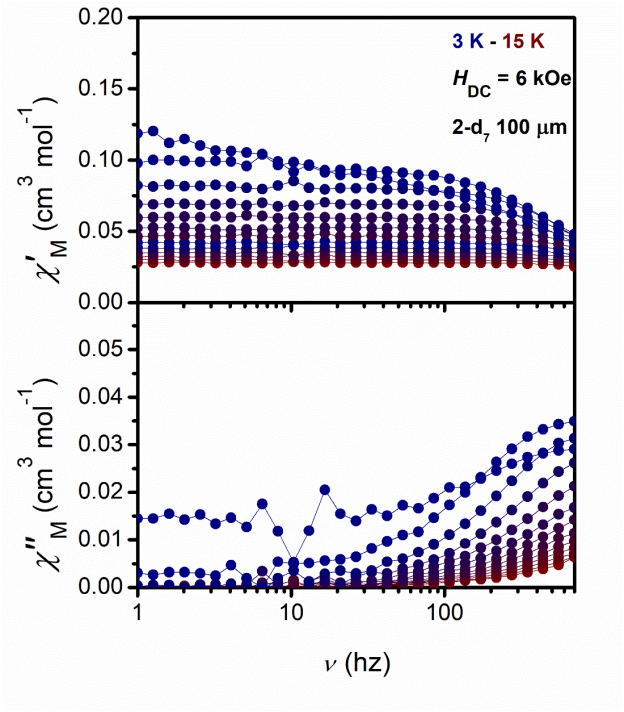

Figure A3.26 Frequency dependence of in-phase AC susceptibility of a powdered sample of **2-d$_7$** with particle sizes between 53 mm and 106 mm, measured at 6 kOe from 3 K to 15 K in 1 K increments.

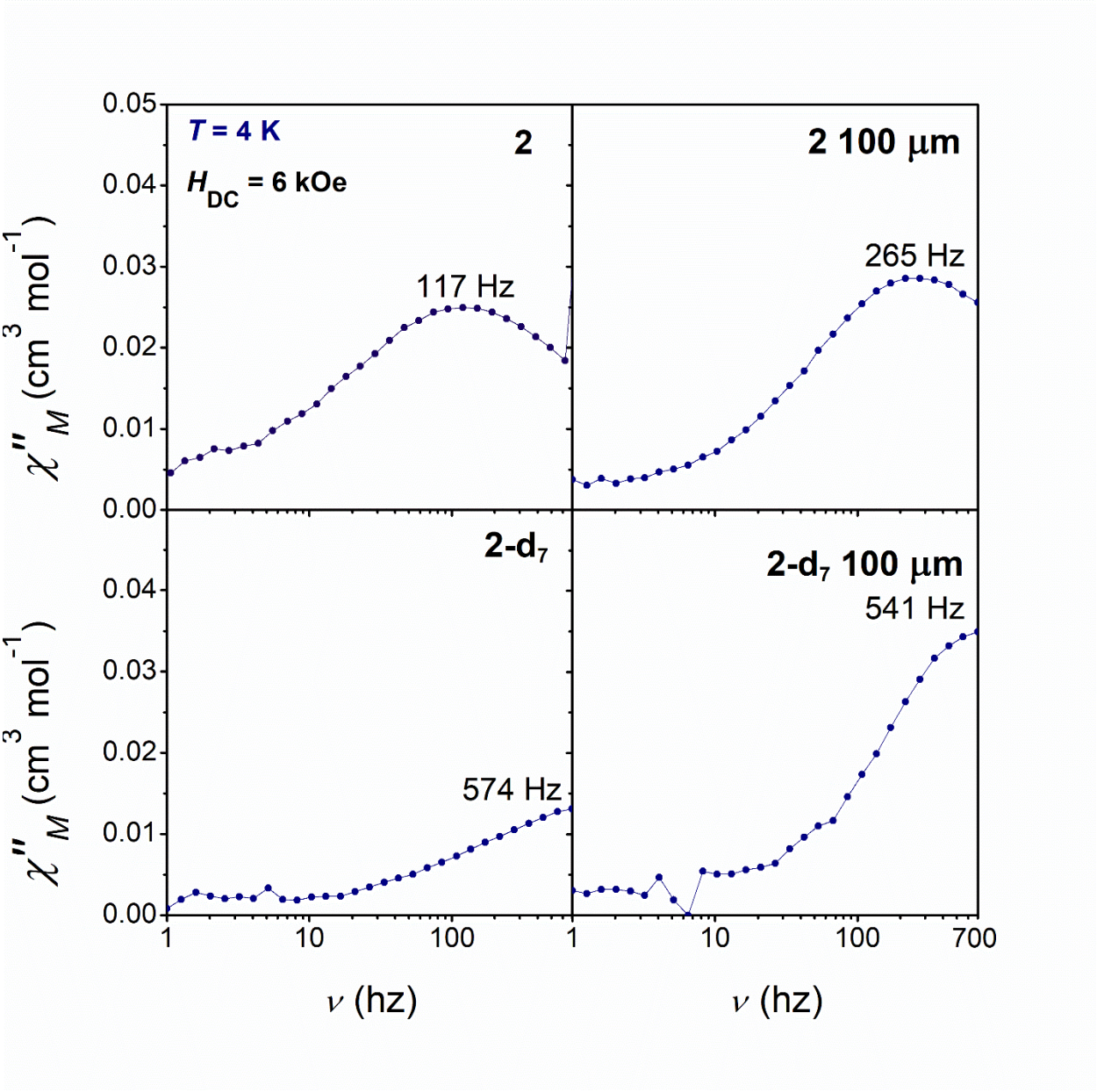

Figure A3.27 Out-of-phase frequency dependence of as-synthesized crystalline and 100 mm particle size samples of **2** and **2-d**$_7$, measured at 4 K with a 6 kOe applied field, with frequencies ranging from 1 Hz to 700 Hz.

AC susceptibility data interpretation for **2**

AC magnetic data were fit using the program CC-Fit2 to extract τ and produce the lines of best fit. For data where the maxima in the χ'' was not visible, the maximum values were generated by using Eq. S5, allowing the variables c_S, c_T, τ, and α refine freely.

$$\chi''(\omega) = (\chi_T - \chi_S)\frac{(\omega\tau)^{1-\alpha}\cos\left(\frac{\pi\alpha}{2}\right)}{1+2(\omega\tau)^{1-\alpha}\sin\left(\frac{\pi\alpha}{2}\right)+(\omega\tau)^{2-2\alpha}} \qquad \text{(Eq. A3.5)}$$

The relaxation profiles of the complexes were fit to several models using the different terms of Eq. S6 and the variables A, B, and n were allowed to refine freely.

$$\tau^{-1} = AT + BT^n + \tau_0 e^{\frac{-U_{eff}}{k_B T}} \qquad \text{(Eq. A3.6)}$$

For completeness, attempts to fit the data to many models (singly or in combination) are shown in Figures S28 and S29. In several cases, including the Orbach term led to analytical expressions that matched up relatively well with the data. Notwithstanding, in the final analysis, we discarded models with non-zero Orbach contributions, as theoretically there are no higher magnetic states for the complex to utilize (as a S=1/2 system without spin-orbit coupling). Instead, only the Raman term was used in the final fits as the data in the log-log plots of relaxation times vs temperature gave nearly linear fits when constrained to the two temperature regimes. Utilizing fits from the $\log(\tau^{-1})$ vs $\log(T)$ plots was a choice made for self-consistency in the presentation of the results; in most cases the extracted parameters are very similar to what was derived from fits to the τ^{-1} vs T data. The results of all fits considered are shown below in Table A35.

Table A3.5 Parameters for fitting AC data to several models. Italicized fits are shown in the main text.

	A	B	n	t_0^{-1} (s^{-1})	U_{eff}/k_B (cm^{-1})	R^2
2 crystalline[a]	97.81	5.01	1.80			0.828
2 crystalline[a]		0.20	2.00	2551	5.90	0.933
2 crystalline LT[a]		1.02	4.76			0.999
2 crystalline LT[b]		*0.14*	*6.30*			*0.986*
2 crystalline HT[a]		275.56	0.71			0.983
2 crystalline HT[a]	145.55					0.901
2 crystalline HT[b]		*292.42*	*0.68*			*0.979*
2 ground HT[a]		32.25	1.50			0.995
2 ground HT[a]	45.60	5.70	2.00			0.996
2 ground LT[a]		3.57	3.12			0.981
2 ground LT[b]		*179.10*	*1.25*			*0.995*
2 ground HT[b]		*516.65*	*0.52*			*0.996*
2 ground[a]	44.20	6.04	2.00			0.989
2 ground[a]		5.42	2.00	1152	8.19	0.99[8
2 100 µm[a]	285.21					0.596
2 100 µm[a]				4271	3.75	0.826
2 100 µm[b]		821.49	0.56			0.820
2 100 µm LT[b]		*207.68*	*1.49*			*1.000*
2 100 µm HT[b]		*1027.60*	*0.32*			*1.000*
2-d_7 crystalline[a]	734.49					0.962
2-d_7 crystalline[a]		1013.88	0.87			0.979
2-d_7 crystalline[b]		*1148.68*	*0.81*			*0.985*
2-d_7 100 µm[a]	748.45					0.964
2-d_7 100 µm[a]		1007.74	0.88			0.976
2-d_7 100 µm[b]		*1136.84*	*0.82*			*0.984*

Fit from τ^{-1} vs T data. (b) Fit from $\log(\tau^{-1})$ vs $\log(T)$ data.

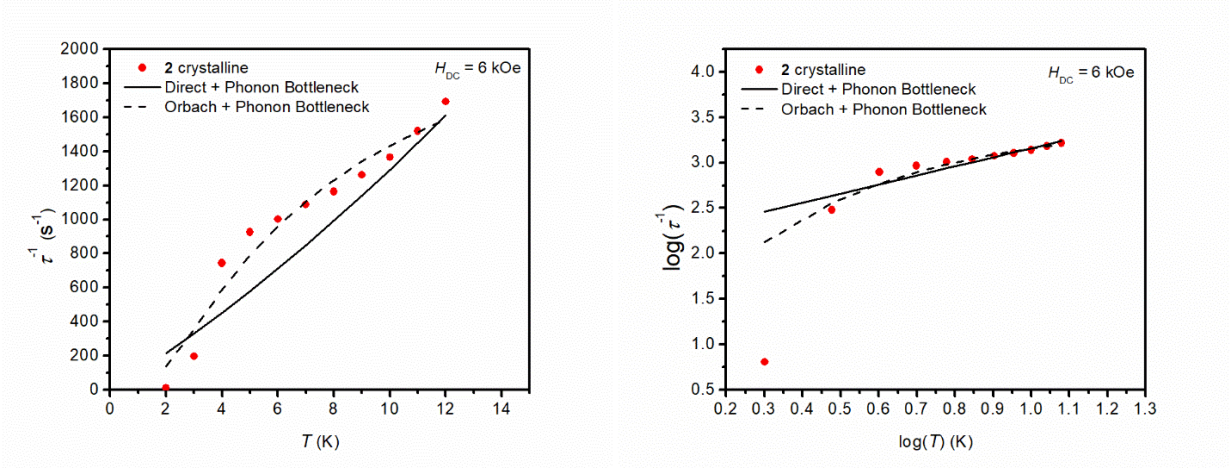

Figure A3.28 Temperature dependence of relaxation rates of a polycrystalline sample of **2** with a 6 kOe applied field. Lines represent the best fit using a hypothetical combination of direct, phonon bottleneck, and Orbach pathways. Left represents a linear plot; right represents a log-log plot of the same data.

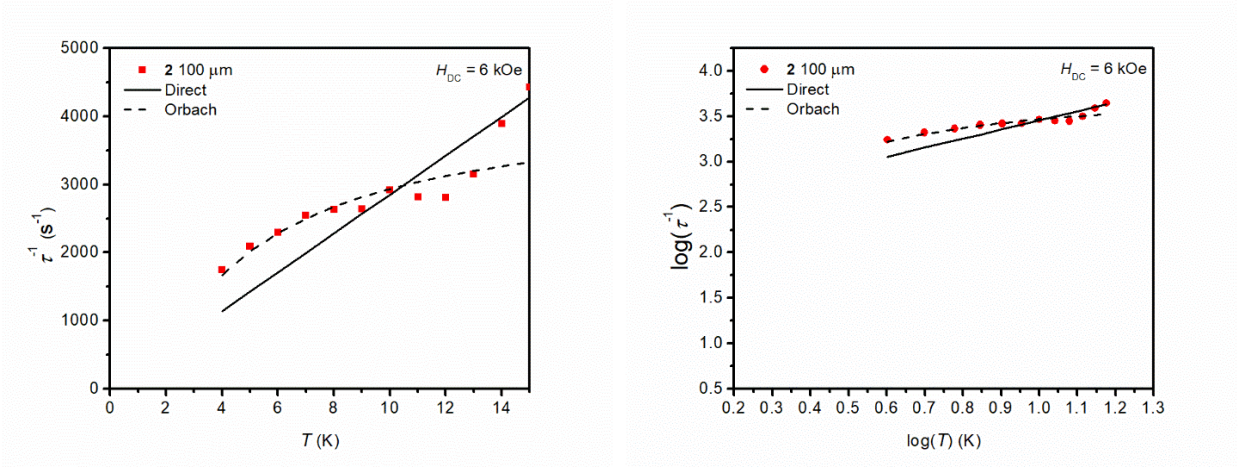

Figure A3.29 Temperature dependence of relaxation rates of a 100 µm sample of **2** with a 6 kOe applied field. Lines represent the best fit using a hypothetical direct or Orbach pathway. Left represents a linear plot; right represents a log-log plot of the same data.

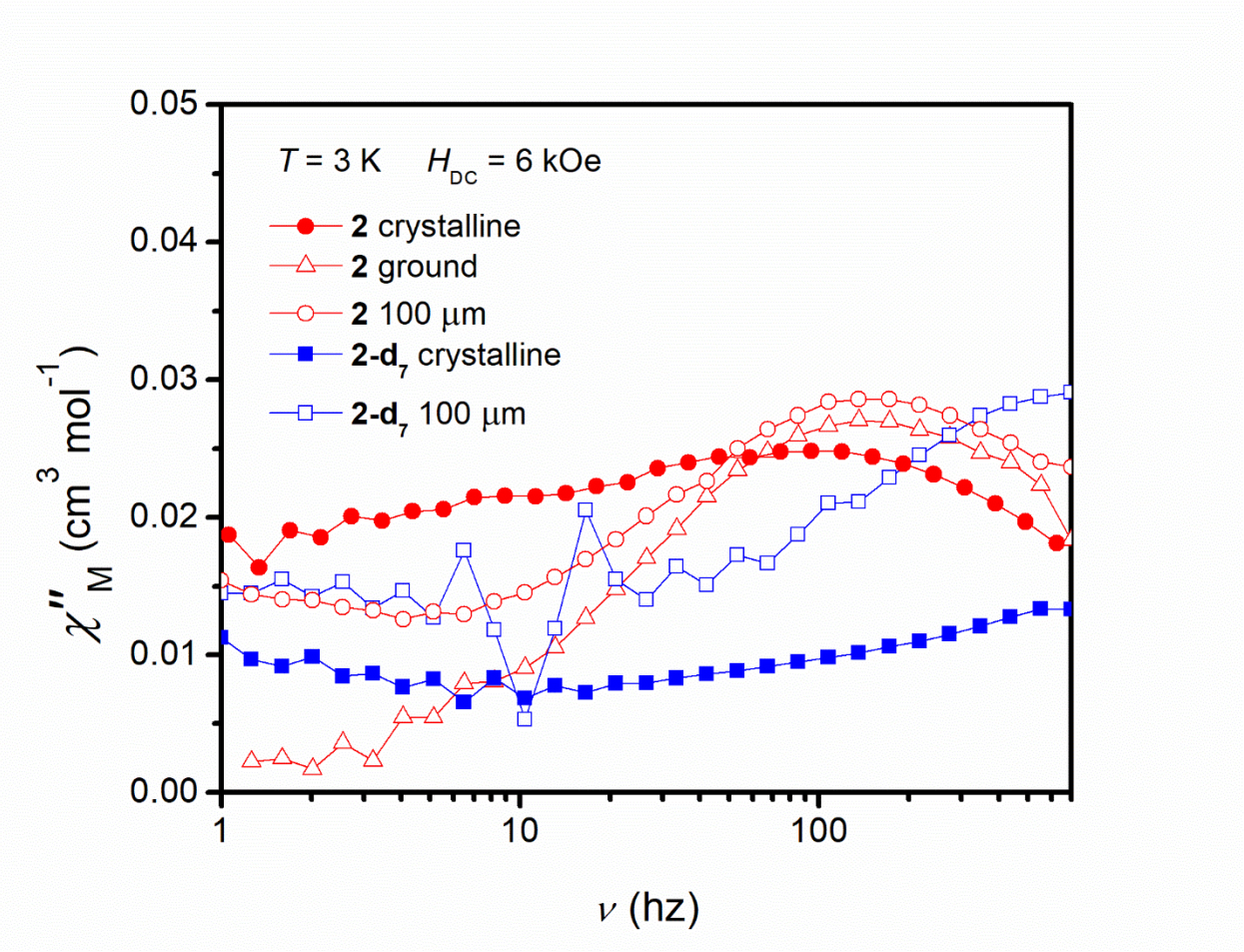

Figure A3.30 Comparison of frequency dependence of out-of-phase susceptibilities based on particle size: polycrystalline, ground polycrystalline, and 100 μm samples of **2**, polycrystalline and 100 μm samples **2-d7**. All samples were measured with a 6 kOe applied field at 3 K.

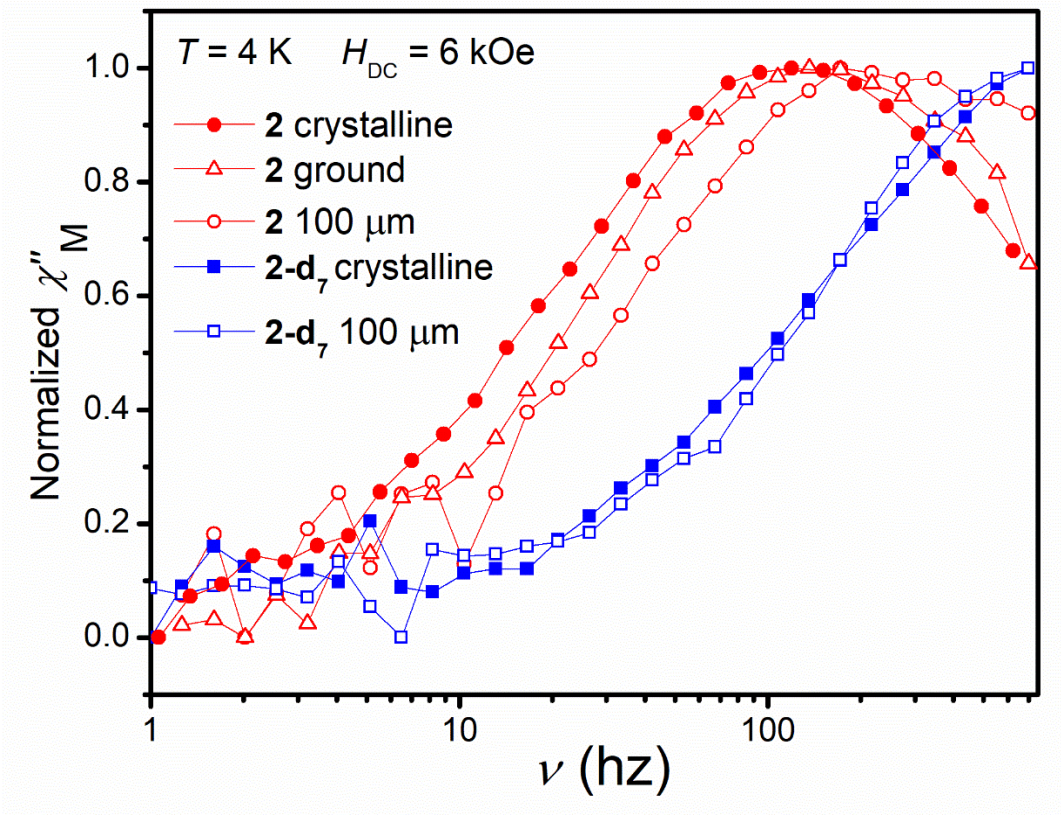

Figure A3.31 Comparison of frequency dependence of out-of-phase susceptibilities based on particle size: crystalline, ground crystalline, and 100 μm samples of **2**, and crystalline and 100 μm samples **2-d**$_7$. All samples were measured with a 6 kOe applied field at 4 K. Data was normalized to peak maxima.

Hirshfeld surface analysis

The program *CrystalExplorer* was used to calculate the Hirshfeld surface plots based on the crystal structures of the materials presented here.[3] The thermal ellipsoids are shown at 50% probability and d_{norm}, the normalized contact distances, were mapped onto the Hirshfeld surface. The 2D fingerprint plots were derived from the Hirshfeld surfaces generated. Overall, the Hirshfeld surfaces highlight the many intermolecular hydrogen bonds. Notably, the fingerprint plots of 2 and 2-d_7 show a striking difference in the spikes resulting from the O-H contacts, particularly the asymmetry in 2-d_7. At first glance this might suggest a difference in the strength of the intermolecular interactions. We provisionally attribute these differences to arise from the different positions of the outer-sphere bisulfate hydrogen (or deuterium) atoms. However, we do note that in the H position in 2 was located from the difference map, whereas the D position in 2-d_7 was not able to be found and was instead calculated.

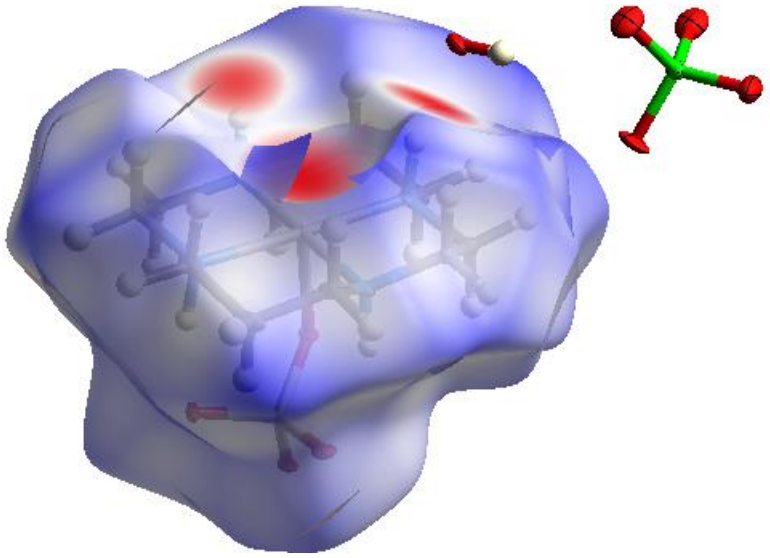

Figure A3.32 Hirshfeld surface (mapped with d_{norm}) of the monomer derived from the crystal structure of **1**, excluding the outer-sphere ions and solvents, showing the intermolecular H-bonding as intense red spots. Note that the central red spot on top is the polymeric bond to the sulfate bridge.

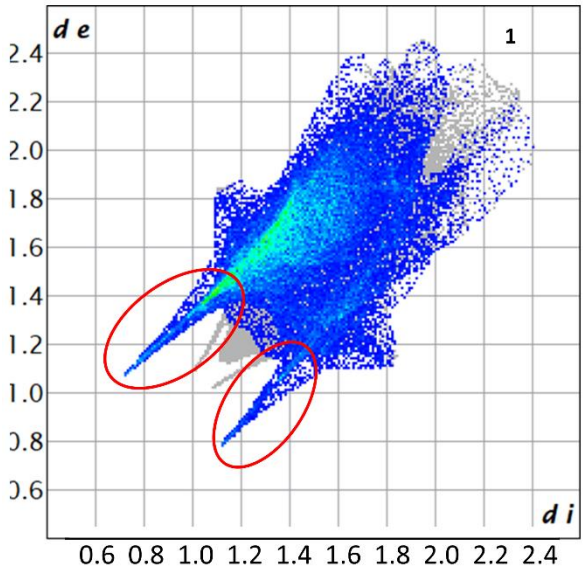

Figure A3.33 Fingerprint plot of **1** excluding the outer-sphere ions and solvents, highlighting the O-H close contacts that make up 52.3% of the surface area. Red circles highlight the O – H hydrogen bonds.

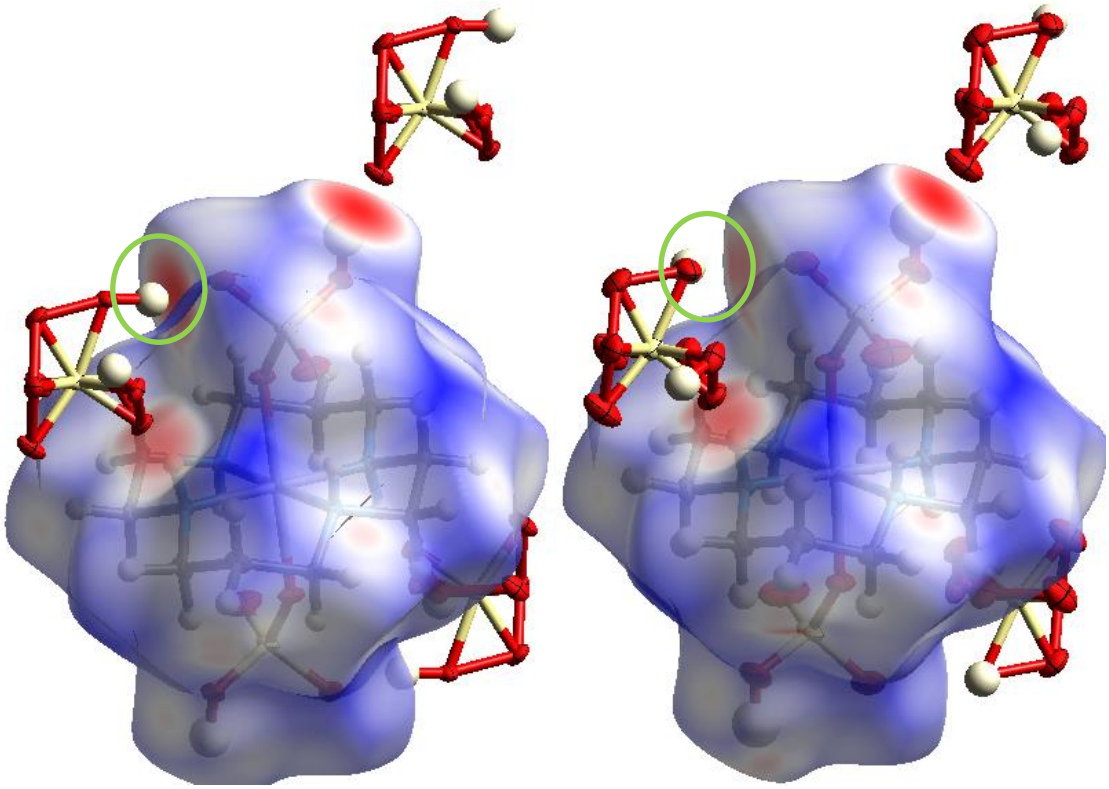

Figure A3.34 Hirshfeld surface (mapped with dnorm) derived from the crystal structure of **2** (left) and **2-d$_7$** (right), excluding the outer-sphere ions, showing the intermolecular H-bonding as intense red spots. Green circles show an example of different placement of the H/D atoms that in principle could modulate intermolecular interaction strengths.

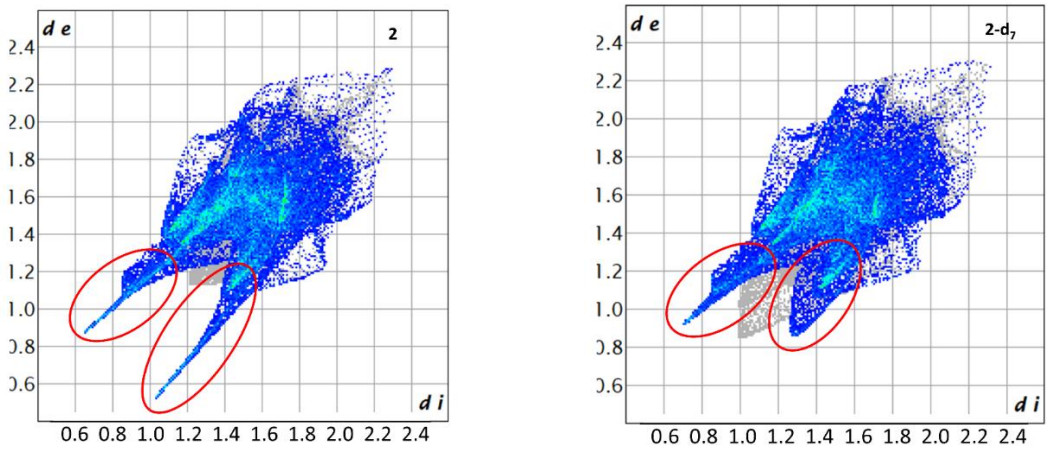

Figure A3.35. Fingerprint plot of **2** (left) and **2-d$_7$** (right) excluding the outer-sphere ions, highlighting the O-H close contacts that make up 55.2% and 53.2% of the surface area, respectively. Red circles highlight the O – H hydrogen bonds.

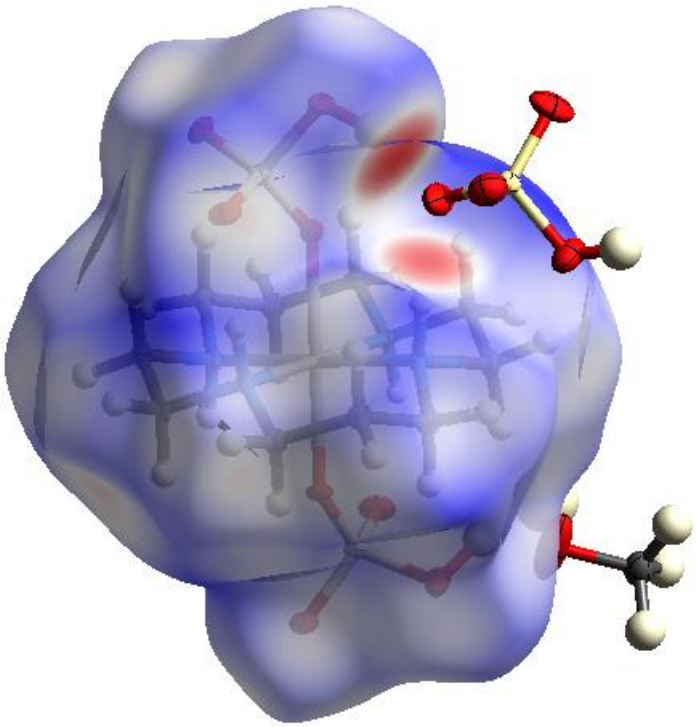

Figure A3.36 Hirshfeld surface (mapped with d_{norm}) of **2 MeOH**, excluding the outer-sphere ion and solvent, showing the intermolecular H-bonding as intense red spots.

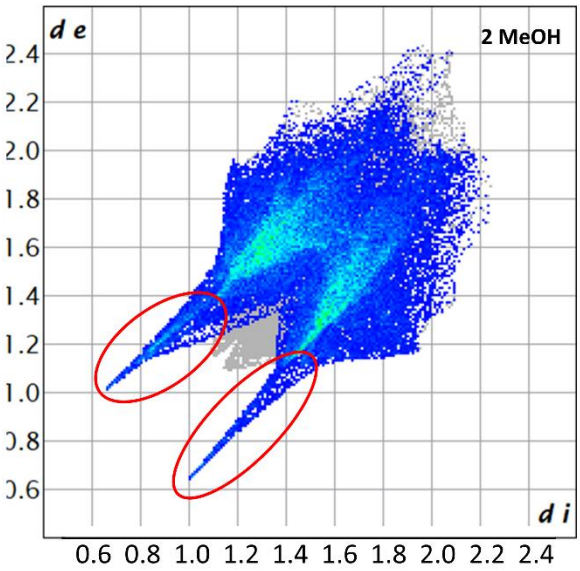

Figure A3.37 Fingerprint plot of **2 MeOH**, highlighting the O-H close contacts that make up 59.6% of the surface area. Red circles highlight the O – H hydrogen bonds.

References

(1) Bendix, J. Electron Paramagnetic Resonance. By Victor Chechik, Emma Carter, and

Damien Murphy. *Angew. Chemie Int. Ed.* **2017**, *56* (9), 2247–2247. https://doi.org/10.1002/anie.201612665.

(2) Chilton, N. F.; Anderson, R. P.; Turner, L. D.; Soncini, A.; Murray, K. S. PHI: A Powerful New Program for the Analysis of Anisotropic Monomeric and Exchange-Coupled Polynuclear d- and f-Block Complexes. *J. Comput. Chem.* **2013**, *34* (13), 1164–1175. https://doi.org/10.1002/jcc.23234.

(3) Spackman, P. R., Turner, M. J., McKinnon, J. J., Wolff, S. K., Grimwood, D. J., Jayatilaka, D. & Spackman, M. A. (2021). *J. Appl. Cryst.* 54, **3**, 1006–1011 https://doi.org/10.1107/S1600576721002910

Chapter 4 Appendix

Table A4.1 Select donor-acceptor distances in **1a**.

1a	Donor-acceptor distance (Å)
Ni1 N1-O	2.875(3)
Ni1 N2-O	2.935(8)
Ni2 N1-O	2.855(2)
Ni2 N2-O	3.065(2)

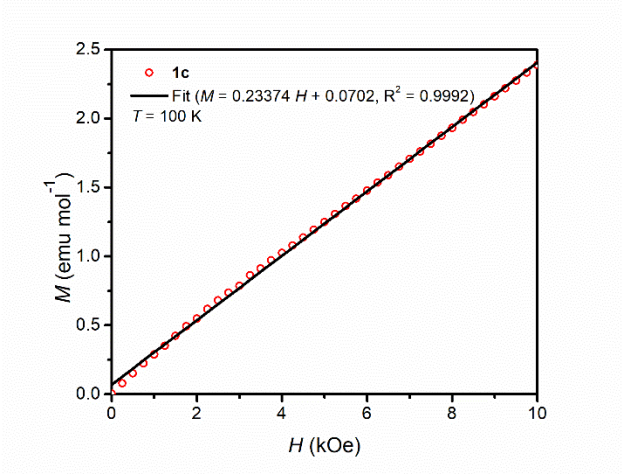

Figure A4.1 Magnetization vs field plot of **1c**, the magnetic dilution of **1a**. We note that the deviation from linearity at low fields may be due to ferromagnetic impurities, however in this case we attribute it due to the low signal of the sample. Each data point is the average of 10 scans, as opposed to the single scan for other samples.

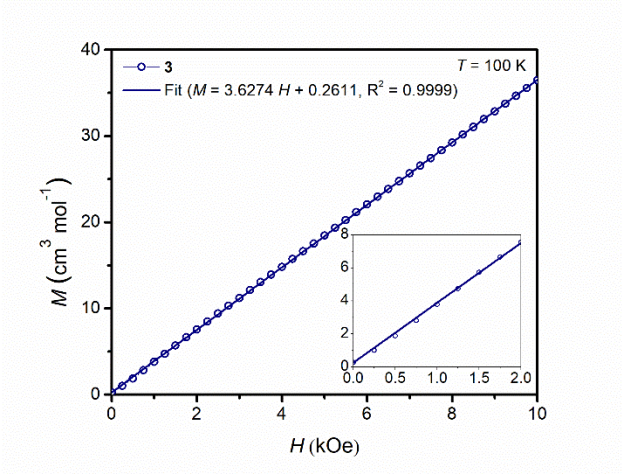

Figure A4.2 Magnetization vs field plot of **3** at 100 K.

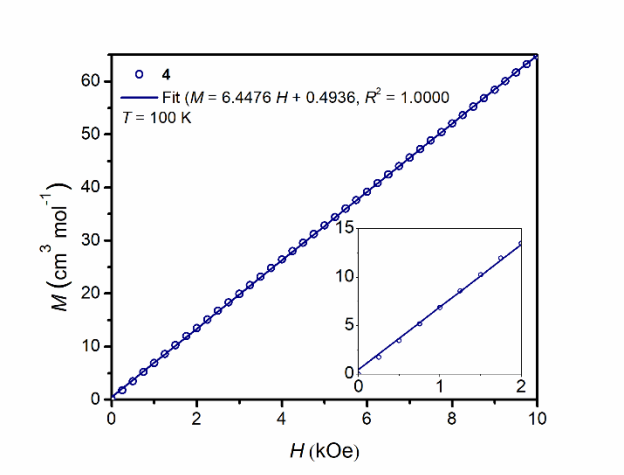

Figure A4.3 Magnetization vs field plot of **4** at 100 K.

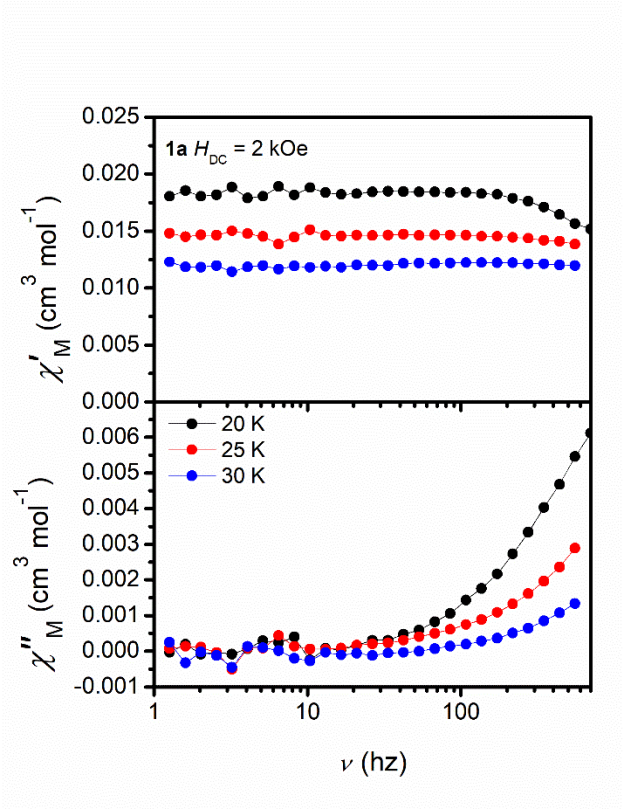

Figure A4.4 Enhanced view of temperature dependence of AC susceptibility of **1a** from 20 – 30 K at 2 kOe.

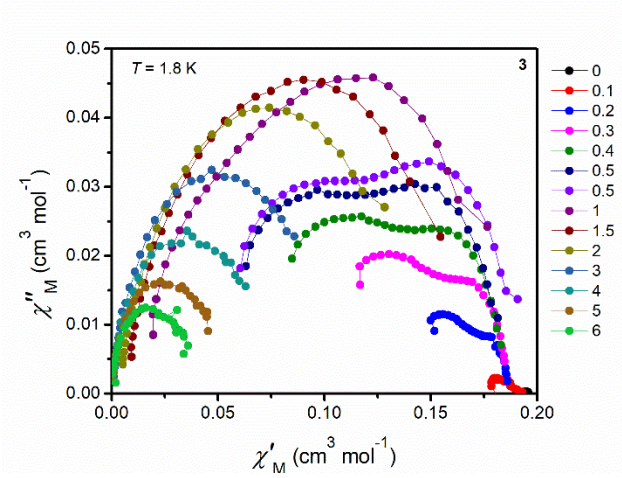

Figure A4.5 Cole-cole plot of **3** at 1.8 K from 0 – 6 kOe.

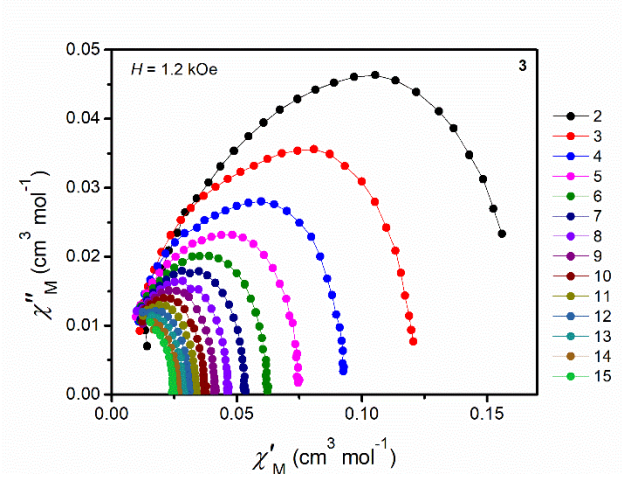

Figure A4.6 Cole-cole plot of **3** at 1.2 kOe from 2 – 15 K.

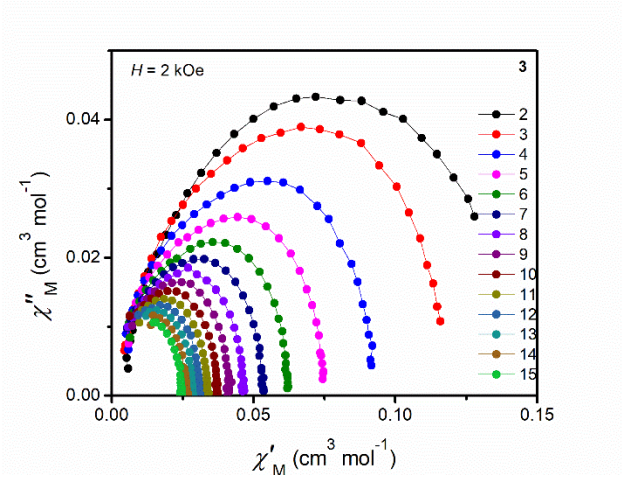

Figure A4.7 Cole-cole plot of **3** at 2.0 kOe from 2 – 15 K.

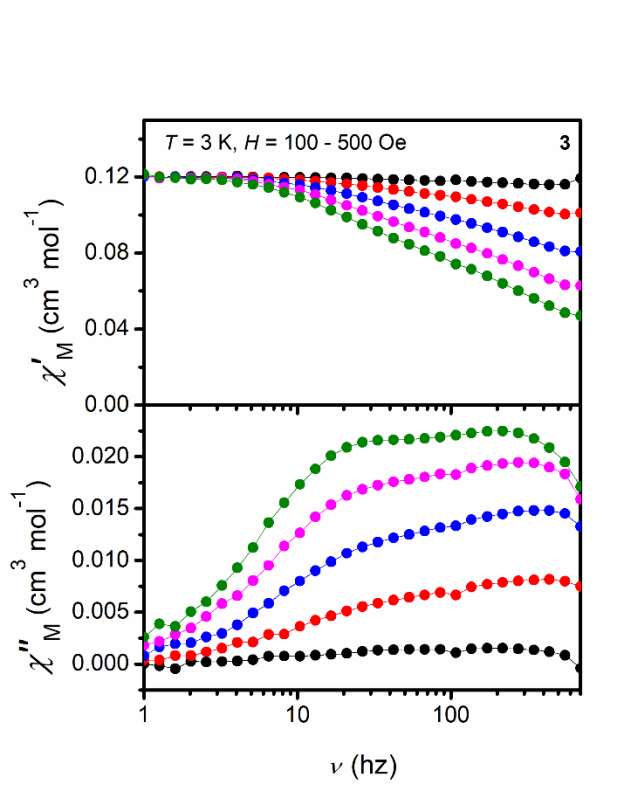

Figure A4.8 AC susceptibility of **3** at 3 K from 100 – 500 Oe.

Table A4.2 Fits of out-of-phase susceptibility of **3** at 1.2 kOe using a two-pathway model.

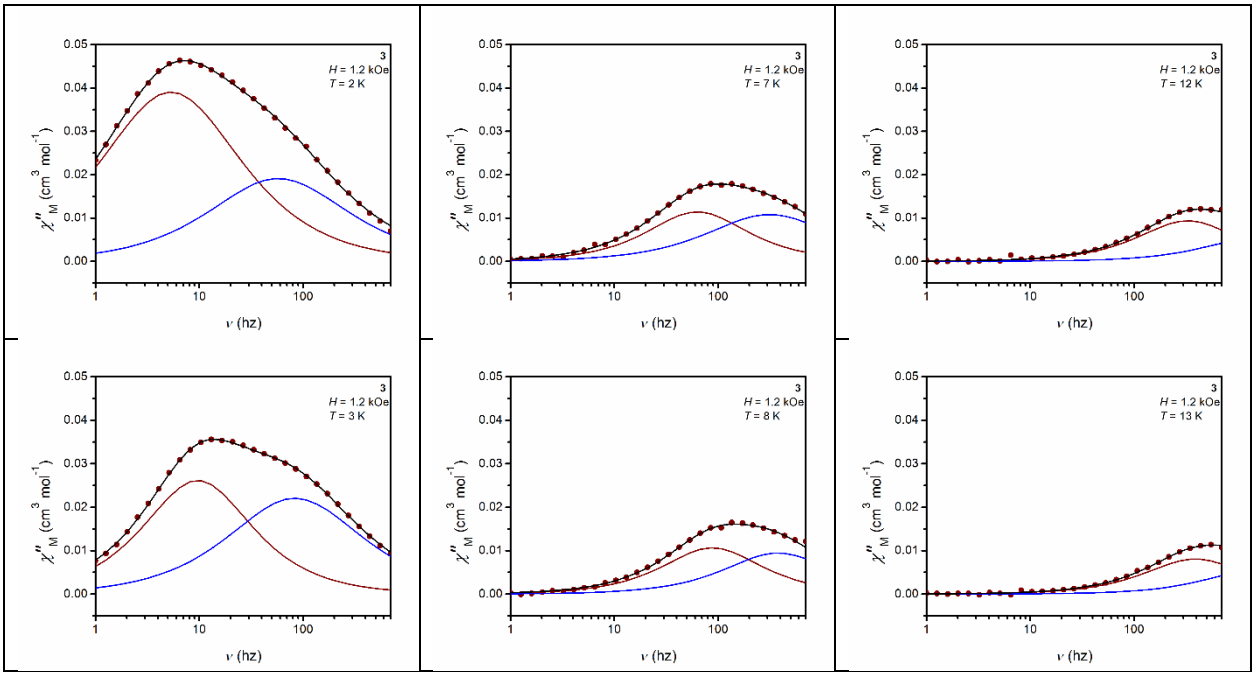

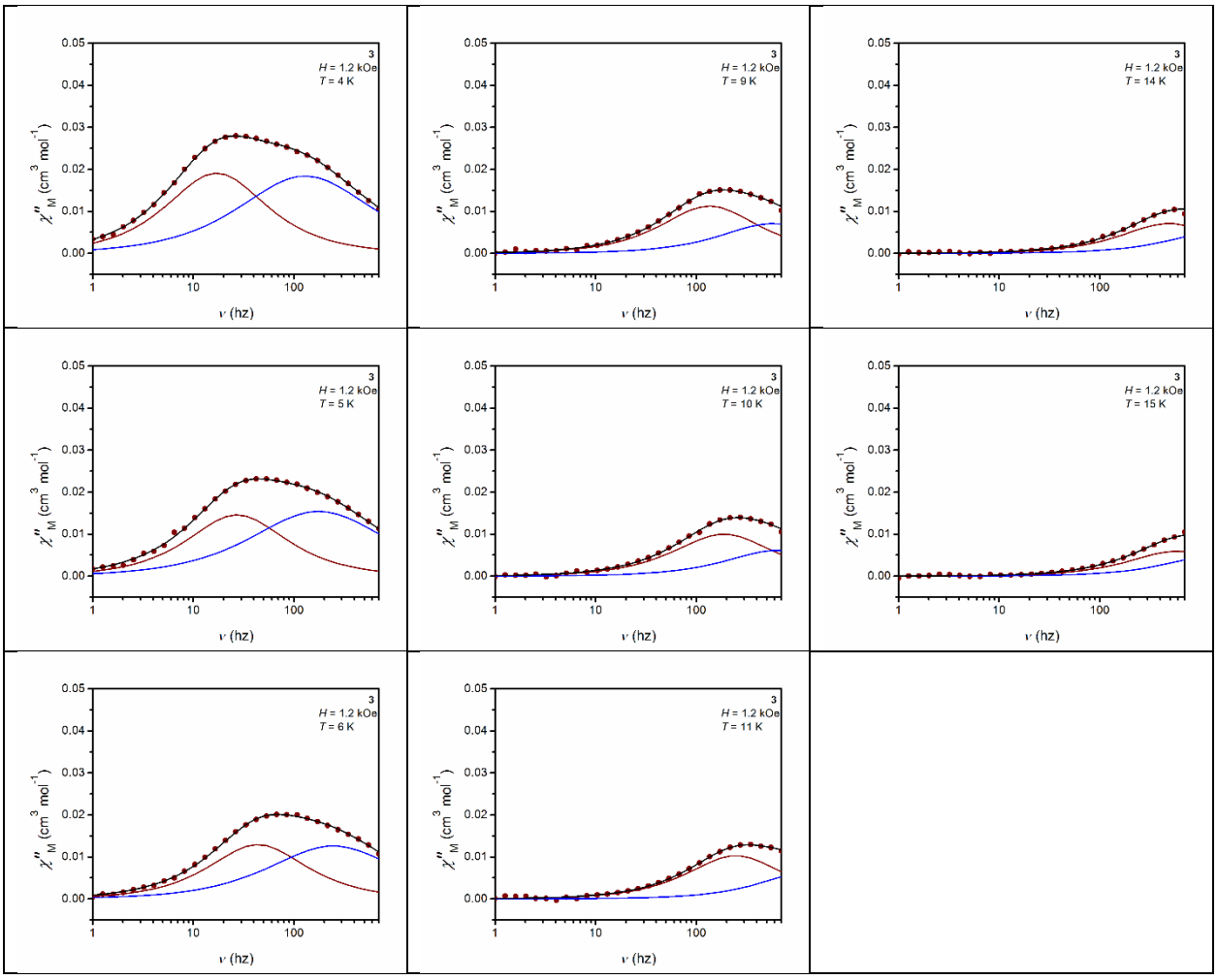

Table A4.1 Fits of out-of-phase susceptibility of **3** at 2 kOe using a two-pathway model.

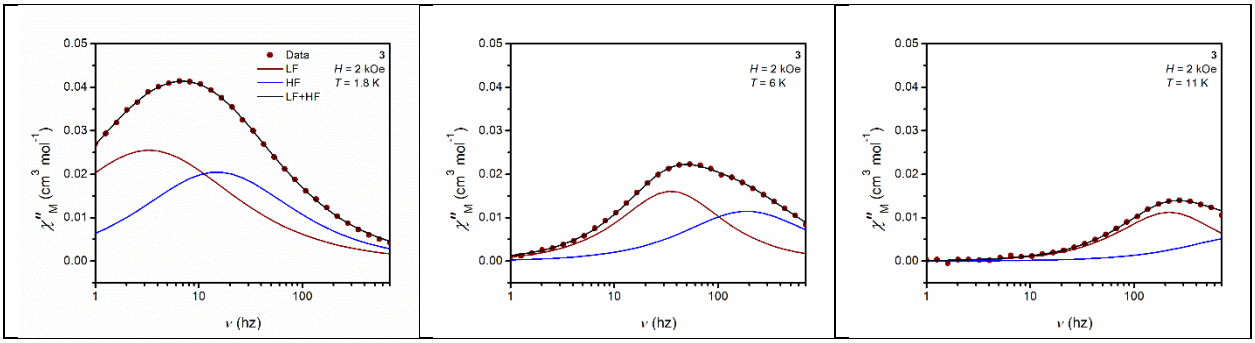

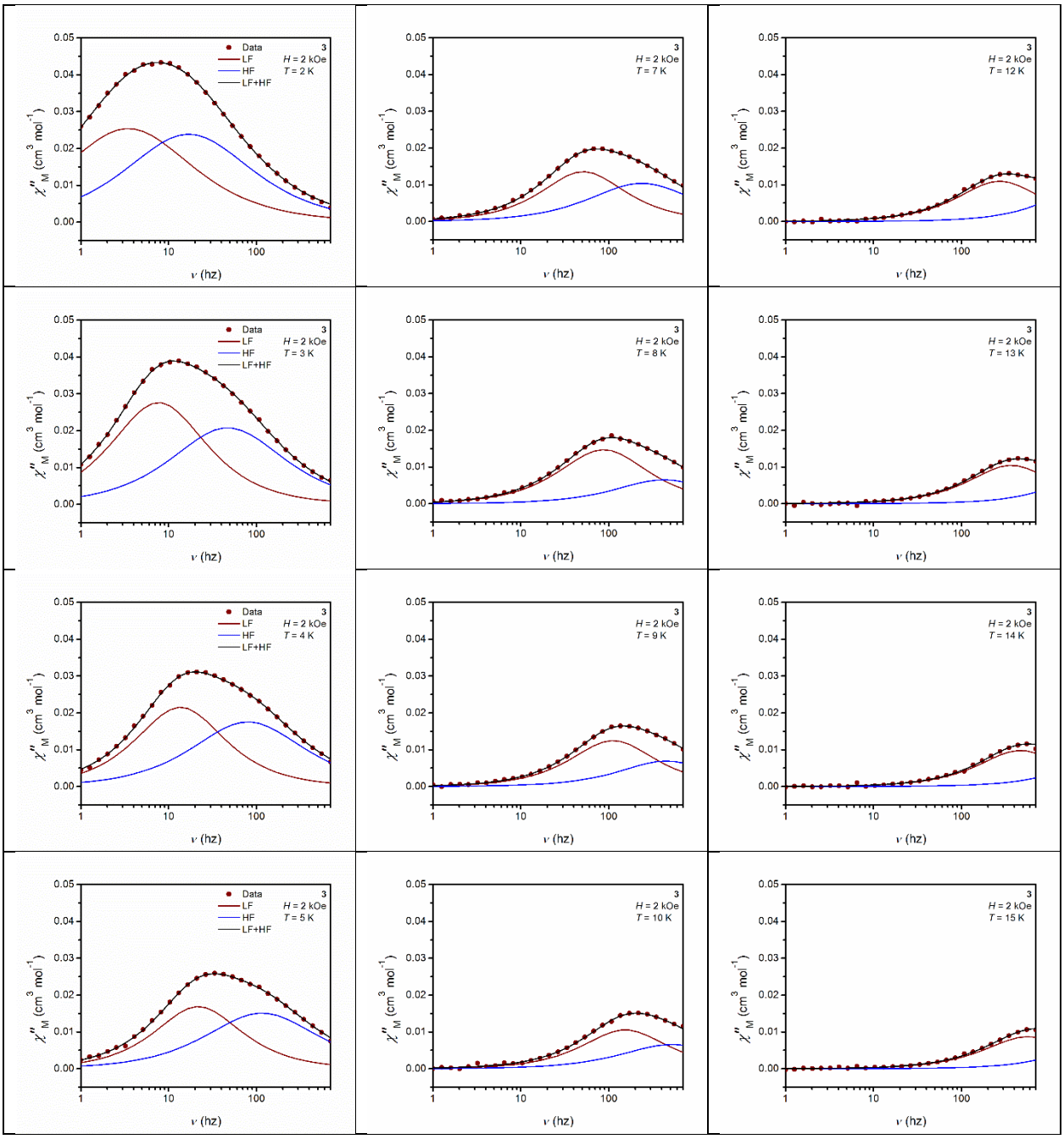
Data
LF
HF
LF+HF
3
H = 2 kOe
T = 2 K
T = 3 K
T = 4 K
T = 5 K
T = 7 K
T = 8 K
T = 9 K
T = 10 K
T = 12 K
T = 13 K
T = 14 K
T = 15 K
χ″M (cm3 mol-1)
ν (hz)

Chapter 5 Appendix

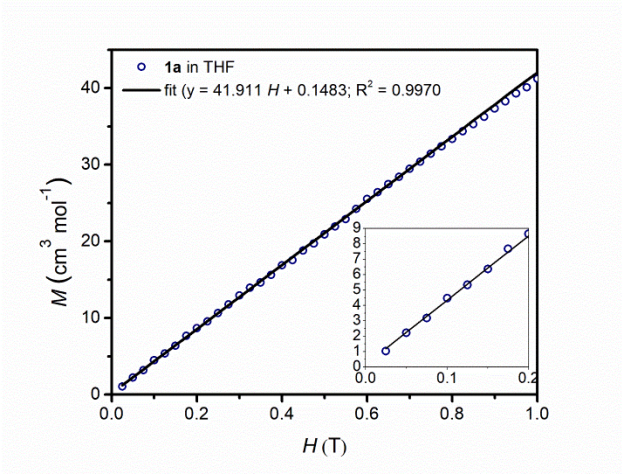

Figure A5.1 Magnetization vs field of **1a** in THF at 100 K.

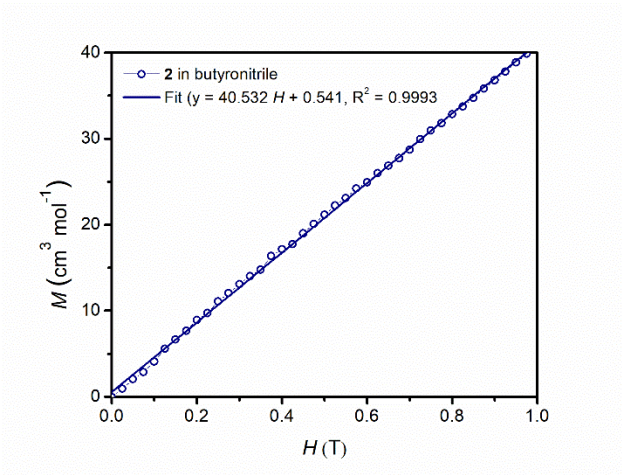

Figure A5.2 Magnetization vs field of **1a** in MeCN at 100 K.

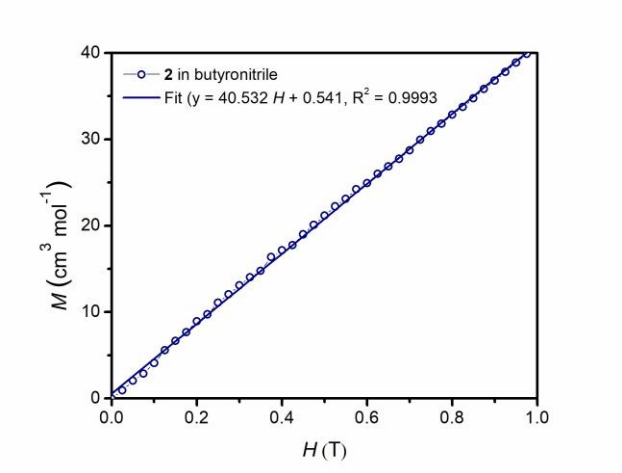

Figure A5.3 Magnetization vs field of **1a** in butyronitrile at 100 K.

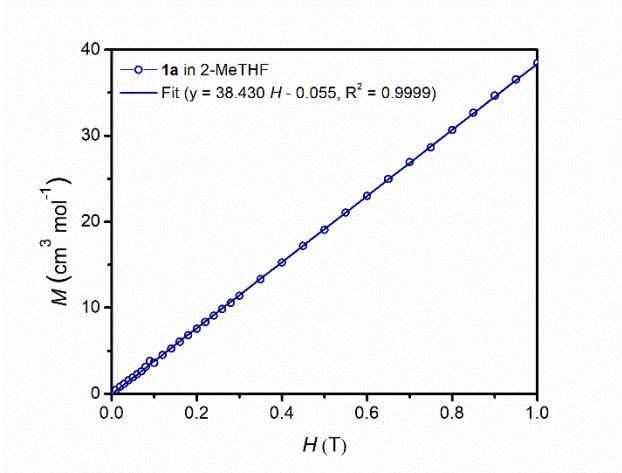

Figure A5.4 Magnetization vs field of **1a** in 2-MeTHF at 100 K.

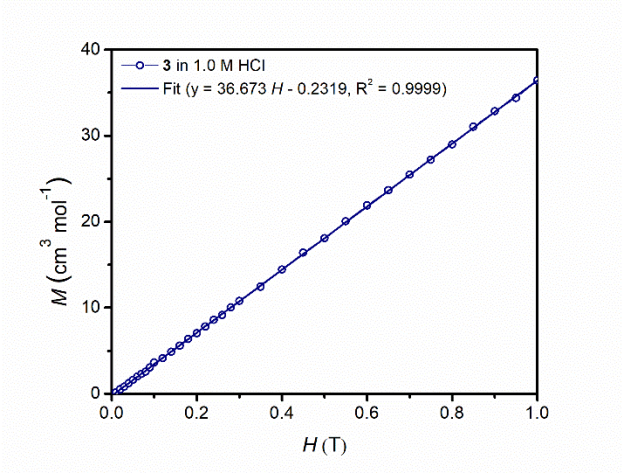

Figure A5.5 Magnetization vs field of **3** in 1.0 M HCl at 100 K.

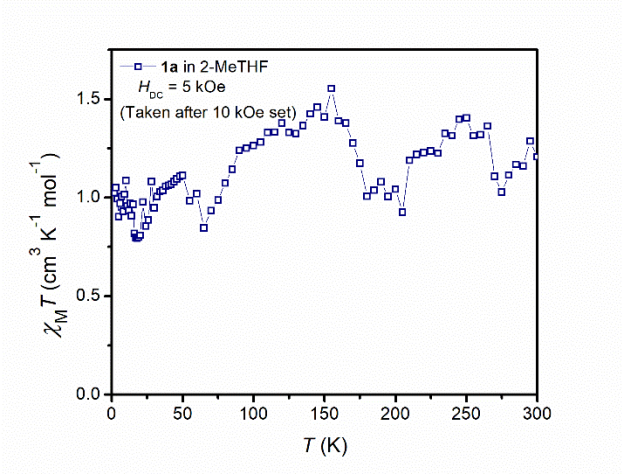

Figure A5.6 DC susceptibility of **1a** in 2-MeTHF at 5 kOe from 2 – 300 K, taken after the increase in susceptibility seen in the 10 kOe susceptibility plot.

Chapter 7 Appendix

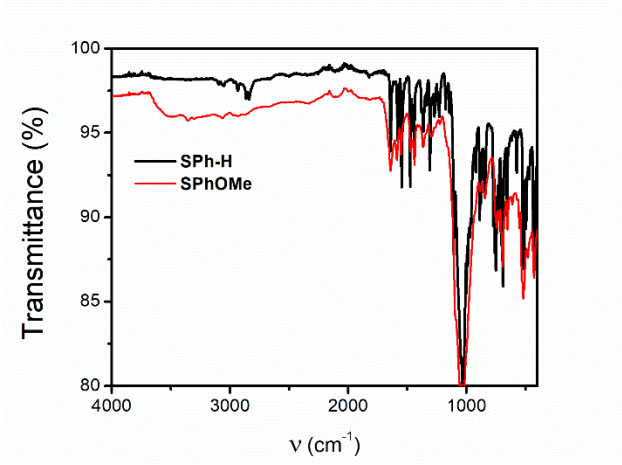

Figure A7.1 IR spectra of **SPh-H** and **SPhOMe** Ni complexes.

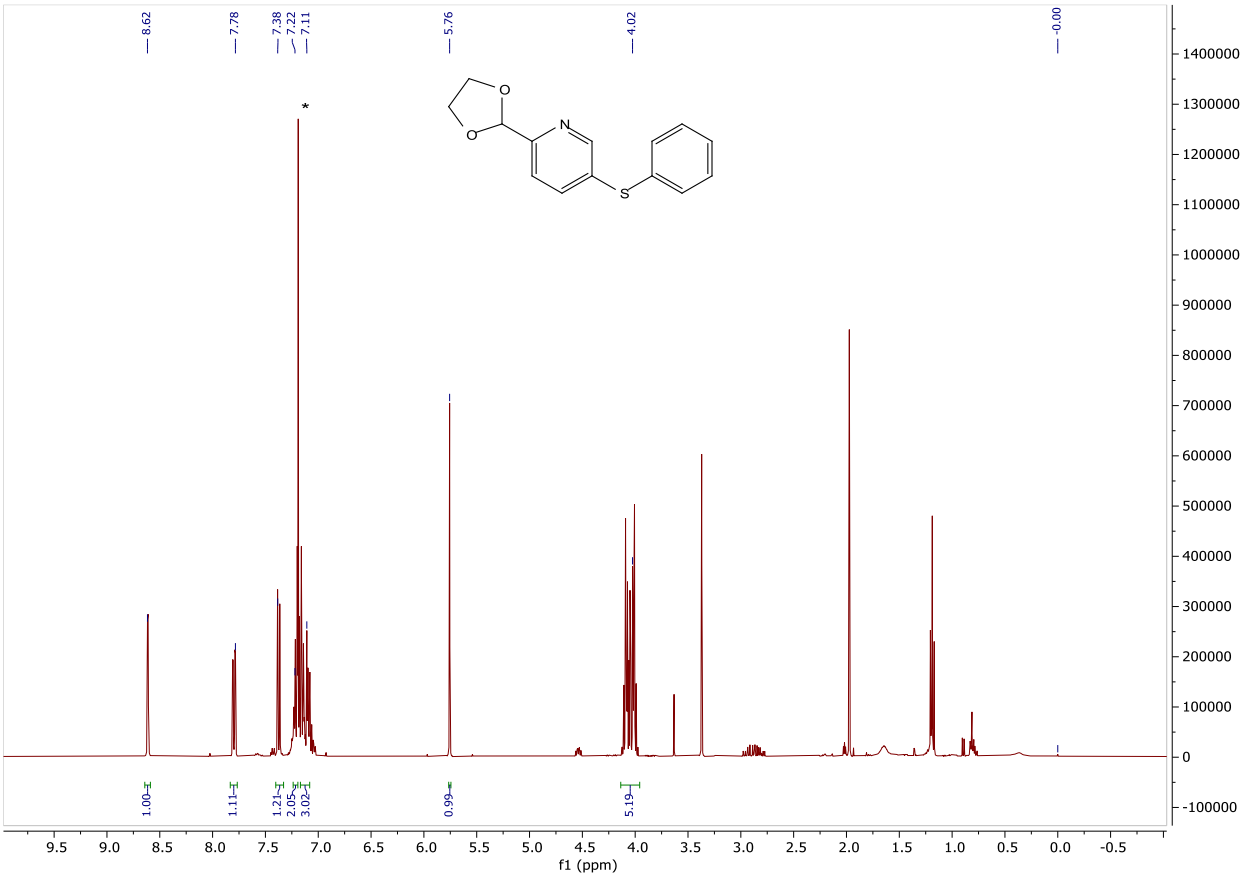

Figure A7.2 NMR of 2-(1,3-dioxolan-2-yl)-5-(phenylthio)pyridine in $CDCl_3$. Asterisk denotes $CDCl_3$ peak. References to TMS (δ 0.00).

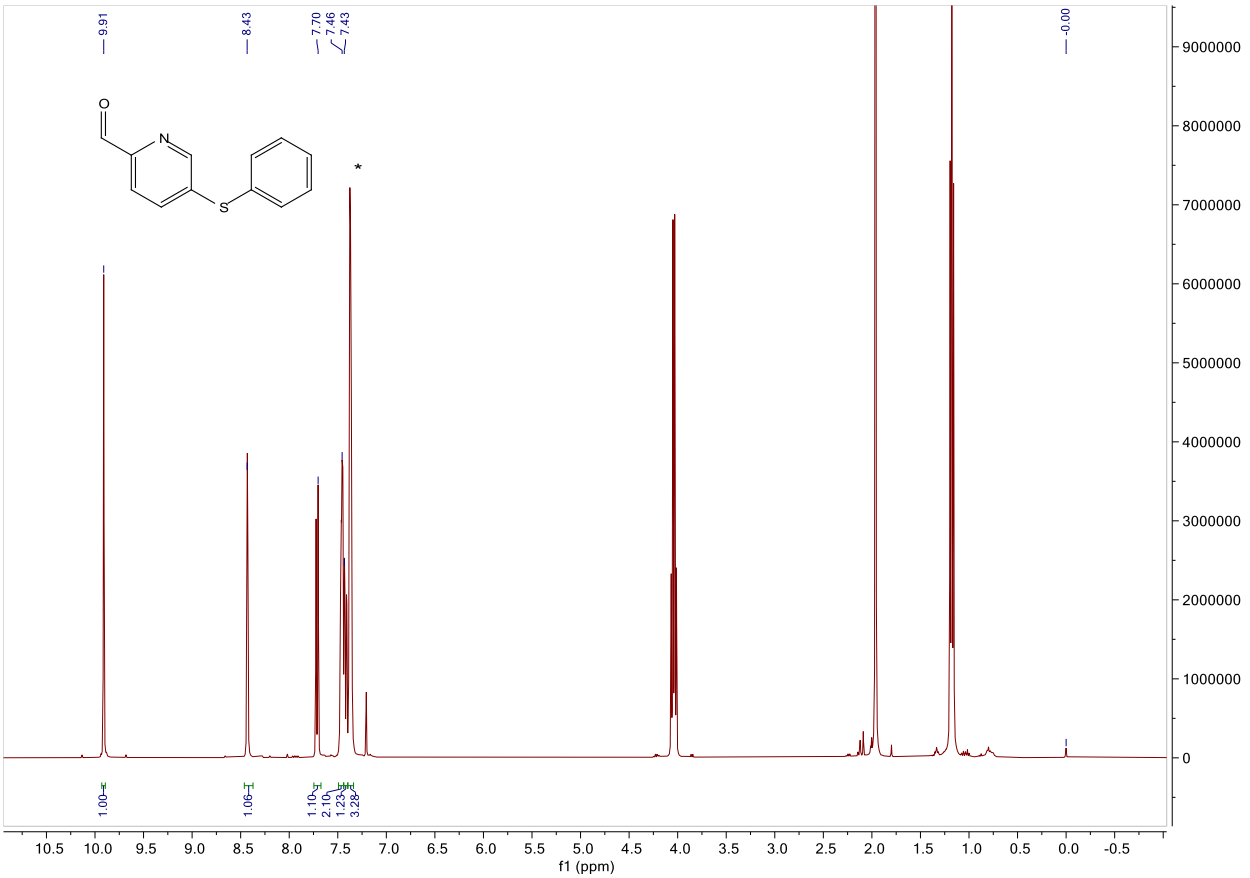

Figure A7.3 NMR of 5-(phenylthio)picolinaldehyde in $CDCl_3$. Asterisk denotes $CDCl_3$ peak. References to TMS (δ 0.00).

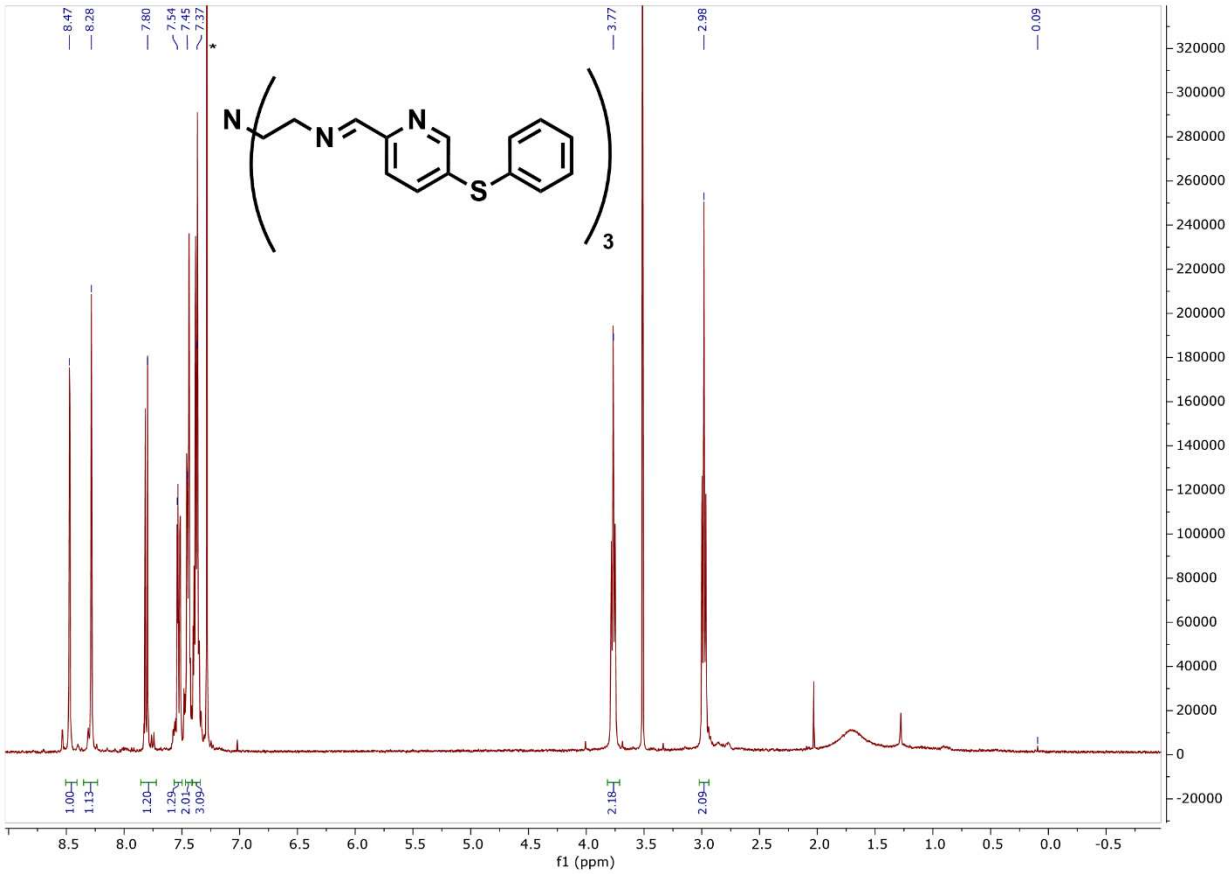

Figure A7.4 NMR of tren(PySPh-H)$_3$ in $CDCl_3$. Asterisk denotes $CDCl_3$ peak. References to TMS (δ 0.00).

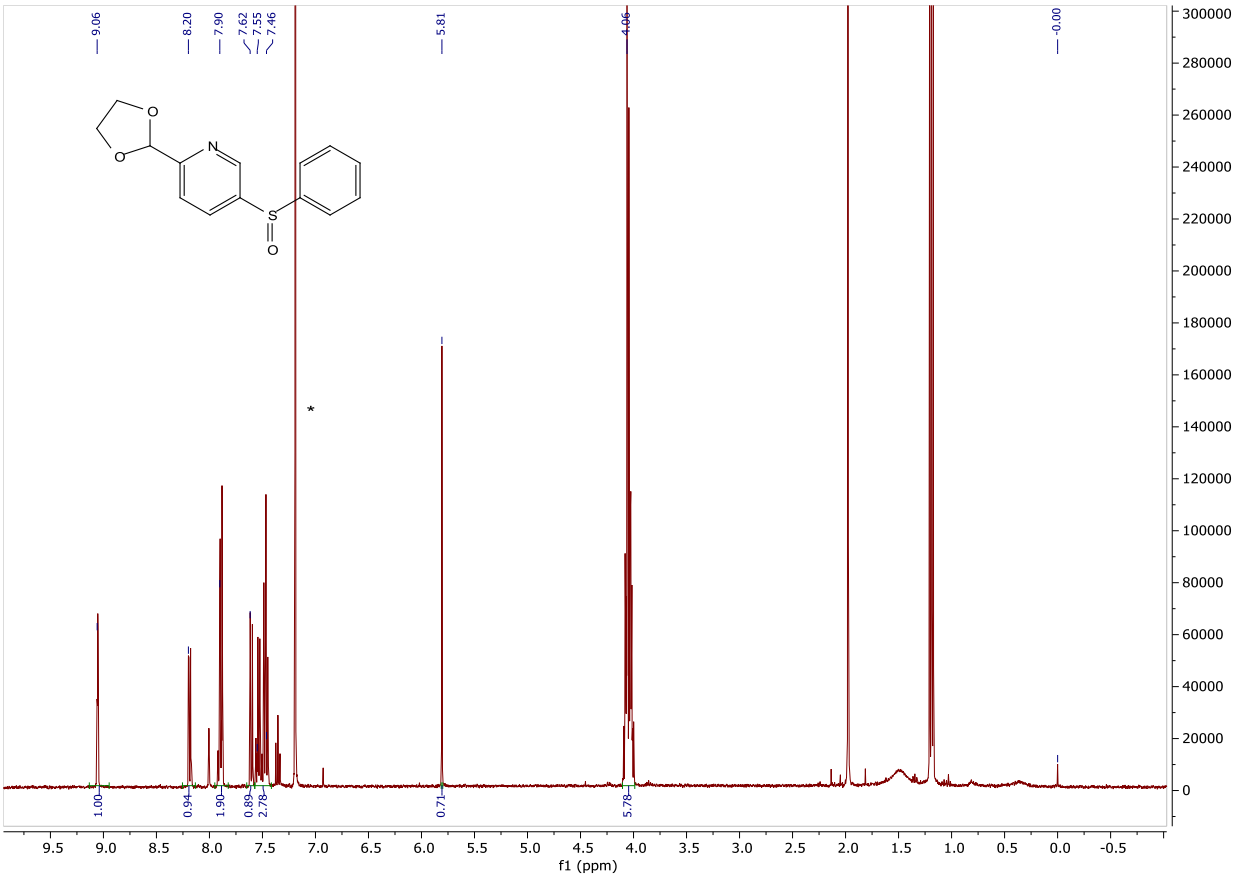

Figure A7.5 NMR of 2-(1,3-dioxolan-2-yl)-5-(phenylsulfinyl)pyridine in $CDCl_3$. Asterisk denotes $CDCl_3$ peak. References to TMS (δ 0.00).

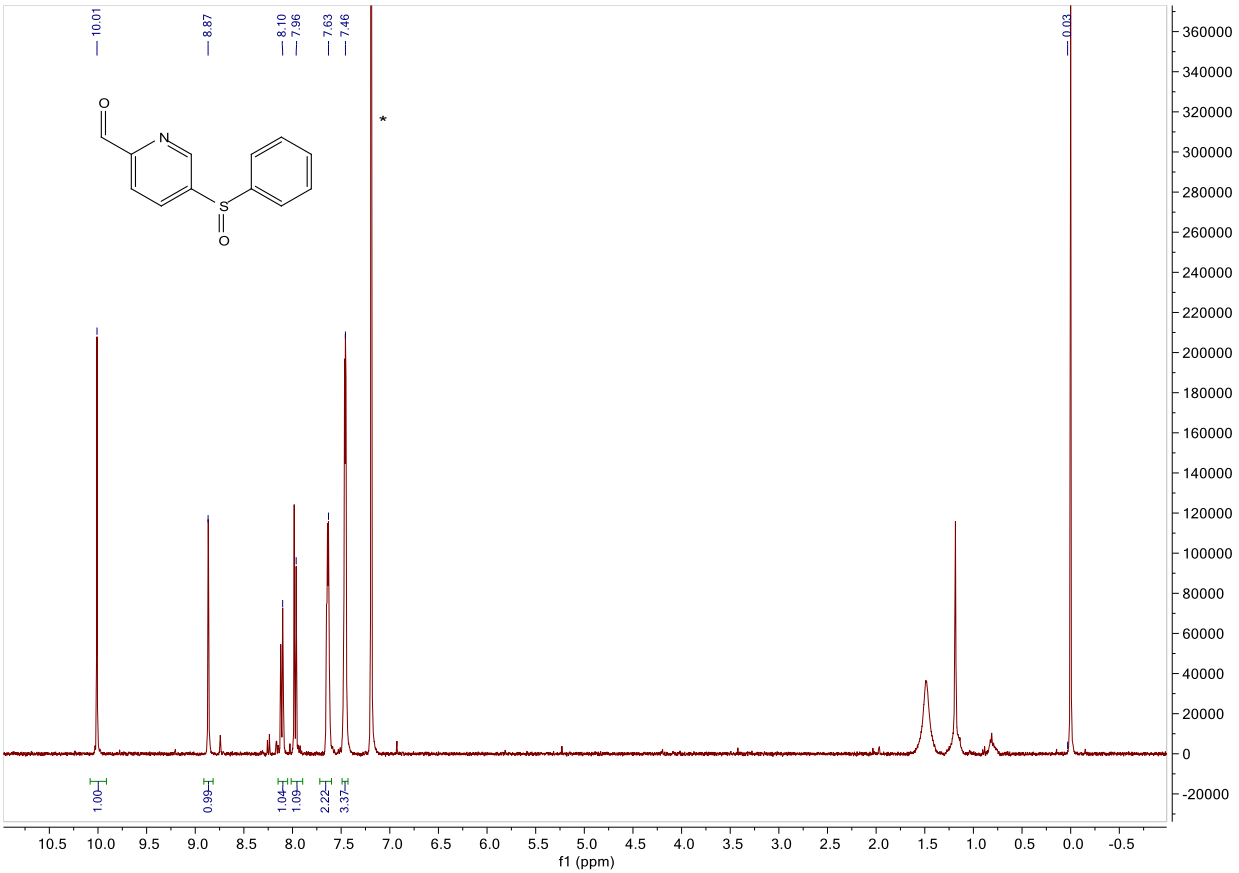

Figure A7.6 NMR of 5-(phenylsulfinyl)picolinaldehyde in $CDCl_3$. Asterisk denotes $CDCl_3$ peak. References to TMS (δ 0.00).

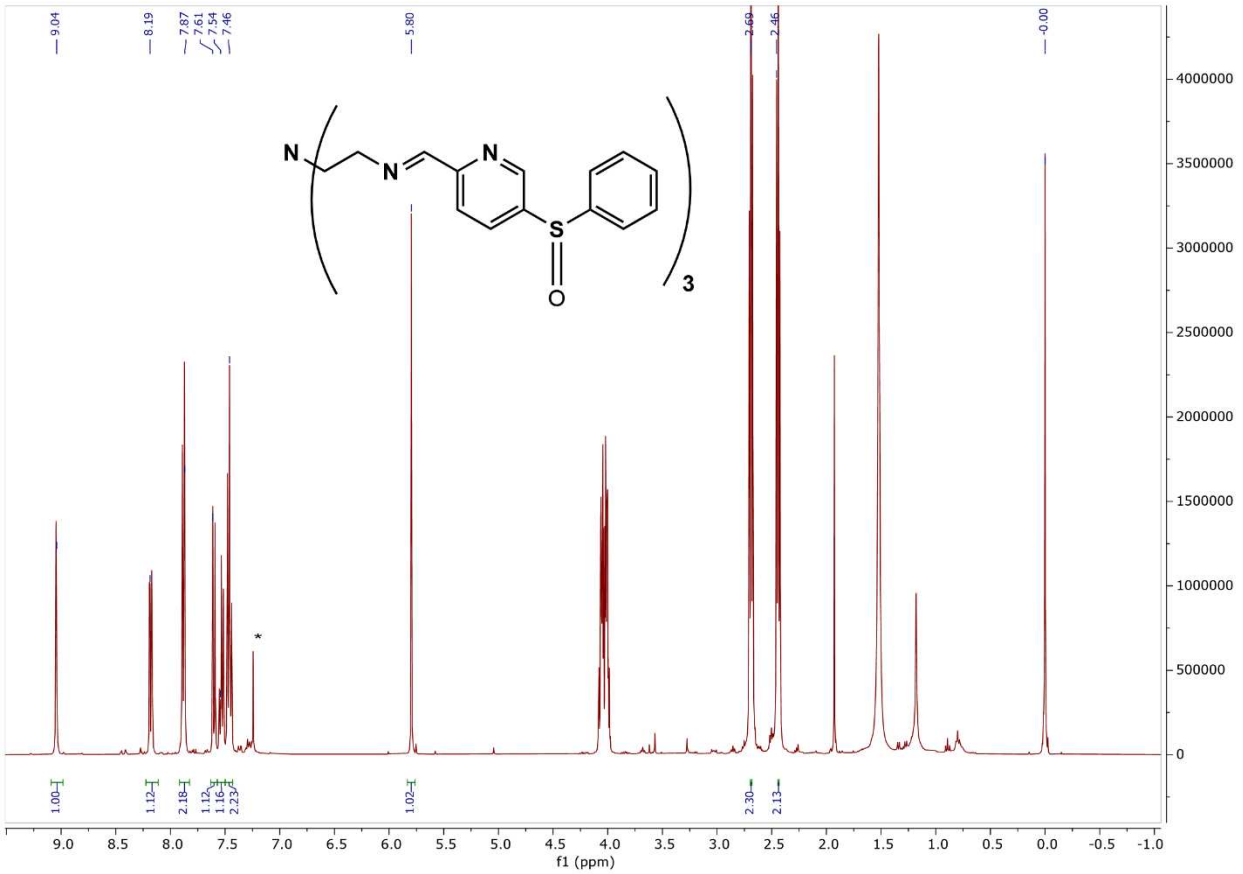

Figure A7.7 NMR of Tren(SOPh)$_3$ in $CDCl_3$. Asterisk denotes $CDCl_3$ peak. References to TMS (δ 0.00).

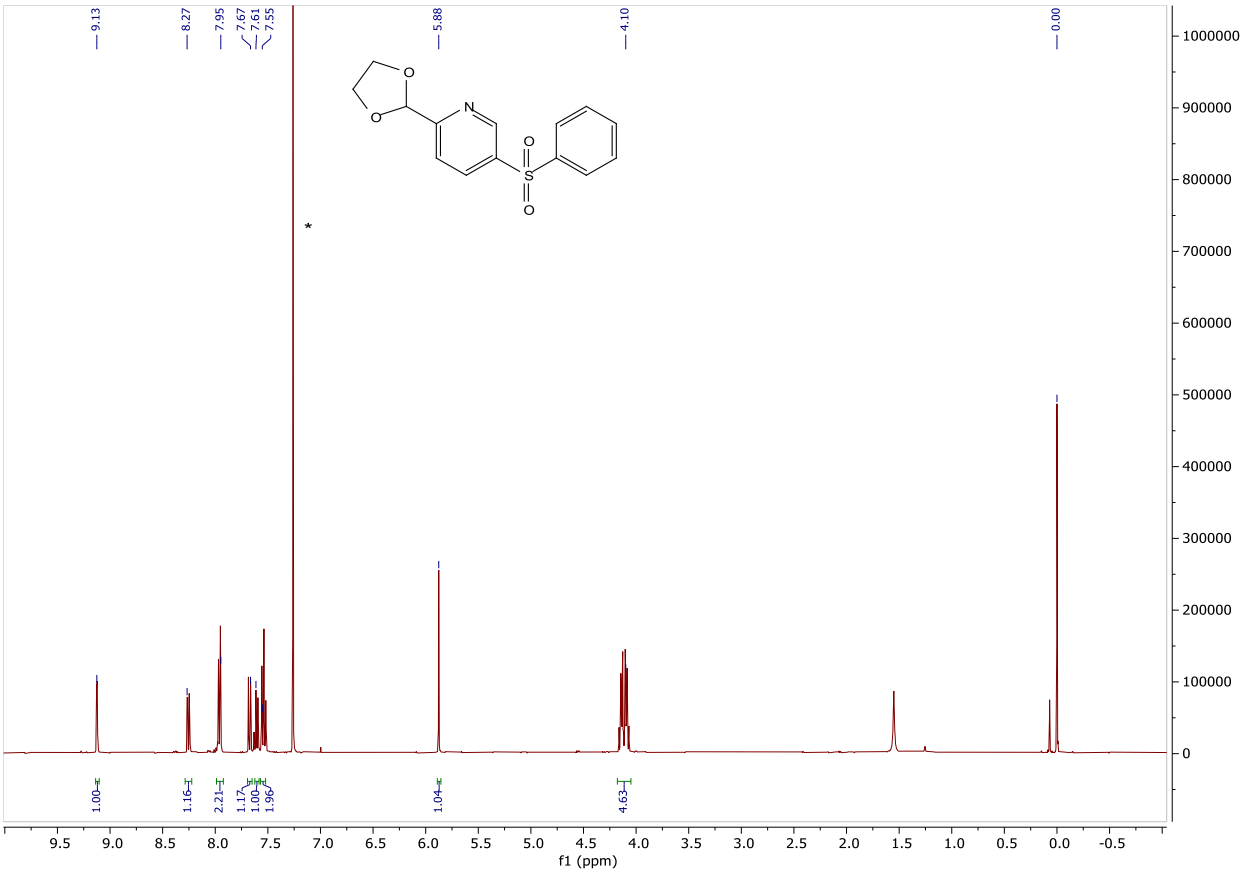

Figure A7.8 NMR of 2-(1,3-dioxolan-2-yl)-5-(phenylsulfonyl)pyridine in $CDCl_3$. Asterisk denotes $CDCl_3$ peak. References to TMS (δ 0.00).

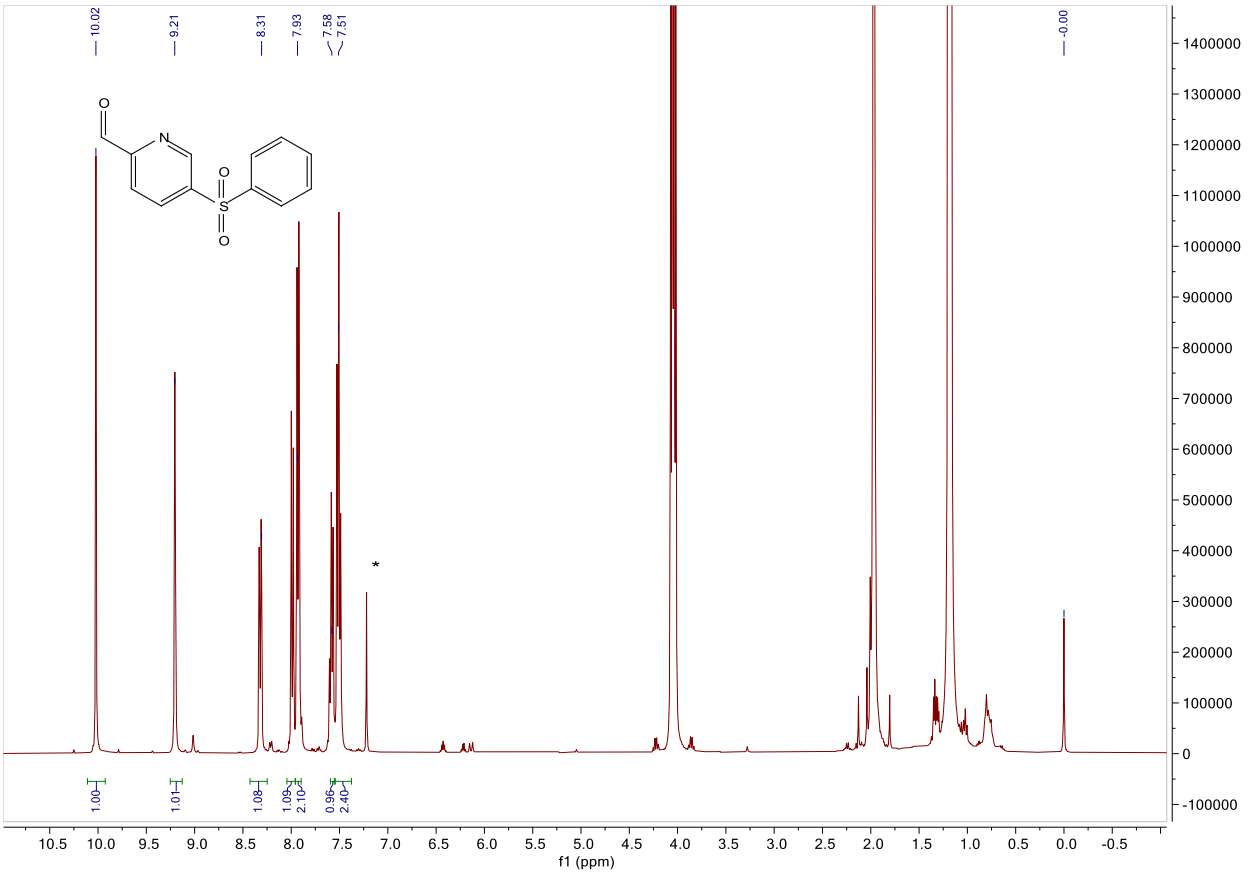

Figure A7.9 NMR of 5-(phenylsulfonyl)picolinaldehyde in $CDCl_3$. Asterisk denotes $CDCl_3$ peak. References to TMS (δ 0.00).

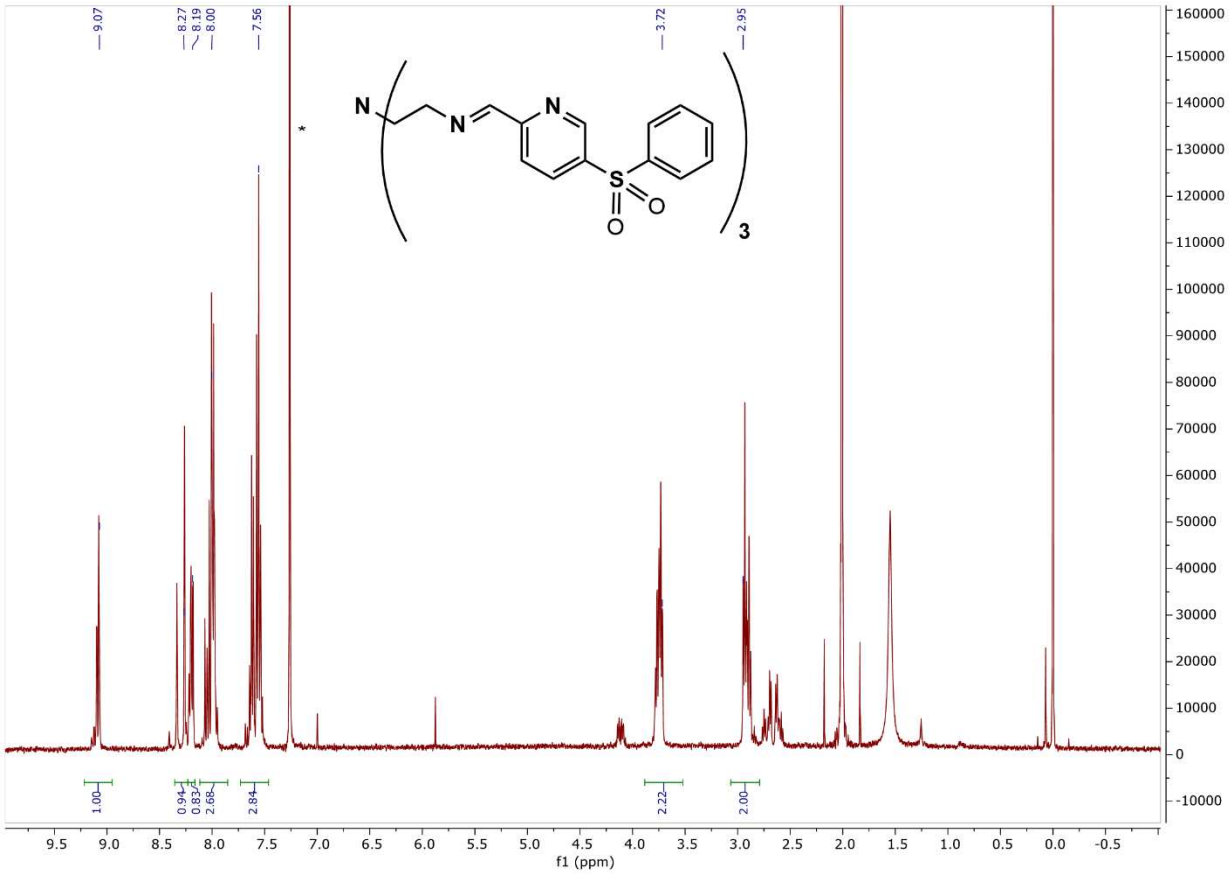

Figure A7.10 NMR of tren(SO_2Ph)$_3$ in $CDCl_3$. Asterisk denotes $CDCl_3$ peak. References to TMS (δ 0.00).

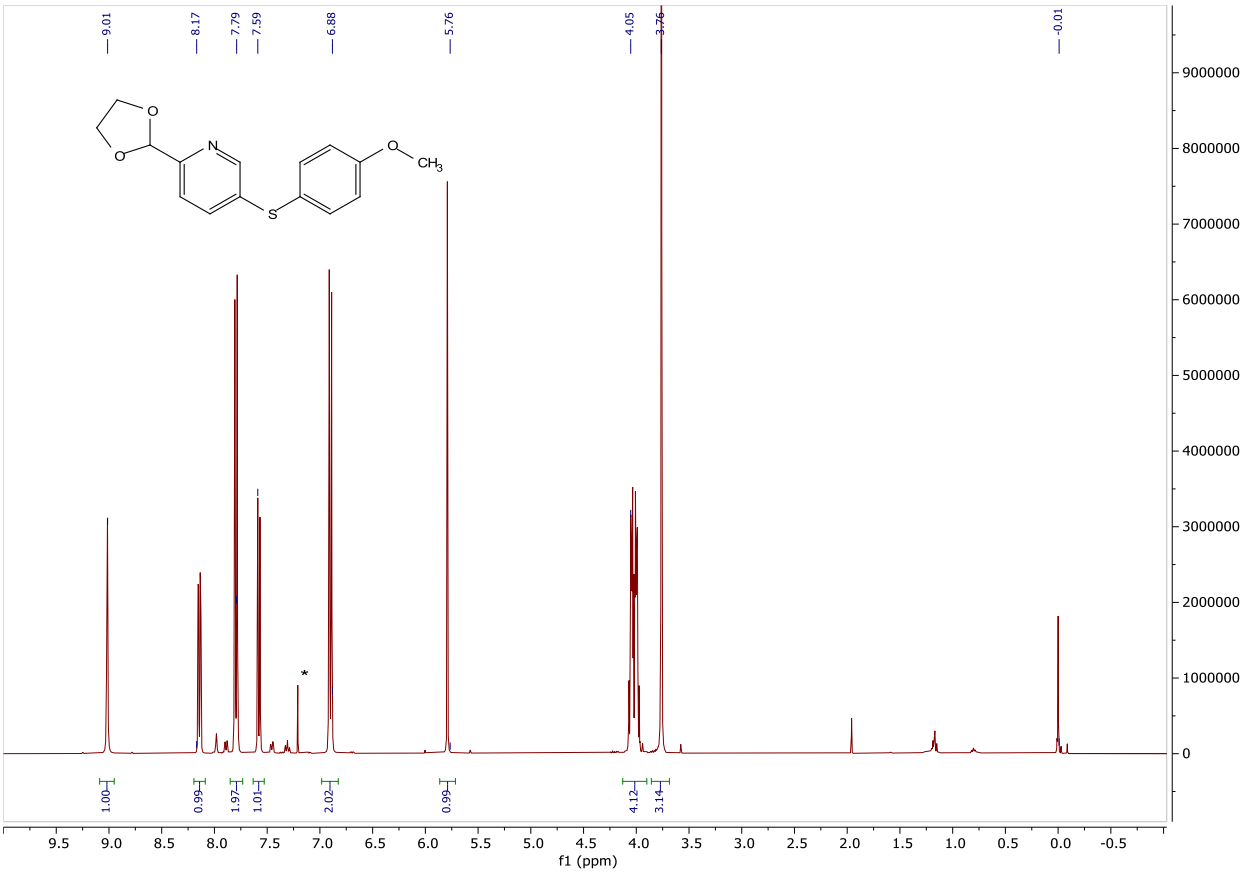

Figure A7.11 NMR of 2-(1,3-dioxolan-2-yl)-5-((4-methoxyphenyl)thio)pyridine in $CDCl_3$. Asterisk denotes $CDCl_3$ peak. References to TMS (δ 0.00).

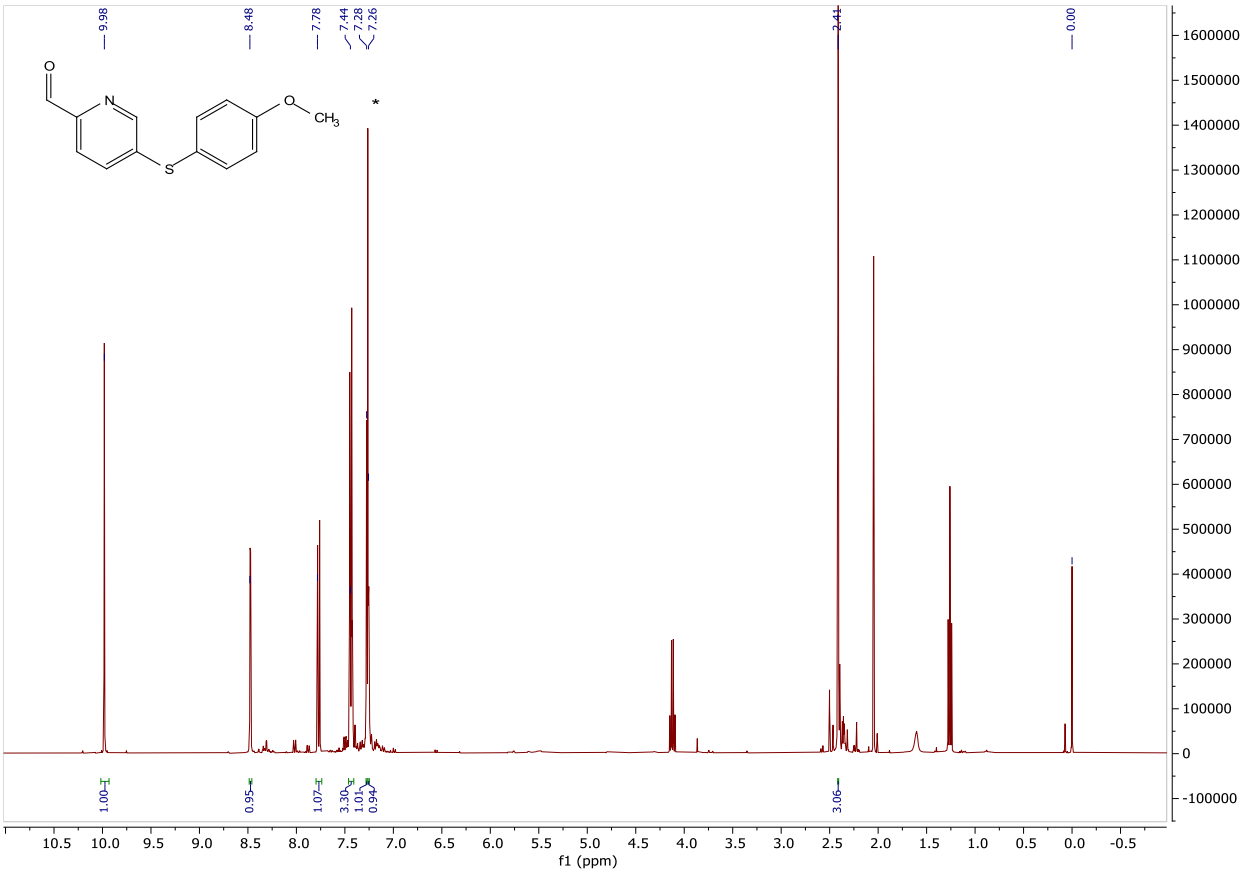

Figure A7.12 NMR of 5-((4-methoxyphenyl)thio)picolinaldehyde in $CDCl_3$. Asterisk denotes $CDCl_3$ peak. References to TMS (δ 0.00).

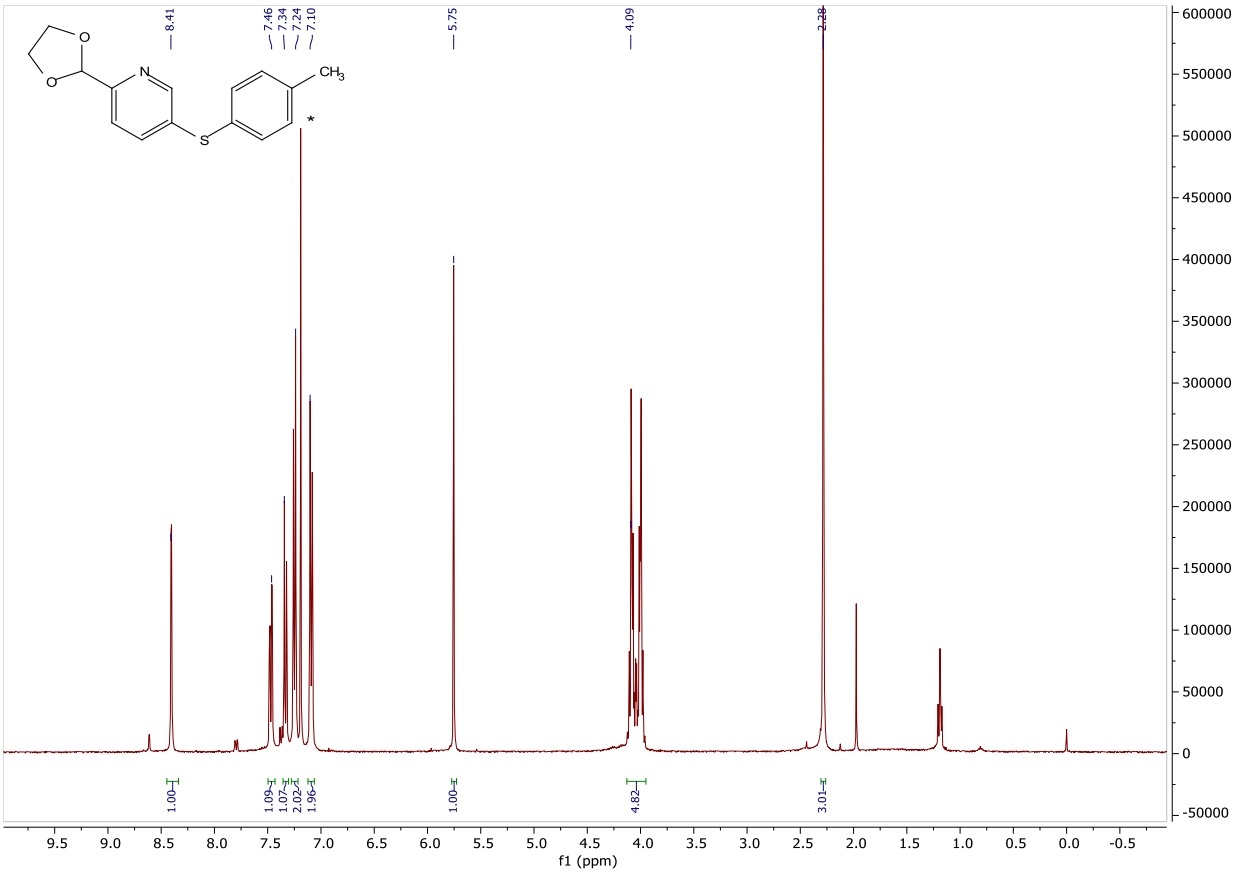

Figure A7.13 NMR of 2-(1,3-dioxolan-2-yl)-5-(p-tolylthio)pyridine in $CDCl_3$. Asterisk denotes $CDCl_3$ peak. References to TMS (δ 0.00).

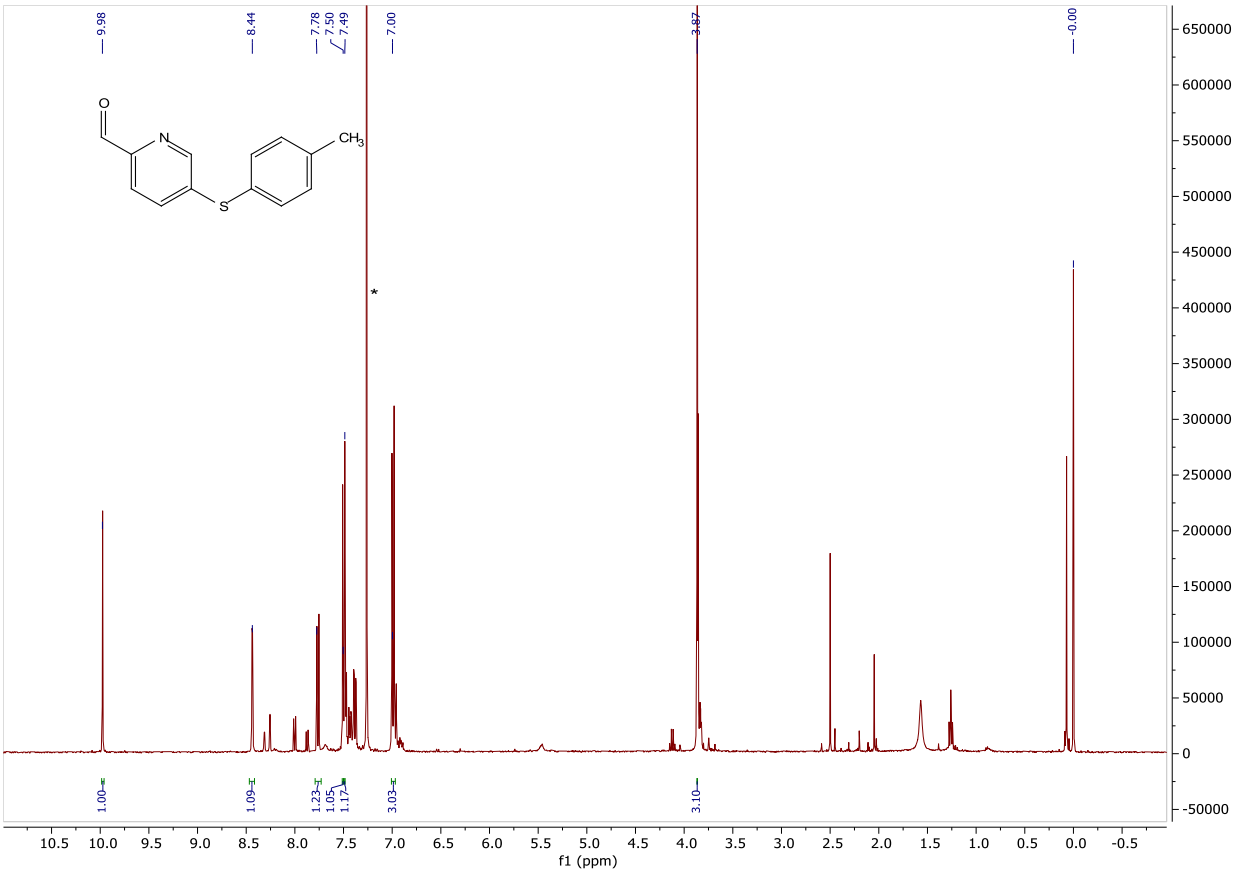

Figure A7.14 NMR of 5-(p-tolylthio)picolinaldehyde in $CDCl_3$. Asterisk denotes $CDCl_3$ peak. References to TMS (δ 0.00).

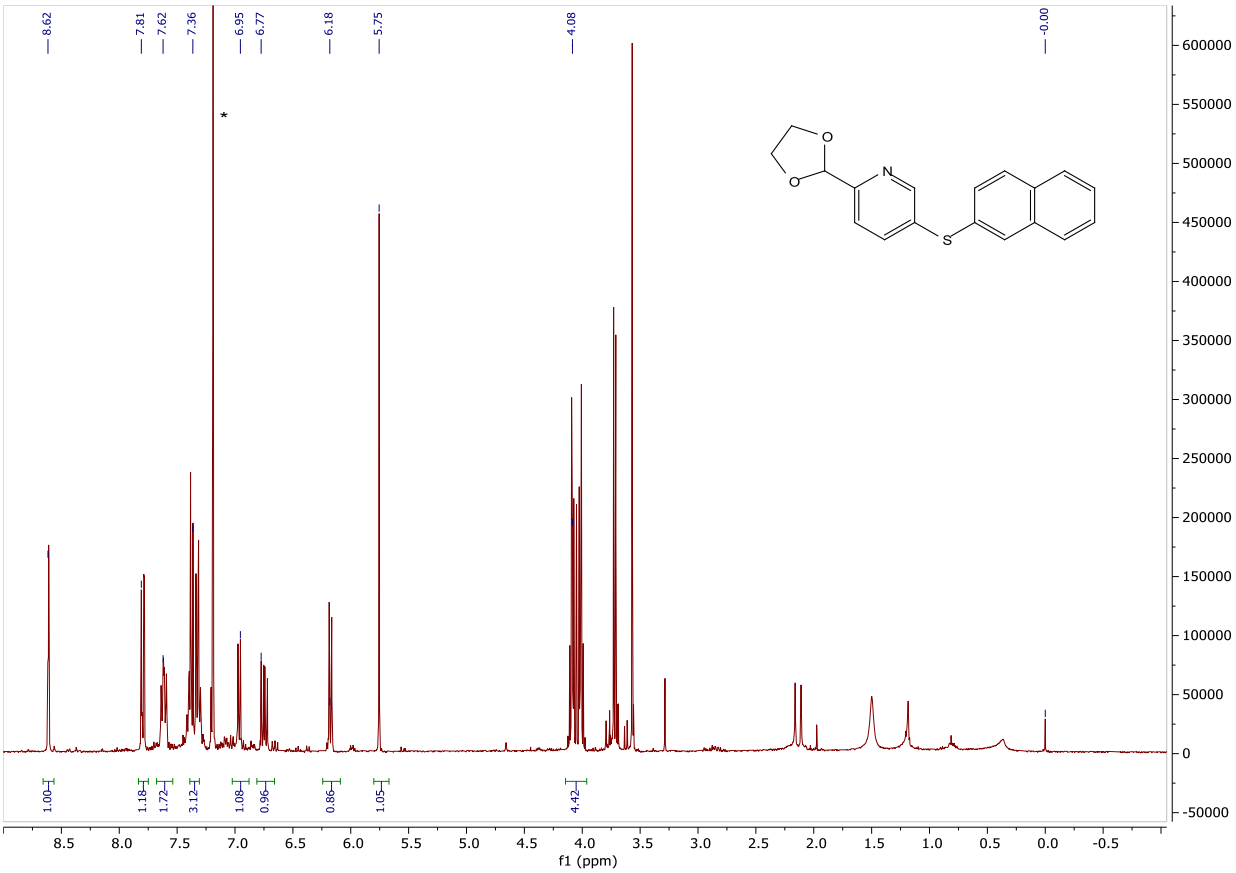

Figure A7.15 NMR of 2-(1,3-dioxolan-2-yl)-5-(naphthalen-2-ylthio)pyridine in $CDCl_3$. Asterisk denotes $CDCl_3$ peak. References to TMS (δ 0.00).

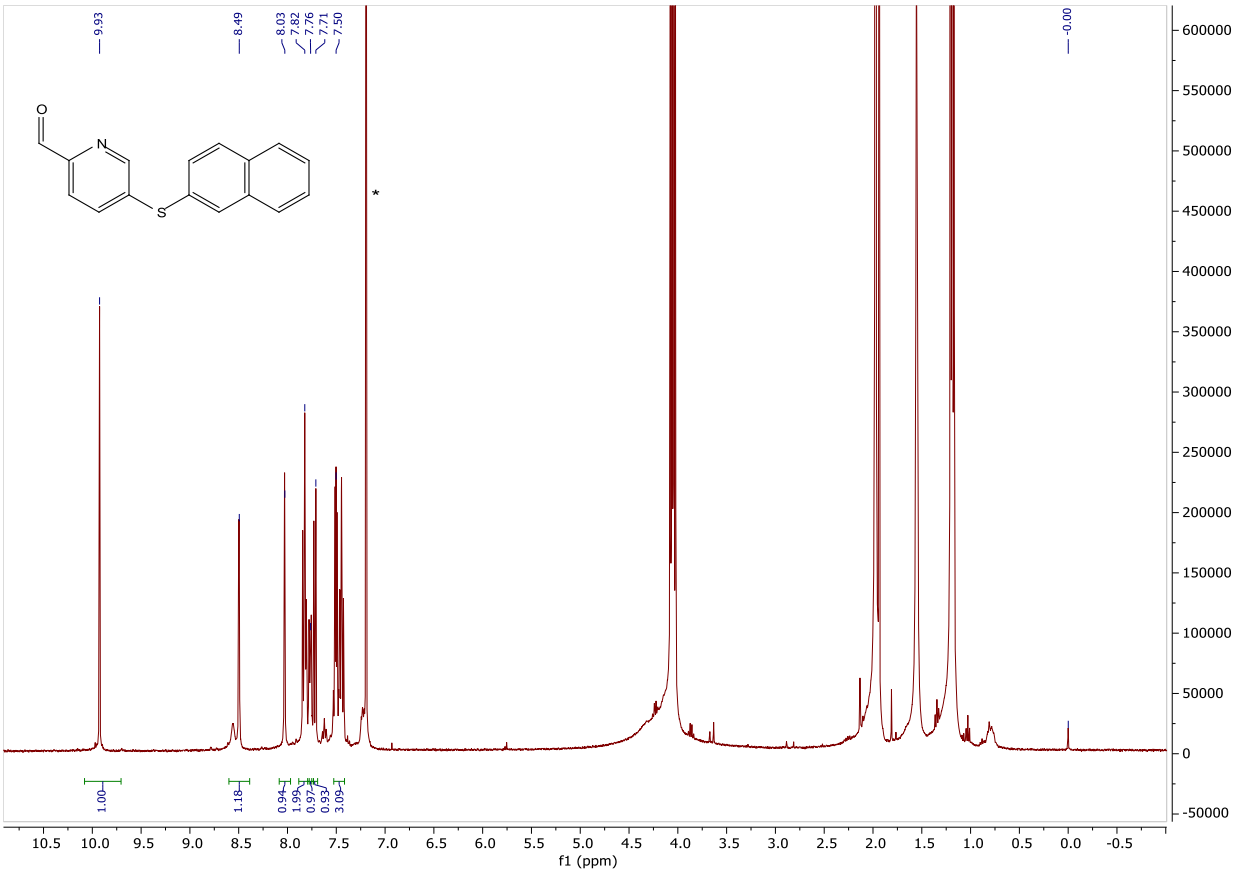

Figure A7.16 NMR of 5-(naphthalen-2-ylthio)picolinaldehyde in $CDCl_3$. Asterisk denotes $CDCl_3$ peak. References to TMS (δ 0.00).

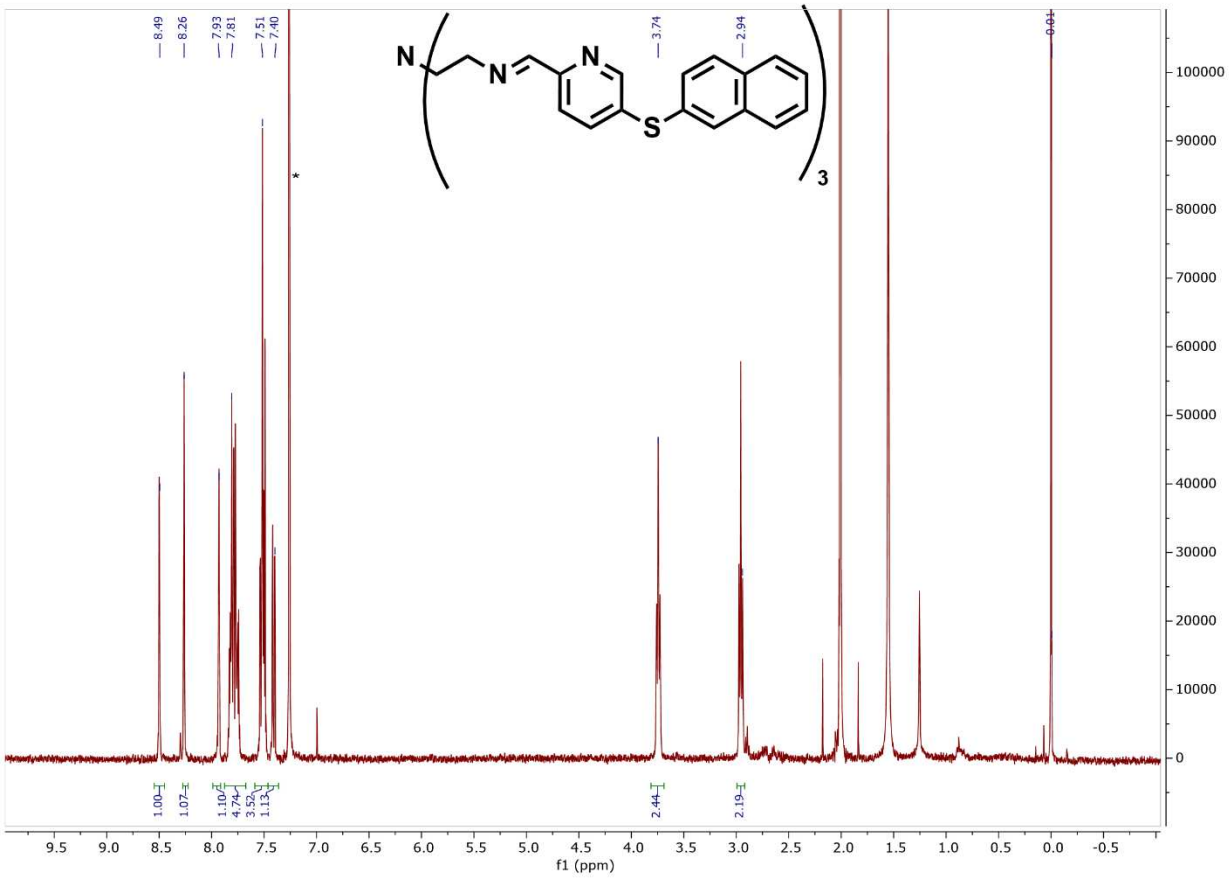

Figure A7.17 NMR of tren(PySNaph)$_3$.

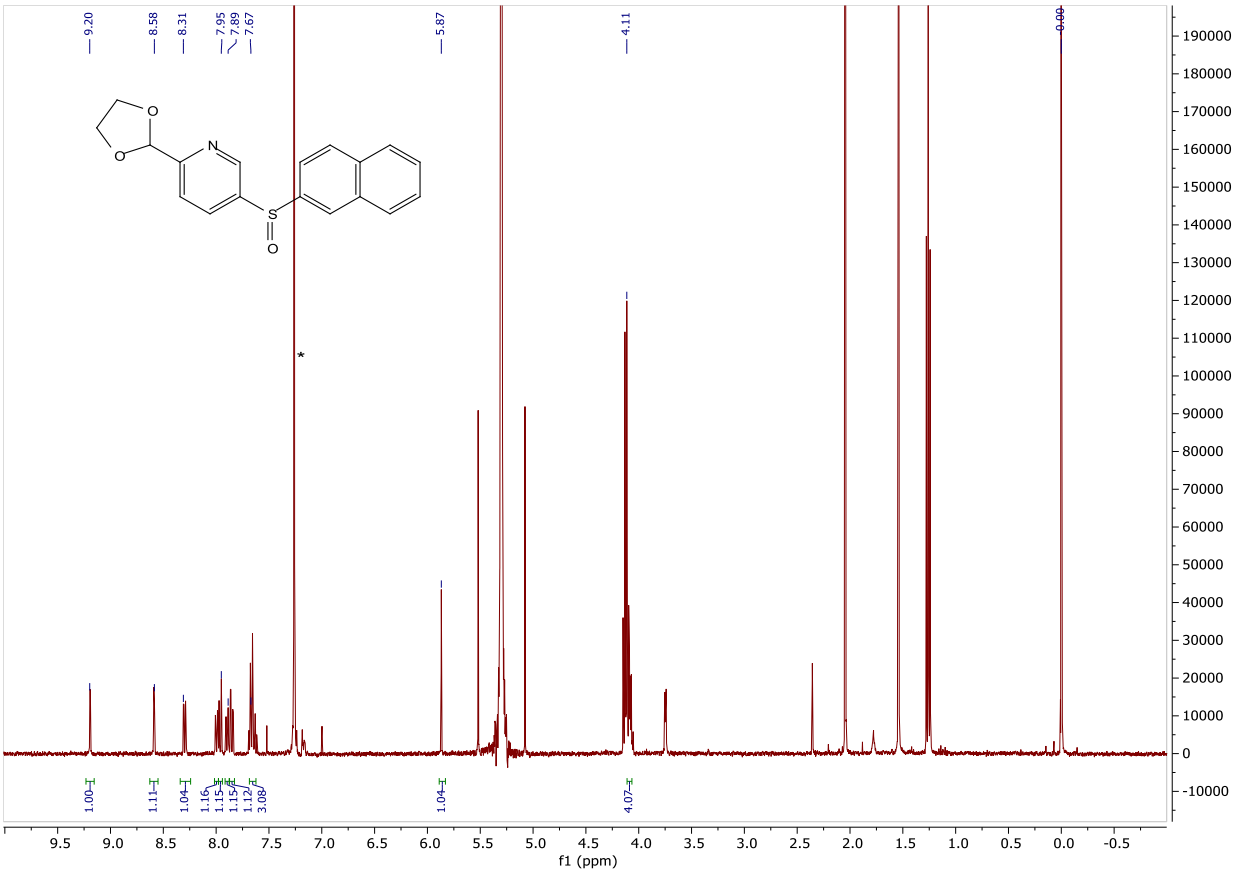

Figure A7.18 NMR of 2-(1,3-dioxolan-2-yl)-5-(naphthalen-2-ylsulfinyl)pyridine in $CDCl_3$. Asterisk denotes $CDCl_3$ peak. References to TMS (δ 0.00).

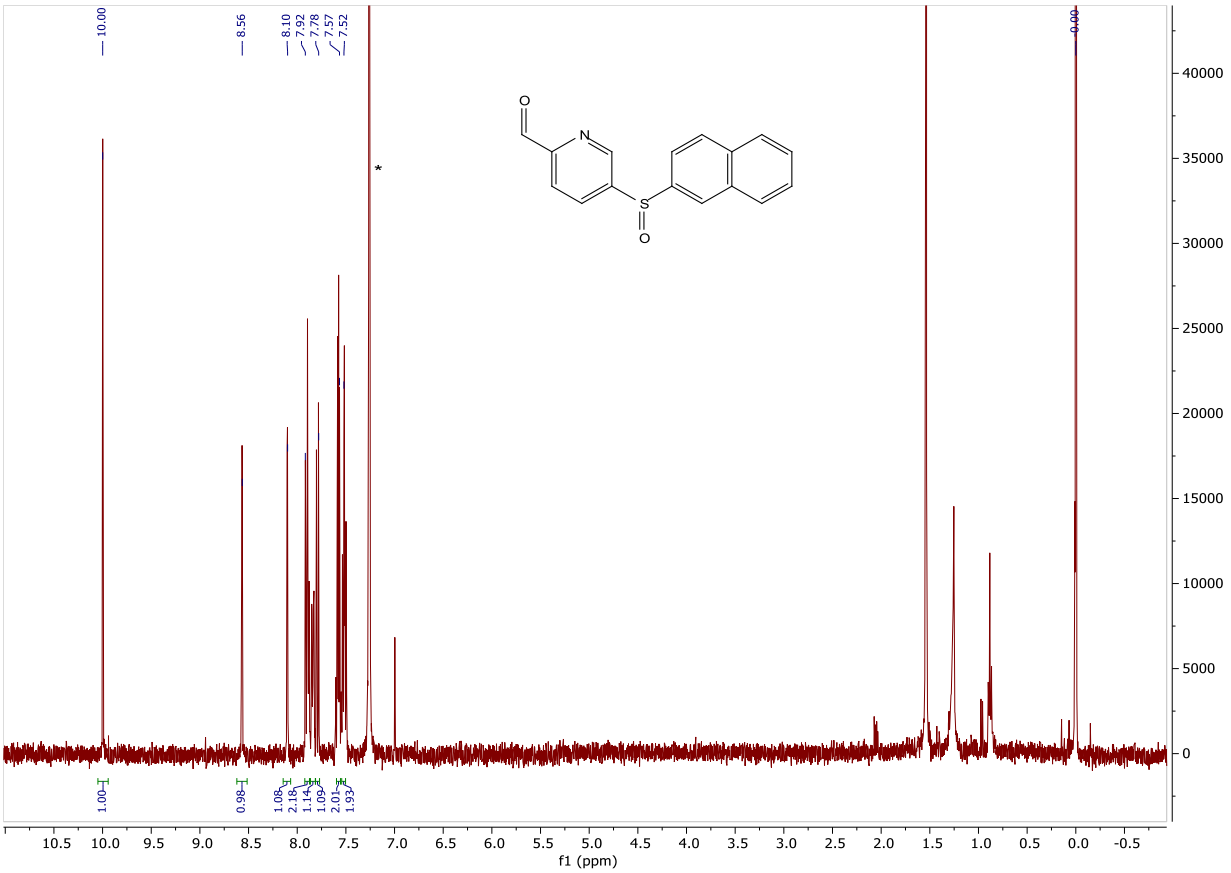

Figure A7.19 NMR of 5-(naphthalen-2-ylsulfinyl)picolinaldehyde in $CDCl_3$. Asterisk denotes $CDCl_3$ peak. References to TMS (δ 0.00).

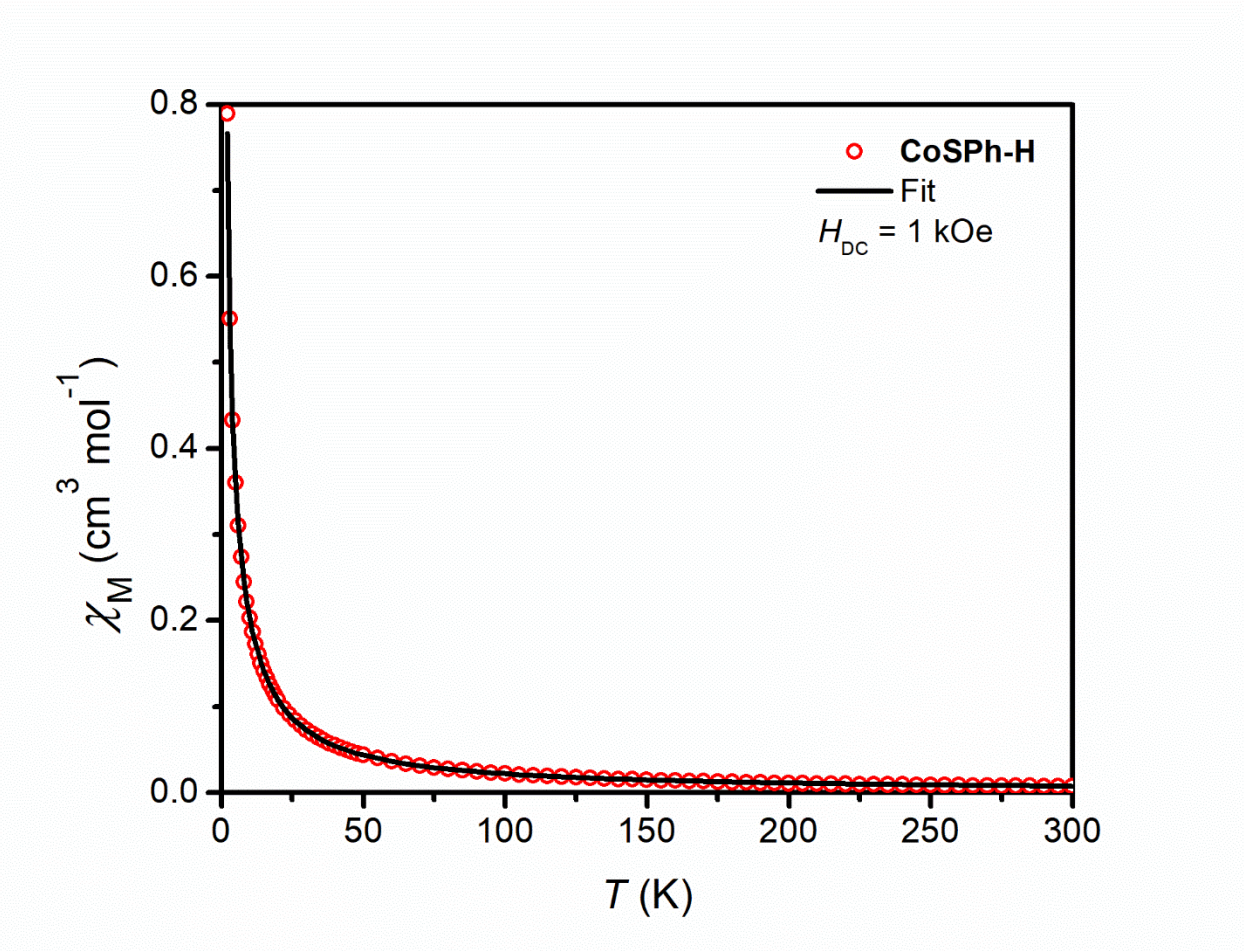

Figure A7.20 Susceptibility vs. temperature plot of **CoSPh-H** at 1 kOe.